UNIVERSITY OF CALIFORNIA

Los Angeles

Predictability and Repeatability of Non-Ergodic Site Response for Diverse Geological Conditions

A dissertation submitted in partial satisfaction

of the requirements for the degree

Doctor of Philosophy in Civil Engineering

by

Pengfei Wang

2020

ABSTRACT OF THE DISSERTATION

Predictability and Repeatability of Non-Ergodic Site Response for
Diverse Geological Conditions

by

Pengfei Wang
Doctor of Philosophy in Civil Engineering
University of California, Los Angeles, 2020
Professor Jonathan P. Stewart, Chair

Ground motion models (GMMs) are used to predict ground motion intensity measures given parameters descriptive of source, path, and site conditions. These GMMs incorporate source, path, and site response models that represent approximately the average conditions in the database from which the GMMs were derived. In the case of NGA-type models, global data is used, potentially with path and site adjustments for large regions with ample data (e.g., California), so the predictions represent either global or regional averages. In contrast, when GMMs are applied for a specific engineering project, the source, path, and site response attributes of interest are those local to the site, which may depart from the global or regional averages represented by the GMM. In this context, I refer to the source, path, and site models in the GMM as ergodic. Alternative models that consider local, or site-specific features, are considered non-ergodic, and have the potential to significantly reduce the ground motion variability that is considered in probabilistic seismic hazard analysis.

My thesis work is concerned principally with the site response component of GMMs, and in particular, with evaluating the effectiveness of predictive models available for non-ergodic site response analysis. The ergodic site amplification within a GMM represents the global or regional average for the site's value of time-averaged upper 30 meters shear wave velocity

and basin depth. Many local effects may introduce departures in site response from the ergodic model, including strong impedance contrasts within the shear wave velocity profile, an unfavorable location relative to a basin edge, complexity of local terrain, and perhaps other factors. Therefore, the ergodic site response model has two drawbacks: (1) potential for a biased estimate of mean site response and (2) because the ergodic model averages over a diverse array of conditions having many different site responses, the model carries a relatively large standard deviation.

The alternative of non-ergodic site response takes into account the particular geologic conditions at a site that control site response. If applied properly, non-ergodic site response can produce unbiased estimates of site response and remove site-to-site variability from the total standard deviation, which is a significant contributor. One method of evaluating non-ergodic site response in practice is to utilize recordings at the site to evaluate misfits from a GMM, and then use this information to construct a median site response model. However, when on-site recordings are not available, site-specific analysis requires the application of various predictive models. The questions addressed in this research relate to the effectiveness of different predictive models for estimation of site response.

The general approach followed in this research was to develop a database of available recordings for sites in a study region, analyze the data to develop non-ergodic site responses, and then either 1) apply existing predictive models to the sites with "measured" (i.e., non-ergodic) site responses and then evaluate their effectiveness over the population of sites or; 2) develop a new predictive model where existing models cannot be reasonably applied. The first approach of evaluating existing tools is applied to a population of 159 sites in California. The second approach of developing a new model is applied to 7 sites in Obihiro (Japan), where soft soil conditions (V_{S30} = 102 to 211 m/s) require the development of a novel modeling framework.

For the California sites, the predictive models considered are ground response analysis (GRA; one-dimensional shear wave propagation through a soil column), square-root impedance method (SRI), and models conditioned on horizontal-to-vertical spectral ratio (HVSR) vs frequency plots. The GRA and SRI methods require a shear wave velocity (V_S)

profile for the site and models for material damping for each soil horizon in the profile. Among the 159 sites, the profile depth range is 30 to 255 m (profile period range is 0.06 to 1.02 sec). The HVSR model requires HVSR data, which can be derived from microtremors or earthquake recordings. A challenge that was encountered in the application of GRA and SRI methods was the lack of soil profiles to accompany V_S profiles. I developed protocols for estimation of soil type parameters that allow geotechnical damping models to be applied. Additional damping models were also considered, including one that is informed by high-frequency spectral decay of site ground motions (κ_0).

Despite the depth of the profiles considered in this work being relatively modest, ground response analyses (or square-root-impedance analyses) are able to improve site response predictions relative to ergodic models for approximately 36% of sites (for periods less than or equal to the site period). The inability of site-specific methods to improve prediction accuracy for the 64% sites could stem from three potential sources: (1) simulations of one-dimension wave propagation do not accurately characterize the physics of site response; (2) the measured V_S profile from the site does not accurately represent site conditions, either because of strong site heterogeneity or inaccurate measurements; (3) portions of the site profile beneath the profile depth significantly impact the site response in the frequency range of the measured profile. These problems are common to some extent in virtually all site response simulations, so understanding their collective impact is of practical importance. The unknown influence of these factors introduces epistemic uncertainties, which we quantify. Lacking any knowledge of whether a given site is well represented with one-dimensional simulations, this epistemic uncertainty is only slightly reduced from that of the site-to-site variability in ergodic models within soil column period range. For the subset of sites where this modeling is effective, the epistemic uncertainty is more substantially reduced by amounts ranging from 0.05-0.10 in natural log units.

The HVSR model considered in this work (adapted from a model in literature) uses the frequency and amplitude of peaks in HVSR spectra. I identify three populations of sites based on microtremor data – those for which a clear HVSR peak is evident (40%), those for which no peak occurs (40%), and intermediate/ambiguous cases (20%). When the ergodic model

is used, sites with a peak are observed to have higher bias and site-to-site variability than sites without peaks; as a result, commonly used models for site-to-site variability represent a blending of these condition because the occurrence of peaks is not accounted for. Use of the HVSR model for sites with peaks does not appreciably change the bias but reduces dispersion at long periods (> 1 sec) relative to what is obtained with an ergodic model. The lack of improvement at short period could be caused by false positives (peaks in HVSR that do not appear in site response) and not well-aligned peak positions between HVSR and site response, and may also be influenced by the model used in our analyses having been derived for conditions in Japan. I recommend a California-specific bias correction for sites without a peak.

For the Obihiro (Japan) sites, I developed a region-specific site amplification model applicable to the peaty organic soils in this region. The analysis of site response from regional data required removal of source-specific biases and careful consideration of source-to-site path effects. These considerations were essential to avoid mapping source- or path-related model misfits into estimates of site response. I considered two subduction ground motion models as reference models. By paying special attention to the conditions for which the path models are effective, and making adjustments for between-island path misfits (Hokkaido to Honshu and vice-versa), I found the proposed approach effectively identifies site effects, and that the results are insensitive to the selected ground motion model. Observed site responses are characterized by strong resonances at first-mode site frequencies as derived from HVSR measurements.

The dissertation of Pengfei Wang is approved.

Frederic R Paik Schoenberg

Yousef Bozorgnia

Scott J. Brandenberg

Jonathan P. Stewart, Committee Chair

University of California, Los Angeles

2020

To my family.

For their endless love, support and encouragement

Table of Contents

List of Figures

List of Tables

ACKNOWLEDGMENTS

First of all, I would like to express my sincere gratitude to my advisor Professor Jonathan P. Stewart for the continuous guidance and support of my whole Ph.D. study. His insights, knowledge, patience, and motivation have helped me to acquire significant and essential skills in the research of geotechnical earthquake engineering and engineering seismology. His guidance helped me in all the time of writing technical reports, journal papers, and this dissertation. I could not have imagined having a better advisor and mentor for my Ph.D. study.

Besides my advisor, I would also like to thank the rest of my defense committee: Professors Scott J. Brandenberg, Yousef Bozorgnia, and Frederic R Paik Schoenberg, for their valuable and insightful comments and questions. Their advice strengthen my research and widen it from various perspectives.

The California sites research was supported by grants from the California Strong Motion Instrumentation Program, California Geological Survey, under Agreement Number 1016-985. Partial support was also provided by the US Geological Survey under contract number G17AP00018. This support is gratefully acknowledged. The Obihiro sites research was supported by California Department of Water Resources (Contract No. 4600010406). I also thank Yi Tyan for sharing her processed seven Obihiro sites metadata, staffs at OCDC for providing access to the ground motion data files, and Tadahiro Kishida for providing advance access to NGA-Subduction ground motion data in support of this work.

Last but not the least, I would like to thank my family: my parents and my wife for all types of support and encouragement they provide during my Ph.D. study. I am also very grateful to meet and make friends with such great people, my labmates, UCLA faculty and staff, and students.

VITA

2011–2015 B.S. (Traffic Engineering), Tongji University, Shanghai, China.

2015–2016 M.S. (Civil Engineering), UCLA, Los Angeles, California.

2017–2020 M.S. (Statistics), UCLA, Los Angeles, California.

PUBLICATIONS

Wang, P., Stewart, J.P., Tsai, Y.T., Brandenberg, S.J. (In Preparation). Region-Specific Linear Site Amplification Model for Peaty Organic Soil Sites in Hokkaido, Japan. *Earthquake Spectra.*

Adhi, S.K., Mazzoni, S., Kishida, T., Wang, P., Nweke, C.C., Kuehn, N.M., Contreras, V., Rowshandel, B., Stewart, J.P., Bozorgnia, Y. (2020). Engineering characteristics of ground motions recorded in the 2019 Ridgecrest earthquake sequence. *Bulletin of the Seismological Society of America.*
https://doi.org/10.1785/0120200036

Wang, P., Zimmaro, P., Ahdi, S.K., Kwak, D.Y., Stewart, J.P.. (2020). Shear Wave Velocity Database and Its Application for Analysis of Non-Ergodic Site Amplification Effects. *USGS.* Report No. G17AP00018.

Brandenberg, S.J., Stewart, J.P., Wang, P., Nweke, C.C., Hudson, K., Goulet, C.A., Meng, X., Davis, C.A., Ahdi, S.K., Hudson, M.B., Donnellan, A., Lyzenga, G., Pierce, M., Wang, J., Winters, M.A., Delisle, M.-P., Lucey, J., Kim, Y., Gallien, T.W., Lyda, A., Yeung, J.S.,

Issa, O., Buckreis, T., Yi, Z.. (2020). Ground Deformation Data from GEER Investigations of Ridgecrest Earthquake Sequence. *Seismological Research Letters.* https://doi.org/10.1785/0220190291.

Wang, P., Stewart, J. P., Bozorgina, Y., Boore, D. M., Kishida, T. (2017). R Package for Computation of Earthquake Ground Motion Response Spectra. Report No. 2017/09. *PEER*, UC Berkeley.

Zheng, N., Dantsuji, T., Wang, P., Geroliminis, N., (2017). Macroscopic Approach for Optimizing Road Space Allocation of Bus Lanes in Multimodal Urban Networks Through Simulation Analysis. *Journal of the Transportation Research Board*, No. 2651, DOI:10.3141/2651-05.

CHAPTER 1

Introduction

1.1 Motivation

Ergodic models for site response provide a mean estimate conditioned on certain site parameters (typically the time averaged shear wave velocity in the upper 30 meters of the site, V_{S30}, and basin depth). The ergodic estimate of site response includes all site amplification mechanisms (impedance, nonlinearity, resonance, two- and three-dimensional wave propagation in basins, etc.), but these effects are smoothed over a large number of sites with different characteristics. As such, the associated site-to-site uncertainties (denoted ϕ_{S2S}) are substantial, increasing mean or $>$ 50th percentile ground motions at long return periods as derived from probabilistic seismic hazard analyses (PSHA) relative to what would be obtained with more accurate methods.

Site-specific or non-ergodic site response is intended to account for wave propagation processes at a specific site that control site response. An unbiased estimate of site-specific site response, for example as derived from analysis of earthquake recordings, substantially reduces ϕ_{S2S} [83, 92]. For sites without recordings, many projects seek to estimate site response using ground response analyses (GRA), which consider the effects of one-dimensional (1D) shear wave propagation and soil nonlinearity. One alternative method used for some applications is the square-root impedance (SRI) method (first introduced as quarter wave length method by [61] and later renamed as SRI by [19]). A different modeling approach, which is not conditioned on assumptions regarding wave propagation, supplements the site amplification from V_{S30}-scaling models with models for peaks in site amplification functions that are related to horizontal-to-vertical spectral ratio (HVSR) vs frequency plots ([52, 53, 72]), typically

from microtermor measurements at the site of interest. Parameters derived from such plots include the peak frequency (f_{peak}) and the amplitude of peaks as site parameters [52, 53, 55, 56, 72]. Open questions related to these practices are: (1) How effective are such methods at capturing observed behavior, and how does this change with period?; and (2) What levels of epistemic uncertainty (ϕ_{S2S}) should be used in PSHA when these site-specific site response methods are used?

Answers to the above questions obviously depend on the availability of models that could be reasonably expected to predict site response for a given region. This study has two major elements in which such models are and are not available. The bulk of this thesis is related to site response in California, where site response models are available and are used in a wide variety of projects developing hazard estimates. The second element of developing a new model is applied to a study region in Obihiro (Japan), where soft soil conditions (V_{S30} = 102 to 211 m/s) require the development of a novel modeling framework.

For the California case in which existing models are to be assessed, a sensible means by which to answer the above questions is through comparisons of prediction results to data. For the case of GRA, this general line of research contains numerous contributions over many years, with a typical application taking various input motions, running them through 1D soil columns, and comparing resulting response spectra to those from recordings [29, 38, 59]. However, with the exception of vertical arrays, this research approach has a limited ability to answer the above questions, because predicted ground surface motions are strongly dependent on input motions, which are often highly uncertain. As a result, the effectiveness of the site response prediction is somewhat obscured.

The use of vertical arrays overcomes this problem because of the availability of recorded input motions, and has produced interesting findings that illustrate limitations, biases, and uncertainties associated with ground response analyses [3, 62, 63, 117]. However, there are limitations associated with the use of vertical arrays to validate GRAs. First, the number of vertical arrays with sufficient ground motion recordings and site characterization is limited (but certainly growing with time). Second, vertical arrays only measure site response over the length domain of the array; as such they are not useful for evaluating long-period features

that involve wavelengths longer than array dimensions. Third, the within-motion boundary condition that is used in analysis of vertical array data does not match that used in typical forward applications, in which outcropping input motions are selected.

To address these limitations, I apply here an alternative method for validating ground response analyses and other methods using data from surface-only instruments. The concept is to use recordings to infer the non-ergodic site response over a wide frequency range. The effectiveness of ground response analysis, and other methods, is then assessed by comparing predicted levels of site response against observation. This departs from the aforementioned prior work in that model effectiveness is not based on ground motions from a particular event (or series of events), but on the site amplification relative to a reference condition. This work was comprised of four components, as described in the following paragraphs.

The first component is assembling the required data. If not already available from another project (such as NGA projects, which involve large-scale data collection and synthesis), this is a substantial task. The information required is identical to that needed for ground motion model development, namely, a database that includes information on source attributes, site conditions at recording stations, and ground motions (with record-specific processing details). In this project, I supplemented the NGA-West2 database with additional sites and events, as described in Chapter 2. A need for the present work that is not shared in ground motion model development projects, is seismic velocity profiles at recording stations (particularly shear-wave velocity, V_S, versus depth profiles).

The second component consists of ground motion analyses targeted at extracting information on site responses at recording stations. The steps involved in developing these results are described elsewhere in [92], so the procedure is not repeated here. What these analyses provide is an estimate of a site term, denoted η_S, for each site and response spectral oscillator period. This site term represents the mean difference between a regionally-unbiased ground motion model and observed motions at the site. For weak shaking conditions that do not induce soil nonlinearity, the sum of η_S and the ergodic site term for the site (F_S), comprises the mean non-ergodic site response ($\mu_{\ln Y}$) relative to the ground motion model's reference

condition:

$$\mu_{\ln Y} = F_S + \eta_S \tag{1.1}$$

The third component consists of predicting site response for each site in the data inventory using available information on site conditions. In the case of GRA, a V_S profile is required, and borehole data indicating soil stratigraphy and soil type characteristics for each layer is also useful (for estimation of modulus reduction and damping relations). SRI also requires soil unit weight and V_S profiles. Methods using horizontal-to-vertical spectral ratios (HVSR) require these spectral ratio plots, preferably from ambient noise measurements or continuously streamed noise from permanent strong motion stations from each site [51, 72].

The fourth component involves model-to-data comparisons in the form of residuals analyses for estimating model bias and uncertainty and the metrics for quantifying the overall model performance.

For the Obihiro (Japan) case, I apply a similar approach as given above, except that the third element (applying models and comparing to data) is replaced with model development. The model considered in this case is conditioned on HVSR-based site parameters.

1.2 Organization

The organization of this dissertation is described as following:

Chapter 2 describes the development of a California database for ground motion studies. In this chapter, the full ground motion database will be introduced including data collection and processing. I also describe the procedures used to assign necessary site and event parameters.

Chapter 3 focuses on developing HVSR-based site parameters. I will first introduce relevant literature regarding HVSR measurements and data processing, as well as prior site amplification models that apply HVSR-based site parameters. Next, I describe the data sources used to obtain HVSR data in my study. Lastly, I present a new procedure for HVSR data processing and its parameterization (fundamental peak identification and fitting).

In Chapter 4, I will describe the ergodic model and each of the three site-specific site response models. The protocols for model inputs of each model will be discussed. Chapter 5 will present the comparison of observed-to-predicted site response given by three site-specific models for California sites. In Chapter 6, I synthesize the results from Chapter 5 to examine overall model biases, model predictability and performance, and the resultant site response uncertainty and variability (ϕ_{S2S}).

Chapter 7 presents the study of site response for peaty organic soil sites in Obihiro. In this chapter, I will discuss the data sources; extract non-ergodic site response by carefully considering effects of source, path, and region; and develop a region-specific site amplification model.

Finally, Chapter 8 summarizes the scope and major findings from this study, and provides recommendations for future work based on what has been learned in this study.

CHAPTER 2

Development of California Database

The non-ergodic ground motion analyses described in Chapter 1.1 require a large database with many recordings (referred to here as *Full Database*). The database requirements for this study match those for ground motion model development projects. A subset of the database is used in components three and four as described in Section 1.1 (*Database Subset for Site Response Studies*).

2.1 Full Database

The database used in this dissertation draws from an expanded version of the NGA-West2 database ([9]), which is a global database for active tectonic regions. There is a significant contribution of data from California to the NGA-West2 database (373 events, 1463 stations, 14,231 recordings) over the time period 1938 to 2010. The site portion of the database ([88]) was developed to provide the principal site parameters used in model development - V_{S30} and various depth parameters denoted as z_x. As part of this project and other complimentary projects, the spreadsheet files that comprised the original NGA-West2 flatfile (pertaining to sources, sites, and ground motions) were converted into tables within a relational database, which is housed on a local server. Data modifications and additions are made within the relational database. The database is accessed using Python scripts within Jupyter notebooks on DesignSafe ([80]).

I have identified earthquakes and recordings since 2011 in California, which significantly extend the NGA-West2 database. Figure 2.1 shows the locations of events sorted by magnitude, most of which occur in five main regions: Bay Area, Eastern Sierra and Nevada,

central California, southern California, and Imperial Valley and northern Mexico. These five zones incorporate most of the urban areas in the state, and contain a large fraction of the ground motion stations. I focus here on the Bay Area and southern California regions. Moreover, since difficulties can be encountered in the analysis of site terms using small magnitude data, I only consider **M** >= 4.0 events ([91]). The data from events within the Bay Area and southern California regions in Figure 2.1 is derived from 25 earthquakes that have produced about 9,300 three-component recordings within the distance cutoffs suggested by [22].

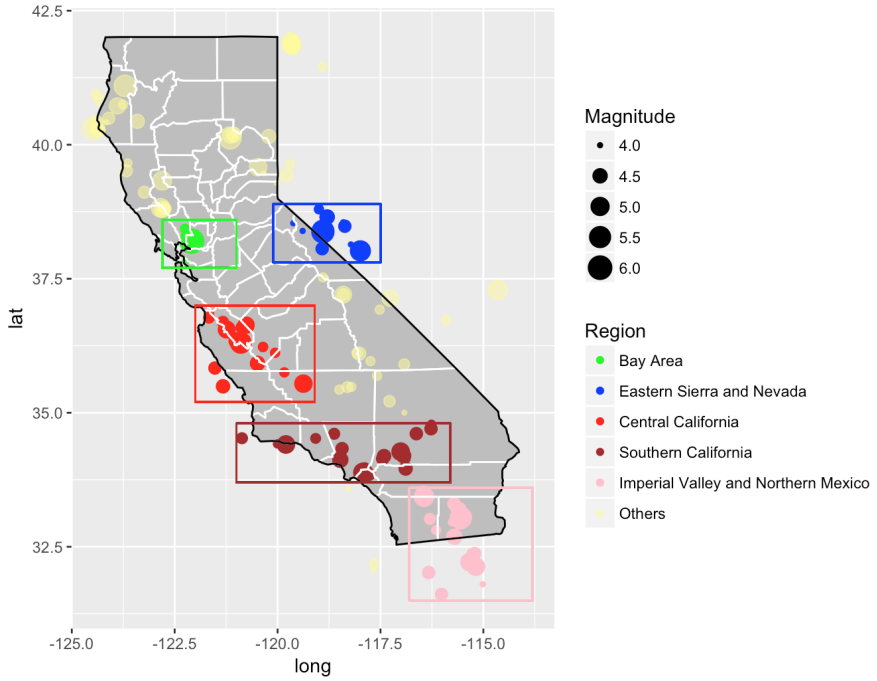

Figure 2.1: Locations of earthquakes in California and northern Mexico with **M** >= 4.0 since 2011 for which ground motion data has been compiled for addition to the NGA-West2 database

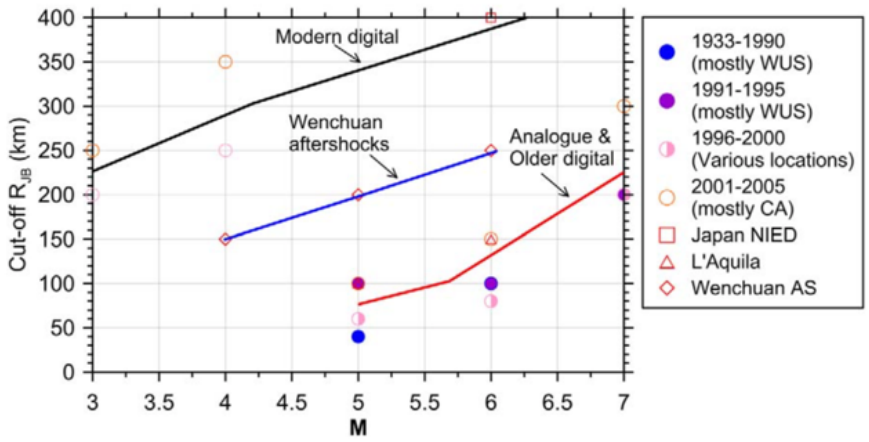

Figure 2.2: The Figure 2.1 in [22] showing magnitude- and distance-dependent cutoff criteria

Not all the data from the selected data events were used. There are well-known problems with sampling bias from recordings at large distance, where the potential exists for only unusually strong records to be present in databases, producing bias. To avoid this problem, I apply magnitude- and distance-dependent screening criteria for modern digital sensors as given by the top black curve in Figure 2.2. The curve is approximately expressed by,

$$R_{max}(km) = 73.08 + 52.31 \times \mathbf{M} \tag{2.1}$$

Only recordings with $R_{JB} < R_{max}$ are used. The data are also further screened for magnitude (requiring $\mathbf{M} >= 4$), to remove duplicate recordings (e.g., seismometers and accelerometers at the same location), and to remove recordings that appear to be unreliable from instrument malfunctions or similar. This leaves about 5873 usable three-component records. Figure 2.3 shows the locations of these events and of the 1185 recording stations with recordings.

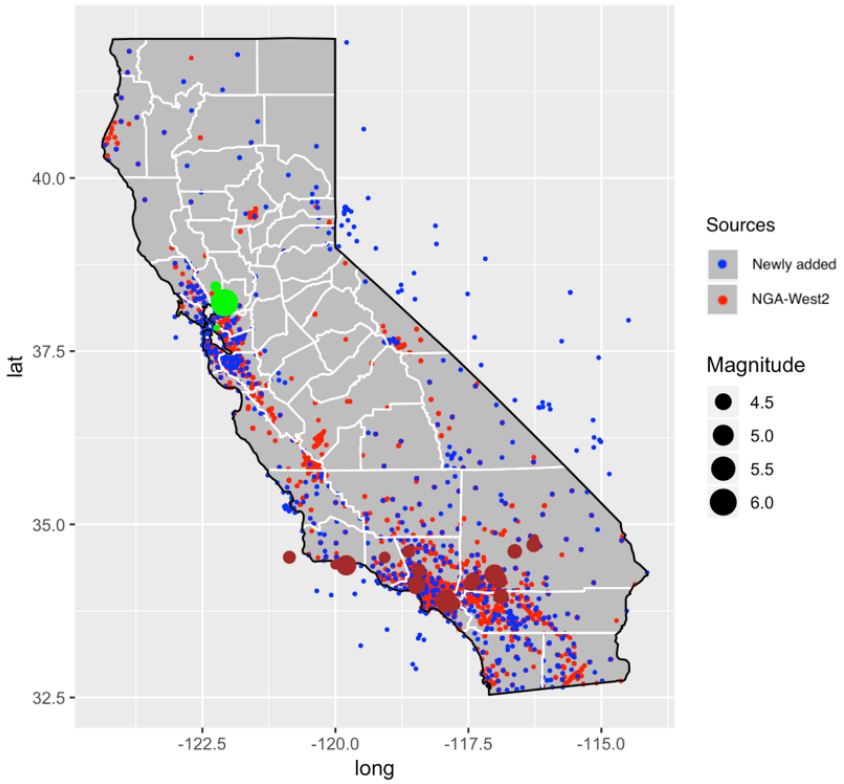

Figure 2.3: Map of California showing locations of considered earthquakes with **M** >= 4.0 since 2011 and locations of stations that recorded the events (blue - new stations, red - stations in NGA-West2 database)

Each of the three-component records has been processed according to standard protocols developed during Pacific Earthquake Engineering Research center (PEER)-NGA projects, as described in [9]. This processing provides a lowest and highest usable frequency for each ground motion component. Horizontal ground motion components are combined to median-component (RotD_{50}) as defined by [18] using the routines given in [109]. I take the lowest useable frequency for RotD_{50} as the higher of the two as-recorded values. This is applied because one compromised component (i.e., by using frequencies lower than its lowest usable frequency) compromises the combination represented by RotD_{50}. Figure 2.4 shows the number of usable RotD_{50} horizontal-component ground motions as a function of oscillator period. The fall-off begins at about 1.0 sec and the data is reduced by 50% at 2.5 sec.

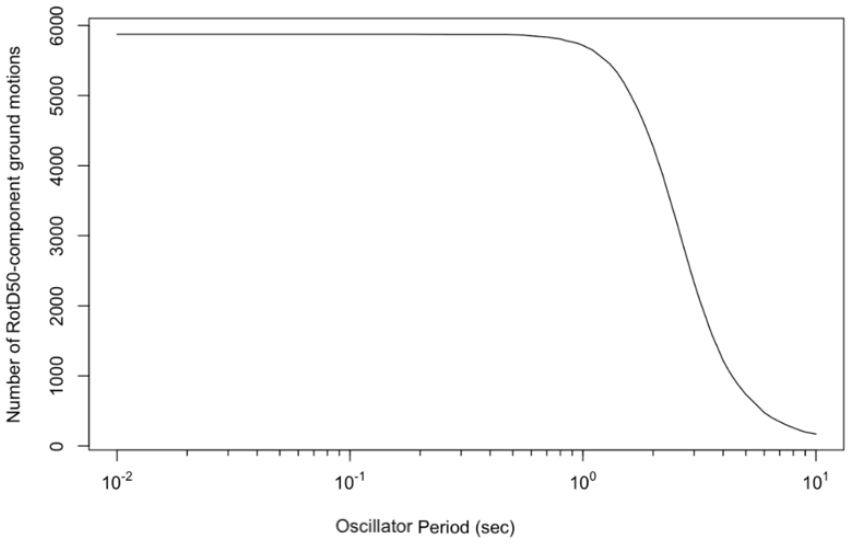

Figure 2.4: Number of usable RotD_{50}-component ground motions as a function of oscillator period for the data added for the Bay Area and southern California regions

2.2 Assignment of site parameters for full database

Considering both the NGA-West2 data and new data, there are 1818 recording sites shown in Figure 2.3. Of those, 1340 are sites that were included in the NGA-West2 site database. Hence, there are 478 new sites that require assignment of site parameters. I use measured V_S profiles to compute V_{S30} when available, and in the absence of this data, I use proxies (slope gradient - [108]; terrain category - [114, 115]; surface geology - originally by [111] and Kriging interpolated by [99], and later updated by [97, 112]).

When more than one proxy-based model for V_{S30} estimation is available, it is customary to employ multiple models to compute a weighted estimate of the mean V_{S30}. In the NGA-West2 project, the mean misfit of a proxy model relative to observations ($\mu_{\ln \mathrm{V}}$) and its aleatory dispersion ($\sigma_{\ln \mathrm{V}}$) were used to compute relative weight as ([88]):

$$\text{relative weight} = \frac{1}{\mu_{\ln \mathrm{V}}^2 + \sigma_{\ln \mathrm{V}}^2} \tag{2.2}$$

Actual weights were adjusted from relative weights to ensure their sum is one. However, that method does not consider correlations between proxy models. An approach was proposed in

[73] to assign weights that accounts for correlations between the inputs used in two proxy-based models. Here, I extend that approach to consider an arbitrary number of n models.

As a problem of linear optimization with linear constraints, it can be formulated in matrix form as,

$$\text{Minimize } \mathbf{w}^\top \mathbf{\Sigma} \mathbf{w} \tag{2.3}$$

$$\text{subject to } \mathbf{0} \leq \mathbf{I}\mathbf{w} \leq \mathbf{1} \text{ and } \mathbf{1}^\top \mathbf{w} = 1 \tag{2.4}$$

where $\mathbf{w}$ is a column vector of length n, $\mathbf{\Sigma}$ is a covariance matrix of dimension $n \times n$ of all available proxy models, $\mathbf{0}$ and $\mathbf{1}$ represent column vectors of length n, and $\mathbf{I}$ is an identity matrix (1 along diagonal, 0 otherwise). The $i-$th row and j-th column entry of $\mathbf{\Sigma}$ is the covariance of proxy models i and j, computed as:

$$\mathbf{\Sigma_{ij}} = \sigma_{\ln V,i} \sigma_{\ln V,j} \rho_{i,j} \tag{2.5}$$

where $\sigma_{\ln V,i}$ and $\sigma_{\ln V,j}$ are standard deviation terms representing the aleatory uncertainty of models i and j, and $\rho_i j$ is the correlation coefficient between the two models.

Equation 2.3 is an objective function that, when minimized, provides the weights $\mathbf{w}$ for the considered proxy models that minimize the aleatory uncertainty of the combined (weighted) model. The first linear constraint in Equation 2.4 requires the estimated weights to be within the range 0 and 1. The second linear constraint in Equation 2.4 ensures that the sum of estimated weights is one. The mean prediction of the combined model is,

$$\hat{V}_{S30} = \mathbf{w}^\top \bar{\mathbf{V}}_{\mathbf{S30}} \tag{2.6}$$

where $\bar{\mathbf{V}}_{\mathbf{S30}}$ contains column vectors of mean V_{S30} estimates for each proxy model.

The optimization process requires a "training" dataset. The dataset includes V_{S30} values from NGA-West2 site database ([89]), measured profiles in California from a profile database (PDB; [5, 85]), and additional V_{S30} values at a USGS web site[1] and CESMD website[2] (the additional sites have a measured V_{S30} but not a measured profile, which is why they do not

[1] `https://earthquake.usgs.gov/data/vs30/us/`

[2] `https://strongmotioncenter.org/wserv/stations/builder/`

appear in the profile database). I excluded V_{S30} values measured using the Remi method due to potential bias associated with that approach ([35]). This results in 994 unique sites with measured V_{S30} values. I considered four proxy models: (1) purely surface geology ([111, 112]), (2) surface geology with local data adjustment ([97, 99]), (3) terrain proxy model ([114]), and (4) surface gradient model ([108]); and denoted them as *geo*, *kri*, *terr*, and *slp* respectively. Except for *slp* model, the other three models are not always available at a given site in California. This various availability of proxy models would lead to different combination of models with different best weights. I develop a flowchart to present each possible scenario and the resultant best weights of each scenario is summarized in Table 2.1. The calculation of best weights was performed using the `constrOptim` function in `R`.

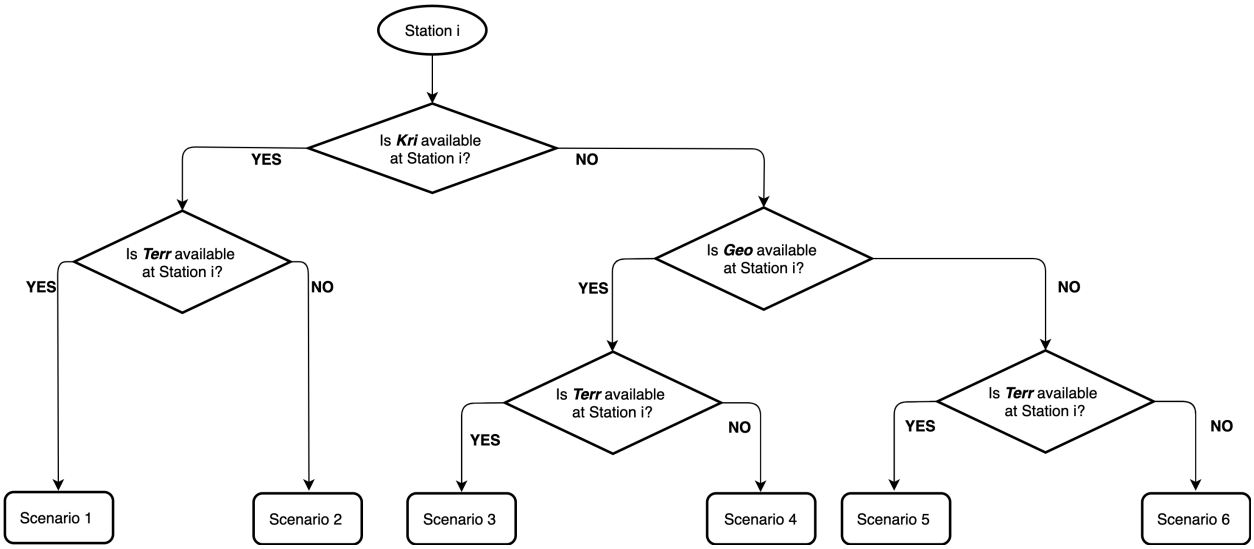

Figure 2.5: The flowchart of each possible scenario for proxy models' availability

There are two important notes: (1) I did not combine *kri* and *geo* when they are both available at a site. This is because they are highly correlated (with correlation coefficient = 0.9), including the two together would cause collinearity issue; (2) *kri* is the preferred approach so the availability of *kri* was examined first following by *geo* and *terr*.

Table 2.1: The best weights of each proxy model under different availability scenarios

	kri	*geo*	*terr*	*slp*
Scenario 1	0.73	-	0.15	0.12
Scenario 2	0.79	-	-	0.21
Scenario 3	-	0.74	0.12	0.13
Scenario 4	-	0.8	-	0.2
Scenario 5	-	-	0.5	0.5
Scenario 6	-	-	-	1

Model *kri* and *geo* play similar roles and perform better than *terr* and *slp*. The relatively low weight for *terr* and *slp* is caused by the larger residuals and dispersion.

2.3 Database subset for site response studies in California

A subset of the full database is applied for site response studies. The criteria used to define this subset are: (1) a minimum number of recordings per site of 10 (applied to ensure statistically robust estimates of site term, η_S); (2) availability of a V_S profile for the site at least 30 m in depth.

Figure 2.6 shows a histogram of the number of recordings at stations in the full database. Of the 1818 sites in the full database, 366 meet the minimum recordings/site criterion.

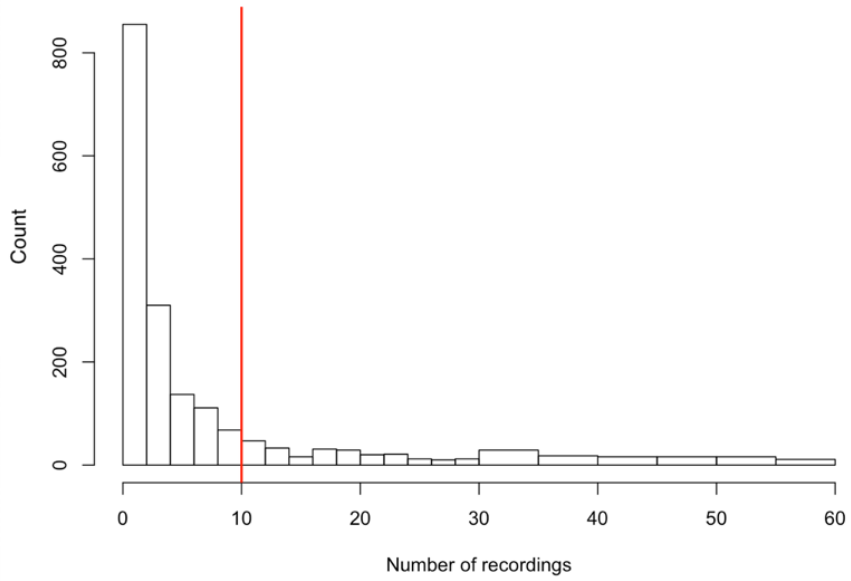

Figure 2.6: Histogram of number of recordings at stations in the full database. Ten is the minimum number of records/station for sites considered in the present research

I performed a search for V_S profiles for each of the sites meeting the first criterion. This was done using the PDB. I find 159 sites with a V_S profile more than 30 m depth and within around 200 m of the strong motion site. Many of these profiles are from [116], which provides V_S profiles from various surface wave tests and H/V spectral ratios from microtremors. Of the 159 sites with V_S profiles, only 9 have a boring log that indicates stratrigraphic details and soil/rock layer descriptions. This geotechnical data is needed to apply models for modulus reduction and damping as a function of shear strain.

Most of the recordings used in this research involve low ground motion amplitudes. Figure 2.7 shows a histogram of strain index, which is defined as:

$$I_\gamma = \frac{PGV}{V_{S30}} \tag{2.7}$$

where PGV is from the surface recording RotD_{50} component. This ratio provides an index related to shear strain ([60, 66]), and can be used to judge the degree to which soil responses are likely to be affected by nonlinearity. As shown in Figure 2.7, 97% of ground motions in the subset have $I_\gamma < 0.03\%$. I conclude that the soil responses are predominantly in the linear range, meaning that modulus reduction is effectively unity and damping is at the

minimum value. I refer to the minimum damping from geotechnical models ([36] for soils with fines; [76] for granular soils) as D^L_{min}. As a result, the primary need for stratigraphic and material description information is to define D^L_{min} as a function of depth.

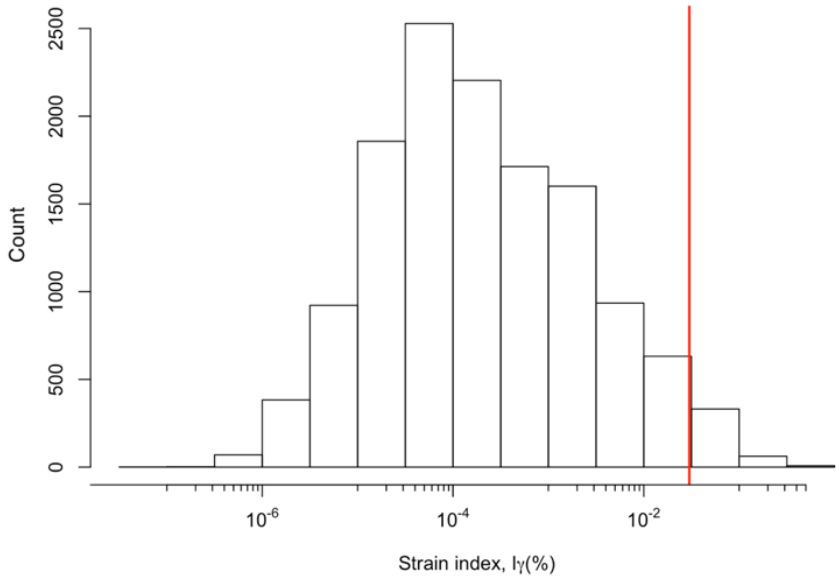

Figure 2.7: Histogram of strain index number of recordings at stations in the full database

To derive D_{min} profiles for use in ground response analyses, the Section 4.2 describes (1) how stratigraphy was inferred to enable estimates of unit weight and D^L_{min} (for sites without borehole logs); and (2) how site spectral amplitude decay parameter (κ) was measured from recordings and then interpreted to constrain small-strain damping. As such, that section supports the development of alternative damping profiles, each of which are being considered in the validation analyses.

CHAPTER 3

HVSR-Based Site Parameters for California

3.1 Introduction of HVSR

One common feature of site response is resonance at one (fundamental site frequency, f_0) or more site frequencies (f_d) [14, 15, 37], which produce peaks that are smoothed out in ergodic models. The use of the horizontal-to-vertical Fourier amplitude spectral ratio (HVSR) has the potential to add this site-specific attribute to predictions of ergodic site response at low cost, relative to non-ergodic procedures. While V_{S30} provides a reasonable, first-order estimate of site response over a wide frequency range [2, 27, 31], f_0 can be effective at describing site amplification for frequencies proximate to f_0, but it has limited utility elsewhere. Hence, the two parameters serve different purposes and they can be most effectively utilized together [25, 47].

Many previous studies, mostly considering data from Europe, Japan, and central and eastern North America, have investigated the use of HVSR. These studies have generally found that HVSR is effective at identifying the peak frequency associated with resonance effects, whereas attempts to associate HVSR peak amplitudes with site amplification levels has been inconclusive [25, 40, 64, 72, 96]. Before going forward, a point of clarification on notation – frequency f_0 is taken as the frequency of the peak site response as obtained from non-ergodic analysis, which is not an independent variable, while frequency f_{peak} is measured from HVSR of noise signals or continuously streamed data and hence is an independent site parameter (in some literature this is referred to as f_0).

In this chapter, I will describe data sources used to obtain HVSR plots for the Database subset for site response studies sites, identified in Chapter 2. I will then present, data

processing procedures developed for this work, the procedures used to compute HVSR from the data, and external (to the database) routines that can be used to evaluate HVSR-related parameters required for site response studies.

3.2 HVSR data sources

There are generally two sources for HVSR data: earthquake strong motions and ambient noise. Ambient noise is preferred for HVSR-based site amplification model development for the following reasons: (1) it does not require the availability of recorded ground motions, which are generally not available at sites where ground motions are to be predicted in practice; (2) ambient noise is an independent data source from earthquake ground motions and as such is better suited to the development of independent variables to be used in GMMs (the converse of using earthquake ground motions to derive parameters to compute those same motions introduces undesirable circularity into the process); and (3) ambient noise can be recorded over long time intervals (several hours), which allows the HVSR to be evaluated over a wider frequency range than may be possible from earthquake recordings. To acquire ambient noise, one approach is to deploy a microtremor array temporarily to measure ground vibrations often referred to as "noise" (denoted MAM below) [54, 116]. Another approach is to record noise (natural ground vibrations from microtremors) from continuously streamed data (CSD), three-component instruments installed temporarily or in permanent housings to record earthquakes. An advantage of using CSD is that the signals are recorded at exactly the location of the station, while MAM sensors may be located at some distance from the ground motion instrument. In this study, I first used the CSD and then MAM when CSD is not available.

It is desirable for HVSR to be measured from signals that represent "natural" ground vibrations with minimal anthropogenic impact. As such, I sought time intervals near mid-night during the pandemic quarantine period (2020/04/28 23:00:00 - 2020/04/29 01:00:00). Checks were also performed to confirm that no earthquake occurred near the selected time window. The data was queried from two data centers: Incorporated Research Institutions for

Seismology (IRIS) and Center for Engineering Strong Motion Data (CESMD). The arrays accessed via IRIS and CESMD are listed in Table 3.1; the main data provider was SCSN.

Table 3.1: The number of sites contribution by network

Network Name	**Southern California Seismic Network (SCSN)**[1]	**USGS Northern California Network (NCSN)**[2]	**ANZA Regional Network (ANZA)**[3]
FDSN code[4]	CI	NC	AZ
Number of sites	122	17	2

For earthquake strong motions, the data are usually acquired from high gain broadband seismometers (with channel code "HH" based on IRIS SEED manual[5]) and strong motion accelerometers (with channel code "HN"). For the measurement of ground vibrations from microtremors, seismometers are preferred. This is because strong motion accelerometers (mainly episensor type of sensor) are designed for large amplitude and high frequency seismic signals; their instrument band is limited at low frequency and the gain is low. As shown below, this causes the noise to be captured for a limited range of frequencies. In contrast, broadband seismometers (including STS-2, CMG-3T, and Trillium types of sensors) have broader instrument bands starting below 0.1 Hz and extending to at least 100 Hz. Figure 3.1 shows the nominal sensor responses[6]. Each sensor response in Figure 3.1 corresponds to an individual instrument. From left to right, the shape of the response is an upward slope at low frequencies, a plateau, and a downward slope at high frequencies. The plateaus occur at different levels, corresponding to different levels of gain (i.e., ratio of volts to measured ground velocity). For HVSR purposes, the most desirable instruments have the widest plateau and the highest gain.

[5] `https://ds.iris.edu/ds/nodes/dmc/data/formats/seed/`

[6] `https://www.passcal.nmt.edu/content/instrumentation/sensors/sensor-comparison-chart`

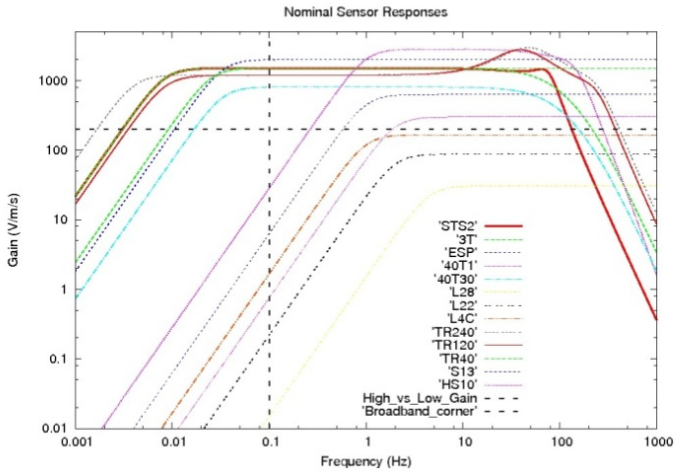

Figure 3.1: The plot of comparison of sensor responses

For many stations in the SCSN, both broadband seismometers and strong motion accelerometers are installed. Therefore, I compared HVSR derived from CSD from the two instrument types. The HVSR data processing procedure will be discussed in next section; only the results are displayed here to illustrate the distinction between instrument types. In Figure 3.2, HVSR from broadband seismometers are plotted on the left side and HVSR from strong motion accelerometers are plotted on the right side for three stations. The sites in Figure 3.2 have peaks from the seismometer data at 0.25 Hz, 1.5 and 5 Hz, and 0.2 Hz, respectively, which are absent from the HVSR derived from accelerometers. HVSR shapes at relatively high frequencies ($>$ about 5 Hz) are similar in both cases. This comparison suggests that the effectiveness of continuously streaming accelerometers for HVSR applications is limited to high frequencies.

A second comparison of HVSR that can be made is between MAM (temporarily deployed sensor for noise measurements) and CSD (noise from permanent instrument). This comparison is facilitated by MAM data retrieved at three stations as documented in [116]. Figure 3.3 compares HVSR from the two sources, which shows that the plots display consistent peaks positions and similar overall shapes. The main differences between the two sets of results are in the amplitudes of the peaks, which could be explained by the differences in measurement locations, measurement durations, instrument gain, or different characteristics of the

recorded signals. The small deviations do not significantly impact forward application in site response modeling (in Chapter 4).

The database subset for California site response studies contains 159 stations (Section 2.3). Of these sites, 111 have CSD from IRIS and CESMD (the providers are listed in Table 3.1) and another 29 stations have MAM data as provided in [116]. Accordingly, there is a total of 140 stations with HVSR from either CSD or MAM.

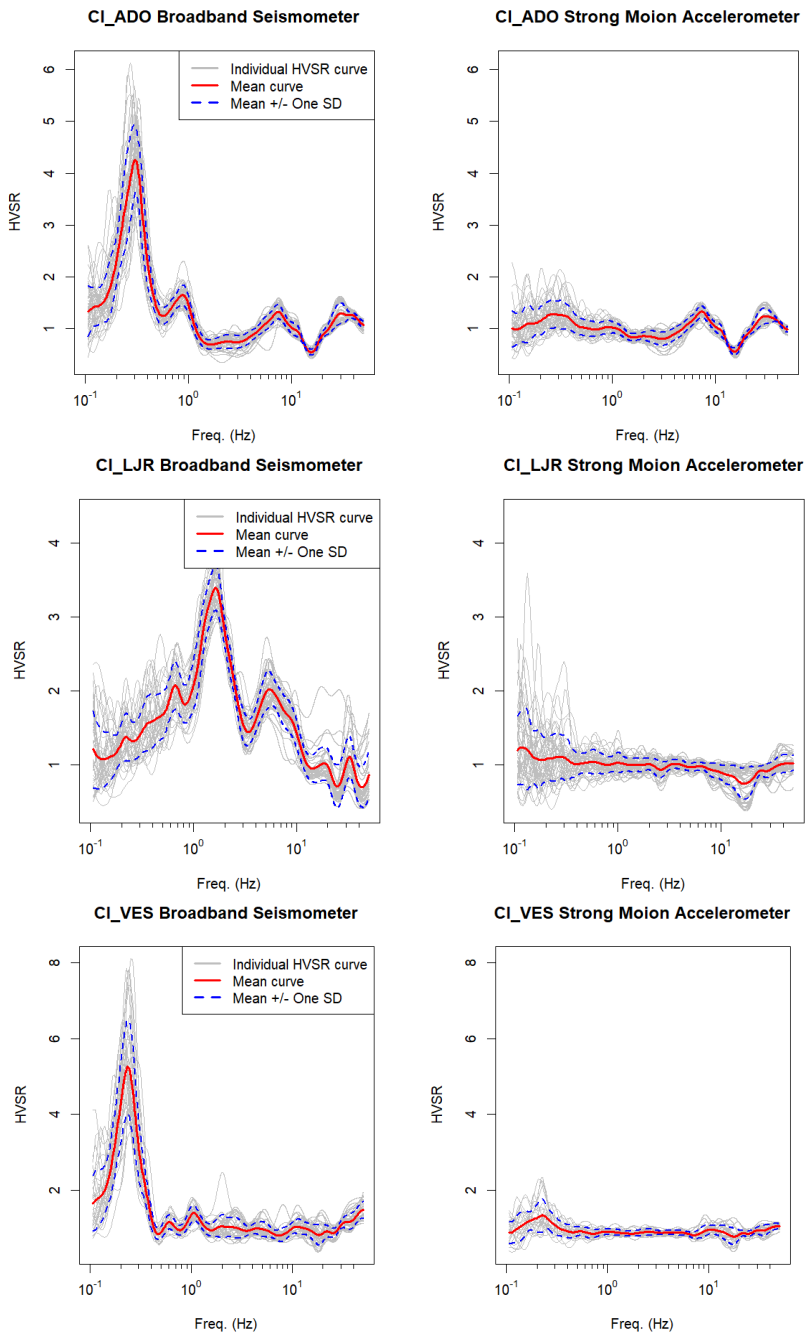

Figure 3.2: The comparison of HVSR between broadband seismometers and strong motion accelerometers from CI_ADO (longitude: -117.43391, latitude: 34.55046, V_{S30} = 375.73 m/s, and surface geology is Quaternary Holocene alluvium), CI_LJR (longitude: -118.86775, latitude: 34.80762, V_{S30} = 303.38 m/s, and surface geology is Mesozoic Cretaceous quartz monzonite), and CI_VES (longitude: -119.08469, latitude: 35.84089, V_{S30} = 392.37 m/s, and surface geology is Quaternary Pleistocene older alluvial terrace deposits)

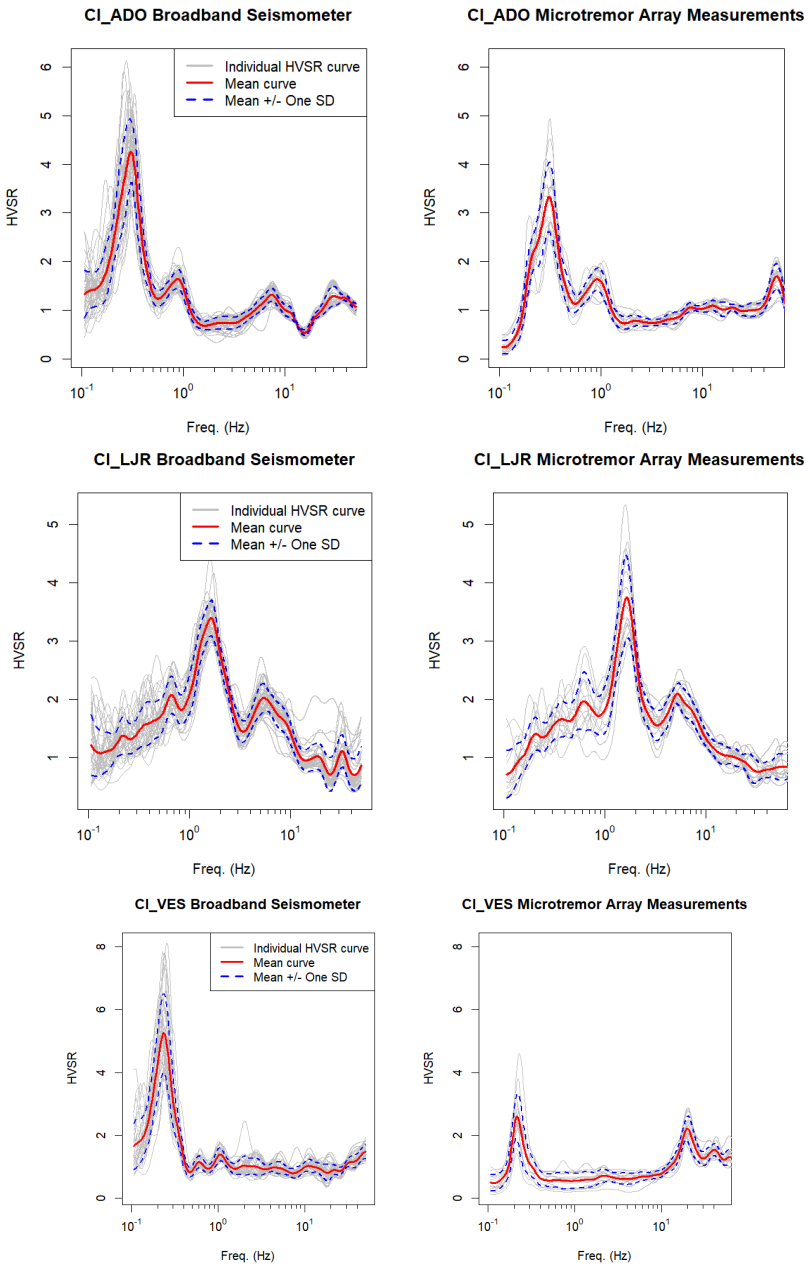

Figure 3.3: The comparison of HVSR between broadband seismometer and microtremor array measurements

3.3 HVSR processing procedure

This section describes procedures used to process microtremor time series and develop HVSR-frequency plots. These procedures extend the framework described in the Site Effect Assess-

ment using AMbient Excitations (SESAME) guidelines [87] and similar protocols often used in California (K. Hayashi, A. Martin, oral and written personal communication, 2018, 2019). The procedures presented here have been developed in consultation with several topical experts (A. Yong, A. Martin, K Hayashi, J. Steidl, B. Cox, J. Vantassel, and L. Schleicher) along with collaborating UCLA researchers (T. Gospe, P. Zimmaro). A code written in R has been developed that has some differences from existing software (Geopsy [110], one of the most popular tools for HVSR; and `hvsrpy`[106], a library written in Python). Elements of the current procedure that differ from those used in other codes/guidelines are explained below.

3.3.1 Windowing

Data from ambient noise usually are recorded over long durations (typically hours). The time series will be cut into multiple sub-windows so that statistics of interest (e.g., mean and standard deviation) can be calculated. More windows result in more robust statistics (30 is the least number for normality in statistics so I took 30 as the minimum number of sub-windows). However, the larger the number of windows, the shorter the window durations, which reduces the resolution of low-frequency HVSR features. SESAME guidelines recommend that the frequency of interest in HVSR should be at least 10 divided by the window duration in seconds. For example, if the frequency of interest is 0.1 Hz (usually the recommended corner frequency of instrument in industry standard for HVSR), then the durations of sub-windows must be at least 10/0.1 = 100 seconds (I used 150 seconds). Therefore, to resolve a minimum frequency of 0.1 Hz (which was used as a default), the duration of ambient noise should be at least 150*30/3600 = 1.25 hours. If the frequency of interest is higher or lower than 0.1 Hz, the duration of signals could be shorter or longer, respectively. For the 140 selected stations in Section 3.2, all CSD have two-hour durations and all MAM signals have at least 1 hour durations.

Each of the sub-windows within the time series is tapered at its time limits using a window function. The window function has a maximum of one within a chosen interval, and decreases

to zero outside of the interval. Ordinates of the function express the proportion of the original data that is used (e.g., 0.5 means the amplitude will be decreased by half). The window function ensures ground motion amplitudes (generally velocities) at the beginning and end are zero. For most applications involving microtremor data, this will also provide nearly zero displacements at the limits of the window. The Tukey window [103] (also known as the tapered cosine window) is a commonly used window function in ground motion processing and is used here. Figure 3.4 illustrates the Tukey window function.

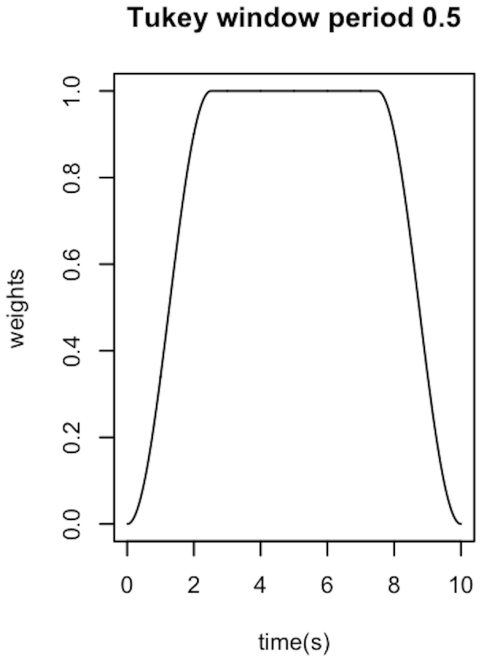

Figure 3.4: Tukey window with period of 5 sec $\alpha = 0.5$

In Figure 3.4, the duration of the Tukey window is 10 seconds and the period (i.e., the length of time over which the tapers are applied at the start and finish of the window) is 5 seconds. In this case, the period is the half of the window duration, which means it will taper the first and last quarter of data but not change the two quarters of data in the middle. The Tukey window can be formulated as,

$$w(n) = \begin{cases} \frac{1}{2}[1 + \cos(\pi(\frac{2n}{\alpha(N-1)} - 1))], & 0 \leq n < \frac{\alpha(N-1)}{2} \\ 1, & \frac{\alpha(N-1)}{2} \leq n \leq (N-1)(1-\frac{\alpha}{2}) \\ \frac{1}{2}[1 + \cos(\pi(\frac{2n}{\alpha(N-1)} - \frac{2}{\alpha} + 1))], & (N-1)(1-\frac{\alpha}{2}) < n \leq (N-1) \end{cases} \tag{3.1}$$

where α is the ratio of period to window duration in the Tukey window (0.5 for the example in Figure 3.4), n is the sequence number of the data point, and N is the total number of data points. The effect of tapering on a time series is illustrated in Figure 3.5.

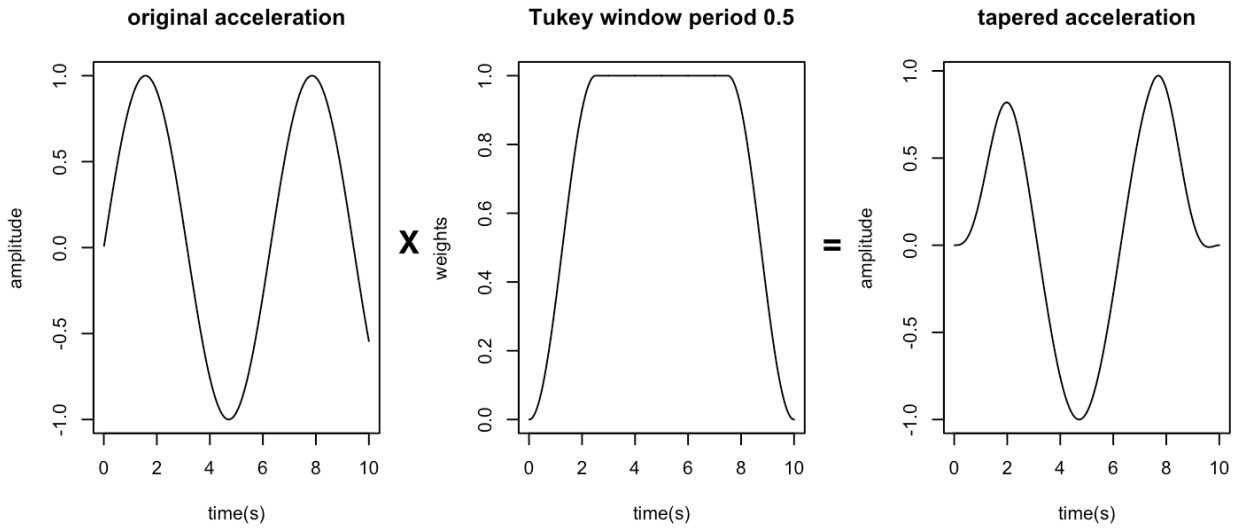

Figure 3.5: An example of Tukey window tapering

For ground motion and ambient noise processing, we avoid taking large values of α to avoid removal of signal. A typical value is $\alpha = 0.05 = 5\%$ (taper the first and last 2.5% of signals).

3.3.2 Mean removal

After windowing, the detrending function is applied as the first step in signal processing to remove any offset or overall trend from the windowed time series. While ground motion processing may adopt detrending functions that comprise a constant that is subtracted from the data, a linear trend line, or a higher order polynomial, for ambient noise HVSR processing, I only subtract the mean from the windowed time series.

3.3.3 Filtering

In earthquake ground motions, the signals generated from earthquakes and ambient noise are both recorded simultaneously in the sensors. Because noise effects are often concentrated at the low (and sometimes high) ends of the frequency range of recordings, filtering is applied to minimize the effects of noise while retaining the earthquake signal. Butterworth filters are applied, which have two required parameters – a filter corner (f_c) and a filter order (n), as illustrated in Figure 3.6. For earthquake data processing, the corner frequency is generally selected where the ratio of signal to noise is around 3 [68]). Filters that remove low and high frequency noise are referred to as low-cut (high pass) and high-cut (low pass), respectively. A schematic of a low-cut filter transfer function is shown in Figure 3.6.

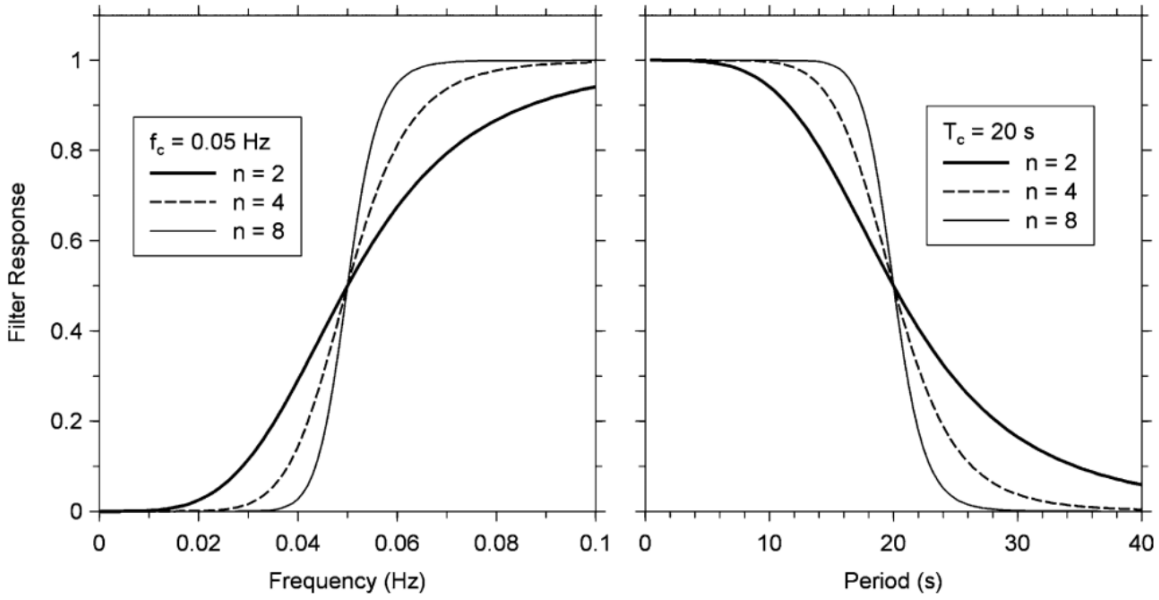

Figure 3.6: Transfer function of low-cut Butterworth filter in both frequency and period domains from [20]

The transfer function (filter response in the figure) is described as a function of frequency on the left, and a function of period on the right. The corner frequency and period, f_c and T_c respectively, are specified by the analyst and indicate the frequency (or period) where the transfer function amplitude is $\sqrt{0.5} = 0.71$. For example, the low-cut transfer function can

be expressed as

$$TF = \sqrt{\frac{(f/f_c)^{2n}}{1+(f/f_c)^{2n}}} \tag{3.2}$$

where n controls the steepness of the transfer function (Figure 3.6).

The high-cut transfer function is defined as

$$TF = \sqrt{\frac{1}{1+(f/f_c)^{2n}}} \tag{3.3}$$

Although low-cut and high-cut corner frequencies must differ, both are denoted as f_c.

Figure 3.7 shows unprocessed and filtered data from an earthquake in Japan in 2003 at the Toitokki station to illustrate the effects of filtering and the selection of low-cut corner frequencies. It shows acceleration, velocity, displacement, and Fourier amplitude spectra (FAS) for the raw data (green) and processed data (blue). The two vertical red lines in the FAS plot indicate the corner frequencies of 0.045Hz and 20Hz. Of these two corner frequencies, the low-cut corner frequency is often more important as it significantly influences the long period waves (best view in displacement) and also determines the highest usable periods of processed data. Figure 3.8 presents the resultant displacements under different choices of low-cut corner frequencies.

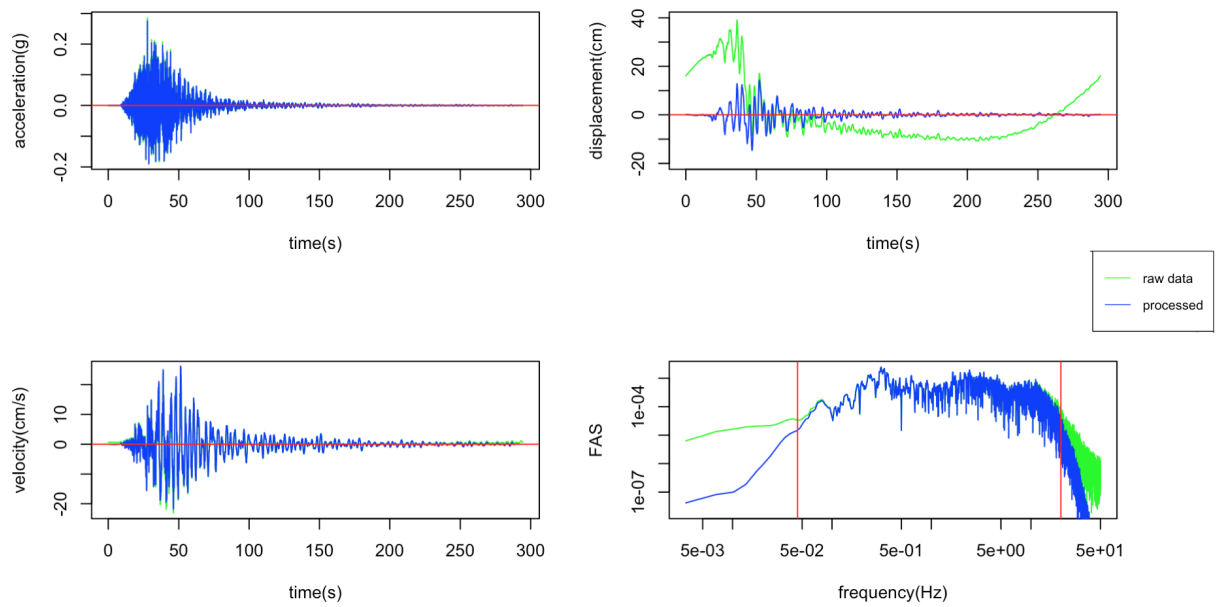

Figure 3.7: Raw and processed data from earthquake in Japan in 2003, at Toitokki station

Figure 3.8 (first frame) shows that without a low-cut filter the displacements can be unrealistic. The offsets at the beginning and end of displacement indicate non-zero permanent displacement. Although windowing with a 5% taper duration has been applied, it does not fix the issue. In order to minimize signal loss, it is desirable to select the minimum possible low-cut corner frequency that removes the baseline problems evident in Figure 3.8. For the present case, this occurs at $f_c = 0.045$ Hz.

In ambient noise, the frequency content is unbounded so the corner frequencies are determined by the limits of the instrument. Accordingly, corner frequencies are selected in a different manner. As shown in Figure 3.1, the frequency range that defines the plateau is different for each type of sensor. For the broadband seismometers considered in this research, the plateau for the sensors ranges from around 0.1 Hz (or lower) to about 100 Hz. As a result, 0.1 Hz and 100 Hz (or the Nyquist frequency if it is less than 100 Hz) are taken as default low-cut and high-cut corner frequencies, respectively. For most engineering applications, the maximum frequency of interest is up to 20-25 Hz (or minimum period down to 0.05 second), which means that high-cut filtering is often not needed (and in some cases Fourier coefficients beyond 25 Hz are simply not used).

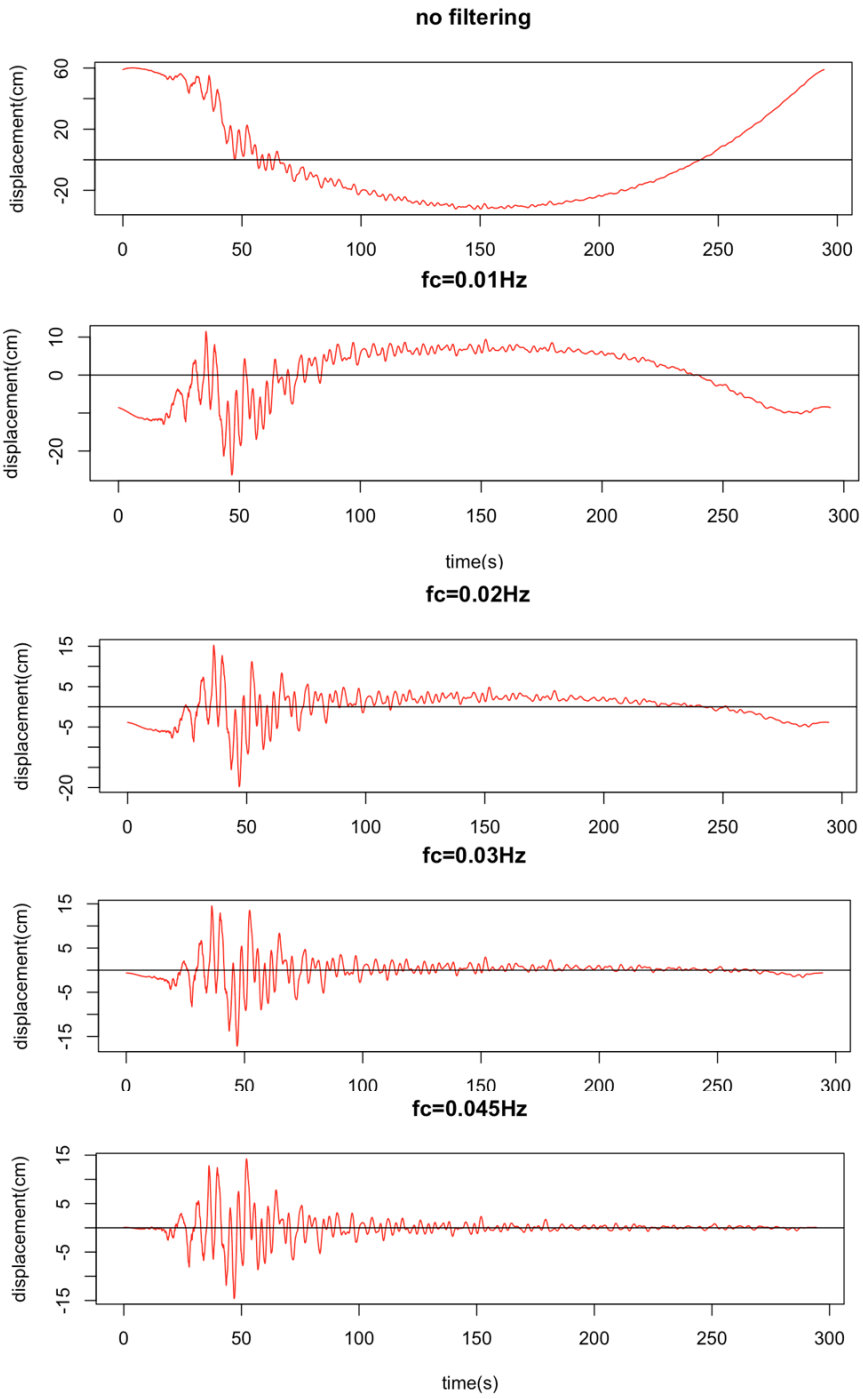

Figure 3.8: Displacement time-histories for a series of filters with different high pass corner frequencies

3.3.4 Horizontal component combination method

Because horizontal microtremor signals (velocity time series) are recorded in two directions, a method to combine these components is required. The geometric mean is typically used in Geopsy. We proposed to use a median-component motion, denoted as RotD_{50} ([18]), because it is a central value of the horizontal component motions that is not dependent on the azimuths of the sensors. Another approach for combining horizontal components is the Effective Amplitude Spectrum, EAS ([49] and [13]). This approach defines the horizontal component for a given frequency as the product of $1/\sqrt{2}$ and the sum of squared Fourier Amplitudes of the two as-recorded components. We prefer our definition of the combined component because it corresponds to the actual ground motion in a particular direction that produces median response.

The analysis of RotD_{50} involves the computation of ground motion amplitudes for a range of azimuths, and taking the median of the results. The component of ground motion rotated by angle θ_k can be calculated as,

$$h_{ROT}(\theta_k; t) = h_1(t)\cos(\theta_k) + h_2(t)\sin(\theta_k) \tag{3.4}$$

where $h_1(t)$ and $h_2(t)$ are the as-recorded signals, rotation angle θ_k is measured relative to the azimuth for component h_1, and $h_{ROT}(\theta_k; t)$ is the combined motion at rotation angle θ_k. All of these signals are in the time domain. The Peak Ground Acceleration (PGA) at each θ_k is calculated and the rotation angle θ_{med} corresponding to the median PGAs is identified for the calculation of RotD_{50}. The time series corresponding to this azimuth is then computed as,

$$h_{\mathrm{RotD}_{50}}(t) = h_1(t)\cos(\theta_{med}) + h_2(t)\sin(\theta_{med}) \tag{3.5}$$

The time series produced by Equation 3.5 is used as the H component in the HVSR calculation.

3.3.5 Smoothing

Fourier amplitude spectra (FAS) are computed for the combined horizontal-component motion and the vertical-component motion. Spectral smoothing is then applied to smooth out the spectrum and to facilitate to identification of peaks. The Konno & Ohmachi (KO) [69] smoothing filter, which accounts for variable numbers of points at low frequency [87], is applied to both the horizontal and vertical components. Figure 3.9 shows the effect of KO smoothing by comparing the raw FAS (in blue) with the smoothed FAS (in red). The smoothed FAS retains the overall shape of the spectrum, including the local peaks.

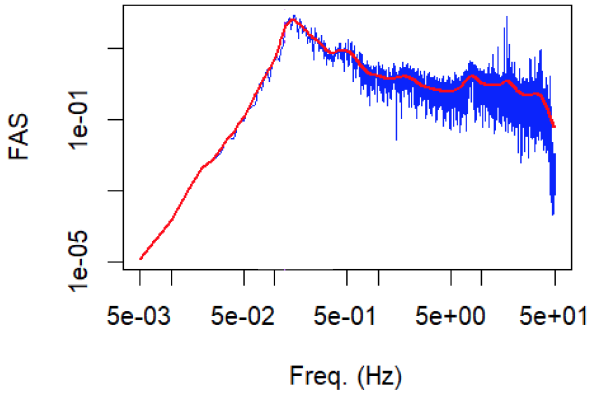

Figure 3.9: Comparison between raw FAS and smoothed FAS

KO smoothing is formulated as,

$$\mathrm{FAS}_{KO}(f_s) = \sum_{\forall f} W_B(f, f_s)\mathrm{FAS}_0(f) \tag{3.6}$$

where FAS_{KO} and FAS_0 represent the smoothed and raw FAS; f_s is the frequency for which the smoothed ordinate is to be computed; f is frequency as used in the weighting function, and $\forall f$ means f will sample all frequencies in the FAS; and $W_B(f, f_c)$ is the window (weight) function, defined by [69] as,

$$W_B(f, f_c) = \left[\frac{\sin(\log_{10}(f/f_c)^b)}{\log_{10}(f/f_c)^b}\right]^4 \tag{3.7}$$

where b is a coefficient for band width controlling the degree of smoothing. The degree of smoothing increases as the bandwidth decreases. I use 20 as the default value.

3.3.6 HVSR calculation

HVSR is computed as a function of frequency by dividing the smoothed FAS of combined horizontal $h_{\mathrm{RotD}_{50}}(t)$ by the smoothed FAS of the vertical-component. This operation is applied to each sub-window. The final HVSR is the arithmetic mean of HVSR coordinates across all windows, and similarly, uncertainties are quantified by the arithmetic standard deviation across all HVSR ordinates. This use of the RotD_{50} component, the arithmetic mean, and the arithmetic standard deviation, differs from the approaches used in Geopsy and hvsrpy. Those codes use the geometric mean of the horizontal components and the natural log standard deviation. The arithmetic moments are selected in lieu of logarithmic moments because the distribution of HVSR amplitudes was investigated and found to be marginally more normal than log-normal. An example of HVSR results at one of the select stations, CI_ADO, is shown in Figure 3.10.

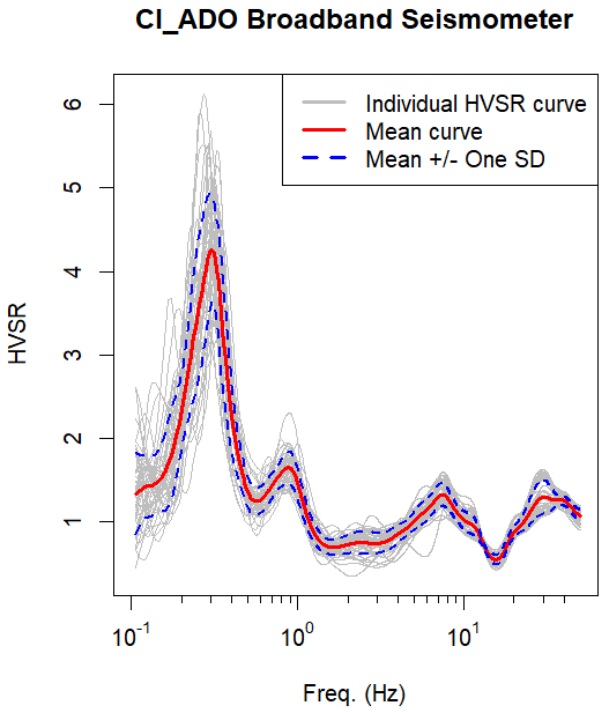

Figure 3.10: Comparison between raw FAS and smoothed FAS

3.3.7 Sub-window selection

The final step in the processing procedure is the selection of sub-windows for FAS and HVSR computations. It is desirable for each sub-window used in HVSR computations to reflect genuine ground vibrations from ambient sources. This may not be the case for some sub-windows, which may be affected by anthropogenic transients or similar effects. Accordingly, not all sub-windows in Section 3.3.1 are valid for final HVSR calculations. Sub-window selection occurs in two steps, one follows windowing and is based on examination of data in the time domain, and another follows HVSR calculation and involves examination of data in the frequency domain.

The time domain examination of the data is intended to identify and remove sub-windows with "triggering". "Triggering" refers to temporary vibration sources affecting a signal, which can compromise the accuracy of HVSR. It is preferred for the ground vibrations producing the signals to be from far-field noise sources that produce approximately constant amplitudes in time. In contrast, local noise will have transient bursts due to the erratic nature of traffic or other anthropogenic sources. Therefore, it is necessary to remove the sub-windows with "triggering" and ensure that the rest of the sub-windows have approximately constant amplitudes in time. One way to identify the potential triggers within a window is based on relative values of the short-term average (STA) and long-term average (LTA) signal amplitudes. The STA and LTA are computed using 5- and 30-sec durations, respectively. The SESAME guideline [87] calls for the amplitude ratios to be within the range of STA/LTA = 0.1 to 10. This method is objective, but the process also benefits from visual checking of sub-windows. I remove the sub-windows with unrealistically large spikes (peak is 3 or 4 times larger than the rest).

For the second selection in the frequency domain, the purpose is to stabilize the mean and standard deviation. It is possible that ordinates of some individual HVSR at some frequencies are unreasonably large or small (e.g., the denominator from the vertical component could be very small, blowing up the ratio). If these HVSRs are included, the mean and standard deviation become unstable. To ensure the stability of moments, sub-windows producing

such results are removed. These criteria are applied based on visual inspection by identifying ordinates (especially near peaks) that are too far away from the mean (more than 3 standard deviations).

3.4 Peak identification

The mean curve of HVSR plots can generally be classified as containing no peaks, one peak, or multiple peaks [72]. If there are multiple peaks, the first two peaks (i.e., the two peaks at the lowest frequencies) are most significant and taken into consideration. A peak may indicate the site has strong impedance contrast(s) near one or more modal frequencies (e.g., [102]) whereas multiple peaks may indicate multiple impedance contrasts at different depths. When there is no peak present in an HVSR, this suggests the site is either underlain with a sediment-filled depth profile that lacks a significant impedance contrast or it is a rock site with nearly depth-invariant near-surface velocities. Therefore, one of the most important characteristics that should be identified is the presence of lack of presence of a peak. In this section, I discuss peak identification and peak parameterization.

3.4.1 Peak versus No Peak

The mean HVSR curve is used for peak identification. SESAME guideline provide a procedure for the identification of peaks that first considers three criteria that assess the reliability of the HVSR curve and then consider six conditions intended to establish the presence of a clear HVSR peak. The first two criteria for the reliability of HVSR curves constrain the minimum required number of sub-windows and duration; in the present study these are satisfied based on the data selection criteria described in Section 3.2. The remainder of this section will focus on the remaining conditions, which are summarized in Table 3.2.

The Reliability 3 criterion in Table 3.2 is for the third condition to establish a reliable HVSR curve. The rows labeled Clear x (x takes numbers from 1 to 6) represent the x-th condition for a clear peak. SESAME suggests that a clear peak must satisfy Reliability 3 and at least five out of six Clear conditions.

Note in Table 3.2, f_{peak} (f_0 was the variable name used in SESAME) is the peak frequency of interest (there could be multiple f_{peak} values in a single curve); f is the independent frequency; $A_{H/V}(f)$ is the amplitude of HVSR mean curve at frequency f; A_{peak} is the amplitude at f_{peak}; $\sigma_A(f)$ is standard deviation of $A_{H/V}(f)$ at f; $\sigma_A(f_{\text{peak}})$ is then standard deviation of $A_{H/V}(f)$ at f_{peak}; and σ_f is standard deviation of f_{peak}. In Table 3.2, the rows labelled Reliability 3, Clear 5, and Clear 6 are f_{peak}-dependent. The greater f_{peak} is, the more stringent are the standards for establishing a peak as reliable and clear. Clear 3 is also considered in [72].

Table 3.2: Criteria of peak identification from SESAME

Parameters	CESAME
Reliability 3: $f_{\text{peak}} > 0.5\,\text{Hz}, f \in [0.5f_{\text{peak}}, 2f_{\text{peak}}]$	$\sigma_A(f) < 2$
Reliability 3: $f_{\text{peak}} < 0.5\,\text{Hz}, f \in [0.5f_{\text{peak}}, 2f_{\text{peak}}]$	$\sigma_A(f) < 3$
Clear 1: $f \in [0.25f_{\text{peak}}, f_{\text{peak}}]$	$A_{H/V}(f) < 0.5A_{\text{peak}}$
Clear 2: $f \in [f_{\text{peak}}, 4f_{\text{peak}}]$	$A_{H/V}(f) < 0.5A_{\text{peak}}$
Clear 3:	$A_{\text{peak}} >= 2$
Clear 4: peak of SD curve $f_{\text{peak}}[A_{H/V}(f) - \sigma_A(f)]$	within $[f_{\text{peak}}/1.05, 1.05f_{\text{peak}}]$
Clear 4: peak of SD curve $f_{\text{peak}}[A_{H/V}(f) + \sigma_A(f)]$	within $[f_{\text{peak}}/1.05, 1.05f_{\text{peak}}]$
Clear 5: $f_{\text{peak}} < 0.2\,\text{Hz}$	$\sigma_f < 0.25f_{\text{peak}}$
Clear 5: $f_{\text{peak}} \in [0.2, 0.5)\,\text{Hz}$	$\sigma_f < 0.2f_{\text{peak}}$
Clear 5: $f_{\text{peak}} \in [0.5, 1.0)\,\text{Hz}$	$\sigma_f < 0.15f_{\text{peak}}$
Clear 5: $f_{\text{peak}} \in [1.0, 2.0]\,\text{Hz}$	$\sigma_f < 0.1f_{\text{peak}}$
Clear 5: $f_{\text{peak}} > 2.0\,\text{Hz}$	$\sigma_f < 0.05f_{\text{peak}}$
Clear 6: $f_{\text{peak}} < 0.2\,\text{Hz}$	$\sigma_A(f_{\text{peak}}) < 3$
Clear 6: $f_{\text{peak}} \in [0.2, 0.5)\,\text{Hz}$	$\sigma_A(f_{\text{peak}}) < 2.5$
Clear 6: $f_{\text{peak}} \in [0.5, 1.0)\,\text{Hz}$	$\sigma_A(f_{\text{peak}}) < 2$
Clear 6: $f_{\text{peak}} \in [1.0, 2.0]\,\text{Hz}$	$\sigma_A(f_{\text{peak}}) < 1.78$
Clear 6: $f_{\text{peak}} > 2.0\,\text{Hz}$	$\sigma_A(f_{\text{peak}}) < 1.58$

I initially applied the SESAME criteria to the data from the California sites, with the result that very few (~ 20) sites are identified as having peaks. I did not consider this result to be reliable, because simple visual inspection of the data indicate far more sites with peaks.

Accordingly, I devised an approach by which two analysts inspected each HVSR to identify sites with or without peaks. The two analysts (the author of this document and my advisor) developed their own criteria for these assessments. Based on these results, I identified the elements of the SESAME criteria that produce different results from the visual inspections. The details of this process are explained in the following paragraphs and Section 3.5.

We consider HVSR from both ambient noise data at 140 stations and earthquake strong motions at all 159 stations. It is important to mention that for strong motions the duration of recordings is usually 1 to 2 minutes. It cannot be sub-windowed. To get a certain number of sub-windows to meet reliability criteria, I take the recordings from multiple events as separate sub-windows. Although the number of recordings for the selected 159 stations is at least 10 (described in Section 2.3), 10 stations are removed due to too few selected sub-windows during HVSR processing (which results in 149 stations for strong motion HVSR). Table 3.3 summarizes the statistics of peaks and no peaks based on SESAME and from visual inspections from the two analysts.

Table 3.3: The summary of statistics of peaks and no peaks

		Number of Peaks	Number of No Peaks
Strong Motions	SESAME	18	131
	Analyst I (PW)	62	87
	Analyst II (JPS)	38	111
Noise	SESAME	25	115
	Analyst I (PW)	74	66
	Analyst II (JPS)	65	75

3.4.2 Peak fitting

If there exists clear peaks in HVSRs, the next step is parameterizing the curve to fit the peak. Previous studies ([48, 51, 72]) have chosen a Gaussian pulse function to fit peaks. The Gaussian pulse function is defined as ([72]),

$$\ln(\hat{F}_{H/V,i}) = \ln(a_{pi})\exp\Big(- \Big(\frac{\ln(f/f_{pi})}{w_i}\Big)^2\Big) \tag{3.8}$$

where $\hat{F}_{H/V,i}$ is the estimated HVSR, a_{pi} is the fitted amplitude term, w_i is the fitted pulse width term, f_{pi} is the fitted peak frequency, i is the order of peak, and f is the frequency. The function is fit with respect to frequency on a log-scale.

Having applied this function to multiple sites, the main drawback is that the Gaussian amplitudes transition to an amplitude of unity at the tails, which may not be the case for many sites. To address this issue, I propose a new form of the Gaussian fitting function,

$$\hat{F}_{H/V,i} = c_0 + c_1 \exp\Big(-\frac{1}{2}\Big(\frac{\ln(f/f_{pi})}{2w_i}\Big)^2\Big) \tag{3.9}$$

where c_0 is a frequency-independent constant adjusting the overall amplitude, c_1 is the peak amplitude relative to c_0, and all other parameters are as defined previously. Comparing to the orignal form in Equation 3.8, besides the new constant term c_0, additional updates include:

- ln is removed from the left side of the equation. This change was made because, as mentioned above, HVSR ordinates were not found to be log-normally distributed.
- I put $\frac{1}{2}$ and 2 in front of w_i in the function to make the form of the equation more Gaussian in form.

Since the HVSR model (forward site response prediction model, which will be discussed in Section 4.1.4) takes inputs of fitted coefficients from the original function and the fitted coefficients from the two functions may not be the same, I fit peaks using both functions. The fitted coefficients from new function will be used for future model development.

3.5 Interpretation

In the last section, I presented the results of peak identification using criteria presented by SESAME and two analysts judgements based on visual inspection. In this section, I identify causes of the differences between these results and propose new recommended criteria for peak identification for HVSR derived from strong motion and noise sources.

3.5.1 Variability of results from different data sources

Table 3.4 presents statistics of sites with peaks and no peaks for 138 selected stations with colocated HVSR from strong motions and noise. Peak identification results from SESAME are not considered here as it gives too few sites with peaks to produce meaningful statistics.

Table 3.4: The comparison of peaks identified from HVSR computed using strong motion and noise data sources

	StrongM vs Noise	Peaks - Peaks	No Peaks - No Peaks	No Peaks - Peaks	Peaks - No Peaks
Analyst I	Count	39	45	35	19
	Percent	$\sim 28\%$	$\sim 33\%$	$\sim 25\%$	$\sim 14\%$
Analyst II	Count	24	65	40	9
	Percent	$\sim 17\%$	$\sim 47\%$	$\sim 29\%$	$\sim 6\%$

In Table 3.4, Column"Peaks - Peaks" represents the number (or proportion) of sites where peaks are identified from both strong motions and noise, while "No Peaks - Peaks" indicates sites where the peak is identified from noise but not from strong motion (vice versa for "No Peaks - No Peaks" and "Peaks - No Peaks"). Figure 3.11 shows examples of "P-P", "N-N" and "N-P" sites. HVSR results based on microtremor data for all sites for which the data is available are presented on a Github site given in the Appendix along with indicators from Analyst I and II regarding the presence of peaks. Similar plots are also presented for ground motion based HVSR data.

Table 3.4 compares the results of sites identified as having or not having peaks from two data sources by aggregating sites into these four categories. There are differences between the identifications from the two analysts (to be discussed later). However, both analysts are in reasonable agreement regarding the identification of peaks from strong motion and noise data sources ($17\% + 47\% = 65\%$ vs $28\% + 33\% = 61\%$). Additional important questions are: 1) if HVSR from both data sources have peaks, then how do the fitted coefficients from the two sources differ?; and 2) are there any indicators for the agreement of peaks from the two data sources?

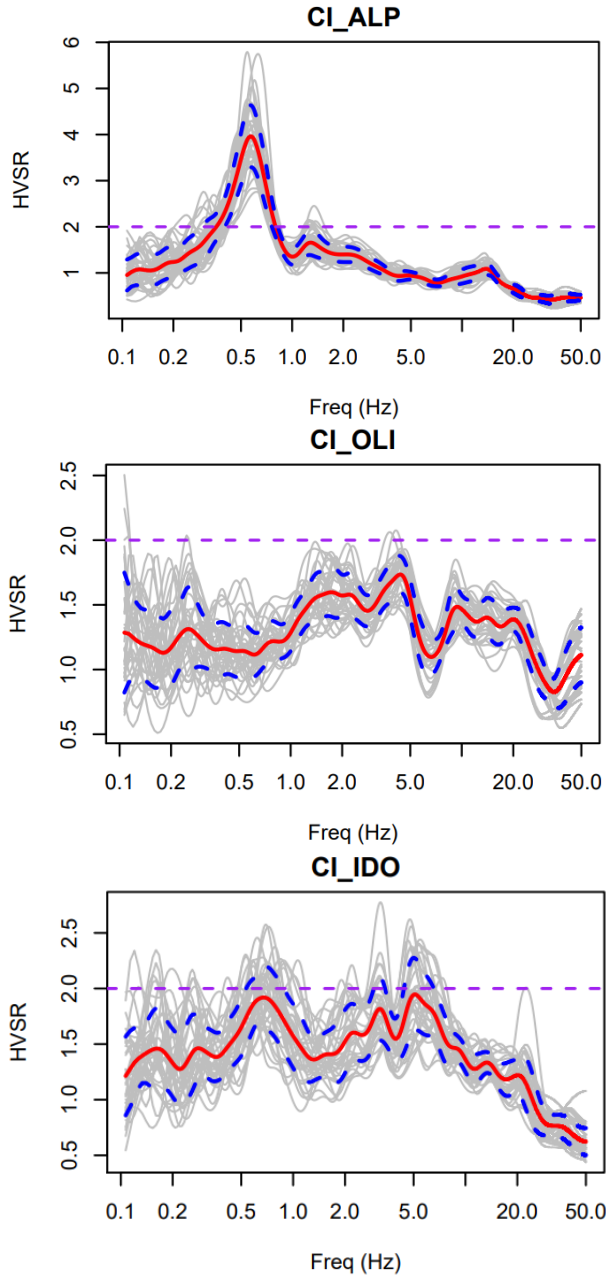

Figure 3.11: The examples of HVSR for "P-P", "N-N", and "N-P" sites

The first question is investigated by comparing fitted parameters in the scatter plot shown in Figure 3.12. In Figure 3.12, 39 points are plotted for sites with peaks identified from both strong motion and noise data based on Analyst I judgements (Analyst II results are similar). The figure shows some dispersion in the plot of f_p, however, most points are along the 45-degree line. This trend demonstrates that the peak frequencies are strongly

correlated (correlation coefficient is 0.65). The plot of a_p indicates a weaker correlation. There are more points below the 45-degree line, which indicates that peak amplitudes from strong motion data are generally slightly larger than those from noise. Both sets of fitted coefficients will be used in the forward HVSR model (although the model was developed based on strong motions [72]).

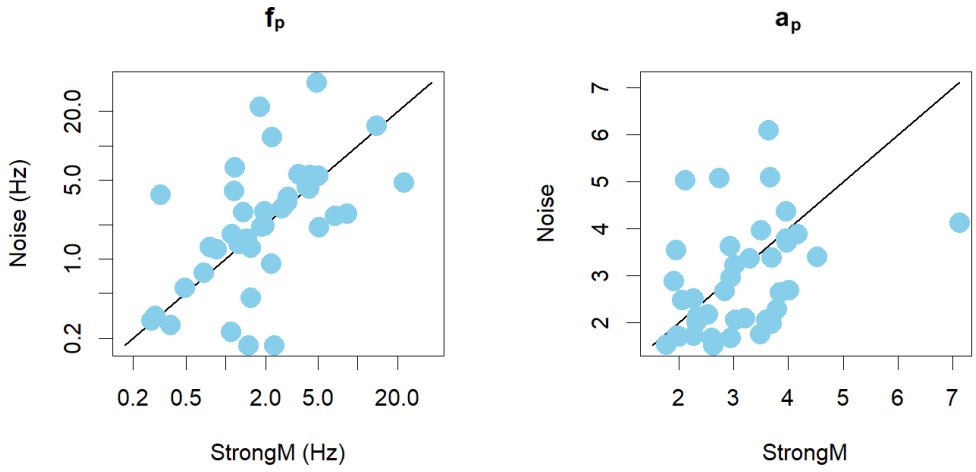

Figure 3.12: Comparison of f_p and a_p between strong motions and noise

Next, I explore two potential indicators for the agreement of peaks from the two data sources. The first potential indicator is V_{S30} and the second is surface geological unit. To investigate the effect of V_{S30}, a box plot for the four categories of sites is shown in Figure 3.13. The category names are the initials of column names from Table 3.4. Additionally, a summary of results for different surface geological units is provided in Table 3.5.

It can be seen that the median V_{S30} for "N-N" is higher than the other three categories. This indicates that clear peaks are less likely at harder sites, potentially due to fewer impedance contrasts for these conditions. The P-P sites have the smallest interquartile range (the length of each box) while it is largest for "N-N". This indicates less variability in site conditions for "P-P" sites.

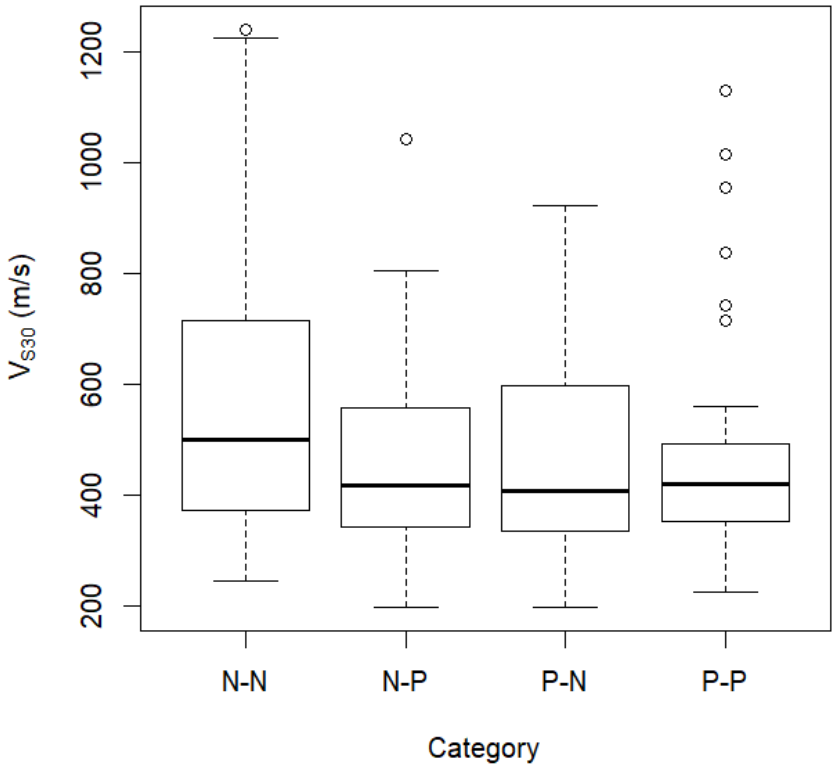

Figure 3.13: Box plot of V_{S30} aggregated by four peak categories

Table 3.5: The statistics of four peak categories aggregated by surface geological units

Geological unit	N-N	N-P	P-N	P-P
crystalline	17	11	6	10
Kjf	3	2	2	0
Qal1	0	1	2	4
Qal2	2	2	1	3
Qal3	7	5	2	8
Qoa	2	7	3	6
QT	3	3	0	1
Serpentine	2	0	0	0
Tsh	3	0	2	1
Tss	5	2	1	1
Tv	1	2	0	5

Table 3.5 shows the disaggregation of results for the 138 sites based on the four peak

categories into a series of surface geological units. These surface geological units will be discussed in detail in Section 4.2.1.2. For the present analysis it is important to recognize crystalline, Kjf, Serpentine, Tsh, Tss, Tv are older and rocky units, while Qal1, Qal2, Qal3, Qoa, and QT are softer soil units. The results indicate that "P-P" is more likely at soft soil sites and "N-N" is more likely at rock sites.

3.5.2 Variability of user judgements

Table 3.4 shows that the judgements made by Analysts 1 and 2 do not completely align. Here we investigate the causes of the different outcomes. Table 3.6 summarizes percentages of sites where both both analysts identify peaks, both identify no peaks, and intermediate cases. Results are provided for 149 selected stations using strong motion data and 140

Table 3.6: The comparison of peaks between two independent judgements

	Analyst II vs Analyst I	Peaks - Peaks	No Peaks - No Peaks	No Peaks - Peaks	Peaks - No Peaks
StongM	Count	34	83	28	4
	Percent	$\sim 23\%$	$\sim 56\%$	$\sim 19\%$	$\sim 3\%$
Noise	Count	54	54	21	11
	Percent	$\sim 39\%$	$\sim 39\%$	$\sim 15\%$	$\sim 8\%$

stations based on noise. The agreement percentages between analysts are $23 + 56 = 79\%$ and $39 + 39 = 78\%$ for strong motion and noise, respectively. The main reason for the differences between analysts is the application of weaker criteria for peak identification from Analyst I than from Analyst II. Analyst II applied the following criteria in his visual analysis:

- the amplitude of peak should be reasonably high (around 2 for strong motion and a little less for noise);
- the peak should not be too close to the boundary of usable frequencies;
- the peak should not be too wide;
- the uncertainty of peak amplitude and frequencies should be not too large;

- and lastly, the peak amplitude should be sufficiently higher than the ordinates at neighboring frequencies (around factor of 2);

Analyst I applied similar rules but with weaker thresholds, for instance, in the third condition he used a factor of 2 or less. This results in more peaks from Analyst I. Comparing to SESAME conditions summarized in Table 3.2, ours reflect almost all of the conditions but in a more subjective way. To make the peak identification more objective and consistent, it is critical to develop similar quantitative criteria as SESAME but the criteria should be weaker and mimic analyst judgements informed by the California data. In next subsection, I will present the recommended criteria.

3.5.3 Recommended criteria for peak identification

As shown in Table 3.3, SESAME gives the minimum number of sites with identified peaks. All of the SESAME sites are included in the sites identified by Analysts I and II. This means that SESAME applies the most conservative rules and it only returns a small subset of sites with peaks. As noted earlier, the SESAME criteria appear to be too conservative, missing sites that clearly have peaks based on visual inspection. I present in Figure 3.14 two example sites where both analysts identified peaks while SESAME does not.

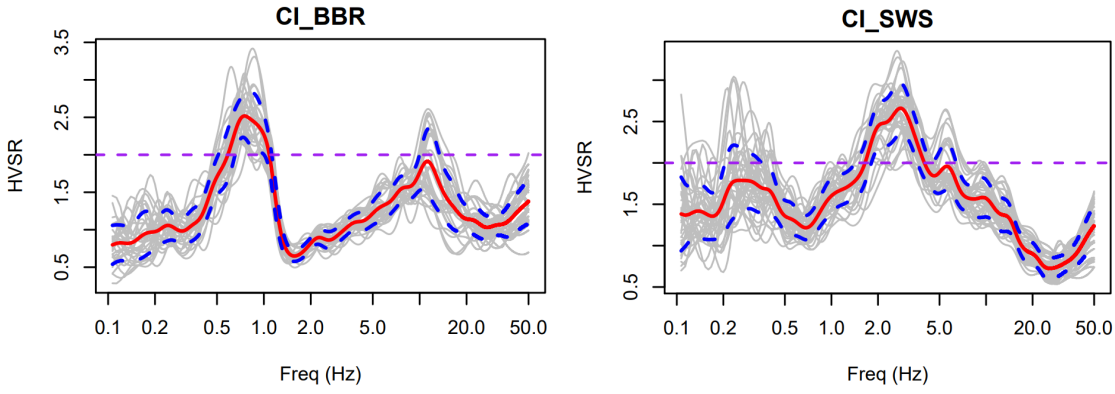

Figure 3.14: Example sites to illustrate the missing peak issue by SESAME

The gray lines are the individual HVSR curves from each sub-window, the red solid line is the mean curve, the dash blue lines are the bounds of mean ± one standard deviation,

and the horizontal purple dash line is at amplitude = 2. Analyst inspections indicate that there is a clear peak with $f_{\text{peak}} \approx 0.7$ Hz at CI_BBR site (on the left) and a clear peak with $f_{\text{peak}} \approx 2.5$ Hz at CI_SWS site (on the right). However, more than one SESAME condition fails to identify the peaks. The estimated statistics for the two sites for each SESAME condition are listed in Table 3.7.

Table 3.7: Criteria of peak identification from SESAME

Site	Parameters	Estimated Statistics	Decision
CI_BBR	f_{peak}	0.75 Hz	
	Reliability 3: $\sigma_A(f)$	0.379	< 2, pass
	Clear 3: A_{peak}	2.52	> 2, pass
	Clear 1: $\min(A_{H/V}(f))$	0.96	$0.96 < 0.5A_{\text{peak}} = 1.26$, pass
	Clear 2: $\min(A_{H/V}(f))$	0.65	$0.65 < 0.5A_{\text{peak}} = 1.26$, pass
	Clear 4-1: peak frequency of mean - SD, f_{peak}	0.73	$0.73 \in [f_{\text{peak}}/1.05 = 0.71, 1.05f_{\text{peak}} = 0.79]$, pass
	Clear 4-2: peak frequency of mean + SD, f_{peak}	0.82	$0.82 \notin [f_{\text{peak}}/1.05 = 0.71, 1.05f_{\text{peak}} = 0.79]$, **fail**
	Clear 5: σ_f	1.34 Hz	$1.34 \not< 0.15f_{\text{peak}} = 0.11$ Hz, **fail**
	Clear 6: $\sigma_A(f_{\text{peak}})$	0.29	$0.29 < 2$, pass
CI_SWS	f_{peak}	2.80 Hz	
	Reliability 3: $\sigma_A(f)$	0.315	< 2, pass
	Clear 3: A_{peak}	2.66	> 2, pass
	Clear 1: $\min(A_{H/V}(f))$	1.22	$< 0.5A_{\text{peak}} = 1.33$, pass
	Clear 2: $\min(A_{H/V}(f))$	1.46	$1.46 \not< 0.5A_{\text{peak}} = 1.33$, **fail**
	Clear 4-1: peak frequency of mean - SD, f_{peak}	2.84	$2.84 \in [f_{\text{peak}}/1.05 = 2.67, 1.05f_{\text{peak}} = 2.94]$, pass
	Clear 4-2: peak frequency of mean + SD, f_{peak}	2.76	$2.76 \notin [f_{\text{peak}}/1.05 = 2.67, 1.05f_{\text{peak}} = 2.94]$, pass
	Clear 5: σ_f	1.46 Hz	$1.46 \not< 0.05f_{\text{peak}} = 0.14$ Hz, **fail**
	Clear 6: $\sigma_A(f_{\text{peak}})$	0.30	$0.30 < 1.58$, pass

Both sites have two failed conditions (SESAME allows at most one failed condition for a site to be identified as having a clear peak, thus neither site is identified as having a

peak by the SESAME criteria). There are many other sites with slightly less clear peaks than these two that are identified as having peaks by our rules but failed by two or more SESAME conditions. To address this overly strict definition of peaks, I propose to change the thresholds in Clear 1, Clear 2, Clear 3, and Clear 4, and to remove Clear 5 (as Clear 5 is barely satisfied by any sites). I also recommend separating the rules for strong motion and noise since the amplitudes in strong motion and noise differ (as shown in Figure 3.12 and discussed in Section 3.5.1). I set the new thresholds to the boundaries where they can best separate peaks and no peaks sites. The new recommended criteria are summarized in Table 3.8.

Table 3.8: The new recommended criteria of peak identification for strong motions and noise

Parameters	Strong Motions	Noise
Reliability 3: $f_{\text{peak}} > 0.5\,\text{Hz}, f \in [0.5f_{\text{peak}}, 2f_{\text{peak}}]$	$\sigma_A(f) < 2$	$\sigma_A(f) < 2$
Reliability 3: $f_{\text{peak}} < 0.5\,\text{Hz}, f \in [0.5f_{\text{peak}}, 2f_{\text{peak}}]$	$\sigma_A(f) < 3$	$\sigma_A(f) < 3$
Clear 1: $f \in [0.25f_{\text{peak}}, f_{\text{peak}}]$	$A_{H/V}(f) < 0.6A_{\text{peak}}$	$A_{H/V}(f) < 0.6A_{\text{peak}}$
Clear 2: $f \in [f_{\text{peak}}, 4f_{\text{peak}}]$	$A_{H/V}(f) < 0.4A_{\text{peak}}$	$A_{H/V}(f) < 0.6A_{\text{peak}}$
Clear 3:	$A_{\text{peak}} >= 2.9$	$A_{\text{peak}} >= 1.6$
Clear 4: peak of SD curve $f_{\text{peak}}[A_{H/V}(f) - \sigma_A(f)]$	within $[f_{\text{peak}}/1.18, 1.18f_{\text{peak}}]$	within $[f_{\text{peak}}/1.15, 1.15f_{\text{peak}}]$
Clear 4: peak of SD curve $f_{\text{peak}}[A_{H/V}(f) + \sigma_A(f)]$	within $[f_{\text{peak}}/1.19, 1.19f_{\text{peak}}]$	within $[f_{\text{peak}}/1.12, 1.12f_{\text{peak}}]$
Clear 5: $f_{\text{peak}} < 0.2\,\text{Hz}$	-	-
Clear 5: $f_{\text{peak}} \in [0.2, 0.5)\,\text{Hz}$	-	-
Clear 5: $f_{\text{peak}} \in [0.5, 1.0)\,\text{Hz}$	-	-
Clear 5: $f_{\text{peak}} \in [1.0, 2.0]\,\text{Hz}$	-	-
Clear 5: $f_{\text{peak}} > 2.0\,\text{Hz}$	-	-
Clear 6: $f_{\text{peak}} < 0.2\,\text{Hz}$	$\sigma_A(f_{\text{peak}}) < 3$	$\sigma_A(f_{\text{peak}}) < 3$
Clear 6: $f_{\text{peak}} \in [0.2, 0.5)\,\text{Hz}$	$\sigma_A(f_{\text{peak}}) < 2.5$	$\sigma_A(f_{\text{peak}}) < 2.5$
Clear 6: $f_{\text{peak}} \in [0.5, 1.0)\,\text{Hz}$	$\sigma_A(f_{\text{peak}}) < 2$	$\sigma_A(f_{\text{peak}}) < 2$
Clear 6: $f_{\text{peak}} \in [1.0, 2.0]\,\text{Hz}$	$\sigma_A(f_{\text{peak}}) < 1.78$	$\sigma_A(f_{\text{peak}}) < 1.78$
Clear 6: $f_{\text{peak}} > 2.0\,\text{Hz}$	$\sigma_A(f_{\text{peak}}) < 1.58$	$\sigma_A(f_{\text{peak}}) < 1.58$

3.6 Conclusions

In this chapter, I have introduced new criteria for categorizing sites based on HVSR. The categories are clear peak sites ("P-P"), no peak sites ("N-N"), and ambiguous sites ("P-N" or "N-P"). The "P-P" sites are defined as sites where both HVSRs from two data sources (strong motion and noise) show a clear peak in Section 3.5.1 or both analysts identify a peak using one data source in Section 3.5.2. Under the definition from Section 3.5.1, I find that "P-P" sites in general are younger geological units and are relatively soft sites with smaller V_{S30}. In the subsequent sections and chapters, I will use the definition of "P-P" sites according to judgements of two analysts from Section 3.5.2.

I have also put forward new protocols for HVSR data analysis. This includes a new procedure for HVSR processing implemented in a program coded in R. This new procedure accepts the framework and many functions from Geopsy and also introduces a few new features (e.g., combining two horizontals by RotD_{50}). Secondly, the aforementioned criteria enable relatively robust identification of sites with peaks, without peaks, and intermediate cases. As will be shown subsequently, this is important information for modeling purposes. I have developed new objective-based criteria adaptable to the different data sources. Lastly, I introduced a new Gaussian fitting function with more flexibility to capture HVSR peak amplitudes.

CHAPTER 4

Site Response Analysis Methods and Protocols

In this chapter the use and applicability of predictive methods for site response are described. Besides the most fundamental ergodic model, I also review site-specific models potentially suitable for non-ergodic analysis, including, ground response analysis (GRA), square root impedance (SRI) method, and a hybrid of V_{S30}-based ergodic models and supplemented with a model conditioned on HVSR-based parameters (HVSR). Protocols for specification of model inputs are also presented.

4.1 Site response models

In this section, I will briefly introduce the site response models considered in the study.

4.1.1 Ergodic model

In the ergodic ground motion model, site amplification F_S (in BSSA14 model [22]) is a function of time-averaged shear wave velocity V_{S30}, distance R_{JB}, magnitude of earthquake $\mathbf{M}$, location $region$, and depth that is used to represent basin effect z_1. It contains three parts, a linear component of site amplification F_{lin}, a nonlinear component of site amplification F_{nl}, and a basin depth effect model $F_{\delta z_1}(\delta z_1)$,

$$F_S(V_{S30}, R_{JB}, \mathbf{M}, region, z_1) = F_{lin} + F_{nl} + F_{\delta z_1}(\delta z_1) \tag{4.1}$$

the coefficients of this function parameters are set based on regressions using a global database [22].

The linear site amplification and nonlinear site amplification were originally proposed by

[88]. The linear site amplification F_{lin} describes the scaling of ground motion with V_{S30} for linear soil response conditions, typically with small strains under weak ground motions. F_{lin} is expressed as

$$F_{lin} = \begin{cases} c\ln(\frac{V_{S30}}{V_{ref}}) & V_{S30} \leq V_c \\ c\ln(\frac{V_c}{V_{ref}}) & V_{S30} > V_c \end{cases} \tag{4.2}$$

where c is the V_{S30} scaling, V_c is the maximum velocity beyond which ground motions no longer scale with V_{S30}, and V_{ref} is a reference velocity (760 m/s). Parameter c and V_c are period-dependent and given by [88].

The nonlinear site amplification F_{nl} is

$$F_{nl} = f_1 + f_2\ln(\frac{PGA_r + f_3}{f_3}) \tag{4.3}$$

where f_1, f_2, and f_3 are model coefficients, and PGA_r is the median peak horizontal acceleration for reference rock where $V_{S30} = 760m/s$. The model takes $f_1 = 0$ to force F_{nl} to 0 for $PGA_r \ll f_3$. f_3 is a transition intensity measure (IM) between linear behavior (lower than f_3) and linear decrease at rate of $f_2\ln(IM)$ (higher than f_3). f_3 is taken as $0.1g$. f_2 expresses the degree of nonlinearity and is a function of V_{S30},

$$f_2 = f_4[\exp\{f_5(\min(V_{S30}, 760) - 360)\} - \exp\{f_5(760 - 360)\} \tag{4.4}$$

where f_4 and f_5 are period-dependent coefficients, also given by BSSA14.

Basin term $F_{\delta z_1}$ is formulated as

$$F_{\delta z_1}(\delta z_1) = \begin{cases} 0 & T < 0.65 \\ f_6\delta z_1 & T \geq 0.65 \& \delta z_1 \leq f_7/f_6 \\ f_7 & T \geq 0.65 \& \delta z_1 > f_7/f_6 \end{cases} \tag{4.5}$$

where f_6 and f_7 are model coefficients, provided by BSSA14. δz_1 (in km) is computed as

$$\delta z_1 = z_1 - \mu_{z_1}(V_{S30}) \tag{4.6}$$

where $\mu_{z_1}(V_{S30})$ is a function of V_{S30} relating to z_1. For California, it can be computed as

$$\ln(\mu_{z_1}) = \frac{-7.15}{4}\ln\Big(\frac{V_{S30}^4 + 570.94^4}{1360^4 + 570.94^4}\Big) - \ln(1000) \tag{4.7}$$

where μ_{z_1} is also in km. Therefore, given V_{S30}, z_1, and PGA_r, the ergodic site response F_S can be estimated. If input motions are weak, there is no need to consider nonlinear site amplification so the inputs are only V_{S30} and z_1.

4.1.2 GRA

One-dimensional ground response analyses (GRAs) model shear wave propagation through horizontal soil layers. As such, these analyses capture impedance and resonance effects on site response, and through the use of equivalent-linear or nonlinear methods, can also capture the effects of stiffness decrease and damping increase with increasing shear strain ([93]). However, additional aspects of wave propagation that contribute to site response are not captured, including basin effects.

Given the partial consideration of the full wave field in GRA, and its widespread utilization in engineering practice, validation is an important topic. The prior validation studies are largely based on the utilization of vertical array data. This study differs from that body of work by using data from surface-only instruments. By so doing, I significantly increase the number of observations that can be considered, but at the cost of the input motion being uncertain. Moreover, the present approach defines long-period site response features for consideration in the validation, which is not possible with vertical array data.

There are three principle considerations in running GRA: (1) selection of an analysis platform, (2) selection of material properties, and (3) development of input motions. I use the analysis platform DeepSoil Ver 7 ([50]), which I run in the linear mode. To run linear GRA, the required input parameters include a V_S profile, soil unit weight, and damping under small-strain conditions ($D_{\min}$). All of the selected stations have measured V_S profiles. The other two parameters, unit weight and $D_{\min}$, are estimated from borehole data (conditioned on soil type and depth) where available, but otherwise are inferred using procedures presented in Section 4.2. Input motions are developed using a deconvolution approach presented in Section 4.2.

4.1.3 SRI

The square-root-impedance (SRI) method, introduced by [61] and subsequently revised and further described by [19], applies principles of wave energy conservation to estimate changes in wave amplitude across layer boundaries. It is widely used in engineering seismology, particularly in combination with semi-stochastic ground motion simulation routines (e.g., [16]). Prior validation studies have considered the SRI method in combination with simulations, but seldom has the method been validated as a stand-alone model. Such validation is undertaken here.

SRI is based on ray theory, whereby conservation of energy requires that the amplitude of motion along a ray path to be inversely proportional to the square root of local seismic impedance ρV, where ρ and V are density and seismic wave velocity, respectively. Therefore, the amplification ratio at a soil site can be expressed as (notation taken from [61]),

$$A = \left(\frac{\rho_R V_R}{\rho_S V_S}\right)^{1/2} \left(\frac{\cos i_R}{\cos i_S}\right)^{1/2} \tag{4.8}$$

where V_R and V_S are the near-surface velocities for rock and soil respectively, ρ_R and ρ_S are the rock and soil mass densities, and i_R and i_S are vertical angles of incidence (0 indicates vertical propagation). It is common to assume a vertical angle of incidence, which causes the cosine terms to cancel out (per Snell's Law, this may be a reasonable assumption near the ground surface for body waves; e.g., [70]).

For a given frequency, amplification is computed using Equation 4.8 by taking reference rock properties as fixed (independent of frequency) and taking the seismic impedance (product of velocity and density) of surface materials as depth-averaged values measured from the ground surface to a depth corresponding to a quarter wavelength ([21]). Because wavelength is frequency-dependent, depth-averaged impedance and amplification are also frequency-dependent. As in [21], I average seismic velocity and density separately instead of their product being averaged. Site amplification for a frequency of interest f is computed as follows:

1. Identify the reference condition for the calculation at depth z_R; taken here as the top

of the last layer in the profile (usually having the fastest velocity). This establishes ρ_R and V_R;

2. Select an arbitrary depth $z < z_R$, and for this depth compute the shear wave travel time $\Delta t_{V_S}(z)$ from surface to depth z;

3. Compute the average density $\overline{\rho_S(z)}$, the average velocity $\overline{V_S(z)} = \frac{z}{\Delta t_{V_S}(z)}$, and the corresponding frequency $f(z) = \frac{1}{4\Delta t_{V_S}(z)}$, which is based on the quarter wavelength;

4. Compute site amplification associated with frequency $f(z)$ as

$$A[f(z)] = \sqrt{\frac{\rho_R V_R}{\overline{\rho_S(z)} * \overline{V_S(z)}}} \tag{4.9}$$

5. Repeat steps 2-4 for different depths $z < z_R$ to develop amplification estimates over the largest possible frequency range. The lowest frequency corresponds to a quarter wavelength equivalent to z_R, which is close to the fundamental-mode resonant frequency of the soil column.

The amplification $A(f)$ obtained from this procedure applies in the frequency domain for the case of zero material damping. The effects of damping are accounted for through application of decay parameter κ ([16]), specifically the change in κ from the surface to depth z_R, denoted $\Delta\kappa$. The correction is applied as

$$A_c[f(z)] = A[f(z)] * \exp(-\pi f \Delta\kappa) \tag{4.10}$$

4.1.4 HVSR model

As described above, V_{S30}-based ergodic models cannot capture peaks from site-specific resonance effects because the model prediction is smoothed over a large number of sites with different characteristics. These features of site-specific site response can potentially be captured by using a hybrid approach consisting of a V_{S30}-scaling model (producing smooth amplification in frequency space) and a peak function conditioned on HVSR parameters (namely f_{peak}) ([52, 53, 55, 56, 72]). In this study, I apply the hybrid model proposed by [72], which modifies the SS14 ergodic model.

The HVSR semi-empirical site response model is given as,

$$F_{Sm} = F_S + F_{HV} \tag{4.11}$$

where F_S is from the ergodic model. F_{HV} is the site amplification term conditioned on the fitting parameters from HVSR (described in Section 3.4).

The F_{HV} model is defined as,

$$F_{HV} = \begin{cases} \bar{c}, & \text{no clear peak} \\ \ln(\hat{\alpha}_1)\exp\Big(-\Big(\frac{\ln(\alpha_p f_{p1} T)}{\hat{\omega}_1}\Big)^2\Big) + \hat{\beta}, & \text{only one clear peak} \\ \ln(\hat{\alpha}_1)\exp\Big(-\Big(\frac{\ln(\alpha_p f_{p1} T)}{\hat{\omega}_1}\Big)^2\Big) + \ln(\hat{\alpha}_2)\exp\Big(-\Big(\frac{\ln(\alpha_p f_{p2} T)}{\hat{\omega}_2}\Big)^2\Big) + \hat{\beta}, & \text{more than one clear peaks} \end{cases} \tag{4.12}$$

where $\bar{c}$, $\hat{\alpha}_1$, $\hat{\alpha}_2$, $\hat{\omega}_1$, $\hat{\omega}_2$, and $\hat{\beta}$ are coefficients; f_{p1} and f_{p2} are frequencies fit to HVSR peaks; and T is the oscillator period. Note if there are more than one peaks, only the first two clear peaks are taken and the subscripts 1 and 2 related to the lower- and higher-frequency clear peaks. The F_{HV} model in [72] produces peaks centered on the peaks from HVSR (f_{p1}, f_{p2}). Since the publication of this model, a number of studies have shown that the peaks in site response can be slightly shifted relative to the peaks from HVSR. Accordingly, I introduce a scaling factor on the peak frequency α_p in Equation 4.12. This parameter is investigated in Chapter 5. A simulation-based study found a value of $\alpha_p = 1.2$ ([55, 56]).

The amplitude terms $\hat{\alpha}_1$ (and $\hat{\alpha}_2$) and pulse width terms $\hat{\omega}_1$ (and $\hat{\omega}_2$) are defined as:

$$\ln(\hat{\alpha}_i) = c_1 + c_2 a_{pi}, \;\; i = \{1 \text{ or } 2\} \tag{4.13}$$

where $c_1 = 0.134$ and $c_2 = 0.103$

$$\hat{\omega}_1 = \hat{\omega}_2 = 0.4 \tag{4.14}$$

and the constant term $\hat{\beta}$ is computed as,

$$\hat{\beta} = \begin{cases} \beta_1, & \text{if } \ln(T) \leq t_1 \\ \frac{\beta_2-\beta_1}{t_2-t_1}(\ln(T)-t_1)+\beta_1, & \text{if } t_1 < \ln(T) \leq t_2 \\ \beta_2, & \text{if } t_2 < \ln(T) \leq t_3 \\ \frac{\beta_3-\beta_2}{t_4-t_3}(\ln(T)-t_3)+\beta_2, & \text{if } t_3 < \ln(T) \leq t_4 \\ \beta_3, & \text{if } \ln(T) > t_4 \end{cases} \tag{4.15}$$

in which β_i and t_i are functions of frequencies (f_{pi}) and amplitudes (a_{pi}) are taken from the fitting of HVSR peaks. The functions for each coefficient are listed in Table 4.1.

Table 4.1: Functions of parameters of β_i and t_i

Parameter	**Function**
β_1	$-0.7+0.35(\ln(a_{p1})+0.5)-0.05(\ln(f_{p1})-1)$
β_2	$0.2\exp(0.3(3-\ln(f_{p1})))-0.7$
β_3	0
t_1	$-2-\ln((\ln(f_{p1})-1)^2+1)$
t_2	$t_1+2\ln(3\ln(a_{p1})+1)-2$
t_3	$t_2+\ln(5(\ln(a_{p1})-1.2)^2+1)$
t_4	$t_3+\ln(a_{p1})+0.3\ln(f_{p1})+1$

The F_{HV} model in [72] was modified for the present applications. There are several rationales for these modifications. First, the model was developed for data in Japan, whereas it is now being applied to sites in California. As a result, I did not consider my use of the model to be "bound" by the published coefficients. Second, as mentioned previously and shown in Equation 4.12, because site response peaks in oscillator period space do not necessarily occur at the inverse of f_p, I sought to enable flexibility in the location of peaks through the α_p parameter. Third, in my use of the model for the diverse conditions at my study sites, I identified some issues with the model, particularly in connection with the $\hat{\beta}$ model (Equation 4.15) when certain periods used in the model are too proximate. In consideration of all these factors, four models adjustments relative to [72] were applied:

1. Parameter t_2 is a period coefficent which should be greater than t_1. This condition is satisfied when $a_{p1} \geq 1.77$. However, if the amplitude of the peak is less than 1.77, t_2 is less than t_1, which produces a step in the $\hat{\beta}$ function. To address this issue, I apply in the model,

$$a'_{p1} = \max\{2, a_{p1}\} \tag{4.16}$$

where a_{p1} is still the parameter from peak fitting and a'_{p1} is the corrected parameter should be used to replace a_{p1} in any subsequent functions.

2. Parameter β_2 should be less than β_1 as indicated in the schematic shown in Figure 4 in [72]. However, for some sites in this study, β_2 exceeds β_1. I address this issue by applying in the model,

$$\beta'_2 = \max\{\beta_1, \beta_2\} \tag{4.17}$$

where β_1 and β_2 are the values calculated based on the functions in Table 4.1 and β'_2 is the corrected parameter applied in this study.

3. Period parameters t_3 and t_2 should not be too close in period space. If the corrected a'_{p1} is around $e^{1.2} = 3.3$, then $t_3 = t_2 + \ln(1) = t_2$. This is addressed by updating the equation for t_3 as,

$$t_3 = \min\{t_2 + \ln(1.2), t_2 + \frac{t_4 - t_2}{2}\} \tag{4.18}$$

The first term $t_2 + \ln(1.2)$ means t_3 is increased by 20% from t_2 in log-scale and the second term $t_2 + \frac{t_4 - t_2}{2}$ means t_3 is the middle point of t_2 and t_4. The reason I made this update is because the model works well when t_3 is greater than t_2 but t_3 should not be greater than the mid-period between t_2 and t_4. 20% was estimated from the curve in Figure 4 in [72].

4. An adjustment in the location of the peak site response relative to $1/f_{pi}$ is allowed through use of the α_p coefficient.

5. An adjustment of coefficient $\bar{c}$ is made based on the California no peak sites data (from $\bar{c} = 0.1$ to $\bar{c} = 0.0625$).

With these adjustments, the F_{HV} term (Equation 4.11) can be estimated from HVSR data.

4.2 Protocols for model inputs

In this section, I describe the development of model inputs for site response analysis, including dynamic material properties and input motions.

4.2.1 Inference of unit weight and $D_{\min}$

Ground response analyses for linear conditions require shear wave velocity, unit weight, and $D_{\min}$ profiles. Shear wave velocity profiles are measured at each of the selected sites. In most forward applications, geotechnical site characterization provides borehole logs that describe site stratigraphy and soil type information, which can be used to derive the input parameters used to predict unit weight and $D^L_{\min}$. As described in Section 2.3, this is not the case for many of the sites considered in this research. This section describes how I estimate unit weight and soil parameters used to estimate material damping.

4.2.1.1 Unit weight

For soil units, I estimate unit weight using phase relationships, which relate unit weight to void ratio, specific gravity, and saturation. Void ratio is taken from an empirical relationship with V_S shown in Figure 4.1 and given as ([84]):

$$V_S = 42.9 + 94.1/e^2 \tag{4.19}$$

where V_S is in units of m/s.

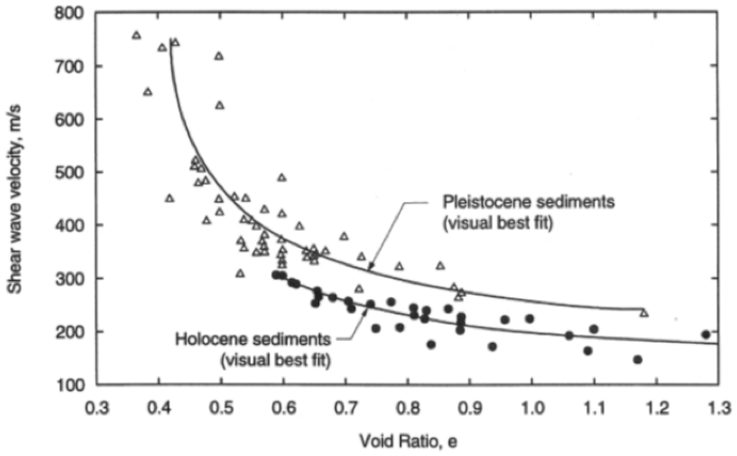

Figure 4.1: Empirical relationships between void ratio, age, and shear-wave velocity for alluvial sediments in southern California ([41]). Equation 4.19 fits the combined data ([84])

Specific gravity is commonly taken as $G_S = 2.7$. Saturation (S) is taken as 1.0 below the first depth where V_P exceeds 1500 m/s. Above that depth, or over the full depth where V_P data is absent, saturation is assumed as 50%. Total unit is then computed as:

$$\gamma = \frac{G_S \gamma_w}{1+e}\left(1 + \frac{eS}{G_S}\right) \tag{4.20}$$

where γ_w is the unit weight of water (taken as $10kN/m^3$).

For rock units, I assigned unit weight based on V_S as follows:

$$\gamma = \begin{cases} 20kN/m^3, & 450 < V_S < 700m/s \\ 22kN/m^3, & \text{otherwise} \end{cases} \tag{4.21}$$

4.2.1.2 Stratigraphy and soil type to estimate $D_{\min}$ in soil layers

Stratigraphic and soil type information is needed to apply the geotechnical model for $D_{\min}$ estimation by [36], which is conditioned on plasticity index (PI), over-consolidation ratio (OCR), and mean effective stress. Effective stress can be calculated using unit weights from the prior section and water table depth (as applicable). PI and OCR are generally derived from laboratory tests on samples retrieved from the field. This section presents procedures used to estimate these parameters for sites without stratigraphic logs (150 out of 159).

I consider two types of available information as potentially useful to assign stratigraphy and soil type information - the mapped surface geology and the V_S profile. Surface geology is used to estimate soil type near the ground surface. The V_S profile is used in combination with the surface unit assignment to estimate variations of stratigraphy with depth.

Surface geology is taken from state-wide geologic maps by [111] and [112]. I assume relationships between surface geological unit and PI/OCR as presented in Table 4.2. Considerations in the development of the relationships in Table 4.2 include:

- Geologically young sediments (Holocene) are assumed to have low OCR, and older units are assumed to have relatively high OCRs. The rationale is that young deposits have relatively limited pseudo-overconsolidation from aging and are unlikely to have experienced significant unloading from natural geological processes.

- Young sediments deposited in quiescent environments (e.g., bays, lakes, central/flat portions of alluvial basins) are assumed to be relatively fines- and clay-rich, thus having high PI. Young alluvial sediments deposited on steeper gradients are assumed to be relatively granular (PI = 0).

- Tertiary sedimentary bedrock units often carry information on rock type (e.g., shale, sandstone, etc.). I assume the bedrock units are similar to corresponding soil units (i.e., shale and sandstone interpreted as clay and sand, respectively).

- For pre-Quaternary units without information on material type or depositional environment, there is no basis for assuming relatively coarse- or fine-grained behavior. I assume an intermediate condition in this case (roughly corresponding to low-plasticity silt).

Table 4.2 is organized in reference to 12 geological units, recommended by [111], that are encountered for the stations in the full database: Qal1, Qal2, and Qal3 are relatively young alluvial sediments likely to be of Holocene age; Qoa is older alluvium of Pleistocene age; QT describes sediments in the early Pleistocene to Pliocene periods, for which the method of deposition is unknown; Tsh, Tss, and Tv comprise Tertiary age bedrock consisting of shale,

sandstone, or volcanic-origin materials (typically basalt or rhyolite), respectively; serpentine is a metamorphic rock of Tertiary age largely comprised of the clay mineral serpentinite; and Kss, Kjf, and crystalline are hard rock, typically of Cretaceous age.

Before assigning one of the hard rock classes (Kss, Kjf, crystalline), I perform a visual check of morphology using Google Earth^{TM}. When this check indicates that the surface appears to be soil, and if the velocity of the nearest-surface layer is compatible with soil, I assign a soil surficial unit and assign rock at greater depths where velocities become fast.

The soil property assignments in Table 4.2 apply for ground surface layers. The assignment of properties at depth is made in consideration of gradients in the V_S profile. If the surface layer consists of sediments or Tertiary rock, the soil index properties are not changed in successive layers absent sudden changes in velocity with depth. Sudden changes can trigger soil type changes - for example, when a granular layer is underlain by a much slower layer, the underlying unit is taken as clay. Similarly, when a fine-grained surface layer is underlain by a much stiffer layer, the underlying material is taken as granular. When a layer velocity exceeds 760 m/s, it is taken as rock. Figure 4.2 shows the flow chart used to assign soil type information as a function of depth.

Table 4.2: The list of 12 geological units and their corresponding PI and OCR. Ma indicates million years

Geological age	**Geol. unit**	**Description**	**Estimated Parameters**
Holocene (< 0.011 Ma)	Qal1	Quaternary Holocene alluvium with flat gradients (< 0.5%).	PI = 30 OCR = 1.2
	Qal2	Quaternary Holocene alluvium with moderate gradients ($0.5 - 2.0\%$).	PI = 10 OCR = 1.2
	Qal3	Quaternary Holocene alluvium with steep gradients (> 2%).	PI = 0 OCR = 1.2
Pleistocene (< 2.6 Ma)	Qoa	Quaternary Pleistocene alluvium. Soil composition unknown.	PI = 10 OCR = 2
Pliocene (2.6-5.3 Ma). Young era within the Tertiary.	QT	Quaternary to Tertiary deposits, including Saugus Fm. in So. CA, Paso Robles Fm. in central Coast Ranges, and Santa Clara Fm. in San Francisco Bay area. Soil composition unknown.	PI = 10 OCR = 2.5
Tertiary (2.6-66 Ma)	Tsh	Shale and siltstone units, such as the Repetto, Fernando, Puente, and Modelo Fms in So. CA.	PI = 15 OCR = 3
	Tss	Sandstone units, such as the Topanga Formation in So. CA and Butano Formation in San Francisco Bay area.	PI = 0 OCR = 3
	Tv	Volcanic units including the Conejo Volcanics in Santa Monica Mtns and the Leona Rhyolite in East Bay Hills.	PI = 15 OCR = 3
	Serpentine	Serpentine rock is clay-rich.	PI = 15 OCR = 3
Cretaceous	Kss	Cretaceous sandstone of the Great Valley Sequence	NA
	Kjf	Franciscan complex rocks, including mélange, sandstone, shale, chert, and greenstone.	NA
	crystalline	Crystalline rocks, including Cretaceous granitic rocks, Jurassic metamorphic rocks, schist, and Precambrian gneiss.	NA

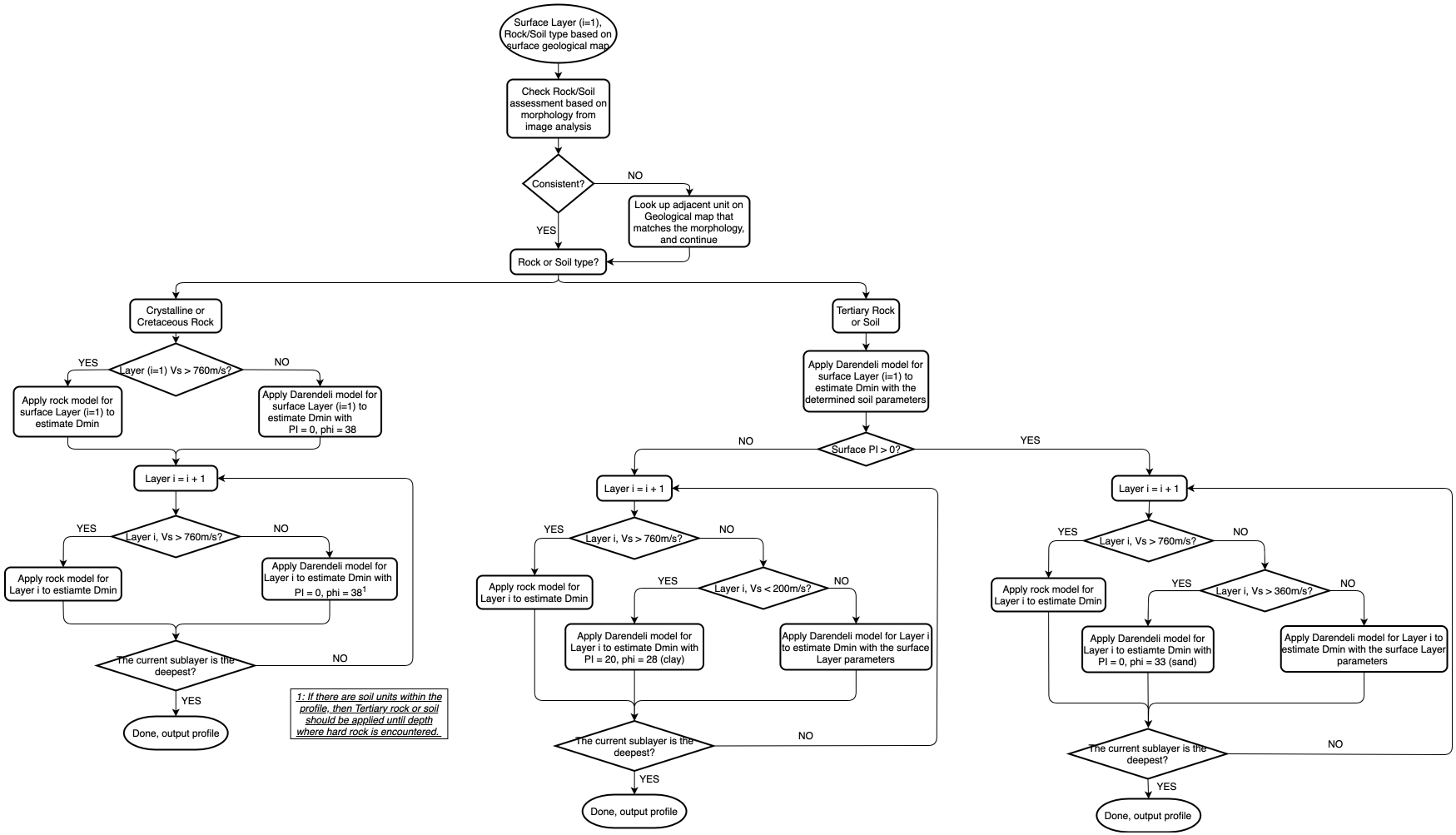

Figure 4.2: Flow chart used to assign soil type information as function of depth

4.2.1.3 $D_{\min}$ in firm rock layers

The Darendeli ([36]) model cannot be used for pre-Tertiary rock (units Kss, Kjf, crystalline). Laboratory data on material damping for such materials is limited. A presumably judgement-based model was presented by [86] and has been widely used since that time. Choi ([32]) performed testing on welded Bandelier Tuff and Topopah Spring Tuff and developed damping models. Models from these two sources are compared in Figure 4.3. The $D_{\min}$-component from Topogah Spring Tuff is considered more representative of bedrock materials in our study region based on its unit weight (Bandelier Tuff has low unit weights). The $D_{\min}$ range for this material is about $0.2 - 1.0\%$ (average $= 0.3\%$). I have used the Choi model for the present work, but acknowledge that its use carries large uncertainty.

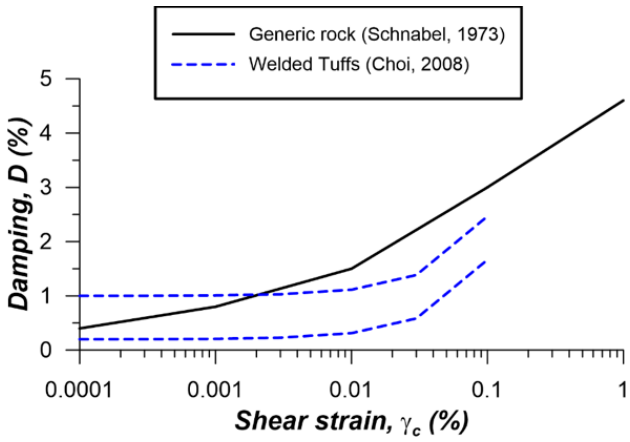

Figure 4.3: Comparison of rock damping model from Schnabel ([86]) and range from Choi ([32])

4.2.1.4 Validation of protocols for estimation of soil type and $D^L_{\min}$

For 150 of the 159 sites considered in this research, material classifications from laboratory tests or borehole logs are unavailable. The procedures for estimating material type and $D^L_{\min}$ for soil and rock materials in Sections 4.2.1.2 and 4.2.1.3, respectively, were developed to overcome this data gap. Here I validate these procedures using data for the nine sites with boring logs. Two types of validation are considered - validation of material type indirectly through the $D^L_{\min}$ assignment, and relatively direct validation of material type via an index

Table 4.3: Validation sites for $D_{\min}^{L}$ and material type assignments

SSN	**Site Name in PDB**	**Surface Geological Category [112]**	**Source Reference**
100473	Wonderland School	crystalline	ROSRINE Phase 2b
100562	Caltech Old Seismology Lab	crystalline	Fumal et al ([42]) and Boore ([17])
1148	Griffith Observatory	crystalline	ROSRINE Phase 2b
1213	Little Rock P.O.	Qal3	Fumal et al ([42]) and Boore ([17])
303	Colton Interchange East	Qal2	Gibbs et al ([45]) and Boore ([17])
3060	San Bernardino Fire Station	Qal2	Gibbs et al ([43]) and Boore ([17])
316	Kagel Canyon	Tsh	ROSRINE Phase 1
337	Obregon Park	Qal3	Gibbs et al ([45]) and Boore ([17])
63	Rinaldi Receiving Station	Qal3	Gibbs et al ([44]) and Boore ([17])

parameter.

The nine validation sites are listed in Table 4.3 with their surface geologic categories ([112]) and the respective sources of borehole data. For the nine validation sites, I estimate $D_{\min}^{L}$ for each layer using material type information from the boring logs, which is compared to estimates derived from the protocols in Section 4.2.1.2 in Figure 4.2. While the profiles from two sources do not align perfectly, the trends with depth and overall levels of damping are similar.

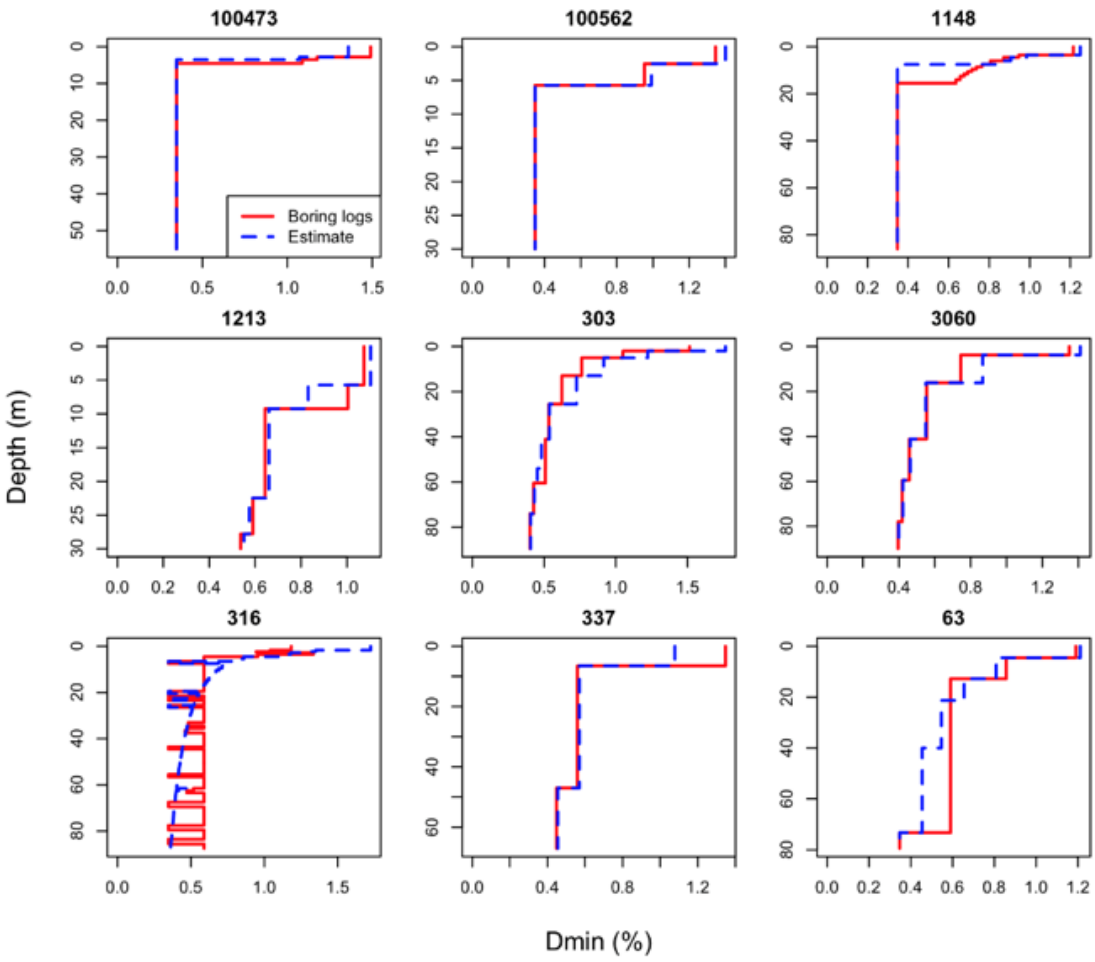

Figure 4.4: Profiles of $D_{\min}$ at nine validation sites

For the second type of validation, I assign a soil behavior type index (I_c) to each soil layer based on its material description (the four bedrock sites are excluded). This is done by first assigning a soil behavior type zone (1-9) as given in Table 4.4, and then assigning a representative I_c for each zone as per the contours shown in Figure 4.5. Figure 4.6 shows the resulting I_c profiles for the five soil sites. The I_c profiles exhibit larger differences than was seen in $D^L_{\min}$. However, because soil type is only important for the present analysis to the extent that it affects V_S (which is measured) and $D^L_{\min}$ (which is not particularly sensitive to material type), the differences shown in Figure 4.6 are rather inconsequential.

[1]Overconsolidated or cemented

Table 4.4: Soil behavior type zones (Robertson [81])

SBT Zone	**Proposed Common SBT Description**	**Representative I_c**
1	Sensitive fine-grained	3.0
2	Clay - organic soil	3.8
3	Clays: clay to silty clay	3.3
4	Silt mixtures: clayey silt & silty clay	2.8
5	Sand mixtures: silty sand to sandy silt	2.3
6	Sands: clean sands to silty sands	1.6
7	Dense sand to gravelly sand	1.3
8	Stiff sand to gravelly sand[1]	2.0
9	Stiff fine-grained	2.6

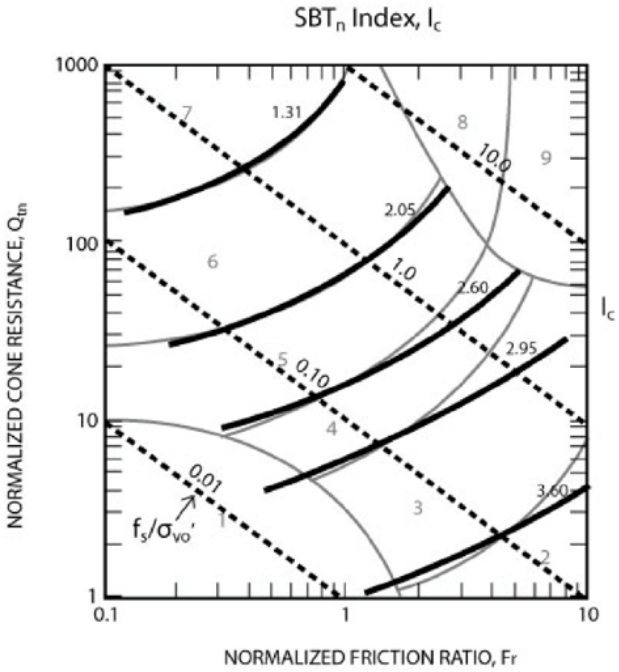

Figure 4.5: Contours of soil behavior type index, I_c (thick lines) and normalized sleeve friction (dashed lines) on normalized normalized cone penetration resistance classification chart ([81])

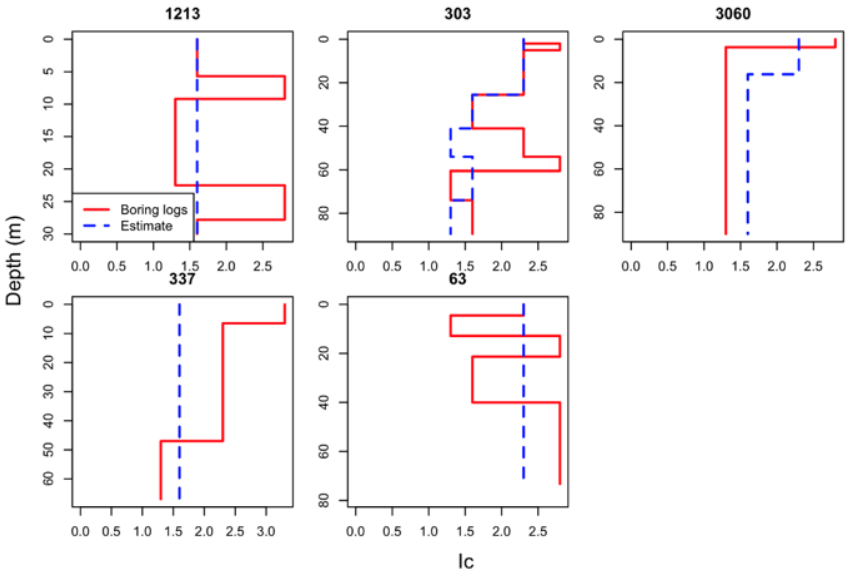

Figure 4.6: Profiles of I_c at five soil validation sites

4.2.2 κ-informed damping model

Figure 4.7 shows Fourier amplitude spectra for ground motions at two examples sites in our database. The spectra show a characteristic feature, which is decay of Fourier amplitudes with increasing frequency for frequencies beyond the peak in the spectrum. This frequency-dependent decay can be described as:

$$D(f) = \exp(-\pi\kappa f) \tag{4.22}$$

where f is frequency in Hz and κ is a decay parameter that can be established through fits to data ([11]). Key aspects of the fitting procedure concern the selection of limiting frequencies and the combination of horizontal components. The protocols followed in the fitting process applied in the present study are as described by ([3]), which were influenced by prior work by [24] and [71].

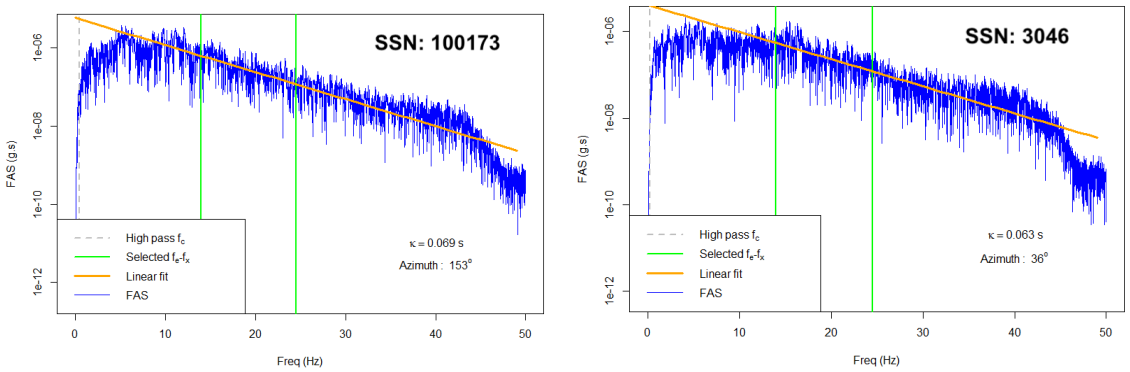

Figure 4.7: Analysis of κ from recordings at two example sites

The decay parameter arises from material damping and wave scattering that occurs on the wave path from source-to-site, often including appreciable contributions from site response. The path and site response contributions to κ combine as (adapted from [10]):

$$\kappa = \kappa_0 + \kappa_R R \tag{4.23}$$

where R is site-to-source distance, κ_R is the slope by which κ increases with distance, and κ_0 represents the cumulative effect of damping and wave scattering through the soil column.

The relationship between κ_0 and profile attributes can be expressed as ([28, 30, 58]):

$$\kappa_0 = \int_0^{z_s} \frac{\mathrm{d}z}{Q_{ef}(z) V_S(z)} \tag{4.24}$$

where z_s is the site column thickness (depth to reference crustal rock) and $Q_{ef}(z)$ is the depth-dependent effective material quality factor, representing both the effects of frequency-dependent wave scattering and frequency-independent soil damping. Q_{ef} can be converted to an effective soil damping as follows ([28]):

$$D_{ef}(\%) = \frac{100}{2Q_{ef}} \tag{4.25}$$

Measurements of κ from recordings can, in principal, inform levels of damping applied in ground response analyses as follows:

1. Measure κ for a set of sites from multiple earthquakes, as shown for example in Figure 4.7.

2. Develop a regionally appropriate model for κ_R.

3. Adjust each measured value of κ, for each event recorded at a given site, to estimate κ_0 by re-arranging Equation 4.23 as $\kappa_0 = \kappa - \kappa_R R$.

4. Since the soil/rock column thickness analyzed in ground response analysis is typically smaller than the full profile to reference crustal rock ($V_S \approx 2.5 \sim 3km/s$), adjust κ_0 from Step (3) as,

$$\Delta\kappa = \kappa_0 - \kappa_{0,b} = \int_0^{z_p} \frac{2D_{ef}(z)}{100} \frac{\mathrm{d}z}{V_S(z)} \tag{4.26}$$

where $\kappa_{0,b}$ is the site decay parameter at the base of the profile and z_p is the depth of the analyzed soil column ($z_p < z_s$).

5. Modify the laboratory damping with a profile-specific adjustment factor F_D to match $\Delta\kappa$ from Step (4), which can be represented by re-writing Equation 4.26 as:

$$\Delta\kappa = \int_0^{z_p} \frac{2D^L_{\min}(z) * F_D}{100} \frac{\mathrm{d}z}{V_S(z)} \tag{4.27}$$

The depth-invariant value of F_D represents the means by which the field observations of κ inform the damping model. In some cases, F_D may be unreasonably high. To constrain F_D so that it provides damping values within a realistic range, I have enforced a maximum value of $F_D = 10$. The approach maintains the scaling of damping with soil type and depth in the laboratory models, while adjusting for other effects encountered in field conditions (scattering). The maximum value of F_D is taken by considering two references [3] and [95]. The former paper studied 21 vertical array sites and estimated F_D and the latter paper studied four vertical array sites and calculated the best multipliers (which has the same meaning as F_D) of $D_{\min}$ to fit observed site responses. The range of the recommended values for F_D and multipliers are from 1.5 up to 9.15, so I take the maximum value as 10.

Implementation of the above procedure requires several model components – distance correction term κ_R and site decay parameter for the base of profile condition $\kappa_{0,b}$. The following sub-sections describe the calculation of κ from recordings, models used for these components, and example results.

4.2.2.1 Fitting of κ from ground motions

I apply the κ-fitting procedures described in [3], which were adapted from [24] and [113]. The fit occurs over a range of frequencies from f_e to f_x (upper and lower bounds, respectively) that is selected for each record.

Search ranges for f_e and f_x are taken as 10-18Hz and 22-28Hz, respectively, each with 0.5Hz increments. For each possible combination of f_e and f_x, κ is computed for combinations of the two horizontal components rotated to various azimuths. The variability of κ with azimuth is computed for each $f_e - f_x$ combination, which is expressed as a coefficient of variation (COV). I seek the combination of f_e and f_x that minimizes the azimuthal variability, and then take κ as the median. The Fourier amplitude spectra for two example sites shown in Figure 4.7 are for the azimuths and frequency ranges identified using this process.

4.2.2.2 Analysis of path- and site contributions to κ

Rates of crustal attenuation vary spatially due to variations in geologic conditions. Conditions producing relatively fast ground motion attenuation rates (i.e., low crustal quality factor, Q) would be expected to increase κ_R. Insight into spatial variations of attenuation rates are provided by maps of frequency-independent Q (denoted Q_S) by [39] for Northern California and [57] for Southern California. Figure 3.8 shows maps of California indicating variations of Q_S at a depth of 10 km from the two sources. I estimate Q_S at a depth of 10 km from [39] by linear interpolation between depths (the model does not provide Q_S at depth of 10 km). There are systematic differences between Q_S from the two sources, with values of southern California model being higher.

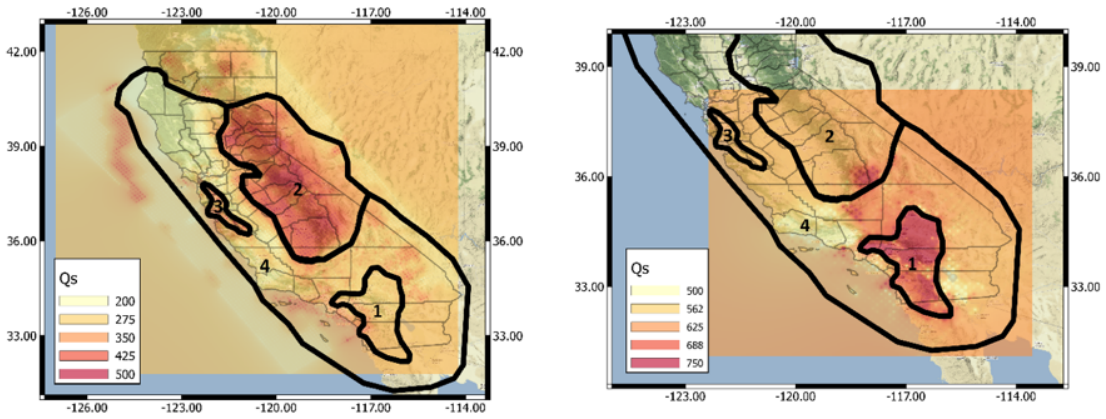

Figure 4.8: Spatial variation of frequency-independent quality factor (Q_S) for California as derived from two models at a depth of 10 km. The heat maps are generated by Inverse Distance Weighting (IDW) in QGIS. Zones considered in mixed-effects analysis of path κ are shown.

Allowing for differences in Q_S between the two sources, considering both maps and calculating the best fit, I have assigned four zones of approximately uniform Q_S, with the intention of computing κ_R separately for each zone. If the value of κ_R for zone i is taken as $\kappa_{R,i}$, then the $\kappa_R R$ term in Equation 4.23 is computed as:

$$\kappa_R R = \sum_i \kappa_{R,i} R_i \tag{4.28}$$

where R_i is the path length (between source and site) through zone i. Distance R_i is zero if the path does not go through zone i.

I use mixed-effects regression (more specifically, random intercept model) to obtain $\kappa_{0,j)}$ for each station j and $\kappa_{R,i}$ for each zone i, by adapting Equation 4.23 as follows:

$$\kappa_{k,j} = \kappa_{0,j} + \sum_{i=1}^{n} \kappa_{R,i} R_{k,i} \tag{4.29}$$

where $\kappa_{k,j}$ is the measured κ from recording k at station j, $\kappa_{0,j}$ is the site-specific decay parameter at station j, n is the number of zones in California, and $R_{k,i}$ is the source-to-site path length for recording k that goes through zone i. Station terms $\kappa_{0,j}$ are taken as random effects and path terms $\kappa_{R,i}$ as fixed effects. Equation 4.29 is solved using an equivalent matrix

form. The matrix form can be expressed explicitly as follows, the an example consisting of three sites,

$$\begin{bmatrix} \kappa_{1,1} \\ \kappa_{2,1} \\ \vdots \\ \kappa_{n_1,1} \\ \kappa_{n_1+1,2} \\ \kappa_{n_1+2,2} \\ \vdots \\ \kappa_{n_1+n_2,2} \\ \kappa_{n_1+n_2+1,3} \\ \kappa_{n_1+n_2+2,3} \\ \vdots \\ \kappa_{n_1+n_2+n_3,3} \end{bmatrix} = \begin{bmatrix} 1 & 0 & 0 \\ 1 & 0 & 0 \\ \vdots & \vdots & \vdots \\ 1 & 0 & 0 \\ 0 & 1 & 0 \\ 0 & 1 & 0 \\ \vdots & \vdots & \vdots \\ 0 & 1 & 0 \\ 0 & 0 & 1 \\ 0 & 0 & 1 \\ \vdots & \vdots & \vdots \\ 0 & 0 & 1 \end{bmatrix} \begin{bmatrix} \kappa_{0,1} \\ \kappa_{0,2} \\ \kappa_{0,3} \end{bmatrix} + \begin{bmatrix} R_{1,1} & R_{1,2} & R_{1,3} & R_{1,4} \\ R_{2,1} & R_{2,2} & R_{2,3} & R_{2,4} \\ \vdots & \vdots & \vdots & \vdots \\ R_{n_1,1} & R_{n_1,2} & R_{n_1,3} & R_{n_1,4} \\ R_{n_1+1,1} & R_{n_1+1,2} & R_{n_1+1,3} & R_{n_1+1,4} \\ R_{n_1+2,1} & R_{n_1+2,2} & R_{n_1+2,3} & R_{n_1+2,4} \\ \vdots & \vdots & \vdots & \vdots \\ R_{n_1+n_2,1} & R_{n_1+n_2,2} & R_{n_1+n_2,3} & R_{n_1+n_2,4} \\ R_{n_1+n_2+1,1} & R_{n_1+n_2+1,2} & R_{n_1+n_2+1,3} & R_{n_1+n_2+1,4} \\ R_{n_1+n_2+2,1} & R_{n_1+n_2+2,2} & R_{n_1+n_2+2,3} & R_{n_1+n_2+2,4} \\ \vdots & \vdots & \vdots & \vdots \\ R_{n_1+n_2+n_3,1} & R_{n_1+n_2+n_3,2} & R_{n_1+n_2+n_3,3} & R_{n_1+n_2+n_3,4} \end{bmatrix} \begin{bmatrix} \kappa_{R,1} \\ \kappa_{R,2} \\ \kappa_{R,3} \\ \kappa_{R,4} \end{bmatrix} \tag{4.30}$$

where each site has n_1, n_2, and n_3 records respectively, then there are $(n_1+n_2+n_3)$ measured κ. In this example, there are three unknown random intercepts $\kappa_{0,1}$, $\kappa_{0,2}$, and $\kappa_{0,3}$, and four unknown slope parameters $\kappa_{R,1}$, $\kappa_{R,2}$, $\kappa_{R,3}$, and $\kappa_{R,4}$. Two matrices, indicator matrix with dimension $(n_1 + n_2 + n_3)$ by 3 and distance matrix with dimension $(n_1 + n_2 + n_3)$ by 4, can be populated knowing source and site locations.

The mixed effect regressions are then performed in R [packages `nlme`([79]) or `lme4`([12])] using the full database (i.e., NGA-West2 stations and records in California as augmented here). The resulting κ_R values are shown for each zone in Figure 4.9, where they are plotted against the Q_S values from the two references. The error bars shown in the figure indicate the estimation error for κ_R from the regressions and the within-zone ranges of Q_S. Regressions provided negative κ_R in Zone 2. This is because the data is not adequate to constrain κ_R. As κ_R physically cannot be negative and the negative estimate of κ_R is not statistically significant (with p-value > 0.05), I take it as zero for subsequent use in this study.

What I had expected to see in Figure 4.9 is a trend of decreasing κ_R with increasing

Q_S, which is expected based on the problem physics. This is not encountered, which may result from limitations in the data set from which κ_R is estimated or from limitations in the California Q_S model. I apply the zone-specific κ_R coefficients in subsequent analysis despite their non-conformance with prior expectation.

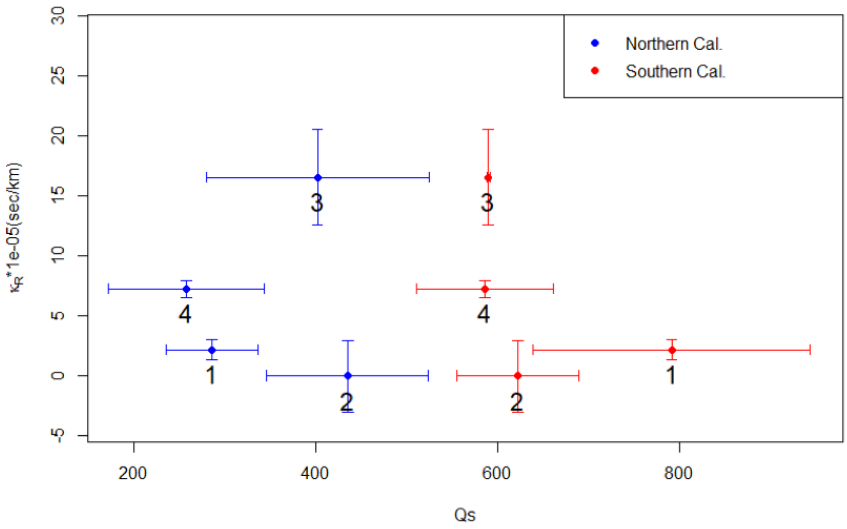

Figure 4.9: Variation of κ_R with average Q_S within the four zones shown in Figure 4.8. Average Q_S is taken from both [39] for Northern California and [57] for Southern California

4.2.2.3 Base of profile site decay parameter, $\kappa_{0,b}$

The base of profile site decay parameter $\kappa_{0,b}$ is needed to estimate the change in site kappa over the profile depth ($\Delta\kappa$) using Equation 4.26. Because the sites considered in this research are surface-only instruments, $\kappa_{0,b}$ cannot be measured (i.e., from a downhole instrument) but instead is estimated from models. Several such models were considered.

Silva et al. ([90]) used California data to relate κ_0 to V_{S30},

$$\kappa_0 = \begin{cases} 0.008\text{sec}, & V_{S30} > 1500m/s \\ 0.020\text{sec}, & 760 < V_{S30} < 1500m/s \\ 0.030\text{sec}, & 360 < V_{S30} < 760m/s \end{cases} \tag{4.31}$$

Van Houtte et al. ([105]) and Xu et al. ([113]) used larger databases from the KiK-net

array in Japan and NGA-West2 data to derive empirical relationships between κ_0 and V_{S30}. Van Houtte et al. ([105]) proposed

$$\ln\kappa_0 = 3.490 - 1.062\ln(V_{S30}) \tag{4.32}$$

where V_{S30} is in units of m/s and κ_0 is in units of sec.

Xu et al. ([113]) proposed

$$\ln\kappa_0 = \begin{cases} k_1(\ln V_1)^2 + k_2\ln V_1 + k_3, & 100m/s < V_{S30} < V_1 \\ k_1(\ln V_{S30})^2 + k_2\ln V_{S30} + k_3, & V_1 < V_{S30} < V_2 \\ k_1(\ln V_2)^2 + k_2\ln V_2 + k_3, & V_2 < V_{S30} < 3000m/s \end{cases} \tag{4.33}$$

where $k_1 = 0.18$, $k_2 = 1.816$, $k_3 = -7.38$, $V_1 = 155m/s$, and $V_2 = 2000m/s$. The units of κ_0 are sec.

I apply the [113] relationship in the present work. To obtain $\kappa_{0,b}$, I estimate the V_{S30} corresponding the base of the soil column by projecting vertically (constant velocity) the V_S at the deepest portion of the profile. I then enter this value into Equation 4.33 to compute $\kappa_{0,b}$. Results of this process for the two example sites are shown in Table 4.5, as are derived values of $\Delta\kappa$ and F_D using Equation 4.26 and 4.27.

Table 4.5: Site kappa results for the SSN = 100173 and SSN = 3046 sites

Site	κ_0**(sec)**	$\kappa_{0,b}$**(sec)**	$\Delta\kappa$**(sec)**	$\mathbf{F_D}$
Keenwild Fire Station, Mountain Center, CA (SSN: 100173)	0.054	0.018	0.036	10
Borrego Springs, CA (SSN : 3046)	0.044	0.026	0.018	10

4.2.3 $Q - V_S$ damping model

An empirical relation between Q_{ef} and V_S was proposed by [26],

$$Q_{ef} = 7.17 + 0.0276V_S \tag{4.34}$$

An equivalent damping can be computed from Q_{ef} using Equation 4.25.

The performance relative to data of ground response analyses with this damping model will be compared in Chapter 5 and 6 to ground response analysis performance when a geotechnical damping model and κ-informed damping model are used.

4.2.4 Development of input motions

For a linear system, site amplification in the frequency-domain (i.e., the site-modification of Fourier coefficients) is independent of input motion attributes. However, the amplification of response spectral ordinates is dependent on the characteristics of input motions, due to sensitivity of oscillator response to the shape of the input spectrum ([91]). As a result, I gave careful consideration to the means by which the input motion was derived, which is explained in this section.

Our approach is to utilize the recorded ground motion at the soil surface as a starting point for derivation of the input motion. I utilize a deconvolution approach, termed here the "inverse transfer function method" (ITF), to convert the surface records to estimates of the equivalent outcropping motion at the reference depth.

Figure 4.10 illustrates the ITF method, which has the following steps:

1. Fourier coefficients (conjugate complex-valued) of the recorded motion are computed, $Z(f)$;

2. The site transfer function amplitude, $|H(f)|$, under linear conditions is derived using DeepSoil and the site soil properties (the program does not provide transfer function phase);

3. I divide the surface record Fourier amplitudes by transfer function amplitudes for each frequency to estimate Fourier amplitudes of the input motion, $|X(f)|$. The phase of the surface record is combined with this amplitude to evaluate Fourier coefficients for the input, $X(f)$. After this calculation, an inverse Fourier transform (IFFT) is performed to compute the estimated input motion in the time domain.

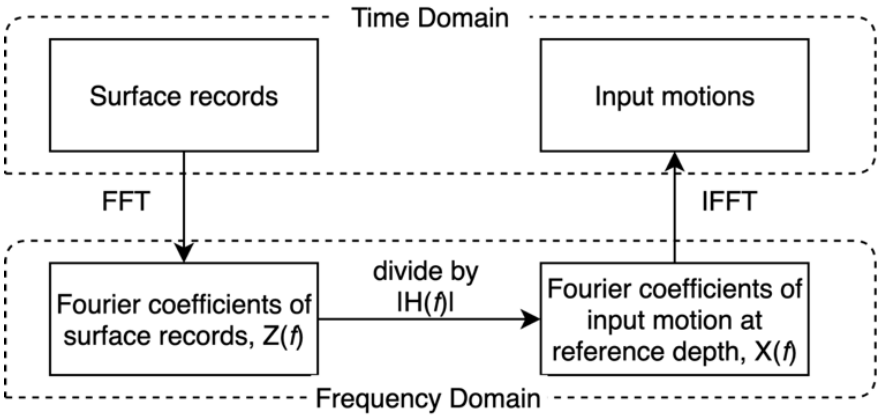

Figure 4.10: Flow chart for the ITF method

Figure 4.11 - 4.16 show for six example sites the V_S profiles, measured (or assumed) soil parameters (unit weight and damping) evaluated using procedures from Section 4.2.1, surface ($|Z(f)|$) and derived input Fourier amplitudes ($|X(f)|$) for a site recording, and response spectra for that same recording. Damping profiles are provided as derived from the geotechnical model ($D^L_{\min}$), the κ-informed model, and the $Q - V_S$ model. As shown in the figures, the changes in Fourier amplitudes and response spectra between the surface and the reference condition are limited to frequencies higher that the fundamental site frequency (f_0). Figure 4.17 compares transfer functions to ratios of response spectra for each site; in each case there is only a single transfer function, but the ratios of the response spectra vary from motion-to-motion. Note that $|H|$ and R.R.S. represent transfer function amplitude and ratio of response spectra of surface records to converted input motions.

There are some sites where the results of the deconvolution process produce unrealistic spectral shapes for input, as shown for example in Figure 4.18(a). This tends to occur when soil damping is high, specifically when high damping scaling factors are applied in the κ adjustment (Section 4.2.2). When this occurs, forward applications in which site amplification is computed using GRA may be unreliable at high frequencies, leading to unusual shapes of the site amplification (Figure 4.18(b)). To overcome this problem, Step (3) in the ITF procedure was modified to use the transfer function derived from geotechnical models for the derivation of the Fourier amplitudes of the input motion, $|X(f)|$, while forward

analyses used the three alternate damping models. This modified (or hybrid) approach was used to produce the results shown in Figures 4.11 - 4.16 and summarized in Chapters 5 - 6.

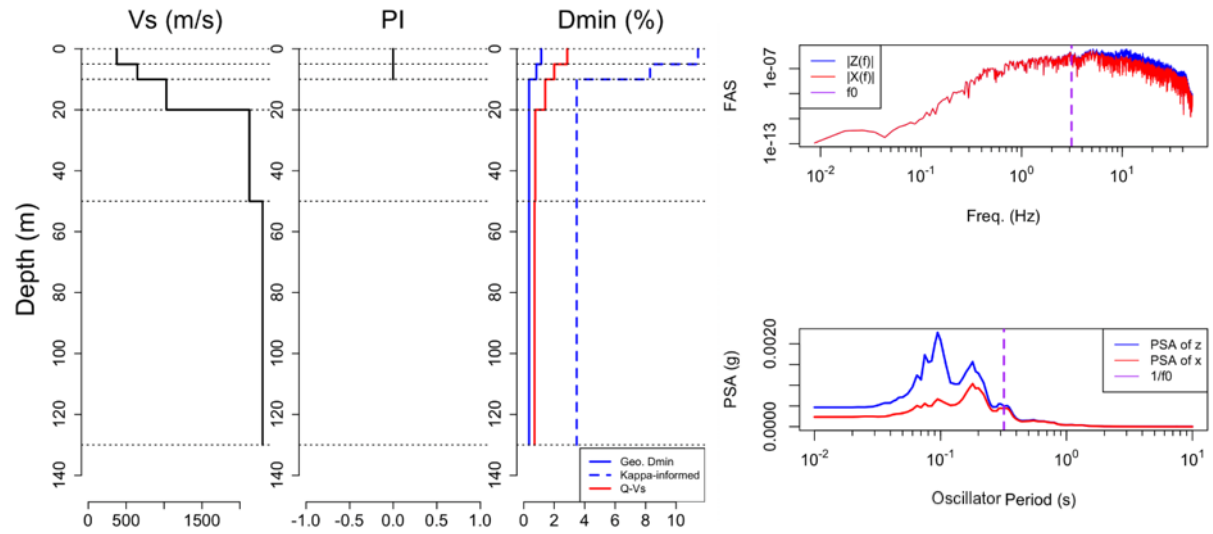

Figure 4.11: Site properties and modification of example surface recording for the site SSN = 100173

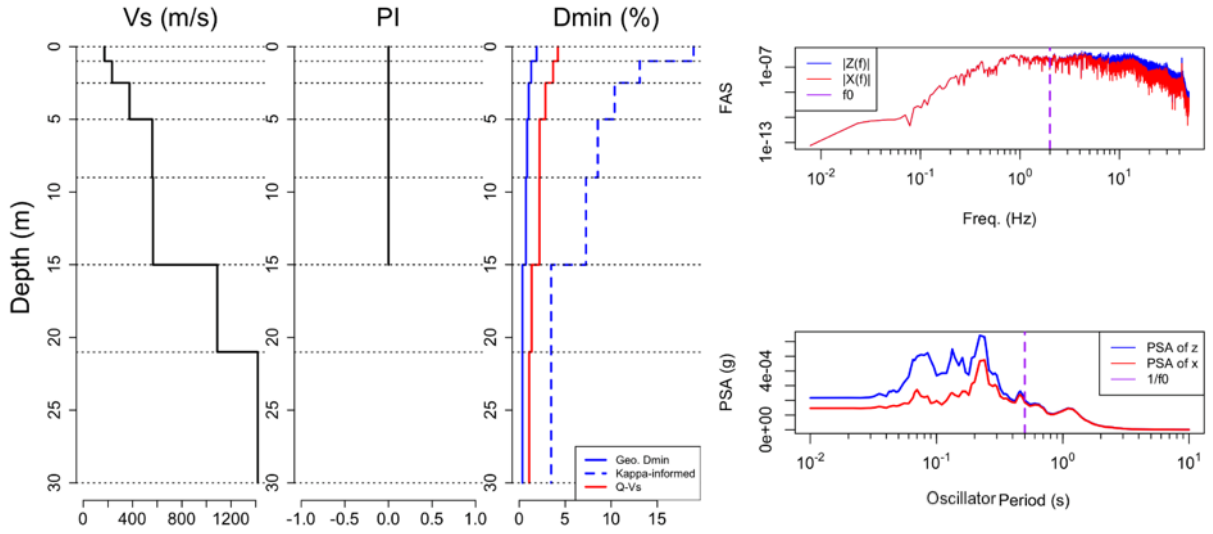

Figure 4.12: Site properties and modification of example surface recording for the site SSN = 3046

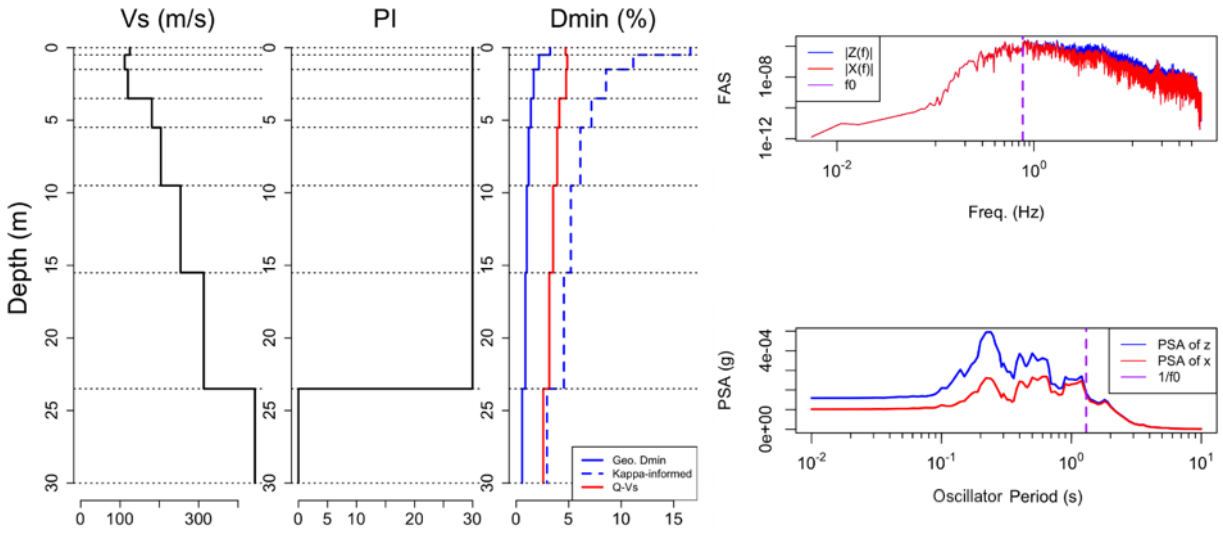

Figure 4.13: Site properties and modification of example surface recording for the site SSN = 100135

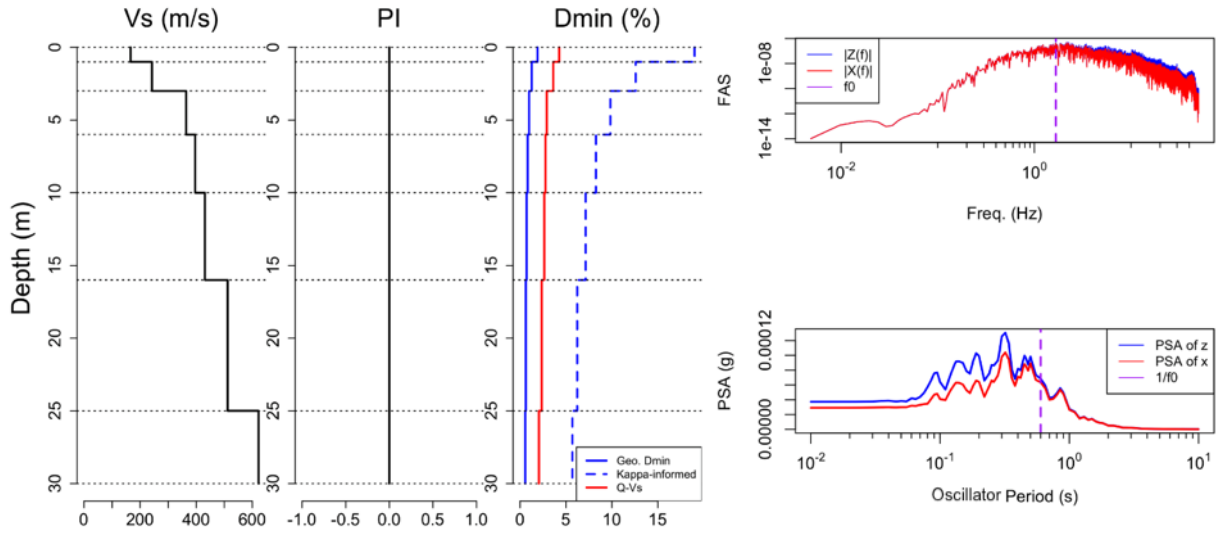

Figure 4.14: Site properties and modification of example surface recording for the site SSN = 3058

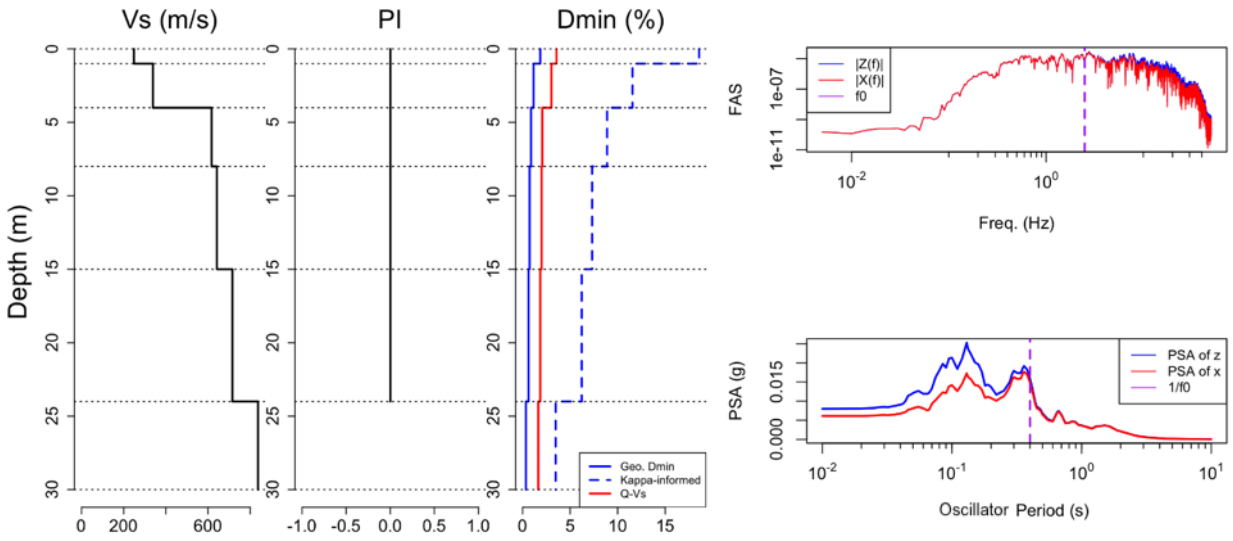

Figure 4.15: Site properties and modification of example surface recording for the site SSN = 100047

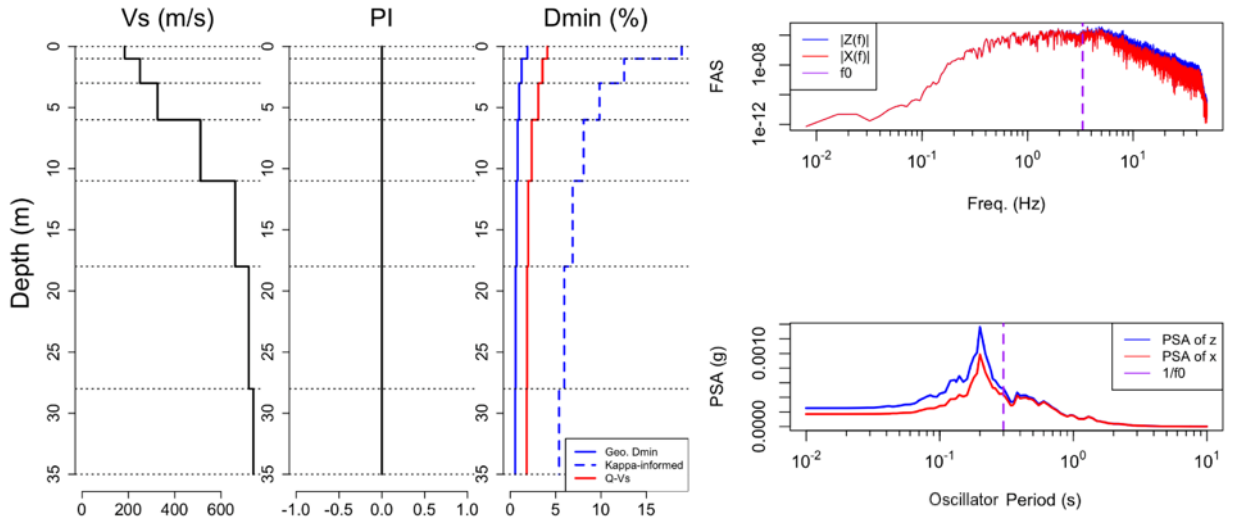

Figure 4.16: Site properties and modification of example surface recording for the site SSN = 3089

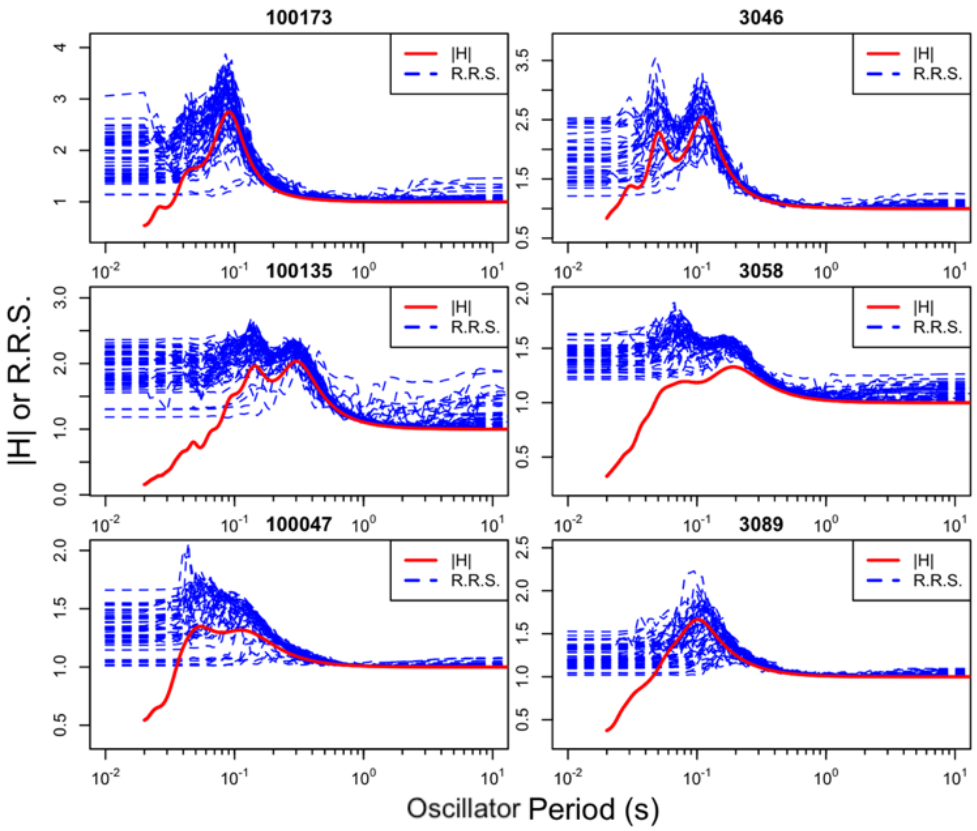

Figure 4.17: Comparison of surface/input transfer functions and response spectral ratios for sites SSN = 100173, SSN = 3046, SSN = 100135, SSN = 3058, SSN = 100047, SSN = 3089.

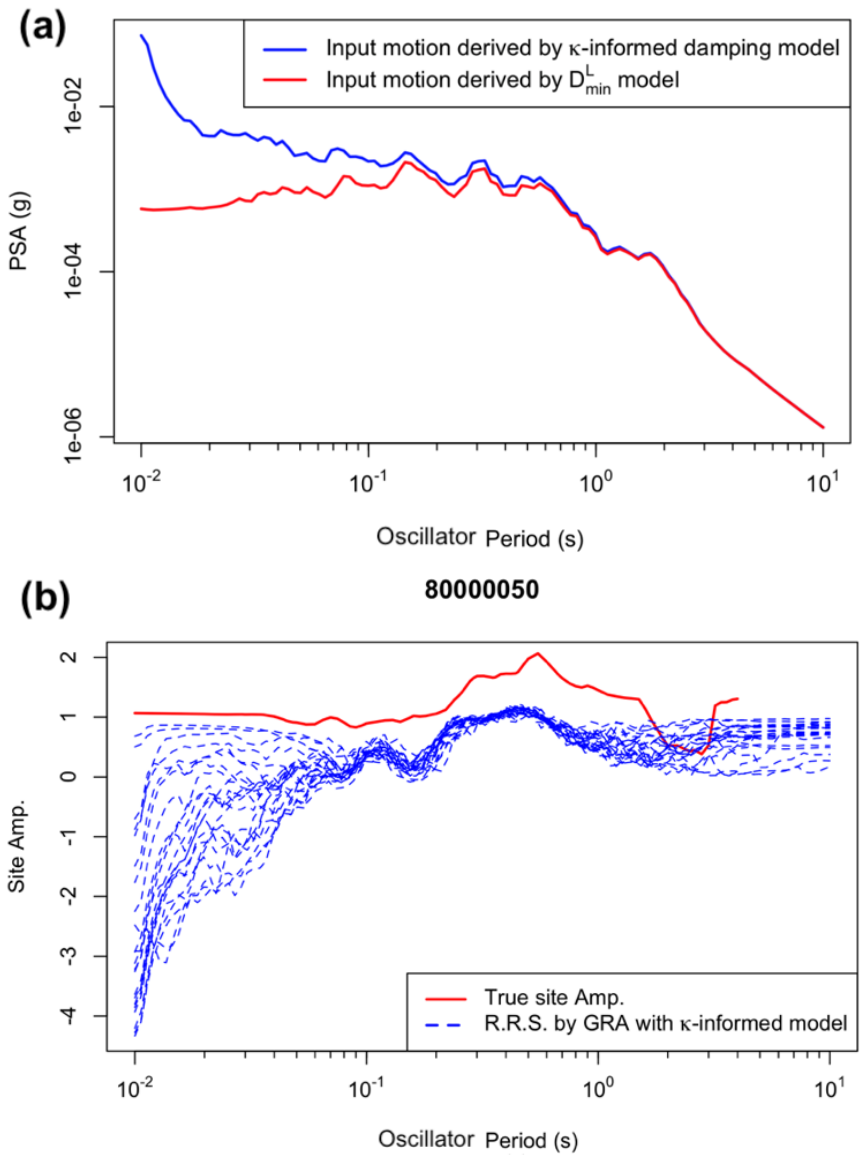

Figure 4.18: (a) Response spectra for input motions derived from deconvolution procedures; where large soil damping is used (κ-informed model), the spectra become unstable at short periods. (b) Site amplifications computed from ground response analysis using the input motions derived using κ-informed damping model; the rapid fall off at short periods is unrealistic and prompted the use of the D^{L}_{min} damping model for the deconvolution. The results in this figure apply for site SSN = 80000050.

Similar to the present work, the variation of surface/reference response spectral ratios was previously investigated by Stafford et al. ([91]). I describe that work here to place the

present results in context. [91] relate response spectra to the zeroth spectral moment, m_0 ([16] and [23]):

$$S_a \propto \sqrt{m_0} \tag{4.35}$$

where S_a is the response spectral ordinate. The zeroth spectral moment of surface motion can be expressed as (Parseval's formula),

$$m_{0,Z}(f_n, \xi_n) = 2 \int_0^\infty |X(f|\mathbf{M}, R)|^2 |H(f)|^2 |H_{osc}(f|f_n, \xi_n)|^2 \mathrm{d}f \tag{4.36}$$

where f_n and ξ_n are the oscillator natural frequency and damping, f is frequency in Hz, $\mathbf{M}$ is the earthquake moment magnitude, R is the source-site distance. The input motion Fourier amplitude is expressed as $|X(f|\mathbf{M}, R)|$. The conditioning on magnitude and distance is provided because [91] predict it using point source simulations. $|H(f)|$ is the soil column transfer function amplitude, as before. $|H_{osc}(f|f_n, \xi_n)|$ is the transfer function of the SDOF oscillator with natural frequency f_n and damping ratio ξ_n. Similarly, the zeroth spectral moment for the reference site condition can be expressed as,

$$m_{0,X}(f_n, \xi_n) = 2 \int_0^\infty |X(f|\mathbf{M}, R)|^2 |H_{osc}(f|f_n, \xi_n)|^2 \mathrm{d}f \tag{4.37}$$

Therefore, the site response expressed as ratio of response spectra is

$$\mathrm{Amp}(f_n, \xi_n) = \frac{S_{a,Z}(f_n, \xi_n)}{S_{a,X}(f_n, \xi_n)} = \sqrt{\frac{m_{0,Z}(f_n, \xi_n)}{m_{0,X}(f_n, \xi_n)}} \tag{4.38}$$

If the reference site input motions are converted surface motions as descried above, then the zeroth spectral moments for surface and at reference site would be

$$m_{0,Z,im}(f_n, \xi_n) = 2 \int_0^\infty \left| \frac{X(f|\mathbf{M}, R)}{H(f)} \right|^2 |H(f)|^2 |H_{osc}(f|f_n, \xi_n)|^2 \mathrm{d}f \tag{4.39}$$

$$m_{0,X,im}(f_n, \xi_n) = 2 \int_0^\infty \left| \frac{X(f|\mathbf{M}, R)}{H(f)} \right|^2 |H_{osc}(f|f_n, \xi_n)|^2 \mathrm{d}f \tag{4.40}$$

And Equation 4.39 can be simplified to

$$m_{0,Z,im}(f_n, \xi_n) = 2 \int_0^\infty |X(f|\mathbf{M}, R)|^2 |H_{osc}(f|f_n, \xi_n)|^2 \mathrm{d}f \tag{4.41}$$

since $|H(f)|$ terms are canceled out.

I compare the amplification computed from using surface motions directly applied as input motions ($\mathrm{Amp}_{sr}(f_n, \xi_n)$) with amplification computed using converted input motions ($\mathrm{Amp}_{im}(f_n, \xi_n)$) by take the ratio of the two,

$$\begin{aligned} Ratio(f|f_n, \xi_n) &= \frac{\mathrm{Amp}_{sr}(f_n, \xi_n)}{\mathrm{Amp}_{im}(f_n, \xi_n)} = \frac{m_{0,Z}(f_n, \xi_n)/m_{0,X}(f_n, \xi_n)}{m_{0,Z,im}(f_n, \xi_n)/m_{0,X,im}(f_n, \xi_n)} \\ &= \frac{(\int_0^\infty |X(f|\mathbf{M}, R)|^2 |H(f)|^2 |H_{osc}(f|f_n, \xi_n)|^2 \mathrm{d}f) * \left(\int_0^\infty \left| \frac{X(f|\mathbf{M},R)}{H(f)} \right|^2 |H_{osc}(f|f_n, \xi_n)|^2 \mathrm{d}f \right)}{(\int_0^\infty |X(f|\mathbf{M}, R)|^2 |H_{osc}(f|f_n, \xi_n)|^2 \mathrm{d}f)^2} \end{aligned} \tag{4.42}$$

Let $|Z_{osc}(f|f_n, \xi_n)|^2 = |X(f|\mathbf{M}, R) * H_{osc}(f|f_n, \xi_n)|^2$ then Equation 4.42 can be simplified as

$$Ratio(f|f_n, \xi_n) = \frac{(\int_0^\infty |H(f)|^2 |Z_{osc}(f|f_n, \xi_n)|^2 \mathrm{d}f) * \left(\int_0^\infty \left| \frac{|Z_{osc}(f|f_n,\xi_n)|}{H(f)} \right|^2 \mathrm{d}f \right)}{(\int_0^\infty |Z_{osc}(f|f_n, \xi_n)|^2 \mathrm{d}f)^2} \tag{4.43}$$

Approximating integration by summation, then Equation 4.43 becomes

$$Ratio(f|f_n, \xi_n) = \frac{(\sum_{i=0}^\infty |H(f_i)|^2 |Z_{osc}(f_i|f_n, \xi_n)|^2) * \left(\sum_{i=0}^\infty \left| \frac{Z_{osc}(f_i|f_n,\xi_n)}{H(f_i)} \right|^2 \right)}{(\sum_{i=0}^\infty |Z_{osc}(f_i|f_n, \xi_n)|^2)^2} \tag{4.44}$$

Per the Cauchy-Schwarz inequality[2], this ratio is greater than or equal to one. The ratio is unity for the case of $H(f) = 1$ for the full frequency range. The ratio increases if $H(f)$ departs from 1. Therefore, use of converted input motions will always decrease the site response computed from GRA relative to direct use of surface records as input motions. This conclusion holds as long as the transfer function $H(f)$ is non-unity for some frequencies within the considered range. As a result, GRAs would over-estimate site response if surface records were used as input motions.

[2] `https://en.wikipedia.org/wiki/Cauchy-Schwarz_inequality`

CHAPTER 5

Comparison of Observed-to-Predicted Site Response for California Sites

The objective of the ground motion analyses conducted in this research was to examine the effectiveness of alternate site response models at predicting observed site responses. This occurs by comparing observations-to-models for individual sites, and by assembling results across groups of sites (including the full inventory). This chapter provides the former examination by illustrating representative example results for individual sites.

Four site response analysis methods are considered. The first is the ergodic model (conditioned on V_{S30} and sediment depth) that comprises the reference model to which others are compared. The second is ground response analysis (GRA), which simulates vertical wave propagation through a damped, elastic medium. The third is the square-root impedance method (SRI), which approximates the impedance components of ground response with simple expressions based on the principle of wave energy conservation across layer interfaces. The fourth is the Horizontal-to-vertical spectral ratio (HVSR) model, which consists of a hybrid of the ergodic model and modifications to that model conditioned on site parameters derived from HVSR, which accounts for potential site-specific resonance effects.

In this chapter, I first describe how site response effects are evaluated from recordings. Then, I present representative results comparing model predictions to observed site responses. As part of these analyses, I describe several approach for quantifying the quality of model-to-data fit. Results for individual sites are provided on a Github site, accessible at `https://github.com/wltcwpf/CSMIP-Report-Supplements`.

5.1 Evaluation of observed site response

5.1.1 Residuals analysis and quantification of non-ergodic site response

Site amplification is represented by variable Y (in arithmetic units), which is the ratio of a ground motion intensity measure on the ground surface (Z) to the intensity measure on the reference condition (typically rock), X:

$$Y = Z/X \text{ or } \ln Y = \ln Z - \ln X \tag{5.1}$$

All three variables (X, Y, Z) are assumed to be log-normally distributed with standard deviations $\phi_{\ln X}$, $\phi_{\ln Y}$, and $\phi_{\ln Z}$, respectively. The use of variable ϕ for standard deviation indicates that it is associated with the within-event dispersion of earthquake ground motions. The total standard deviation (σ) also includes contributions from between-event variability τ.

Earthquake ground motions are affected by source, path, and site effects, each of which has corresponding terms in ground motion models (GMMs). Each of those terms may be systematically in error for a particular earthquake source, wave path, and site. Provided sufficient data exists, those systematic component errors can be estimated through mixed effects methods of residuals analysis (e.g., by `nlme` library in R [79]). A general expression to help visualize such effects is as follows (adapted from [7]):

$$\ln Z_{ij} = (\mu_{\ln X})_{ij} + (F_S)_{ij} + c_k + \eta_{E,i} + \eta_{P,ij} + \eta_{S,j} + \epsilon_{ij} \tag{5.2}$$

where Z_{ij} represents a recorded ground motion for event i and site j, $(\mu_{\ln X})_{ij}$ represents the mean from a GMM for a specified reference site condition, $(F_S)_{ij}$ represents the mean site amplification from an ergodic site term relative to the reference condition, c_k represents the mean model misfit relative to the data population (evaluated from mixed effects analyses), and $\eta_{E,i}$, $\eta_{P,ij}$, and $\eta_{S,j}$ represents event, path, and site terms, respectively. The term ϵ_{ij} represents the remaining residual when each of the above so-called random effects are removed. For the present work, I am not studying non-ergodic path effects; hence, I use a slightly simplified form of Equation 5.2:

$$\ln Z_{ij} = (\mu_{\ln X})_{ij} + (F_S)_{ij} + c_k + \eta_{E,i} + \eta_{S,j} + \epsilon_{ij} \tag{5.3}$$

Note that the sum $(\mu_{\ln X})_{ij} + (F_S)_{ij}$ is simply the GMM log mean $(\mu_{\ln Z})_{ij}$. The difference between the observation and the mean prediction comprises the total residual R_{ij}:

$$R_{ij} = \ln Z_{ij} - [(\mu_{\ln X})_{ij} + (F_S)_{ij}] \tag{5.4}$$

The Full Database (Section 2.1) is significantly expanded (in California) relative to that used to develop NGA-West2 models. Accordingly, I recomputed residuals for the full data set used in the derivation of the model by [22] supplemented with the additional California data. Event terms and site terms were evaluated by partitioning total residuals as

$$R_{ij} = c_k + \eta_{E,i} + \eta_{S,j} + \epsilon_{ij} \tag{5.5}$$

where c_k is the overall model bias for the model k. The partitioning in Equation 5.5 used mixed effects analysis procedures (`lmer` by [12] or `nlme` by [79]). With the residuals having been derived in this manner, the true (non-ergodic) site response relative to the reference condition used in the ergodic site response model (typically $V_{S30} = 760m/s$) is computed as:

$$\mu_{\ln Y,j} = (F_S)_j + \eta_{S,j} \tag{5.6}$$

As a first approximation, the mean site response $(\mu_{\ln Y})_{ij}$ is independent of event i if the magnitude is greater than four and the amplitude of shaking is sufficiently weak than the effects of nonlinearly are modest. As a result, mean site amplification is denoted $(\mu_{\ln Y})_j$.

Equations 5.2 - 5.6 strictly apply only for the case of an ergodic site amplification model. For the case of ground response methods in which the base condition may be different from the ergodic reference, Equation 5.3 and 5.4 can be re-written as

$$\ln Z_{ij} = (\mu^B_{\ln X})_{ij} + (F^k_S)_j + c_k + \eta_{E,i} + \eta^k_{S,j} + \epsilon_{ij} \tag{5.7}$$

$$R_{ij} = \ln Z_{ij} - [(\mu^B_{\ln X})_{ij} + (F^k_S)_j] \tag{5.8}$$

where F^k_S is the mean site response relative to the reference condition as computed using the GRA or SRI methods (index k would refer to one of these specific methods), $\mu^B_{\ln X}$ is the GMM mean ground motion for the base-of-profile reference condition, and η^k_S is the site term for ground response model. Equation 5.3 and 5.7 can be re-arranged as

$$\eta_{S,j} + \epsilon_{ij} = \ln Z_{ij} - [(\mu_{\ln X})_{ij} + (F_S)_j] - c_k - \eta_{E,i} \tag{5.9}$$

$$\eta_{S,j}^{k} + \epsilon_{ij} = \ln Z_{ij} - [(\mu_{\ln X}^{B})_{ij} + (F_S^{k})_j] - c_k - \eta_{E,i} \tag{5.10}$$

Consider the case of F_S taken from an ergodic model; for such models reference conditions can be relatively easily modified to different velocities. For this case, the terms in the brackets on the right side are different between Equation 5.9 and 5.10, but their sum is the same (i.e., a change in reference site condition maps into and equal and opposite changes to the GMM and site term). Accordingly, site terms (η_S) have the same meaning regardless of reference condition and therefore can be compared for different modeling approaches (which may have different reference conditions) in an "apples-to-apples" sense. Of course, when comparing two different site response modeling approaches, the two site terms would be expected to be different because of differences between the terms in brackets. The c_k and $\eta_{E,i}$ terms are assumed to be identical, because they are computed using the global data and the number of sites considered in this research (159) is much smaller than the number in the global dataset (1818). Equations 5.9 and 5.10 can be re-arranged to place site-related parts together on the left side of the equations,

$$\eta_{S,j} + (F_S)_j + \epsilon_{ij} = \ln Z_{ij} - (\mu_{\ln X})_{ij} - c_k - \eta_{E,i} \tag{5.11}$$

$$\eta_{S,j}^{k} + (F_S^{k})_j + \epsilon_{ij} = \ln Z_{ij} - (\mu_{\ln X}^{B})_{ij} - c_k - \eta_{E,i} \tag{5.12}$$

Based on Equation 5.6, the sum of the first two terms on the left side of Equation 5.11 can be recognized as being the non-ergodic mean site responses ($\mu_{\ln Y}$). Making this substitution, recognizing that the mean of the ϵ_{ij} terms is zero and the bias and event terms are identical, and taking the difference of the two equations (Equation 5.12 - Equation 5.11), provides:

$$\eta_{S,j}^{k} + (F_S^{k})_j - \mu_{\ln Y,j} = (\mu_{\ln X})_{ij} - (\mu_{\ln X}^{B})_{ij} \tag{5.13}$$

The means for the two reference conditions are related by

$$(\mu_{\ln X}^{B})_{ij} = (\mu_{\ln X})_{ij} + (F_S^{B})_j \tag{5.14}$$

where F_S^B is the site amplification from an ergodic model for the reference condition (relative to the reference condition in F_S, which is 760 m/s in this study). Making this substitution in

Equation 5.13 and moving the non-ergodic site response ($\mu_{\ln Y,j}$) and mean site amplification for model k to the right side,

$$\eta_{S,j}^{k} = \mu_{\ln Y,j} - (F_S^k)_j - (F_S^B)_j \tag{5.15}$$

Hence, the site term for model k is the non-ergodic site response (Equation 5.6) minus the model prediction, adjusted for differences in reference condition (as applicable). For the present study, $(F_S^B)_{ij}$ is zero for the HVSR model and is non-zero and site-dependent for the ground response models (GRA, SRI). Analogous to Equation 5.6, the non-ergodic site response relative to the ground response reference condition can be evaluated from Equation 5.15 as,

$$(\mu_{\ln Y}^B)_j = \eta_{S,j}^{k} + (F_S^k)_j = \mu_{\ln Y,j} - (F_S^B)_j \tag{5.16}$$

This version of site amplification is used in plots presented subsequently in Chapter 5 and 6.

Site terms in the Full Database are based on a wide range of available site recordings, including some with as few as one recording. In contrast, the Database Subset for Site Response Studies (Section 2.3) only considers sites with at least 10 recordings along with meeting other site characterization criteria. As a result, the uncertainty in site terms and mean site responses is much lower for the subset than for typical sites in the larger database. However, as period increases, some motions for individual sites within the subset are beyond their usable range (i.e., when period exceeds the inverse of the lowest usable frequency, as defined in Section 2.1). To illustrate this effect, Figure 5.1 shows the decay of the number of sites with usable site terms with period, where a site is no longer considered usable once the available number of recordings at that site is less than 5. Fall-off in the number of available sites occurs beyond a period of 2 sec, but the data loss is modest even out to 10 sec.

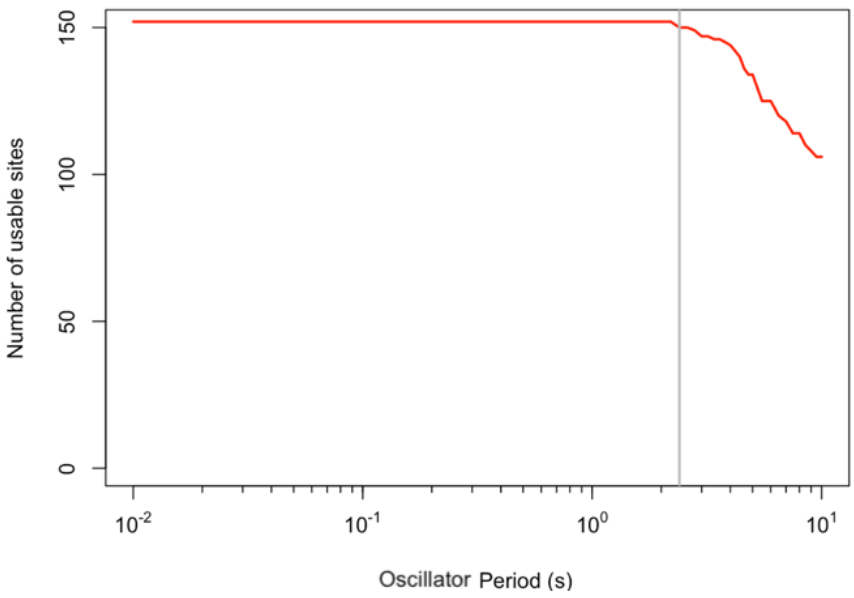

Figure 5.1: Decay of number of usable sites with oscillator period due to exceedance of usable period range. For this plot, the minimum number of records for a site to be considered usable is 5

Each of the residuals terms in Equation 5.3 and 5.5 has an accompanying standard deviation. The standard deviation of $\eta_{E,i}$ is denoted τ and represents the event-to-event variability. The standard deviation of $\eta_{S,j}$ is denoted ϕ_{S2S} and represents the site-to-site standard deviation. The standard deviation of ϵ_{ij} is denoted ϕ_{SS} and represents the "single station" within-event dispersion that combines effects of path-to-path variability and event-to-event variability in site response.

Figure 5.2 shows histograms of site terms for two intensity measures (peak acceleration and velocity) and their correlation. The degree of correlation is strong, as reflected by a correlation coefficient of 0.822. Figure 5.3 shows the dispersion terms evaluated from this process as a function of oscillator period.

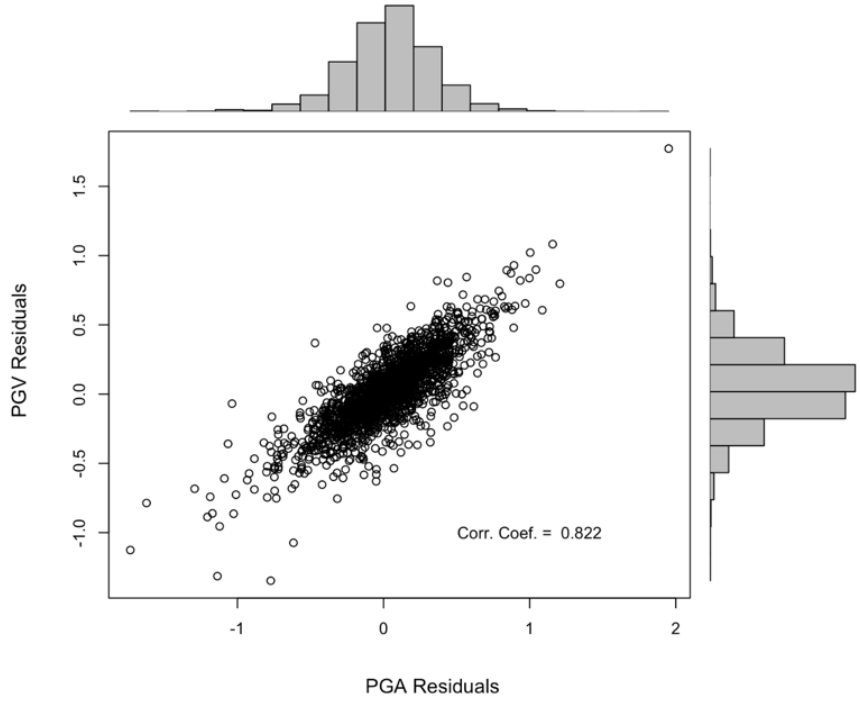

Figure 5.2: Histograms of PGV and PGA and their scatter plot

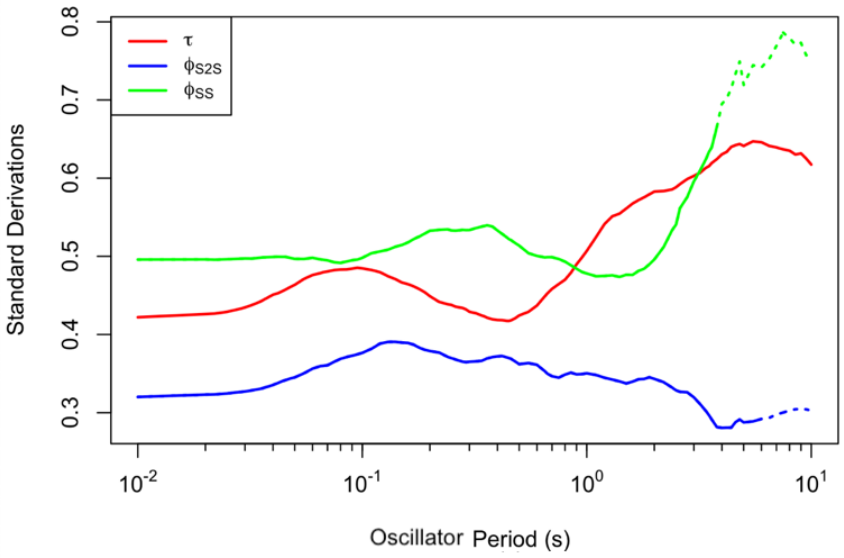

Figure 5.3: Standard derivations of partitioned residuals τ, ϕ_{S2S}, ϕ_{SS}. Shown as dotted when data population is reduced by 25% from the number for PGA.

By default, the above residuals analyses and dispersion terms apply to ground motion

predictions using the ergodic site amplification model. Chapter 6 describes how the residuals analyses are modified for cases where site-specific models are used in lieu of ergodic site amplification models, which produces different estimates of the site-to-site variability ϕ_{S2S}.

5.1.2 Identification of site response peaks

Observed site responses established from data using Equation 5.6 may, for some sites, exhibit peaks when site amplification is plotted with respect to oscillator period. For the assessment of site response prediction methods (particularly HVSR), it is useful to have an assessment of the presence of peaks in observed site responses. The procedures described in Chapter 3 for use with HVSR data are not directly applicable for this application, because the amplitudes of peaks are different (often lower). Instead, I adopt the Analyst II visual identification method described in Section 3.4 with modifications (e.g., the amplitude of peak could be small, and the peak amplitude is not necessarily 2 times larger than the ordinates at neighboring frequencies).

Figure 5.4 shows results for nine example sites, three of which unambiguously exhibit peaks (based on visual inspection), three of which have no peaks, and three intermediate cases. For sites with peaks, the new proposed function in Equation 3.9 is fit to the data (lowest frequency peak) and the fitted peak frequency $1/T_{osc}^{p}$ is identified. This frequency may be slightly different from the oscillator frequency having the largest site response (denoted as f_0; corresponding period is $T_0 = 1/f_0$).

Table 5.1: Breakdown of sites with peaks, no peaks, ambiguous cases as derived from site response

	Number	Percentage	Mean of V_{S30}	Mean of $1/T^p_{osc}$
Peaks	77	48%	493.8	3.7 Hz
No Peaks	32	20%	513.8	–
Intermediate	50	32%	454.0	–

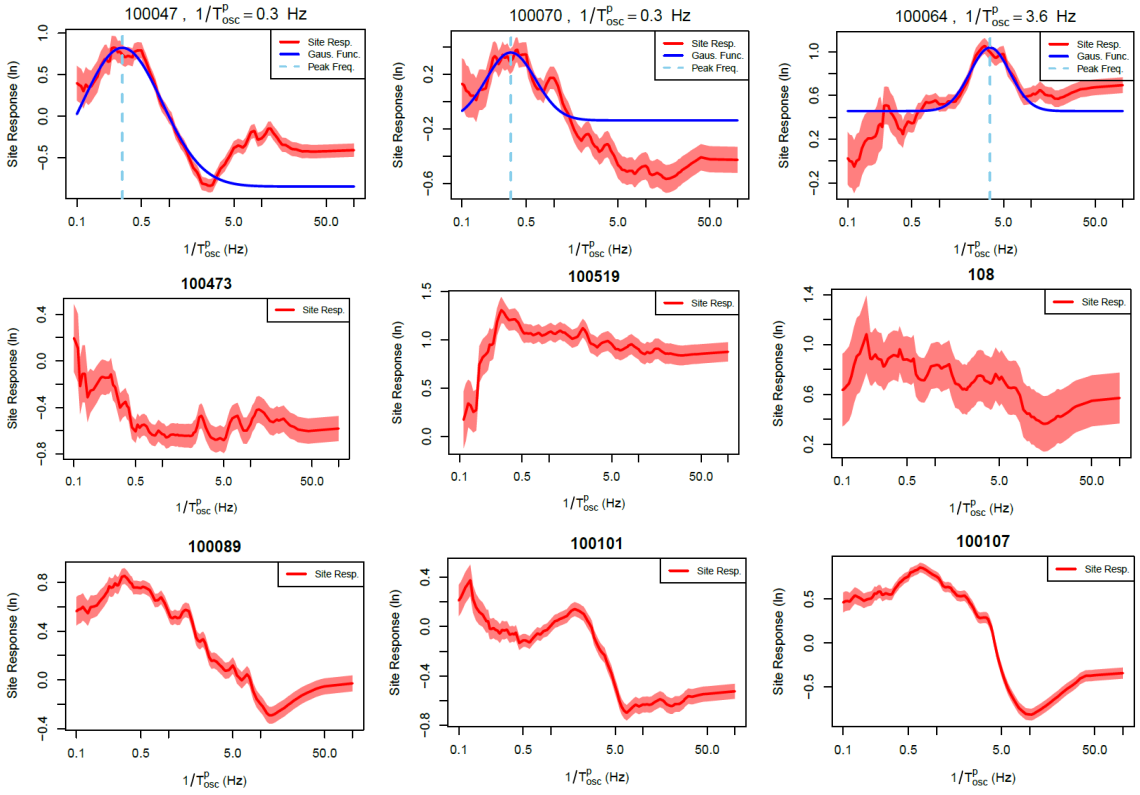

Figure 5.4: Nine example sites illustrating peaks (first row), no peaks (second row), and intermediate peaks (third row) for site response

In the Github site, I present observed site responses for all sites (159) considered in this research. For sites with peaks, fits as described above are shown and peak frequencies are identified. Table 5.1 summarizes the results.

5.2 GRA

5.2.1 Representative results

I provide here example results for the same set of six example sites introduced in Section 4.2.4 (Figure 5.5 - 5.7). The full set of analysis results for 159 sites are uploaded in my Github site. For each site, the observed site response (Equation 5.16) is compared to the site response predicted from an ergodic model ([88]) adjusted to be referenced to the base-of-profile condition ($F_S - F_S^B$) and site-specific GRA. The three damping models described in Sections 4.2 (geotechnical, κ-informed, $Q - V_S$) are applied in GRA, such that their relative levels of effectiveness can be assessed. Site fundamental periods are shown in the figures as estimated by the simplified Rayleigh method suggested by [104]. Maximum usable periods, beyond which the available numbers of recordings is ≤ 5, are also shown.

The results in Figure 5.5 - 5.7 show that the relatively smooth variations of site amplification with period that are predicted by the ergodic model seldom align with observed site responses, which often have local peaks and troughs. Figure 5.5 shows results for two sites (SSNs 100173 and 3046) that visually appear to exhibit good "fit" over a broad period range (i.e., the shapes of the site amplification vs period plots are similar, even if they are shifted relative to each other). Both are predominantly rock sites with shallow surficial layers of soil or weathered rock and large impedance contrasts (apparent from V_S profiles in Figure 4.11 - 4.12). These conditions give rise to large amplification near short fundamental periods ($\sim$0.1-0.2 s), and rapid fall-off of amplification for longer periods. This condition is well represented with the GRAs, with the κ-informed $D_{\min}$ and the $D_{\min}^L$ best representing short period amplifications for the two sites, respectively.

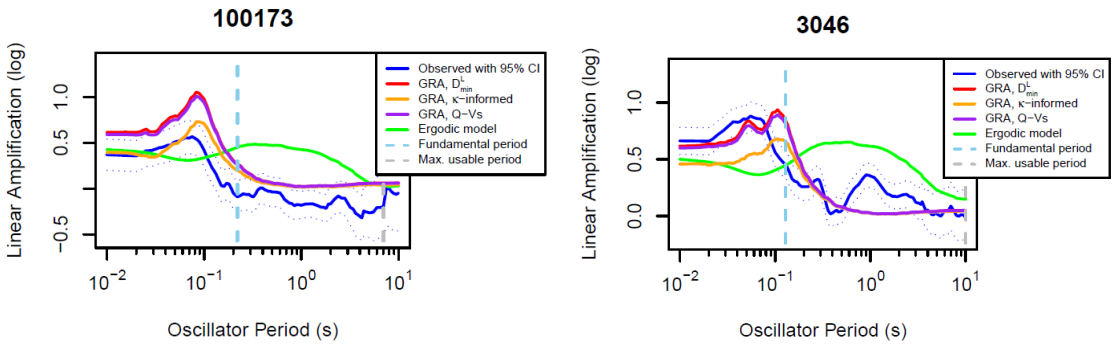

Figure 5.5: Non-ergodic site responses at the site SSN = 100173 and site SSN = 3046, compared with site response predictions obtained with use of ground response analysis and an ergodic model. The maximum period used in the plots is the median of the maximum usable periods from data processing. The ground response model provides a good estimate of the shape of the amplification function in these cases.

The favorable conditions for the two sites depicted in Figure 5.5 are not typical (similar findings of good fit over the full period range occur for around 14% of the 159 sites in the inventory). More commonly, comparisons indicate significant misfits over some or all of the period range. The sites in Figure 5.6 (SSNs 100135 and 3058) exhibit generally good fit of GRA to observation at short periods and poor fit at long periods. These sites have profiles of gradually increasing stiffness with depth to 25 m. A modest impedance contrast occurs for SSN 100135 (Figure 4.13), whereas 3058 has no interface with a large contrast (Figure 4.14). The modeled soil columns produce resonant periods near 0.35 s and 0.25 s, respectively, with amplification shapes up to resonance captured well by GRAs, although the amount of amplification is over-estimated. The misfits occur at longer periods, where the data indicate significant amplification continuing up to overall peaks near about 2.0 sec (100135) and 0.45 sec (3058), whereas the GRAs fall off to zero amplification beyond the modeled soil column periods of ∼0.25-0.35 sec. This indicates that the soil portions of these profiles may continue beyond the maximum depths of the site models (30 m). This highlights both a benefit and a limitation of GRA:

- Benefit: Despite the incompleteness of the profile, the use of GRA is nonetheless

beneficial within the period range of the soil column, relative to the ergodic model. There is about 28% of the 159 sites having good fit within the soil column period.

- Limitation: GRA cannot capture site response for periods beyond the soil column period, which instead is better represented by the ergodic model (especially for 100135). This conforms with recommendations of [93] to only consider results of GRA up to the soil column period, and to transition site amplification to ergodic prediction at longer periods.

Among the three $D_{\min}$ models, again κ-informed damping performs best at short periods.

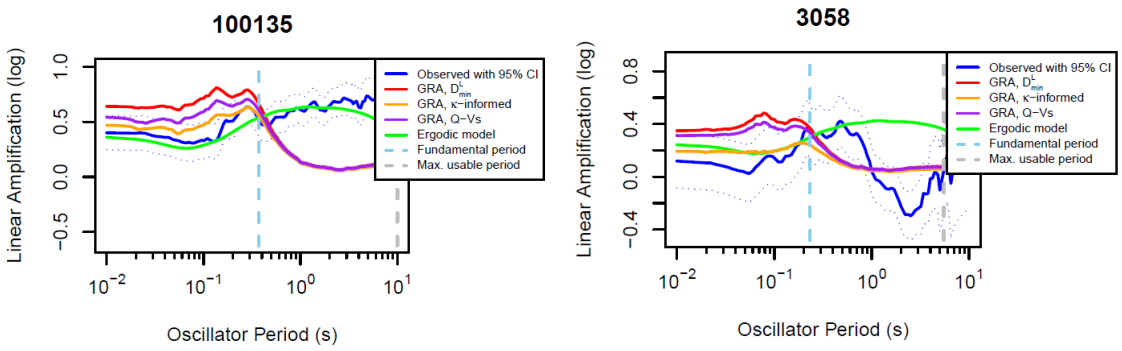

Figure 5.6: Non-ergodic site responses at the sites with SSN = 100135 and 3058, compared with site response predictions obtained with use of ground response analysis and an ergodic model.

The sites in Figure 5.7 (SSNs 100147 and 3089) exhibit poor fit of GRA to observation for all periods. Other than a large velocity step at 4 m for SSN 100147, these sites have profiles of gradually increasing stiffness with depth and no significant impedance contrasts. In both cases, the sites de-amplify ground motion (relative to the reference site condition of $V_{S30} = 760m/s$) at short periods (i.e., $T < 0.4 - 1.0$ sec), but amplify ground motions at long period with peaks near 2.0 sec. The inability of GRA to model long period site response is similar to that shown in Figure 5.6, and as before, the ergodic model provides improved performance. What distinguishes these sites is the poor GRA performance at short periods, which is caused the de-amplification. De-amplification over at least a log cycle of period

(as in Figure 5.7) occurs for around 25% of sites in the inventory, and thus is a relatively common condition. In the case of the sites in Figure 5.7, the reduction may be influenced by attenuation of high frequency motions from damping in deep sediments (e.g., SSN = 100047 site has $z_{1.0}$ = 567.5 m and $z_{2.5}$ = 840.2 m given in NGA-West2 flatfile).

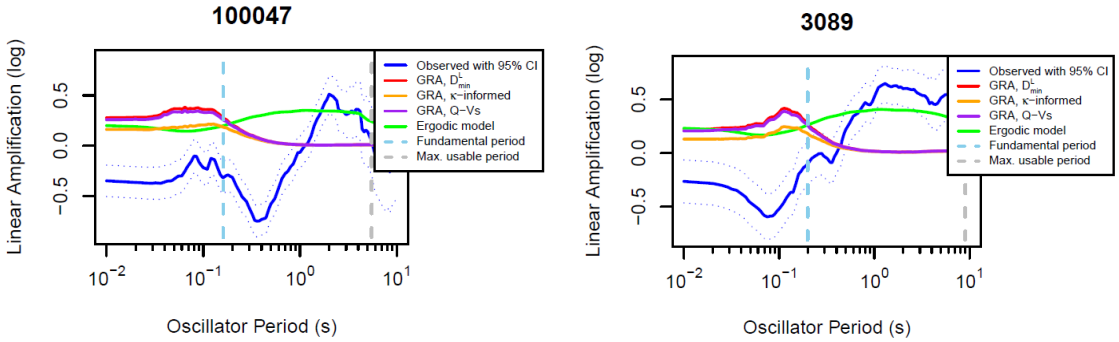

Figure 5.7: Non-ergodic site responses at sites with SSN = 100047 and 3089, compared with site response predictions obtained with use of ground response analysis and an ergodic model.

5.2.2 Goodness of fit

In the last section, I judged goodness-of-fit visually. In judging the quality of the fit, there are two considerations: (1) the general proximity of two site amplification vs period plots and (2) similarity of shapes of the plot. Visual judgements of goodness-of-fit have the drawbacks of being subjective and non-automated (time-intensive). Here I describe alternative quantitative metrics to measure the goodness-of-fit.

Residuals of site amplification defined similarly to Equation 5.4 (difference between observation and model prediction in natural log units) are useful for individual intensity measures, but not for judging the relative positions of period-dependent quantities. Pearson's sample correlation coefficient r has been used to quantify the overall goodness-of-fit of observed and simulated transfer functions from vertical arrays ([98] and [3]). Here I apply the same concept to compare oscillator period-dependent amplification functions. The correlation is

computed for a given site j and recording i as,

$$r_{ij} = \frac{\sum_{t\in T}\left((F_S^k)_i(t) - \overline{(F_S^k)_i}\right)(\mu_{\ln Y}(t) - \overline{\mu_{\ln Y}})}{\sqrt{\sum_{t\in T}\left((F_S^k)_i(t) - \overline{(F_S^k)_i}\right)^2}\sqrt{\sum_{t\in T}(\mu_{\ln Y}(t) - \overline{\mu_{\ln Y}})^2}} \tag{5.17}$$

Subscript j applies to all terms and is not shown. Subscript k is an index representing model type (ergodic, GRA with alternate damping models). T represents the period range, t represents a particular period, $t \in T$ (i.e., t can be any possible value in T). $(F_S^k)_i(t)$ is the site amplification for model k at period t, $\overline{(F_S^k)_i}$ is the average of $(F_S^k)_i(t)$ over T. $\mu_{\ln Y}(t)$ is the observed site amplification for site j (Equation 5.16) and $\overline{\mu_{\ln Y}}$ is the average of $\mu_{\ln Y}(t)$ over T. For a given site j, there is only one $\mu_{\ln Y}(t)$, while there are multiple $(F_S^k)_i(t)$ (one for each recorded earthquake.

The mean value of r across all events, denoted as $\bar{r}$, is used to measure goodness-of-fit. Large positive values indicate good fit. Table 5.2 shows $\bar{r}$ values for the six example sites over the full period range and for periods up to the fundamental soil column period in both cases of ergodic and GRA-based predictions using the κ-informed $D_{\min}$ damping model. In the case of GRA, for the sites visually identified as "good fit" (Figure 5.5), the correlation coefficients for full range of periods (scenario one) range from 0.72 to 0.89 and for the periods up to fundamental periods (scenario two) range from 0.48 to 0.89, whereas "poor fit" sites (Figure 5.6 and full period range for Figure 5.7) have low or negative correlation over the full period range and correlations less than 0.25 over the more restrictive (short period) range. In the case of the ergodic model, correlation coefficients are low for four of the six sites, including the first two "good fit" sites, indicating less favorable fit. In summary, the mean correlation coefficients reflect good performance of GRA for good fit sites and the poor performance of poor fit sites. Correlation coefficient does not reflect what was visually judged as good fit at short periods for the intermediate sites.

Table 5.2: The summary of correlation coefficients for six example sites for both ergodic and GRA-based site response estimates

Site	$\bar{r}$ for ergodic over the full period range	$\bar{r}$ for ergodic for the periods up to fundamental periods	$\bar{r}$ for GRA over the full period range	$\bar{r}$ for GRA for the periods up to fundamental periods
SSN = 100173	0.587	-0.939	0.891	0.891
SSN = 3046	-0.670	-0.863	0.724	0.475
SSN = 100135	0.852	0.781	-0.785	0.145
SSN = 3058	-0.170	0.784	0.317	-0.039
SSN = 100047	0.315	0.006	-0.118	0.251
SSN = 3089	0.883	0.953	-0.852	-0.206

A limitation of mean correlation coefficient is that it does not capture misfit related to vertical offsets between amplification functions. For example, the short-period, GRA mean correlation coefficient for site SSN = 100047 are relatively high, whereas vertical offsets are large (about one in ln units). An alternative metric used to quantify the similarity of two curves is Fréchet distance . As illustrated in Figure 5.8, if a person and a leashed dog walk along separate curved paths, each can change velocity to maintain slack in the leash. The Fréchet distance between the two curves is the length of the shortest leash sufficient for both to traverse their separate paths, under the condition that neither is allowed to move backwards. If the velocities of the person and dog were the same, Fréchet distance would be the longest distance between their position over the duration of the walk. Fréchet distance is reduced by allowing velocities to change.

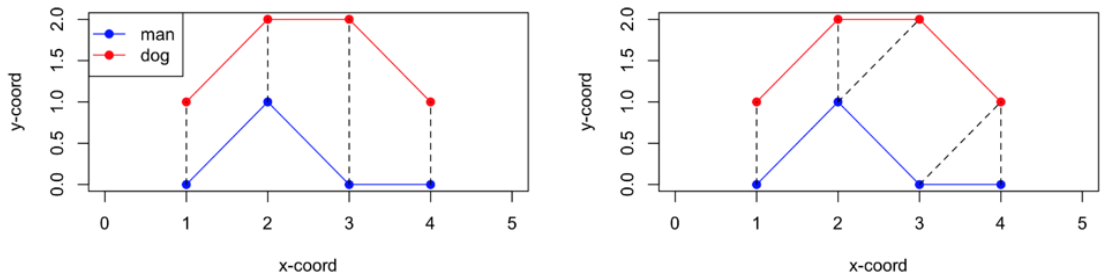

Figure 5.8: Schematic comparison of vertical distance between paths (left, max of 2) and Fréchet distance (right, max of $\sqrt{2}$)

The application of Fréchet distance as a means by which to compare alternate site amplifications can be expressed as,

$$\Psi(\bar{F}_S^k, \mu_{\ln Y}) = \min_{t_1,t_2 \in T} \max\{|\bar{F}_S^k(t_1) - \mu_{\ln Y}(t_2)|\} \tag{5.18}$$

where $\bar{F}_S^k$ is the mean linear site amplification from model k across all events, and t_1 and t_2 are the periods of $\bar{F}_S^k$ and $\mu_{\ln Y}$. As before, all of the arguments in Equation 5.18 apply for a given site (i.e., site j). I allow t_1 and t_2 to not match, but the calculation starts from short period and progresses to long periods without moving backwards. The calculation is made using function `Frechet` as provided in library `SimilarityMeasures` (Toohey, 2015) in R. In addition, I also compute Fréchet distance normalized by the range of $\mu_{\ln Y}(\max(\mu_{\ln Y}) - \min(\mu_{\ln Y}))$.

Table 5.3 - 5.4 show Fréchet distances and normalized Fréchet distances for the six example sites for the same model-to-observation combinations considered in Table 5.2. Low Fréchet distances, or normalized Fréchet distances, indicate better fit than large values. Site 100173 has large Fréchet distances, despite the similarity of shapes, due to the vertical shift. For the other sites, Fréchet distances, especially over the period range below the site period, are lower for good fit sites than for poor fit sites (Table 4.3). This trend also holds for normalized Fréchet distances (Table 5.4), except that even 100173 has relatively small values due to its large range. The range of normalized Fréchet distances for "good fit" sites is less than 0.9, whereas the normalized Fréchet distances for "intermediate fit" is around 1, and "poor fit" is greater than 1.5.

Table 5.3: Summary of Ψ for six example sites for both ergodic and GRA

Site	Ψ for ergodic over the full period range	Ψ for ergodic for the periods up to fundamental periods	Ψ for GRA over the full period range	Ψ for GRA for the periods up to fundamental periods
SSN = 100173	0.624	0.542	0.677	0.566
SSN = 3046	0.724	0.355	0.352	0.326
SSN = 100135	0.269	0.140	0.814	0.446
SSN = 3058	0.765	0.187	0.404	0.397
SSN = 100047	1.004	0.555	0.767	0.687
SSN = 3089	0.734	0.734	0.839	0.839

Table 5.4: Summary of normalized Ψ for six example sites for both ergodic and GRA

Site	Normalized Ψ for ergodic over the full period range	Normalized Ψ for ergodic for the periods up to fundamental periods	Normalized Ψ for GRA over the full period range	Normalized Ψ for GRA for the periods up to fundamental periods
SSN = 100173	0.568	0.871	0.616	0.910
SSN = 3046	0.900	0.669	0.438	0.615
SSN = 100135	0.406	0.339	1.228	1.078
SSN = 3058	1.079	0.543	0.569	1.155
SSN = 100047	0.987	1.746	0.753	2.161
SSN = 3089	0.580	1.297	0.664	1.483

5.3 SRI

The square-root-impedance (SRI) method, introduced by [61] and subsequently revised and further described by [19], applies principles of wave energy conservation to estimate changes in wave amplitude across layer boundaries. It is widely used in engineering seismology, particularly in combination with semi-stochastic ground motion simulation routines (e.g., [16]). Prior validation studies have considered the SRI method in combination with simulations, but seldom has the method been validated as a stand-alone model. Such validation is undertaken here; I present example results for the same set of 6 sites considered from Section 5.2.

Example results from SRI calculations are presented here for the same six example sites considered in Section 5.2.1. Results are presented in Figure 5.9 - 5.11 following the same format used for GRA comparisons – observed site response (Equation 5.16) is compared to an adjusted ergodic model prediction and site-specific SRI. The three damping models described in Section 4.2 (geotechnical, κ-informed, $Q - V_S$) are applied in GRA, such that their relative levels of effectiveness can be assessed.

Figure 5.9 shows results for the "good fit" sites (SSNs 100173 and 3046). The fit of the SRI results over the full period range appears to be quite good, similar to the findings from GRA. Figure 5.10 - 5.11 show results for the second and third groups of sites. As before, the fits of SRI results to observation generally mirror the trends encountered for GRA. In particular, the fits are uniformly poor for these sites at long periods where SRI (and GRA) does not provide information on site amplification. However, a distinction from GRA is that the κ-informed damping model overestimates short period attenuation relative to alternative damping models, whereas that damping model provided the best outcomes with GRA.

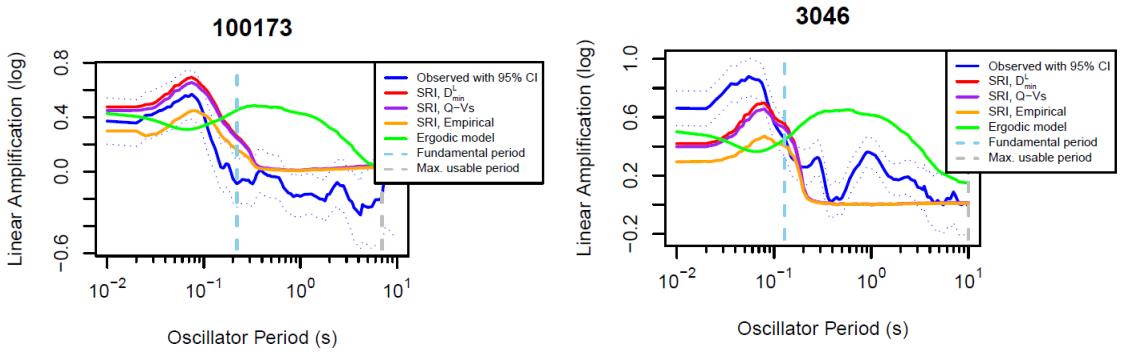

Figure 5.9: Non-ergodic site responses for sites with SSN = 100173 and 3046, compared with site response predictions from ergodic model and from site-specific SRI.

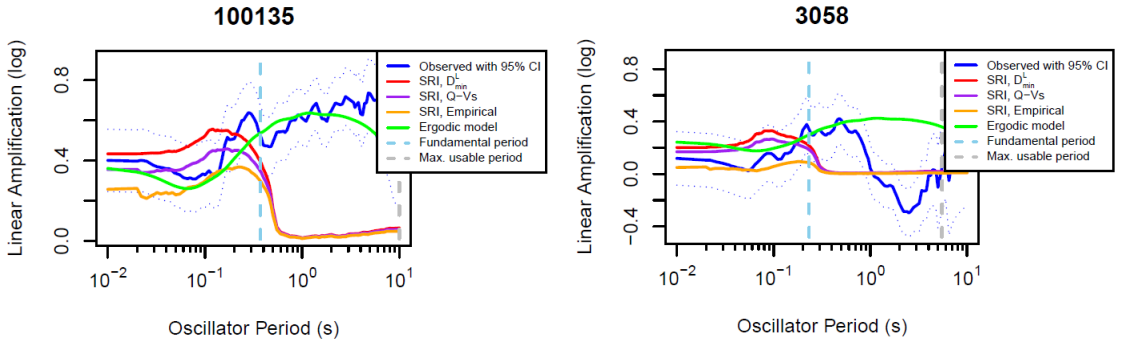

Figure 5.10: Non-ergodic site responses for sites with SSN = 100135 and 3058, compared with site response predictions from ergodic model and from site-specific SRI.

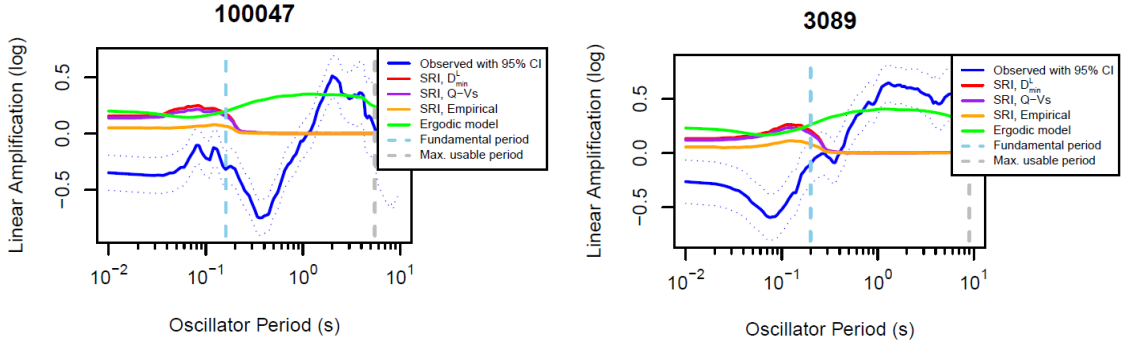

Figure 5.11: Non-ergodic site responses for sites with SSN = 100047 and 3089, compared with site response predictions from ergodic model and from site-specific SRI.

Table 5.5 lists goodness-of-fit metrics of SRI-based predictions using the D^L_{min} damping

model for the six example sites for the same observation-to-model combinations considered previously for GRA. Interestingly, shape-based metrics for the good-fit sites for the period range up to fundamental periods are improved for SRI relative to GRA, and (Normalized) Fréchet distances are reduced. The trends of comparisons across sites and for different period ranges are as discussed in Section 5.2.2.

Table 5.5: The summary of Fréchet distance, normalized Fréchet distance, and correlation coefficients for SRI

Site	$\bar{r}$ for SRI over the full period range	$\bar{r}$ for SRI for periods up to fundamental period	Ψ for SRI over the full period range	Ψ for SRI for the periods up to fundamental period	Normalized Ψ for SRI over the full period range	Normalized Ψ for SRI for periods up to fundamental period
SSN = 100173	0.907	0.980	0.658	0.290	0.599	0.466
SSN = 3046	0.821	0.909	0.374	0.145	0.464	0.274
SSN = 100135	-0.820	-0.120	0.866	0.270	1.306	0.653
SSN = 3058	0.179	-0.019	0.359	0.244	0.507	0.711
SSN = 100047	0.007	0.482	0.729	0.560	0.716	1.761
SSN = 3089	-0.866	-0.311	0.748	0.748	0.591	1.322

5.4 HVSR model

The Horizontal-to-vertical spectral ratio (HVSR) model consists of a hybrid of the ergodic model and modifications to that model conditioned on site parameters derived from HVSR, which accounts for potential site-specific resonance effects. In this section, I will use the model described in Section 4.1.4 to predict site response using HVSR parameters derived from strong motions and noise data. The first sub-section below focuses on the compatibility of peaks in model predictions and observed site responses. The second sub-section compares observed and predicted amplification function shapes in the same manner as undertaken previously for GRA and SRI. All site responses presented in this section are relative to the

GMM reference condition (760 m/s); non-ergodic site responses are taken from Equation 5.6.

5.4.1 Observed and predicted site response peaks

As discussed in Chapter 3, sites can be classified based on their HVSR shape into three categories: clear peak sites, no peak sites, and ambiguous sites. This section provides for each category representative example results for model-to-data comparisons and a synthesis of findings.

Clear peak sites

Here I consider two sites identified as having peaks by both analysts. Figure 5.12 shows for each site the HVSR plot but with the frequency axis transformed to period (not an oscillator period) and the empirical site response (and the model predictions) also plotted against oscillator period. The site with station sequence number SSN = 100296 (V_{S30}=442.27 m/s) has a peak at $1/f_{p1}$ = 1.5 sec from HVSR, which is also in the observed site response. The fundamental period of the soil column over which V_S is measured, also marked in the figure, is much smaller (0.2 sec) due to the limited depth range of the measured profile. The site with SSN = 3061 (V_{S30} = 743.19 m/s) has a clear HVSR peak at 1.0 sec, which again is apparent in the site response.

For both of these sites, the ergodic model does not predict the specific features of the peaks. The models shown in Figure 5.12 are ergodic and HVSR models. The HVSR model captures the peaks in the site response; this occurs because the HVSR peak coincides with that of the site response.

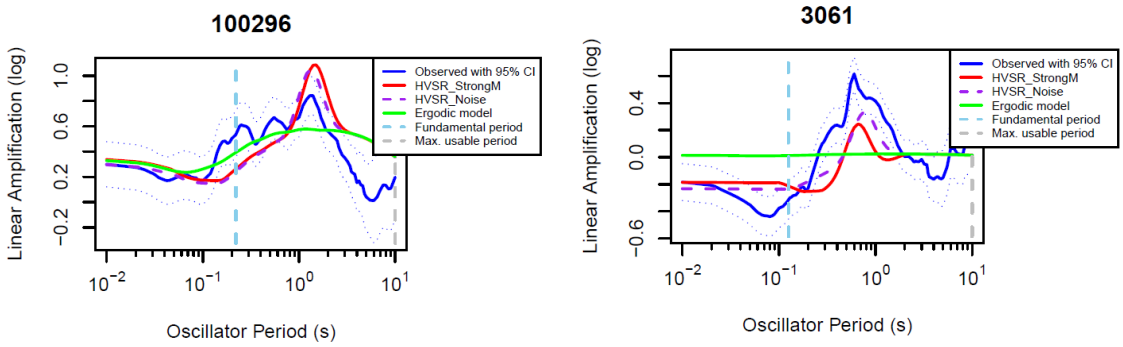

Figure 5.12: Non-ergodic site responses for clear peak sites with SSN = 100296 and 3061, compared with site response predictions from ergodic model and from HVSR model.

The alignment of the peaks that is seen in Figure 5.12 does not happen for all clear peak sites. From Section 3.5.2, based on analysts visual interpretation, the database contains 34 and 54 clear peak sites for strong motion and noise data sources, respectively. The alignment of the peaks from these clear peak sites with site response peaks can be summarized as follows:

- For strong motion: Of the 34 clear peak sites, 19 (56%) also have site response peaks. Of those 19 sites, the peaks from HVSR and site response reasonably align for 18 (95%) and for 12 of the aligned sites (63%), their peak amplitudes are also similar.

- For noise: Of the 54 clear peak sites, 28 (52%) also have site response peaks. Of those 28 sites, the peaks from HVSR and site response reasonably align for 20 sites (71%) and for 15 of the aligned sites (54%), their peak amplitudes are similar.

These results show that strong motion-based HVSRs better align with observed site response than do HVSRs derived from ambient noise. This might be anticipated because there is a certain degree of circularity in using the same data source (earthquake strong motions) to derive HVSR and site response. On the other hand, the effectiveness of noise-based HVSR at identifying the presence of peaks and predicting the locations of the peaks is quite good for these sites. This is encouraging regarding the potential effectiveness of noise HVSR-based models to assist in ground motion prediction (which is the case for the sites in Figure 5.12). One way of quantifying this effectiveness is the false positive rate, which is

defined as the percentage of sites that lack a peak despite HVSR suggesting the presence of a peak. The false positive rate is 48% for the noise-based HVSR (slightly higher if judged on the basis of peak alignment).

No peak sites

Here I consider two sites identified as not having peaks by both analysts. Figure 5.13 shows for each site HVSR and site response plots in the same format as Figure 5.12. The site with SSN = 100609 (V_{S30}=514.40 m/s) has some fluctuations in site response that could be interpreted as peaks at 0.1 and 0.8 sec, whereas the site with SSN 3070 (V_{S30}=244.42 m/s) has broad and smooth variations of site amplification with period similar to those of the ergodic model, and no peaks. For both of these sites, the HVSR model shifts vertically the predictions of the ergodic model due to the lack of identified HVSR peaks (the shift is by an amount $\bar{c} = 0.0625$ based on the data, per Equation 4.12), which modestly reduces bias in both cases.

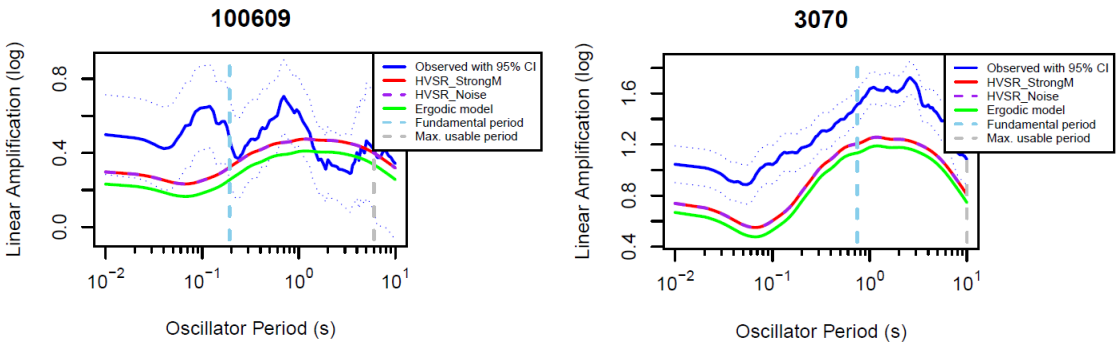

Figure 5.13: Non-ergodic site responses for clear peak sites with SSN = 100609 and 3070, compared with site response predictions from ergodic model and from HVSR model.

As shown in Table 3.6, the numbers of no-peak sites based on HVSR are 83 and 54 for strong motion and noise sources, respectively. For these no-peak sites, the alignment with features of observed site responses can be summarized as follows:

- For strong motion: Of the 83 no peak sites, 44 (53%) lack site response peaks. Hence the rate of false negatives is 47%.

- For noise: Of the 54 sites, 28 (52%) lack site response peaks (false negative rate of 48%).

These results show that the strong motion- and noise-based HVSR are similar in their effectiveness at identifying sites without site response peaks. The false negative rate (about 47-48%) is similar to the false positive rate for clear peak sites.

Sites with ambigous peak assignments

Here I consider two sites with mixed peak identifications (peak identified by Analyst I but not Analyst II). Figure 5.14 shows for each site HVSR and site response plots in the same format as Figures 5.12 - 5.13. The site with SSN = 100096 (V_{S30}=1015.75 m/s) has a site response peak at 0.12 sec that is a little lower than that predicted by the HVSR model with a peak at $1/f_{p1} = 0.15$ sec. The site with SSN 100177 ($V_{S30} = 452.47$ m/s) generally has broad and smooth variations of site amplification with period, although a relatively local peak may be present at 1.5 sec that is not well predicted by Analyst I HVSR peaks at 0.6 sec (strong motion) and 2.5 sec (noise). Other than the aforementioned peaks, the ergodic model provides a reasonable first-order representation of the site response for these sites.

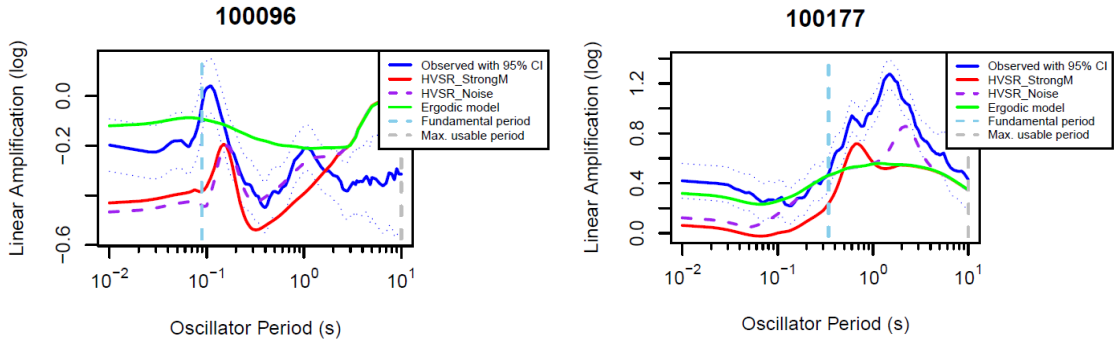

Figure 5.14: Non-ergodic site responses for clear peak sites with SSN = 100609 and 100177, compared with site response predictions from ergodic model and from HVSR model.

Analyst interpretation of HVSR derived from strong motion and noise data sources led to 32 ambiguous peak sites. For these sites, I evaluate the occurrence of peaks in observed site responses, with results summarized as follows:

- For strong motion: Of the 32 sites, 16 (50%) have site response peaks. Of that group of 16 sites, 8 sites have peak frequencies aligned with those from HVSR and 4 sites have comparable amplitudes.

- For noise: Of the 32 sites, 17 (53%) have site response peaks. Among those 17 sites, 10 sites have peak frequencies alighted with those from HVSR and 5 sites also have comparable amplitudes.

In summary, slightly more than 50% of ambiguous sites have peaks in site response, and many of those sites have their peaks successfully predicted by HVSR.

5.4.2 Representative results and goodness-of-fit

Table 5.6 lists goodness-of-fit metrics for HVSR model predictions using the parameters fitted from strong motion and noise HVSR. Unlike the GRA and SRI models, the HVSR model does not have a restricted period range based on the depth of V_S profiles. Accordingly, the goodness-of-fit metrics were evaluated over the full period range.

The most favorable goodness-of-fit metrics are obtained for the two clear-peak sites, with relatively mixed results for the other pairs of sites. A compilation of goodness-of-fit statistics across all of the sites in the clear-peak, no peak, and ambiguous peak groups is provided in Chapter 6.

Table 5.6: The summary of Fréchet distance, normalized Fréchet distance, and correlation coefficients for HVSR models

Sources	**Site**	$\bar{r}$ for HVSR model over the full period range	Ψ for HVSR model over the full period range	Normalized Ψ for HVSR model over the full period range
Strong Motion	SSN = 100296	0.700	0.382	0.611
	SSN = 3061	0.761	0.549	0.396
	SSN = 100609	-0.512	0.370	0.628
	SSN = 3070	0.817	0.947	0.479
	SSN = 100096	-0.403	0.414	0.591
	SSN = 100177	0.910	0.875	0.695
Noise	SSN = 100296	0.728	0.397	0.635
	SSN = 3061	0.864	0.468	0.338
	SSN = 100609	-0.512	0.370	0.628
	SSN = 3070	0.817	0.947	0.480
	SSN = 100096	-0.393	0.414	0.591
	SSN = 100177	0.845	0.709	0.563

CHAPTER 6

Synthesis of Site Response Model Performance Results for California Sites

6.1 Approach

The results for the 12 sites (six for GRA and SRI, and another six for HVSR model) presented and discussed in Chapter 5 are useful to illustrate the proposed approach of using non-ergodic site response as a means to validate site response models, and to show examples of "good" and "poor" predictions. To fully realize the benefits of this approach for site response model validation, it is necessary to assimilate results over many sites, since many more sites can be used than with validation using vertical arrays.

The assimilation of results across multiple sites is undertaken with residuals analyses, using procedures described in Section 5.1 and elaborated upon here. Term c_k represents overall model bias, which is computed across the full global data set and not just the subset of 159 sites considered in this work. Hence c_k is not useful for site response validation. Term $\eta_{S,j}$ on the right side of Equation 5.5 is a random effect indicating how well ground response analyses predict site response for site j relative to the overall model bias (in this chapter, η_S is written without subscript k, and is understood to be different between site response analysis methods). If ground response analyses were unbiased for all sites, site-specific random effects $\eta_{S,j}$ for site j and its average over all sites for which ground response analyses are performed ($\bar{\eta}_{Sj}$) would both be zero. Conversely, statistically significant absolute values of $\eta_{S,j}$ indicate biased predictions of site response.

An important role of site-specific analysis is to predict differences in site response between

sites with different properties; this is quantified using the standard deviation of $\eta_{S,j}$. As discussed further below, this dispersion includes effects from modeling uncertainty and soil property uncertainty, and its evaluation is an important objective of this research. Term ϵ_{ij} represents the remaining variability after fixed event and site effects are subtracted. The standard deviation of ϵ_{ij} reflects the effects of path-to-path variability and event-to-event variability in site response for a given site. This variability is commonly referred to as single-station within-event variability, ϕ_{SS} (given by [7]).

6.2 Overall and model bias

Overall bias c_k is plotted in Figure 6.1. This bias is computed using the Full Database described in Section 2.1. The bias is relatively small but non-zero, which occurs because the data used in the present study has been expanded by 30% relative to that used in the development of the GMM. Figure 6.1 also shows $\bar{\eta}_S$ for the four site response models (ergodic, GRA, SRI, HVSR), which were computed using the subset of 159 sites considered in the present work. The GRA and SRI results are shown with the three considered damping models (geotechnical, κ-informed, $Q - V_S$). The HVSR model is shown with peaks fitted from strong motions and noise data sources. If the subset of sites considered in this research were to have a similar average site response as the global average, the $\bar{\eta}_S$ for the ergodic model would match c_k. As shown in Figure 6.1, $\bar{\eta}_S$ is actually smaller than c_k, suggesting a lack of bias in the database subset relative to the larger global database.

The performance of each site response prediction method in an average sense can be evaluated from the individual $\bar{\eta}_S$ results. In particular, their performance relative to the $\bar{\eta}_S$ for the ergodic model is of interest. To help guide such interpretations for the cases of GRA and SRI, Figure 6.1 shows median site profile periods and the 5-95% confidence intervals; these represent maximum usable periods for such analyses. The results in Figure 6.1(a) indicate that the site-specific methods exhibit small biases over their usable period range ($<\sim$ 0.2 sec). Biases for the ergodic model are also small, generally being closer to zero than the site-specific methods. Among the ground response (GRA and SRI) results in Figure 6.1(a),

the κ-informed damping model produces the smallest biases among the alternate damping models for periods in the usable range. The ground response models also show large positive biases for periods beyond the usable range, indicating under-prediction. This is expected, as most sites have amplification at these long periods, whereas GRA and SRI predict effectively zero site response for such conditions. The HVSR model is usable over the full period range and produces the smallest biases among the site-specific methods at both short and long periods.

An important question related to site response prediction with ground response methods (GRA and SRI) is – under what conditions do these methods provide reliable estimates of site effects? This question is addressed in Section 6.3. Another interesting subject, addressed here and Section 6.5, is how aggregated statistics for "good fit" sites compare to those for the data population as a whole. For this purpose, I define "good fit" as normalized Fréchet distances < 0.6 over the usable period range, which applies to 38 sites based on GRA with the D^L_{min} damping model. As shown in Figure 6.1(b), biases of GRA and SRI models for these good fit sites are smaller than biases for the overall data population within the usable period range (i.e., $T <\sim 0.3$ sec), much smaller (except for SRI with κ-informed damping model) at long periods than those from Figure 6.1(a), and are also smaller than those from the ergodic model over the full range of periods.

Similar questions related to the use of HVSR methods are – (1) does the use of such methods improve site response predictions generally and (2) are the biases of predictions with these methods, and their dispersions, different for sites with different HVSR peak characteristics (clear peak, no peak, ambiguous)? These questions are addressed in Sections 6.4 and 6.6.

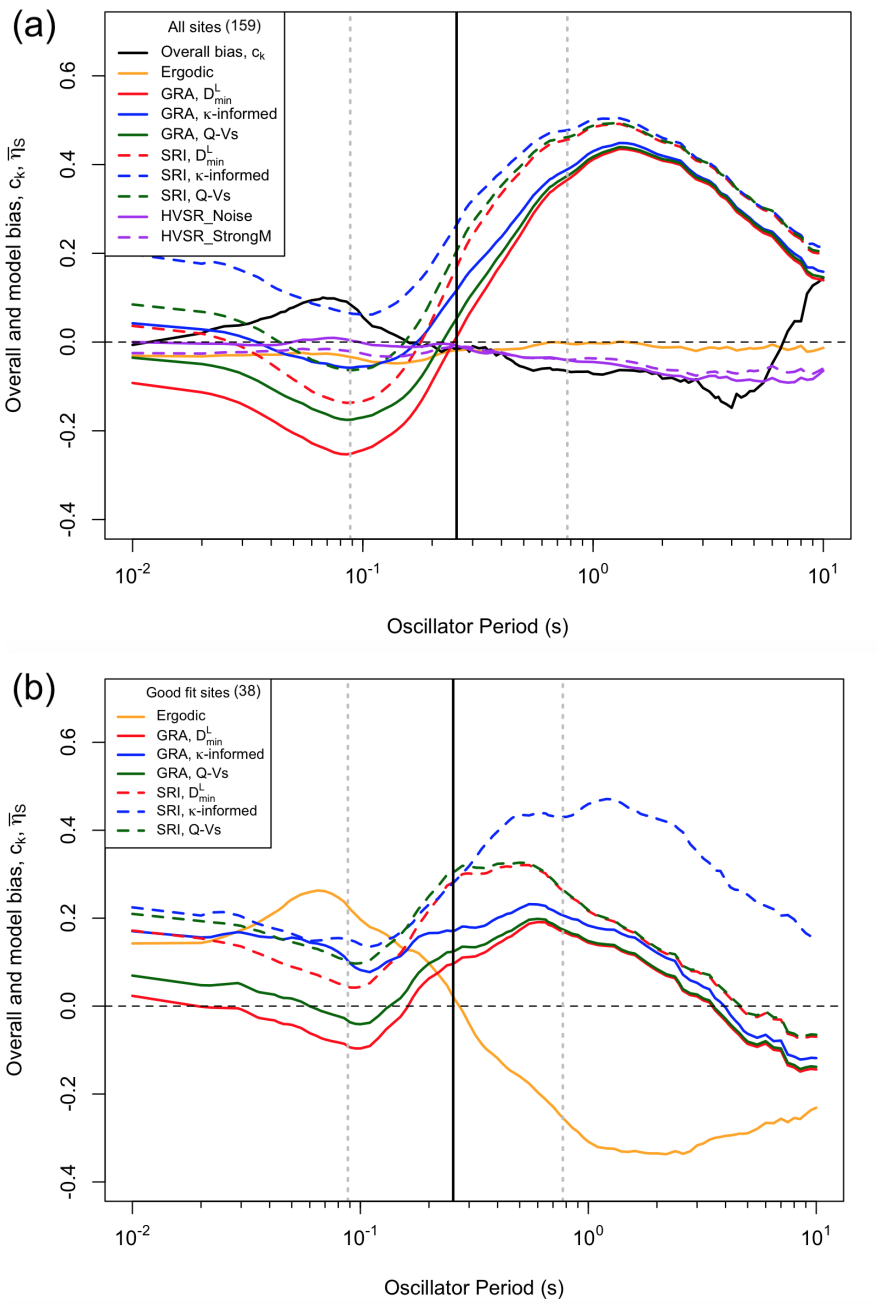

Figure 6.1: Comparison of model bias using GRA and SRI with three damping models, HVSR model, and ergodic model for (a) full database of 159 sites and (b) for subset of 38 sites with "good fit" using GRA by D^L_{min} damping model, as defined by normalized Fréchet distances < 0.6 over the usable period range and full period range, respectively. The vertical black solid line represents the median of soil column fundamental periods of 159 sites (as estimated using simplified Rayleigh method in Urzúa [104]). The two gray dotted lines represent 5 and 95th percentiles.

6.3 Predictability of GRA effectiveness

I evaluate four parameters for their potential to identify sites for which ground response analyses reliably predict observed site response. Prediction quality is judged from between-site residuals for individual intensity measures (η_S) and normalized Fréchet distance. Low absolute values of η_S and low values of normalized Fréchet distance indicate good fit. Parameters considered for their ability to identify good fit sites are:

- Velocity ratio, R_V ([4]): the ratio of time-averaged shear wave velocities over 5 m intervals at the base and top of each array ($R_V = V_{SDH}/V_{S5}$).
- Maximum between-layer amplification over profile, A_{max}: The square root of the impedance ratio (Equation 4.8) is computed across all interfaces in an array, and the maximum value is taken as A_{max}.
- Time-averaged shear wave velocity for profile, V_{SZ}.
- Shear wave velocity at base of profile, V_{Sb}.
- Profile thickness, z_p.

Figure 6.2 shows trends of between-site residuals as derived from GRA with the geotechnical damping model with each of these parameters. Figure 6.3 shows the same information, but with the κ-informed damping model. Site residuals η_S are shown for PSA at oscillator periods of 0.01 sec (PGA), 0.2 sec, and 0.5 sec. The data are shown with symbols (one per site). I do not necessarily expect a strong trend of the residuals with the parameters on the abscissa, hence no fit line is provided. Rather, I provide binned means and binned standard deviations. A parameter could be considered as having predictive power for GRA effectiveness if either the mean of site residuals trends towards zero for a certain range of that parameter, or if the dispersion of site residuals appreciably decreases for a certain range of the parameter.

Examining the results in Figure 6.2, I do not find an appreciable trend of binned means with any of the considered parameters because the means are generally near zero, hence that

indicator of parameter effectiveness does not apply in this case. Moreover, I find no trend of decreasing dispersion with any of the considered parameters. Figure 6.3 illustrates the effectiveness of GRA with κ-informed damping model against the same five parameters. The trends are similar to those shown in Figure 6.2.

One limitation of using site residuals η_S to evaluate model effectiveness is that they only quantify misfits at individual periods, and as such, do not describe fit across a range of periods (i.e., compatibility of shapes). Goodness-of-fit metrics (Section 5.2.2) provide a means by which to describe such cross-period fits. In next section, I show that normalized Fréchet distance represents well curve similarity, so this metric is used here.

Figure 6.4 shows the variation of normalized Fréchet distance with the five site parameters. The Fréchet distance used here is computed over the usable period range for each site (i.e. periods less than site period). Because Fréchet distance is always positive, trends in binned means occur that were not evident with residuals. The trends are towards reduced normalized Fréchet distance as R_V, V_{SZ}, and V_{Sb} increase, indicating improved fit for higher-impedance conditions. As shown in Figure 6.4, log-linear fit lines trend downward, with the slopes and p-values as shown in the figure. All of the slopes are statistically significant, but the slope for the V_{Sb} parameter has the smallest p-value, indicating the most significance.

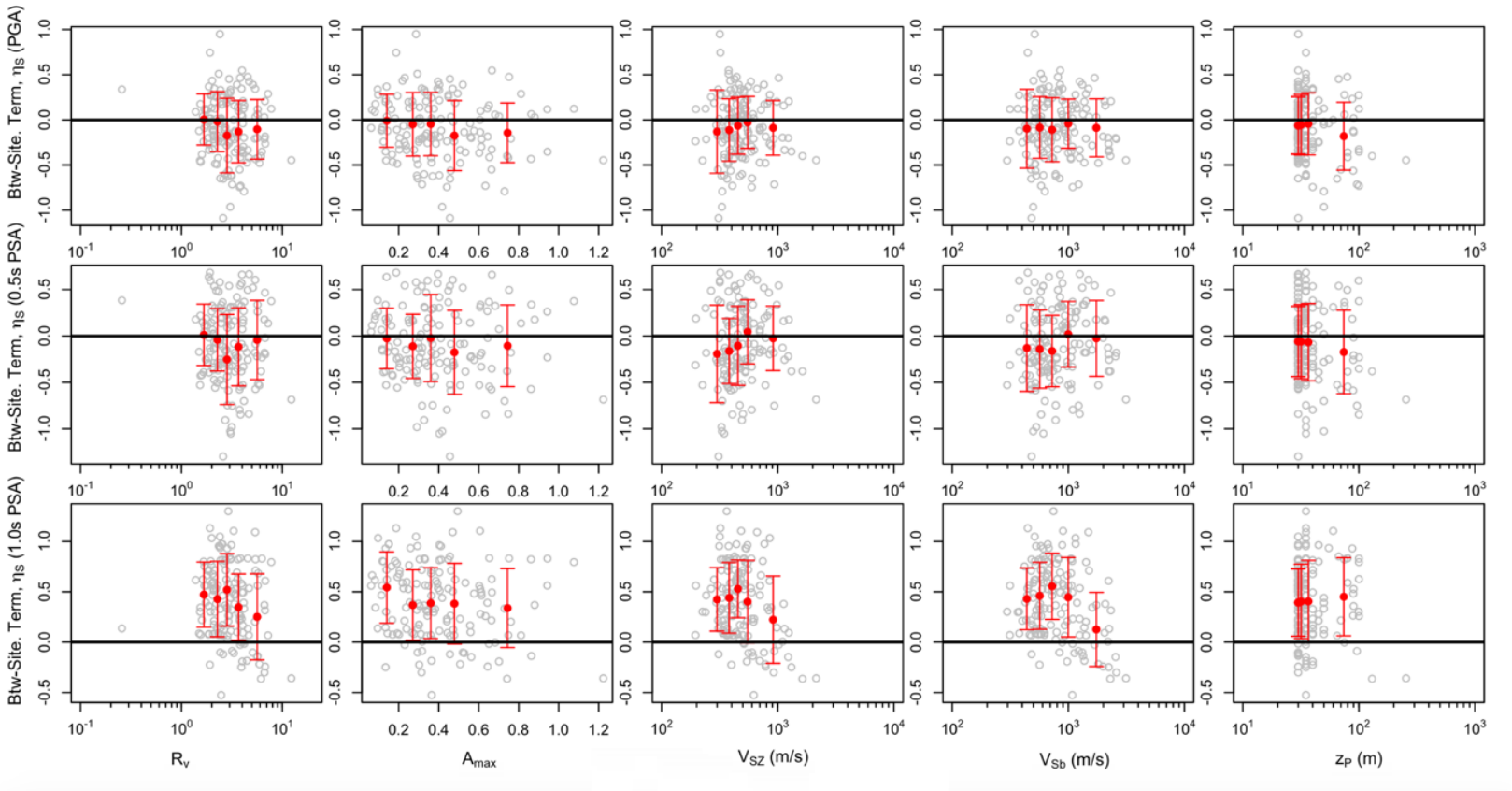

Figure 6.2: Trends of between site residuals (η_S) computed using geotechnical damping model with site parameters R_V, A_{max}, V_{SZ}, V_{Sb}, and z_p

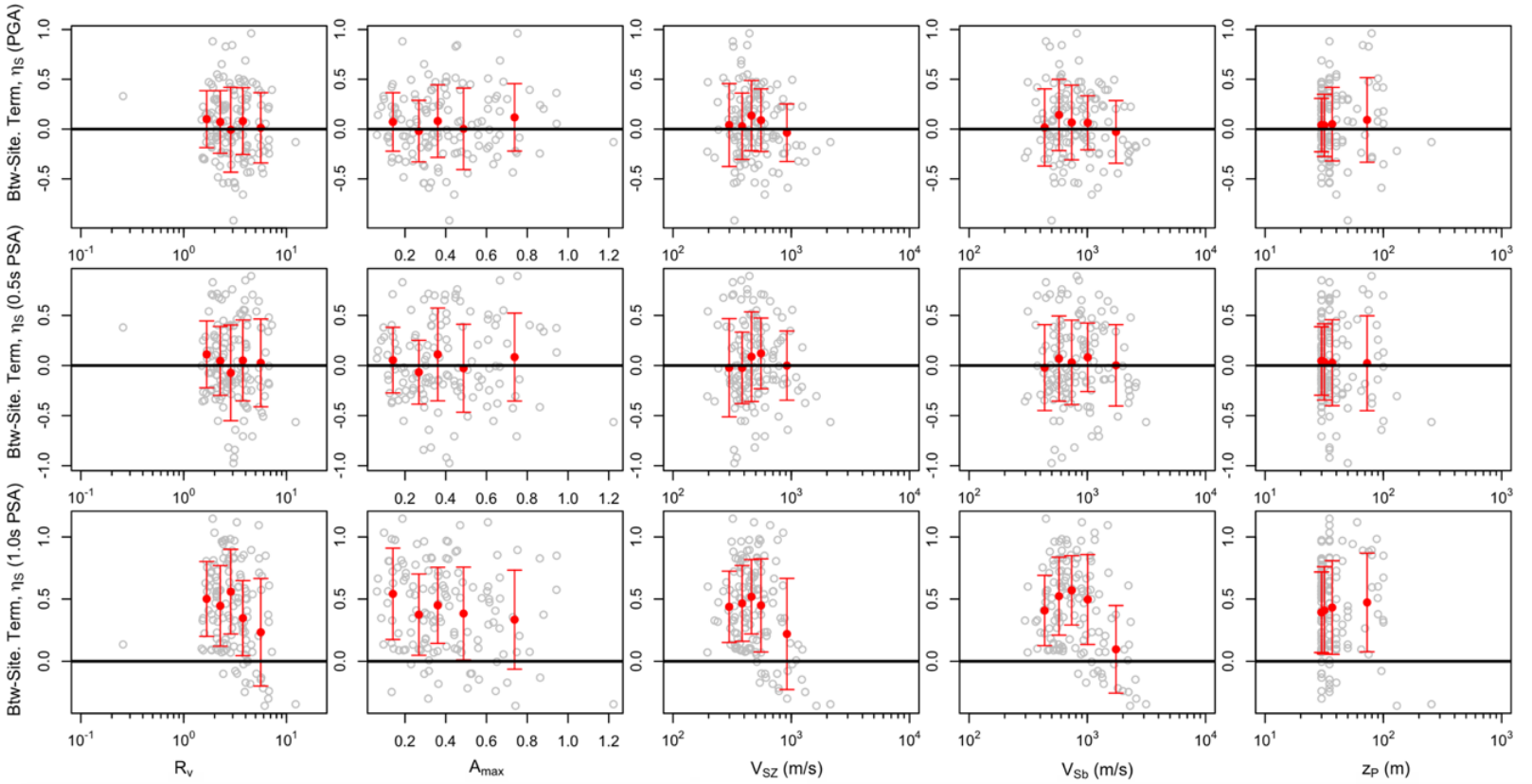

Figure 6.3: Trends of between site residuals (η_S) computed using κ-informed damping model with site parameters R_V, A_{max}, V_{SZ}, V_{Sb}, and z_p

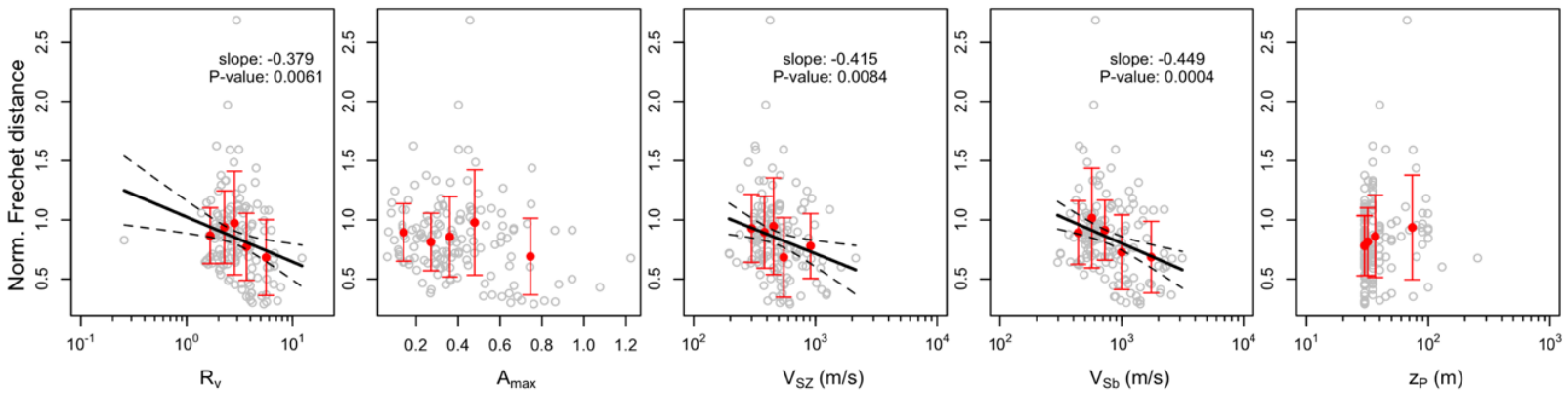

Figure 6.4: Trends of normalized Fréchet distances (Ψ) computed using geotechnical damping model with site parameters R_V, V_{S30}, V_{SZ}, and V_{Sb}

6.4 HVSR model effectiveness

In Section 3.4, I described groups of sites based on their HVSR signatures: clear peak, no peak, ambiguous. It might be expected that the HVSR-based site response model would have different levels of predictive power for sites belonging to these different groups. In this section I evaluate biases and trends against independent variables using the η_S terms. Analysis of dispersions (ϕ_{S2S}) is deferred to Section 6.6.

First, I examine the compatibility of f_{p1} (from HVSR) with the oscillator period of the peak site response (T^p_{osc}) (Section 5.1). The database used in this analysis consists of the sites for which peaks were identified from both HVSR and site response. I consider the 54 sites with noise-based HVSR clear peaks combined with the 20 ambiguous sites with noise-based HVSR peaks from Analyst I. Among those 74 sites, 41 also have a site response peak, which comprises the data set used for the peak comparison. Figure 6.5 shows the product $f_{p1}T^p_{osc}$ vs f_{p1}. Of the 41 sites, 24 have reasonably close alignment of f_{p1} with $1/T^p_{osc}$, based on the product being within a factor of two of unity (i.e., < 2 or > 0.5). For these 24 sites, the site response and HVSR peaks are likely related to the same resonances. On the other hand, when the ratio is beyond a factor of two from unity, the peaks may be unrelated (these data points are labelled as "outliers" in Figure 6.5). Based on the data in this plot with aligned peaks, the ratio of periods (equivalent to the product of frequency and period used in the plot) has an average value of 0.93. The outlier data suggest there could be a trend with f_{p1}, but the "good fit" sites lack this trend, and I do not seek to capture it. On the basis of this analysis, I select $\alpha_p = 0.93$ for use in Equation 4.12.

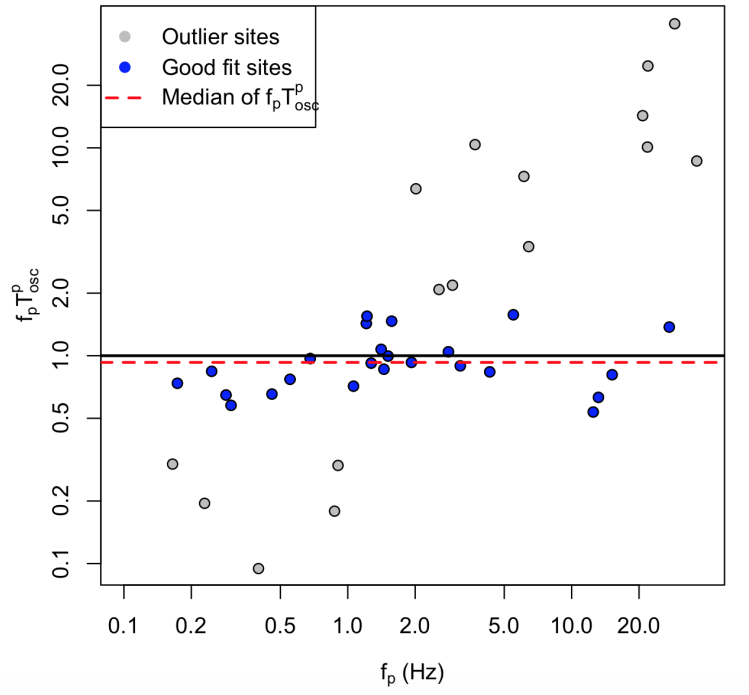

Figure 6.5: The relation between $f_{p1}T^p_{osc}$ and f_{p1}. There are 17 outlier points (in gray) with $f_{p1}T^p_{osc} > 2$ or $f_{p1}T^p_{osc} < 0.5$

Figure 6.6 shows the means of site terms (η_S) for all sites in the clear peak, no peak, and ambiguous peak groups. Means produced using the ergodic model for each group of sites are also shown for comparative purposes. Interestingly, the ergodic model is unbiased for three of the four groups (all sites, P-P, N-N). The smallest mean (closest to zero) for the HVSR model is encountered for the all sites group. The clear peak and no peak groups produce positive and negative biases, respectively. The largest bias is encountered for the ambiguous peak group (e.g., 0.22 at 0.07 sec for HVSR from noise), where again the ergodic model produces less bias. For ϕ_{S2S}, the HVSR model in the no peak group reduces uncertainties relative to the ergodic model over the full period range and with the largest reduction (about 0.15 natural log unit) occurring at period 0.4 sec. For the clear peak group, the uncertainties are reduced beyond period 1 sec, which may be be a consequence of the HVSR model capturing long period peaks. The HVSR model does not reduce uncertainties relative to the ergodic model for the clear peak group at short periods nor in the ambiguous group. There are

several reasons for HVSR model misfits that produce large uncertainties: (1) there are false positives in the clear peak group (sites without peaks in site response) and instances of offset peaks (Figure 6.5) – no adjustments have been made to reduce these effects; and (2) the model used for the present work was developed for conditions in Japan, and has not been customized for California. It remains to be seen whether a model customized for California conditions can outperform an ergodic, V_{S30}-based model.

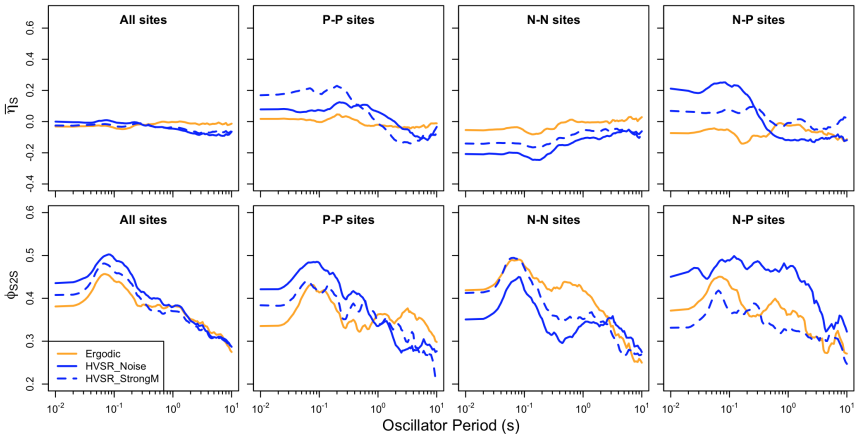

Figure 6.6: Comparison of between-site standard deviations (ϕ_{S2S}) from adjusted HVSR model categorized by clear peak sites, no clear peak sites, and ambiguous sites, and ergodic model.

Figure 6.7 shows the means of site terms (η_S) for the 24 sites with $0.5 \leq f_{p1}T_0 \leq 2$. Conditioning the site periods to align in this manner substantially reduces the mean bias for the P-P category, particularly for the case of peaks derived from strong motion data. In addition, the period range over which ϕ_{S2S} is reduced by the HVSR model is broadened to periods beyond 0.2 sec (it was > 1.0 sec in Figure 6.6).

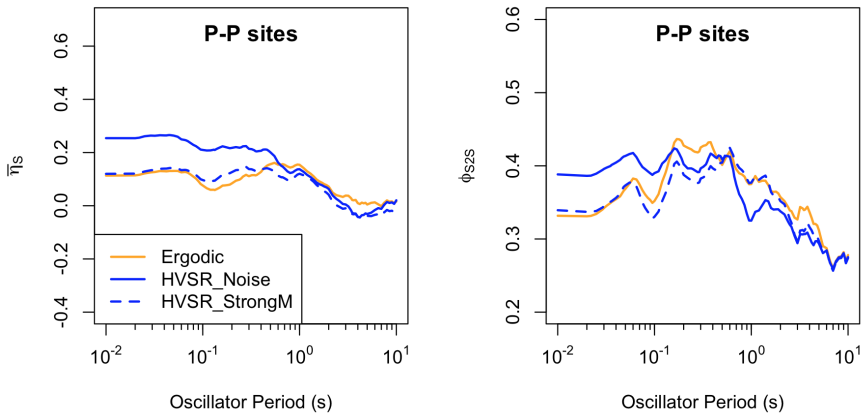

Figure 6.7: Comparison of between-site standard deviations (ϕ_{S2S}) from adjusted HVSR model for peak well-aligned sites

Figure 6.8 plots values of η_S sampled at f_{p1} for the 74 sites with peaks in noise-based HVSR. The 74 sites are from the 54 clear peak sites and 20 sites from the ambiguous peak group with peak identification by Analyst I. The $\bar{\eta}_S$ values are plotted against f_{p1} (Figure 6.8(a)) and peak amplitude α_1 (Figure 6.8(b)). The plot shows a weak trend between the mean of $\bar{\eta}_S$ and f_{p1} in which the mean of $\bar{\eta}_S$ is increasing as f_{p1} gets larger. However, the plot of bias with α_1 indicates no trend.

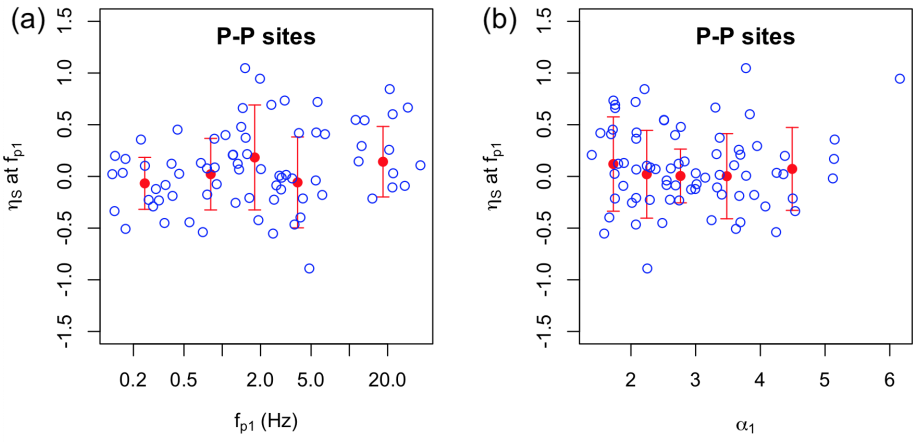

Figure 6.8: The scatter plot of mean of η_S over the full period range against f_{p1} and α_1 for 74 peak sites

6.5 Full-population comparisons of GRA goodness-of-fit metrics

As described in Section 5.2.2, I have considered three metrics of multi-period goodness of fit, which are mean correlation coefficient, Fréchet distance, and normalized Fréchet distance. In this section, I compare the effectiveness of these metrics for the full data population using GRA residuals.

For the interpretation of results derived from ground response methods, our approach is based on a classification of each site as having good, intermediate, or poor fit (denoted as Categories 3, 2, 1) based on visual inspection. Then I identify the degree to which the various goodness-of-fit metrics are able to distinguish between the three qualitative categories.

Figure 6.9 shows histograms of the three goodness-of-fit metrics from GRA using the $D^L_{\min}$ damping model (the histograms for the other damping models are similar). Green bars indicate good fit, blue intermediate fit, and red poor fit. All three metrics are able to distinguish the qualitative categories, in the sense that green sites are clustered at low Fréchet distance and high correlation coefficient, whereas red sites have demonstrably higher Fréchet distances and lower correlation. However, neither of the goodness-of-fit metrics are able to perfectly separate the three categories.

Among the various goodness-of-fit metrics, normalized Fréchet distance exhibits the best performance, because it most clearly distinguishes performance categories. Whereas correlation coefficient has mixing of green and blue bars with red bars, normalized Fréchet distance better distinguishes green and blue bars from red. It is also helpful that the range of the parameter is relatively broad.

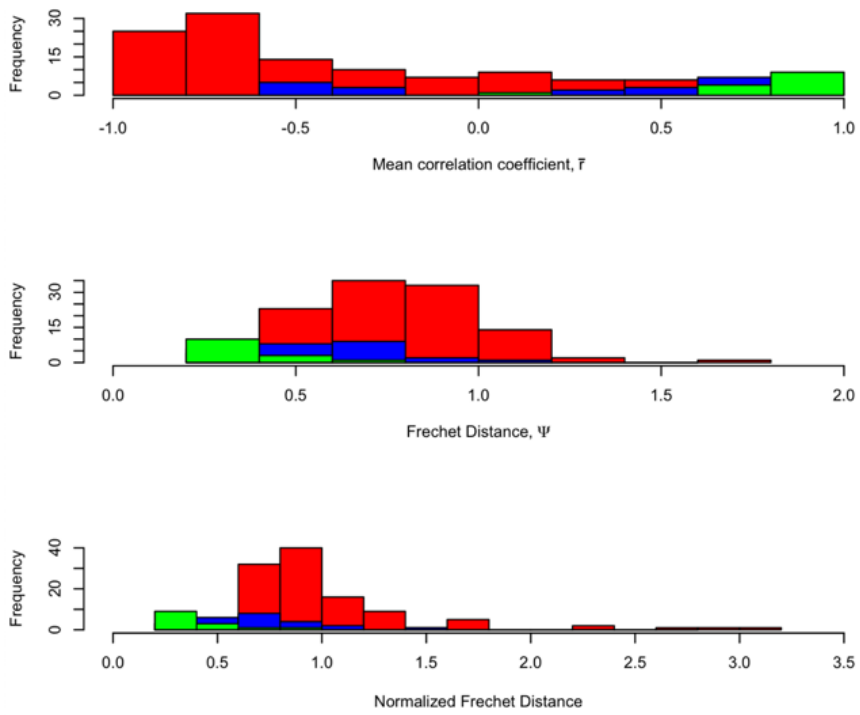

Figure 6.9: Histograms of three metrics for goodness of fit

I use the one-way analysis of variance (ANOVA) F-test statistic to evaluate if the three goodness-of-fit metrics are statistically distinct between the three categories. The F-test statistic is formulated as[1],

$$F = \frac{\text{between group variability}}{\text{within group variability}} \tag{6.1}$$

Distinction can be quantified from p-values, in which values less than 0.05 indicate that the three categories exhibit statistically distinct values of the goodness-of-fit metrics. As shown in Table 6.1, all of the metrics provide for statistically significantly distinct categories.

I apply optimization to search for the boundaries of each metric that can best separate the three categories so as to minimize the error (the proportion of mis-classified sites). Error is defined by differencing the class specified by the metric, on the basis of optimized boundaries, with the label from visual inspection and then normalized by the total number of sites as

[1] `https://en.wikipedia.org/wiki/F-test`

Table 6.1: Summary of F-test for each metric

Metric	p-value
Correlation coefficient	< 2e-16
Fréchet distance	2.96e-9
Normalized Fréchet distance	2.86e-7

follows:

$$Err_j = \frac{\sum_{i=1}^{n} \mathbb{1}\{\text{class}_{ji} \neq \text{label}_i\}}{n} \tag{6.2}$$

where n is the number of sites, $\mathbb{1}\{\}$ is an indicator function which returns one if the condition in bracket is satisfied and zero otherwise. class_{ji} is the category classified for site i by the metric value m_{ji} and boundary θ_j while label_i is the "true" category labeled by visual inspection. Suppose the two boundaries are θ_{j1} and θ_{j2}, then I will have the category classified by correlation coefficient as,

$$\text{class}_{1i} = \begin{cases} 1, & m_{ji} \leq \theta_{j1} \\ 3, & m_{ji} \geq \theta_{j2} \\ 2, & \text{otherwise} \end{cases} \tag{6.3}$$

and the category classified by (normalized) Fréchet distance ($\{j = 2, 3\}$) as,

$$\text{class}_{ji} = \begin{cases} 1, & m_{ji} \geq \theta_{j1} \\ 3, & m_{ji} \leq \theta_{j2} \\ 2, & \text{otherwise} \end{cases} \tag{6.4}$$

The inequality signs for correlation coefficient and (normalized) Fréchet distance are different because the good fits correspond to large positive correlation coefficients but small (normalized) Fréchet distances.

Table 6.2 shows the optimal boundaries for each metric and the corresponding errors. Based on those results, normalized Fréchet distance gives the smallest minimum error, so it appears to be the best suited means by which to categories goodness-of-fit. The sites are considered to be "good fit" sites if their normalized Fréchet distances ≤ 0.6 (category 2 or 3).

Table 6.2: Summary of minimum error for each metric

Metric	θ_1	θ_2	Min.Err
Correlation coefficient	-0.51	0.64	0.375
Fréchet distance	0.64	0.31	0.230
Normalized Fréchet distance	0.65	0.45	0.171

6.6 Site response uncertainty and variability

The standard deviations of the random variables (non-constant) terms in Equation 5.4 are related as follows:

$$\sigma = \sqrt{\tau^2 + (\phi_{S2S})^2 + (\phi_{SS})^2} \tag{6.5}$$

where σ, τ, ϕ_{S2S}, and ϕ_{SS} are the standard deviations of R_{ij}, η_E, η_S, and ϵ_{ij}, respectively. Our principal interest is in ϕ_{S2S}, which represents the between-site variability of the misfits in predicted ground motion using ergodic, GRA, SRI, or HVSR models. There are two sources of this variability: (1) modeling uncertainty, which is caused by the analysis method not representing accurately the site response physics, and (2) soil property uncertainty, which occurs if the measured input parameters (V_S profile, inferred damping profile, and HVSR-based) for the sites have some deviations from actual properties.

Figure 6.10 shows the period-dependence of ϕ_{S2S} when site response is evaluated using site-specific models (GRA, SRI, and HVSR) and the ergodic model. The site specific results are shown for GRA and SRI with three considered damping models (geotechnical, κ-informed, and $Q - V_S$) and for the HVSR model with both data sources (ground motion and noise). As in Figure 6.10, the range of site V_S profile fundamental periods is shown to indicate the useful period range. Figure 6.11 shows the same information but for the subset of "good fit" sites (38 sites) with normalized Fréchet distance < 0.6 based on GRA with the $D^L_{\min}$ damping model; because these "good fit" sites are defined for the case of ground response models, ϕ_{S2S} is only shown for those model.

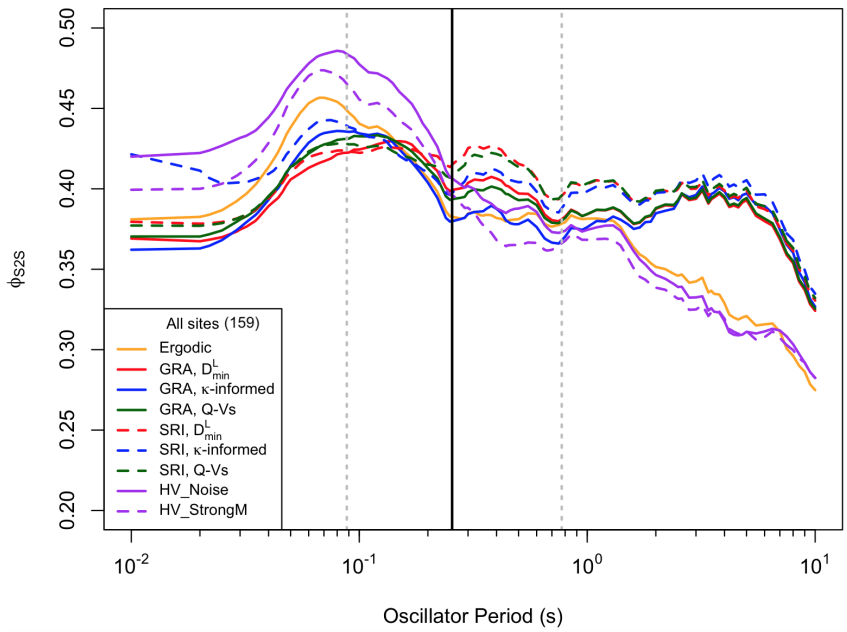

Figure 6.10: Comparison of between-site standard deviations (ϕ_{S2S}) from site-specific analyses (GRA and SRI) using three damping models and ergodic model. Statistics represent results across all sites

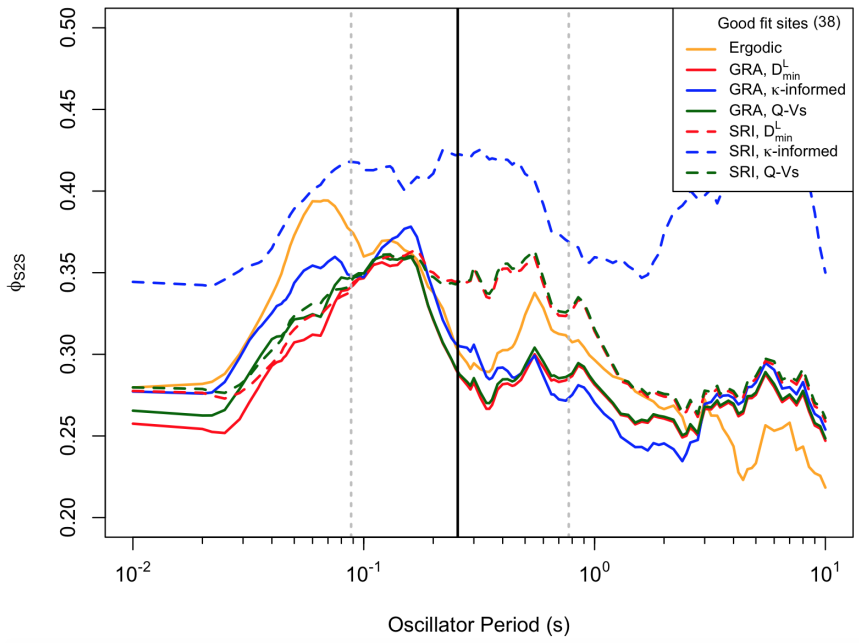

Figure 6.11: Comparison of between-site standard deviations (ϕ_{S2S}) from site-specific analyses (GRA and SRI) using three damping models and ergodic model. Statistics represent results across "good fit" sites with normalized Fréchet distance less < 0.6 based on GRA with the D^L_{min} damping model.

A general observations from Figure 6.10 is that ϕ_{S2S} is not appreciably different for the ergodic model and the various site-specific models. The lack of appreciable ϕ_{S2S} reduction through the use of site-specific methods indicates that such analyses are, on average, not improving ground motion estimates significantly relative to the use of an ergodic model.

Important elements of Figure 6.10 are summarized:

1. With the exception of HVSR models, site-specific ϕ_{S2S} values for $T < 0.2$ sec are lower than the ergodic model; these short periods are within the usable period ranges for the sites. In particular, the peak in ϕ_{S2S} at 0.06 sec that is produced by the ergodic model is reduced through the application of ground response methods by about 0.1 natural log units (this local peak of uncertainty is not a feature of the ergodic model itself, but rather it is a feature of the data set).

2. In the period range of $0.2 - 1$ sec, where the data "fall off" as modeled profile periods

are exceeded, but also where many peak site responses occur, there are relatively large differences between results of GRA and SRI among damping models, with κ-informed damping models providing the smallest ϕ_{S2S} values.

3. At long periods ($T > 0.6$ sec), the ergodic model has lower ϕ_{S2S} than ground response methods (GRA and SRI). I do not expect good results from GRA or SRI in this period range, which is beyond the fundamental period of the modeled soil columns and hence little-to-no site response is predicted. The HVSR models significantly outperform ground response methods in this period range, and slightly reduce ϕ_{S2S} relative to the ergodic model. This reduction occurs because HVSR methods are able to capture long period resonance effects that are missed by ergodic models or ground response methods.

Part of the reason for the moderate ϕ_{S2S} reduction in Figure 6.10 is that site responses for some of the sites are not well represented by GRA and SRI, even over the applicable period range of the modeled soil column. However, as shown in Figure 6.11 for the subset of "good fit" sites where relatively shallow ground response is an important driver of site response, I find reductions of ϕ_{S2S} over a broader period range (up to 2 sec) and on the order of up to 0.10. These reductions are most consistently achieved from the use of GRA, whereas SRI provides some relatively high dispersions. Among the various damping models, κ-informed damping produces higher dispersion for the subset of good-fit sites. This occurs because (1) the "good fit" sites are defined based on the D^L_{min} damping model, not the κ-informed damping model, and (2) the κ-informed damping model over-predicts damping comparing to D^L_{min} at 9 of the 38 "good fit" sites (SSN = 100109, 100114, 100283, 100341, 100542, 100545, 3055, 3076, 3088), which produces large short-period biases that inflate the dispersion.

Site-to-site variability also provides an effective means by which to evaluate the performance of the HVSR model. I evaluated HVSR model performance, in terms of means and standard deviations of site terms for the full population and various subsets with different peak characteristics, in Section 6.4 and Figure 6.6.

CHAPTER 7

Region-Specific Linear Site Amplification Model for Peaty Organic Soil Sites in Hokkaido, Japan

7.1 Project introduction

The application of ergodic site terms in ground motion models (GMMs) to regions having very soft, peaty organic soils is a process that carries large epistemic uncertainty. One substantial driver of this uncertainty is that the ground conditions at peat sites can have very slow time-averaged shear wave velocities in the upper 30 m (V_{S30}), perhaps $100m/s$ or less. Figure 7.1 shows V_{S30} histograms from site databases in the NGA-West2 and NGA-Subduction projects. The slowest V_{S30} values in these histograms are in the range of $150 - 200m/s$. As a result, the application of ergodic models to soft peat sites represents an extrapolation beyond the data range – the ergodic mean site response is simply unknown.

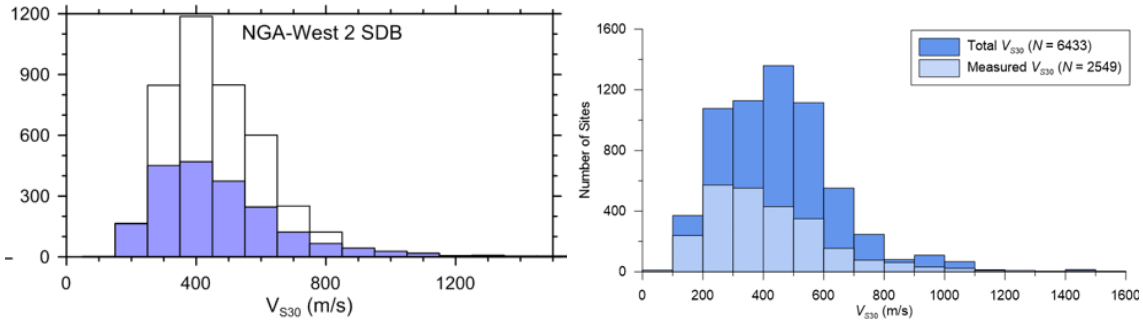

Figure 7.1: Histograms of total and measured V_{S30} values for sites in NGA-West2 database (left) and NGA-Subduction database (right). From [88] and [6], respectively.

A second driver of large uncertainty can be anticipated because soft peats usually overlie relatively firm, non-organic soils at depth. As a result, there exists within the site profile

steep velocity gradients that can give rise to more pronounced impedance and resonance effects than would be typical at non-peat sites. Such effects produce site response transfer functions with strong peaks at one or more site frequencies. These features of site response cannot be captured by V_{S30}-based models as used in typical GMMs, although they could potentially be captured by a model that combines V_{S30}-scaling terms with site resonance terms that take the peak frequency (f_{peak}) as a site parameter (e.g., [52, 53, 55, 56, 72]).

As a result of these issues, the ergodic site terms in current GMMs for subduction earthquakes in Japan, whether based on V_{S30} directly (Abrahamson et al, 2018, [1]) or V_{S30}- and site period-based site classes (four such classes are used in Zhao et al, 2016a and 2016b [118, 119]) (denoted as the Aea and Zea GMMs, respectively) are expected to have bias and large uncertainty when applied to peaty organic soil sites in Hokkaido. As a result, our objective in this study is to improve ground motion estimates by developing region-specific ergodic site amplification models derived from non-ergodic site responses at recordings sites. In other words, I seek to gain insights into the features of local site response from non-ergodic analyses, including impedance contrast and resonance effects, and then to build a more generic (local but ergodic) model from those results.

The approach taken in this paper is to develop a linear site amplification model using recordings with relatively low amplitudes, for which significant nonlinear effects are not expected. I then examine nonlinear effects through residuals analysis using data from one event that produced relatively strong shaking. The direct outcome of this study is a site amplification model for a soft soil region in Japan that is useful for case history analyses ([101]) and hazard applications. However, the broader value of the work presented here is to illustrate an approach for developing regional site amplification models for relatively data-rich regions with unique geological conditions.

7.2 Data sources

The region-specific analysis performed in this study applies to the portion of the Tokachi River in Hokkaido, Japan passing through peaty organic soil layers that extend roughly from

the river mouth to 40 km upstream of the river mouth, as shown in Figure 7.2. This region contains seven instruments operated by Obihiro Development and Construction Department (ODCD), for which I have obtained recordings from ten earthquakes in the NGA-Sub database. This section discusses the data compiled for analysis of non-ergodic site responses at these seven stations.

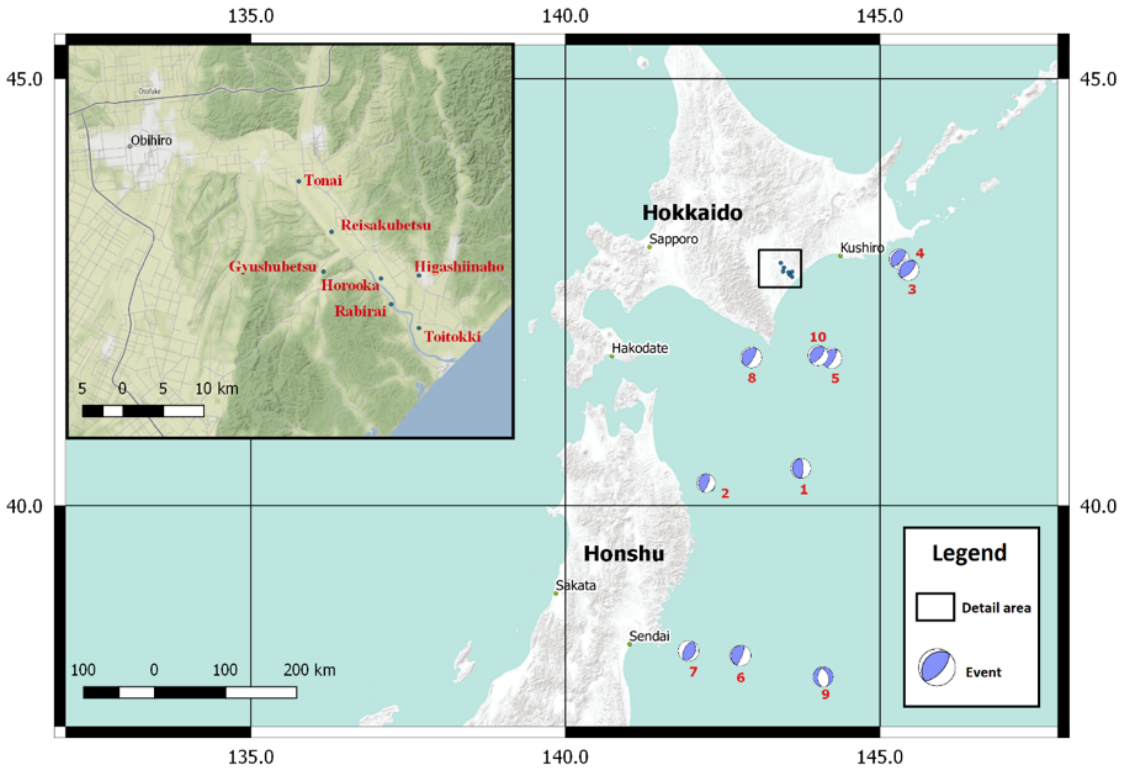

Figure 7.2: Map of northern Japan showing event locations considered in this study and location of Tokachi River study region. Detail map of study region shows locations of local ground motion stations

7.2.1 Ground motions and related metadata

Table 7.1 provides metadata for the seven ODCD stations in the study region. The station locations were provided by ODCD and the basis for the site information (V_{S30} and classification) is provided in next section. As shown in Figure 7.2, the station locations are roughly evenly distributed across the study region. The site classes referred to in Table 7.1 range from

Table 7.1: Metadata of seven stations owned and operated by Obihiro Development and Construction Department (ODCD)

Station Name	Gyushubetsu	Higashiinaho	Horooka	Reisakubetsu	Rabirai	Toitokki	Tonai
Longitude	143.4622	143.6063	143.5489	143.4744	143.5642	143.6043	143.4250
Latitude	42.7921	42.7876	42.7841	42.8359	42.7556	42.7281	42.8917
$\mathbf{V_{S30}}$ (m/s)	130.83	211.54	102.17	181.36	150.48	117.18	181.36
$\mathbf{f}_{\text{peak}}$ (Hz)	1.14	1.60	1.42	1.62	1.14	1.60	1.50
Site Class	IV	III	IV	IV	IV	IV	IV

I to IV, with larger-numbered classes corresponding to softer site conditions ([118, 119]).

The stations in Table 7.1 have recorded ten earthquakes. Figure 7.2 shows the locations of these events, each of which has ground motion data that is incorporated into the NGA-Subduction database ([67]). Event metadata for the ten events is provided in Table 7.2 along with the numbers of processed recordings produced by each event in the NGA-Subduction database. The numbers of records per event range from 13 to 1293; there is a dramatic increase in station density and data quality since the 1995 Kobe earthquake.

Limiting distance criteria are intended to avoid potential bias with instrument trigger levels, and operate by eliminating data beyond a distance R_{max} where an appreciable fraction of recordings may not appear in the data as a result of having amplitudes below the trigger threshold. As described in Section 4.5.2 of [33], R_{max} depends on earthquake magnitude and instrument type. In some cases, where the rupture distances of Obihiro stations are modestly larger than R_{max}, I extend the NGA-Subduction values of R_{max} (by no more than 40%) to include in the analyses stations at these distances. Backarc stations are not used because the Obihiro sites of interest in this study are located in forearc regions, and our principle interest is source-site wave paths within the forearc region. Event 2 data are excluded because of the 13 recordings in the NGA-Sub database, nine do not meet the R_{max} criteria, and the remaining four have rupture distances much less than those for ODCD stations (113 km vs 300 km). Despite not using Event 2, I do not renumber other events (Events 1 and 3-10).

Table 7.2: Summary of event metadata and numbers of recordings for the ten considered earthquakes

Event	1	2	3	4	5	6	7	8	9	10
Date/Time	1994/12/28, 12:19	1995/01/06, 22:37	2004/11/28, 18:32	2004/12/06, 14:15	2008/09/11, 00:21	2011/03/11, 05:46	2011/04/07, 14:32	2011/11/24, 10:25	2012/12/07, 08:18	2003/09/25, 19:50
Magnitude	7.7	7.0	7.0	6.7	6.8	9.1	7.1	6.2	7.3	8.29
Strike/Dip/Rake	180/30/90	179/21/69	211/24/81	222/26/90	228/21/108	200/20/88	24/37/87	223/16/103	174/61/82	230/20/90
Fault Type	Reverse	Reverse	Reverse	Reverse	Reverse	Reverse	Reverse	Reverse	Reverse	Reverse
Event Type	Interface	Interface	Interface	Interface	Interface	Interface	Slab	Interface	Slab	Interface
Longitude	143.75	142.31	145.28	145.34	144.15	142.86	141.92	142.89	144.12	144.09
Latitude	40.43	40.22	42.95	42.85	41.78	38.10	38.20	41.75	37.84	41.78
Hypocenter Depth (km)	10	47.8	48.17	45.84	30.86	23.74	65.9	43.21	52	25
Number of Recordings in NGA-Sub	31	13	378	204	407	1293	799	177	866	645
Number of NGA-Sub Recordings selected	10	0	84	57	64	692	439	57	353	173
Number of Recordings ODCD array	3	3	7	7	6	7	7	6	7	6

The NGA-Subduction data for the ten events did not include recordings at the ODCD stations. I was provided with raw (digital but unprocessed) recordings from the seven ODCD stations by S. Takashi (personal communication, last update 10 November 2017). The data were processed following standard procedures as given in [67], which includes instrument correction, application of both high and low pass acausal filters at operator-determined corner frequencies, and baseline correction of the processed signals. Following the application of this processing, I computed median-component intensity measures RotD50 ([18]) for peak acceleration, peak velocity, and 5% damped pseudo-spectral accelerations (PSA) using the R package by [109].

As shown in Figure 3, Events 1-9 produced relatively weak motion recordings at the ODCD stations, which are useful for developing the linear component of a regional site amplification model. In contrast, Event 10 (2003 Tokachi-Oki Earthquake) produces appreciably stronger shaking. Accordingly, our approach to model development is to develop a linear model using data from Events 1-9, and then to perform residuals analysis using data from Event 10 to investigate potential nonlinearity effects.

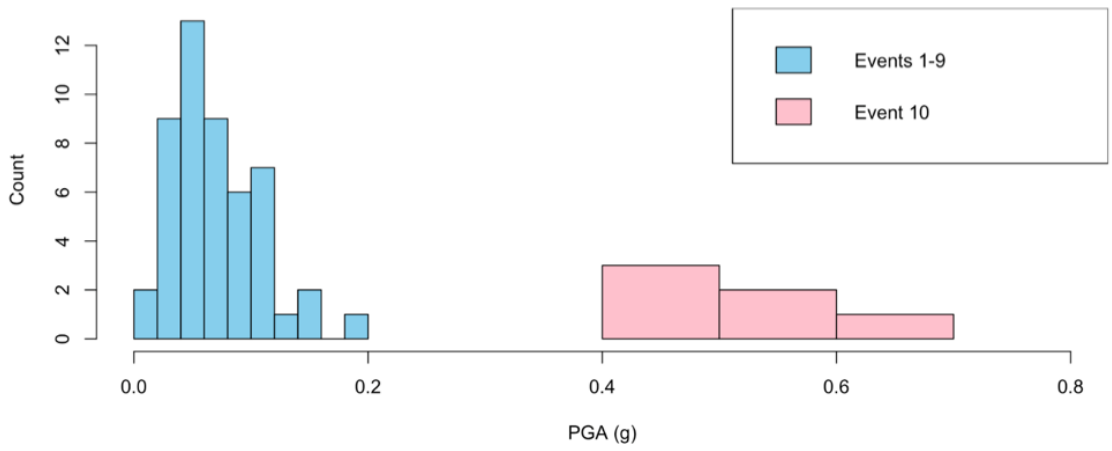

Figure 7.3: Histogram of median-component peak accelerations at ODCD sites

7.2.2 Site conditions

Each of the seven ODCD sites in the study region are underlain by peaty organic soils in the Tokachi River basin. The geomorphic terrain class for six of the seven sites per the Japanese

Engineering Geomorphologic Classification scheme ([107]) is 'back marsh' (the seventh, in the furthest downstream area, is 'delta and coastal lowland'). The site class as given by [118] is IV, which is described as soft soils with $V_{S30} < 200m/s$ and site period $T \geq 0.6s$. The peaty organic soils extend to a depth of 2 - 6 m, and are underlain by alluvial deposits of sandy, silty and clayey sediments. Under the levees, the peat layer is typically 0.5 - 1.0 m thinner due to consolidation of the soft peat beneath the levee fill. Penetration resistance measured during CPTs and SPTs, as well as shear wave velocities are low in the area. Relatively firm material, likely Pleistocene in age, is located at greater depths generally around 35 - 40 m.

We performed geophysical testing at or in the vicinity of the Toitokki, Horooka, Rabirai, Reisakubtsu, and Gyushubetsu stations using Spectral Analysis of Surface Wave (SASW) and ambient noise techniques. Rayleigh wave dispersion curves and horizontal-to-vertical spectral ratio vs frequency plots (HVSR plots) were obtained from these tests and plotted in Figure 7.4 - 7.5. The HVSR data was processed by the procedure described in Section 3.3. Sites Tonai and Higashiinaho were not part of the site exploration program. For these sites, HVSR plots were developed using pre-event noise in acceleration signals by first estimating the p-wave arrival time, and then taking preceding portions of the signals for use in analysis; and their V_{S30} values were also estimated by proxy-based models in Table 7.1.

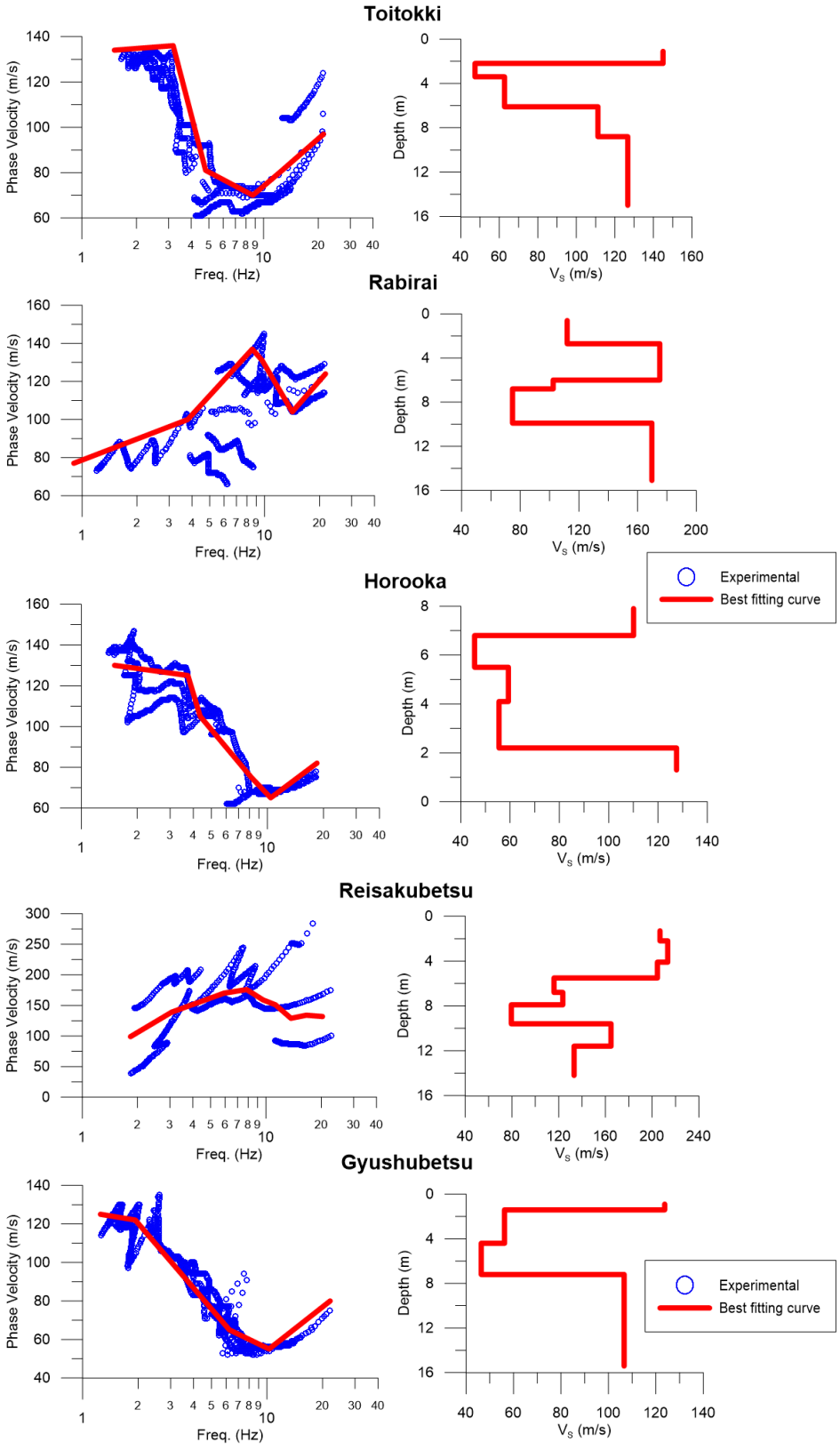

Figure 7.4: The dispersion curves and V_S profiles for ODCD sites.

Figure 7.5 plots the resulting H/V spectral ratios (from microtremors where available, for pre-event noise otherwise) for the seven Obihiro stations. Gaussian pulses (described in Section 3.4.2) were fitted to prominent peaks in the H/V spectra ([48, 72]). The resulting f_{peak} values, established from the pulse fitting procedure, are given in the figure. Sites Toitokki and Rabirai have two HVSR peaks, which raises the question of how to select f_{peak} for such cases. I adopt this approach: (1) if the peaks are of comparable amplitude but distinct in frequency (ratio of the peak frequencies is greater than about 3-5), adopt as f_{peak} the value for the lower frequency peak; (2) if the peaks are of significantly different amplitude ($>$ factor of two), use the peak with the larger amplitude (this is usually the lower frequency peak); and (3) if the peaks are of comparable amplitude and the frequencies are similar (ratio of the peak frequencies is less than about 3-5), re-fit the Gaussian function to encompass both peaks together. Case 1 applies to the Rabirai site and Case 3 applies to the Toitokki site. For the Toitokii site, a combined fit of the two peaks is shown in the figure. The relatively large uncertainty in HVSR that is shown for sites Tonai and Higashiinaho is associated with the use of pre-event noise data of relatively short duration. Sites Toitokki, Rabirai, and Gyushubetsu also have a lower frequency peak (around 0.2 Hz) that is with comparable height as the selected peak. Per the criteria in analyst II's visual analysis described in Section 3.5.2, these low frequency peaks are not selected because their scatterings (uncertainties) are large and they are near the limits of the frequency range of the HVSR plot.

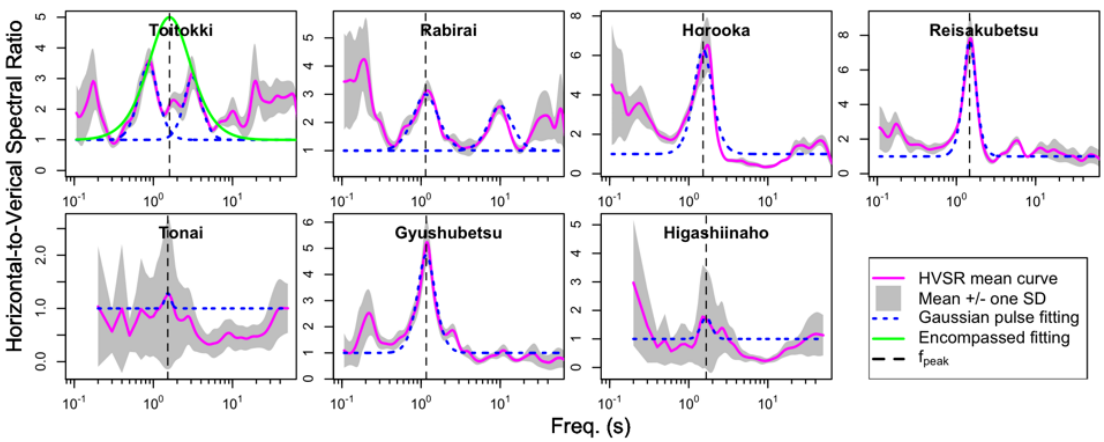

Figure 7.5: HVSR vs frequency plots for ODCD sites as established from microtremor or pre-event noise data, and fitted pulse with identified peak frequencies.

7.3 Ground motion data analysis

This section presents the analyses of ground motion recordings to support model development. I first describe the analysis of residuals and the main data trends. Next I evaluate event-specific biases and regional (between-island) complexities in path. The intent of those analyses is to provide region-adjusted, within-event residuals for each event and recording at the seven ODCD sites. Finally, I evaluate non-ergodic site responses for each site.

7.3.1 Residuals analysis and trends

The approach to data analysis operates on residuals, which are the difference between the natural log of an observation and its prediction from a GMM (the same approach as presented in Section 5.1). "Observation" in this case is a computed $RotD_{50}$ intensity measure from an earthquake under consideration; as shown in Table 7.2, the analyses consider all recordings that meet data selection criteria (not just those in the study region). The GMMs applied in these analyses are Zea, which is specifically intended for use with Japan subduction earthquakes, and Aea applied with Japan-regionalized path correction terms. Two GMMs are used to investigate sensitivity of derived site terms to the alternate reference GMMs. The

maximum rupture distances recommended for use with these GMMs are 300 km. I consider data at distances beyond these limits, although measures are taken to minimize path biases at large distances.

Total residuals are computed using the reference GMMs as:

$$R_{ij} = \ln(Y_{ij}) - (\mu_{\ln Y})_{ij} \tag{7.1}$$

where Y_{ij} is an observed RotD_{50} intensity measure for site j from event i, and $(\mu_{\ln Y})_{ij}$ is the natural log mean prediction from the alternate GMMs given event magnitude, site-source distance, site condition, and other parameters used in the models. Non-zero residuals have many potentially causative factors. An event can produce ground motions systematically low or high relative to the GMM. Likewise, a source-to-site path may be associated with attenuation rates that are relatively fast or slow in comparison to the model. Our goal ultimately is for the residuals to be used to analyze site response. As a result, if the residuals include systematic effects related to source or path, our ability to infer site response is compromised. This problem is addressed in the analysis by removing, to the extent justified by the data, systematic (repeatable) source and path effects from total residuals. The remainder of this section describes how these adjustments were made.

Figure 7.6 plots total residuals vs distance for four events and at four periods (0.005, 0.08, 0.8, 5.0 sec) from the Zea GMM (qualitatively similar results are obtained for other events and from the Aea GMM; results provided in Figure 7.7 - 7.8). The figure is organized by event location; Part (a) applies to events off the coast of Hokkaido, Part (b) to Honshu. Important attributes of the data to consider in Figure 7.6 are (1) the slope of the data relative to distance and (2) offsets in residuals between islands or different attenuation rates for ground motions recorded on the two islands.

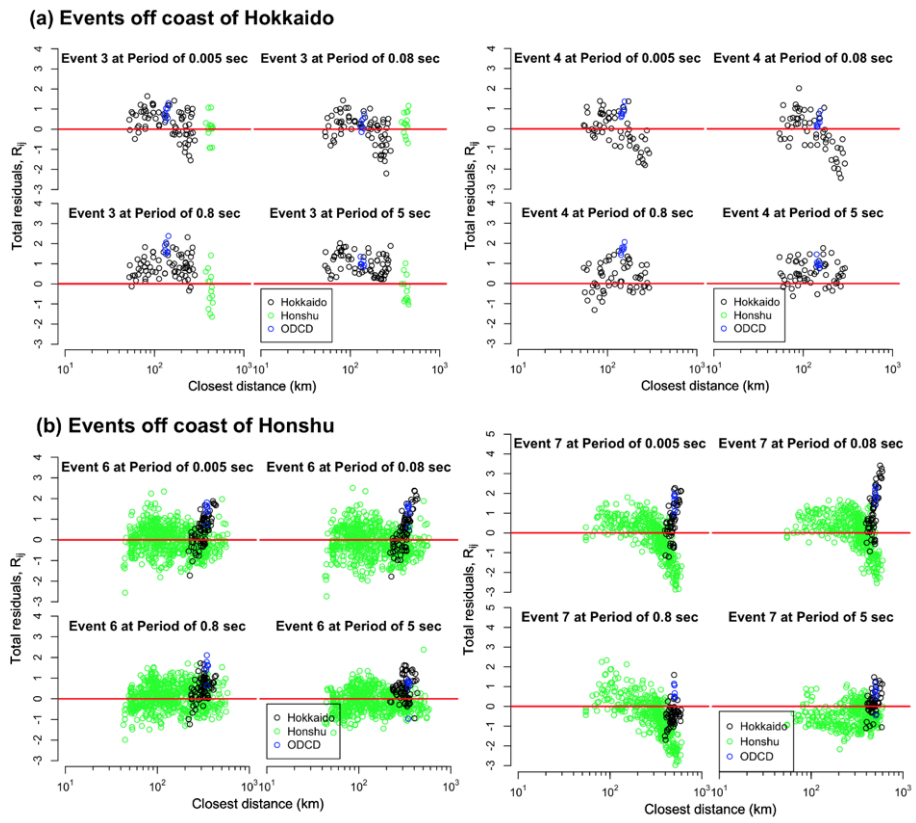

Figure 7.6: Variation of Zea total residuals with distance for four events at periods 0.005, 0.08, 0.8, and 5 s.

Based on Figure 7.6 - 7.8, I find:

- A flat slope of residuals for a particular island indicates an unbiased GMM path term, whereas a gradient indicates path term bias. Events 3, 4, and 7 exhibit gradients in short-period (0.005 and 0.08 s) residuals from recordings on the event-adjacent island, specifically a downward trend for Hokkaido stations beyond 200 km (Events 3 and 4) and Honshu stations beyond 200-300 km (Event 7). Event 6 data lacks downward-gradient features, which is also the case for other events (Figure 7.7 - 7.8).

- The data show diverging trends for Hokkaido and Honshu stations beyond about 300 km. This suggests the presence of between-island regional attenuation effects not captured by the GMMs.

I considered adjusting the GMM to correct these problems, but ultimately elected to limit the maximum considered distances for these events to 200 km (Events 3 and 4) and 300 km (Event 7). Within these distances, residuals for event-adjacent islands are nearly flat. For the other considered events where residual gradients did not occur, the maximum considered distance was taken as R_{max}.

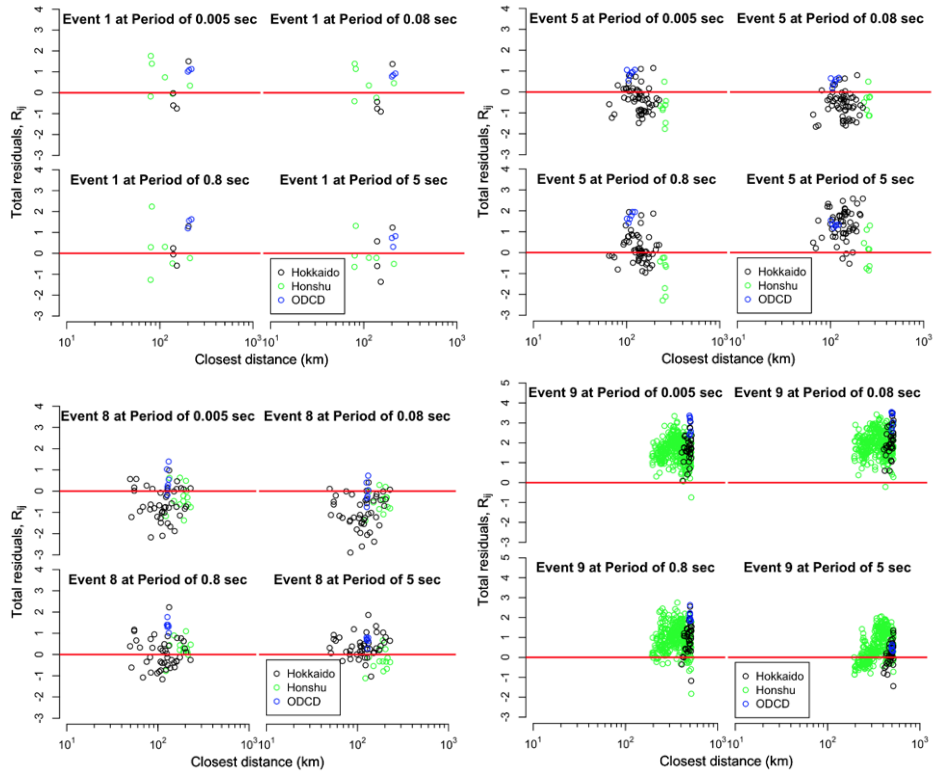

Figure 7.7: Variation of Zea total residuals with distance for the other four events at periods 0.005, 0.08, 0.8, and 5 s.

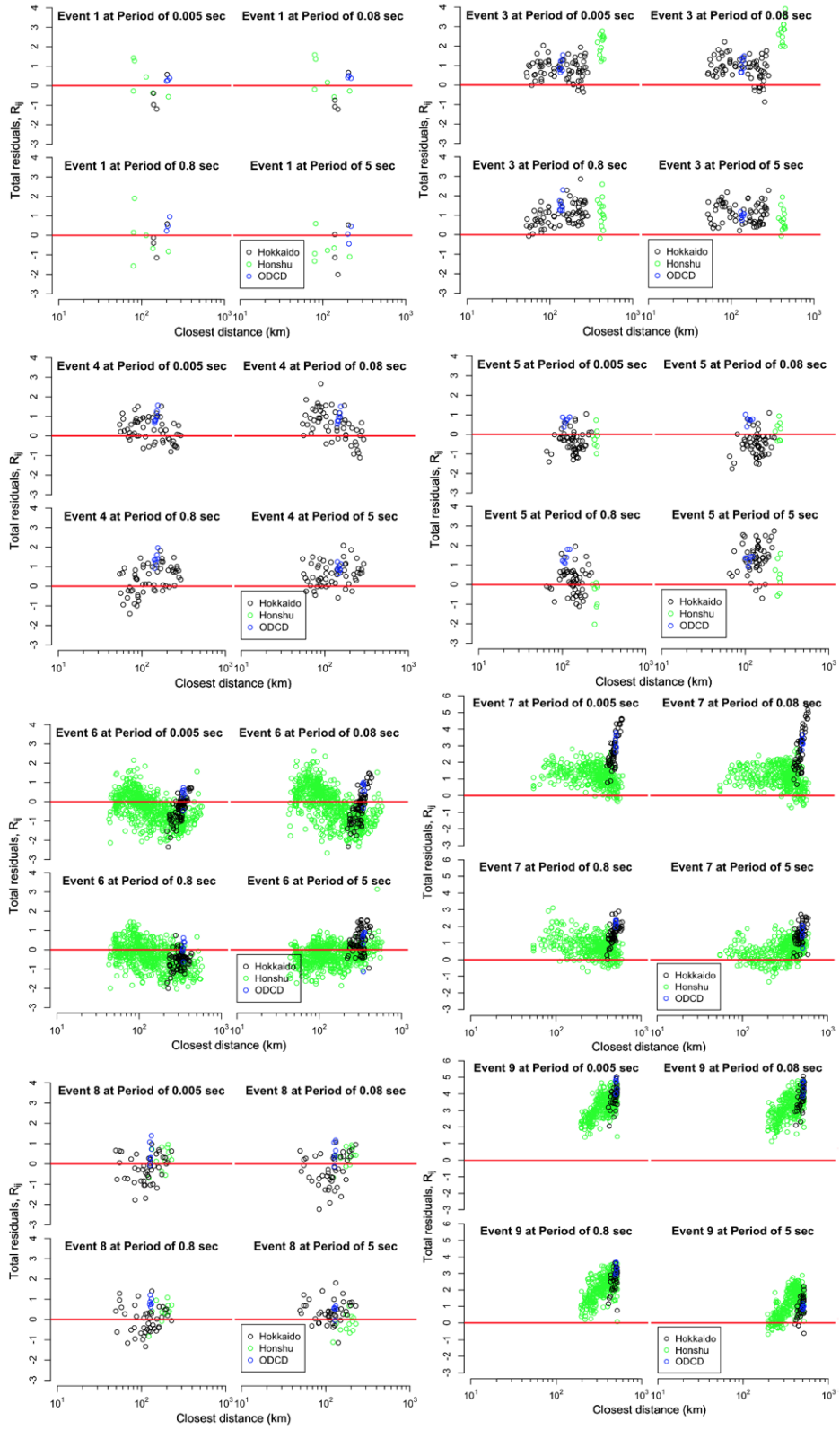

Figure 7.8: Variation of Aea total residuals with distance for all eight events at periods 0.005, 0.08, 0.8, and 5 s.

7.3.2 Event terms

The vertical offset from zero of the total residuals in Figure 7.6 - 7.8 is an event attribute referred to as an event term. I take the event term for a given event i as the average of the residuals from stations within the range of applicability of the selected GMM:

$$\eta_{E,i} = \frac{1}{n_i} \sum_{j=1}^{n_i} R_{ij} \tag{7.2}$$

where n_i is the number of recordings available for event i. Note that the use of Equation 7.2 implies the lack of an overall bias (across all events) in the GMM, which if present would be a constant term added to the left side of Equation 7.2. As described above, stations in the backarc and with site-to-source distances beyond maximum limiting distance of NGA-Subduction data are excluded. Data are also excluded beyond the aforementioned limiting distances for Events 3, 4, and 7.

Event terms obtained from Equation 7.2 are shown in Figure 7.9. Positive and negative event terms indicate under- and over-prediction, respectively, and both conditions are encountered. The event terms for Event 9 are very large – values above 1.5 for periods less than about 0.3 sec.

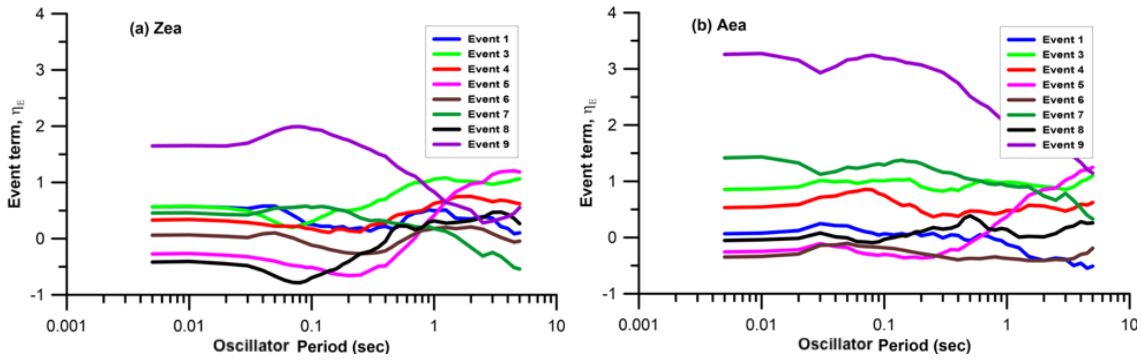

Figure 7.9: Event Terms (PSA) for the eight events recorded in the ODCD array from Zea GMM (left) and Aea GMM (right)

7.3.3 Regional (between-island) terms

Japan is known to have strong regional variations in anelastic attenuation (e.g., [46]). These effects, if not included in a GMM, can introduce large differences in residuals for recordings on opposite sides of the volcanic front (i.e., forearc vs backarc sites), and potentially for recordings on different islands. The effects of paths crossing the volcanic front was addressed in our analysis by screening out backarc data. Additional regional complexities in the forearc, where encountered (Events 3, 4, 7) were addressed with application of distance cutoffs. The remaining issue considered here is potential effects of source-to-site paths passing between islands, specifically Honshu to Hokkaido and vice-versa. To investigate this, I first compute within-event residuals as

$$\delta W_{ij} = R_{ij} - \eta_{E,i} \tag{7.3}$$

Next, I plot δW_{ij} with binned means and $\pm$ one standard derivations vs distance for Honshu and Hokkaido stations using data from all events. As shown in Figure 7.10, there are divergences of within-event residuals for these data groups for distances beyond about 300 km, particularly at short periods. Because these divergences are a path issue, they should be corrected to the extent practical prior the analysis of site terms. Accordingly, I separate sources as Hokkaido-adjacent (denoted North; latitude $>$ 39 degrees) and Honshu-adjacent (denoted South; latitude $<$ 39 degrees), and sites by location (Hokkaido or Honshu). The North events are 1, 3, 4, 5, and 8, and the South events are 6, 7, and 9. This categorization of events and sites facilitates analysis of between-island terms that correct ground motions when an earthquake occurs in one region (e.g., South) and a subset of the recordings are in the other region (e.g., North).

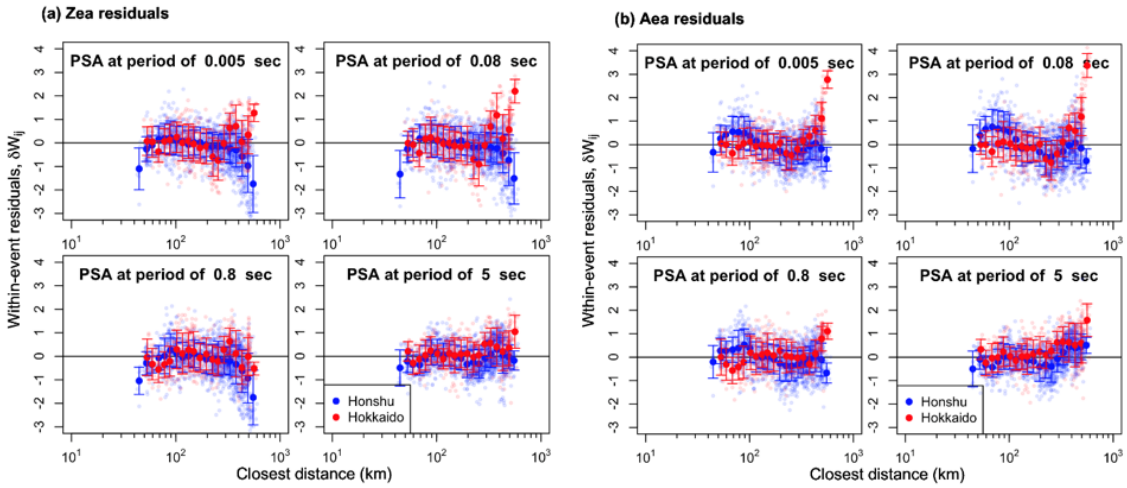

Figure 7.10: Event-corrected within-event residuals for eight events, separated by region, derived using the (left) Zea GMM and (right) Aea GMM.

Region terms are computed for each combination of event and station regions as the average of within-event residuals,

$$\eta_{lk}^{reg} = \frac{1}{n_{lk}} \sum_{\forall i \in l, \forall j \in k} \delta W_{ij} \tag{7.4}$$

where the $\forall$ symbol in combination with $\in$ (e.g., $\forall i \in l$) indicates 'for any value of i among the set specified by array l', which is used to parse the data into source-site groups. As before, i is the event index and j is the site index. I take $l \in \{0, 1\}$ (i.e., l can be 0 or 1) to segregate event regions (0 refers to South Events and 1 refers to North Events) and $k \in \{0, 1\}$ to segregate station regions (0 refers to Honshu and 1 refers to Hokkaido). Figure 7.11 plots region terms over the period range 0.08 sec to 5 sec with their 95% confidence intervals for each source-site regional combination.

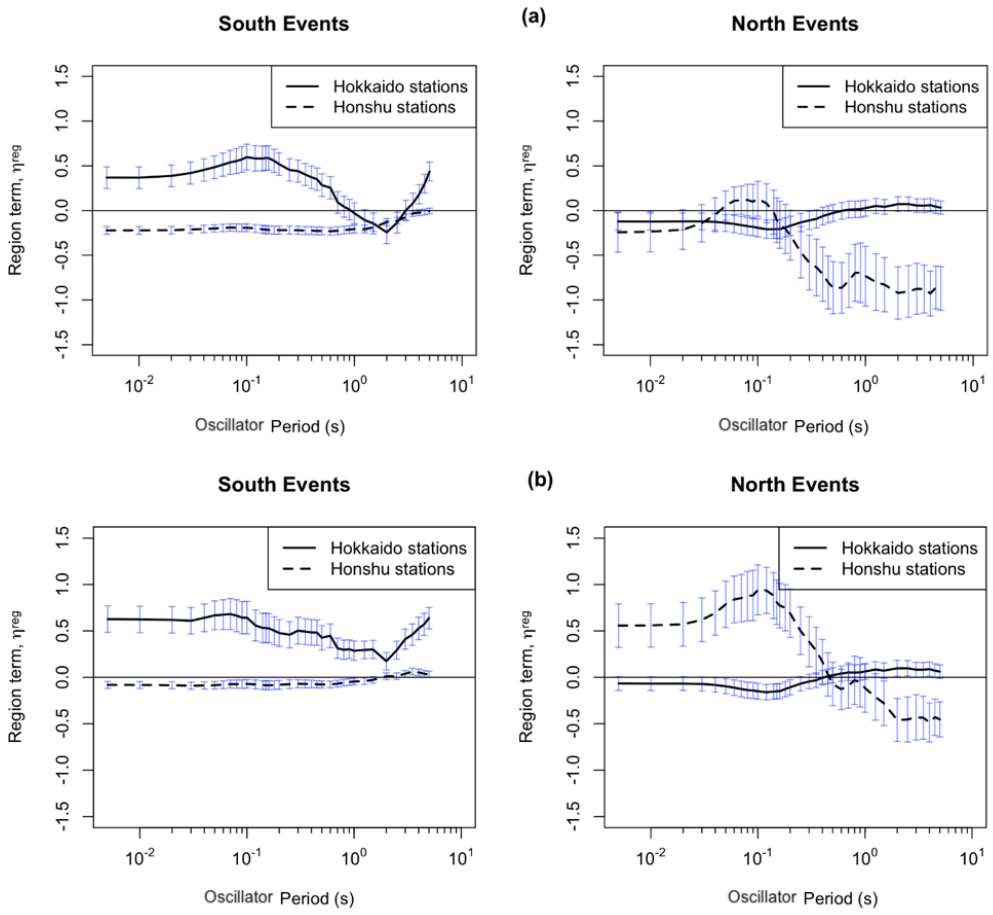

Figure 7.11: Region terms for Hokkaido and Honshu stations from South and North regional events, as derived from (a) Zea GMM and (b) Aea GMM.

The results in Figure 7.11 show that for common source-station regions, such as South events and Honshu stations (index $l = 0$ and $k = 0$), region terms of both models are relatively small (less than 0.2) and have little trend with period. However, when the indices differ, there are large biases. The large positive region terms at short periods ($<\sim 1$ sec) for South events and Hokkaido stations are consistent with the corresponding upward (positive) trends of residuals in Figure 7.10. There is a large negative bias at long periods for North events and Honshu stations from both GMMs, whereas the Aea GMM also has a large positive bias at short periods for this combination.

Because this between-island effect is a new finding, before incorporating these regional effects into our analyses, I tested the statistical significance of the distinctions between data

groups by applying the statistical F test ([34]). This test examines whether a data set is better described by a combined single model or a set of sub-models. The combined model in this case would be to not consider regional terms, whereas the sub-models include the four regional combinations. I compute the F statistic as:

$$F = \frac{(RSS_f - \sum_{l=0}^{1}\sum_{k=0}^{1} RSS_{l,k})/(\sum_{l=0}^{1}\sum_{k=0}^{1} m_{l,k} - m_f)}{\hat{\sigma}^2} \tag{7.5}$$

where RSS stands for residuals sum of squares, $RSS_{l,k}$ represents the residuals sum of squares of the sub-model for the l event region and k station region, and m refers to the number of fitted parameters in the full model and sub-models. Since the 'models' are simple means, $m = 1$ in each case (for combined model and each individual sub-model). As a point of clarification regarding notation, m is not referred to as a degree of freedom in the statistics literature, although that term has been used in some engineering applications ([77, 94]). I adopt here the statistics terminology.

The denominator is expressed by,

$$\hat{\sigma}^2 = \frac{\sum_{l=0}^{1}\sum_{k=0}^{1} RSS_{l,k}}{\sum_{l=0}^{1}\sum_{k=0}^{1}(N_{l,k} - m_{l,k})} = \frac{\sum_{l=0}^{1}\sum_{k=0}^{1} RSS_{l,k}}{\sum_{l=0}^{1}\sum_{k=0}^{1} df_{l,k}} \tag{7.6}$$

where $N_{l,k}$ is the number of recordings for the data belonging to source group l and station group k, $m_{l,k}$ is the number of fitted parameters for that sub-model, and $df_{l,k} = N_{l,k} - m_{l,k}$ is the degree of freedom for that sub-model. The degree of freedom of the full (combined) model is $df_f = N - m_f = \sum_{l=0}^{1}\sum_{k=0}^{1} N_{l,k} - m_f$. In this case, sums in Equation 7.5 - 7.6 unrelated to RSS are $(\sum_{l=0}^{1}\sum_{k=0}^{1} m_{l,k} - m_f) = df_f - \sum_{l=0}^{1}\sum_{k=0}^{1} df_{l,k} = 3$ and $\sum_{l=0}^{1}\sum_{k=0}^{1} df_{l,k} = 1802$.

This F statistic can be compared to the F distribution to evaluate a significance level (p) for the test. Large values of p (i.e., > 0.05) are taken to indicate that the sub-models are not distinct. Table 7.3 shows for four periods the results of F testing for the case of one overall combined model in comparison to four sub-models. The F statistic, the minimum value of the F statistic for $p = 0.05$, and the significance level are provided. In each case, the testing indicates that the sub-models are distinct, meaning that the use of regional terms is justified.

Table 7.3: F-test for significance of region effects for both sources and sites. Underlined results apply to the Zea GMM, results in parenthesis apply to the Aea GMM, and results without special markings apply to both.

		Full Model f	**Submodels** $l = \{0, 1\}$ $k = \{0, 1\}$	**F-statistics**	**F-critical$_{3,1802}$ value at significance level p = 0.05**	**p-value**
T = 0.005s	*RSS*	<u>1162.80</u> (976.16)	<u>1066.56</u> (880.98)	<u>54.20</u> (64.89)	2.61	0
	df	1805	1802			
T = 0.08s	*RSS*	<u>1197.04</u> (1369.93)	<u>1083.47</u> (1245.25)	<u>62.96</u> (60.14)		0
	df	1805	1802			
T = 0.80s	*RSS*	<u>1175.42</u> (821.11)	<u>1092.85</u> (799.82)	<u>45.38</u> (15.99)		0
	df	1805	1802			
T = 5.00s	*RSS*	<u>703.74</u> (800.22)	<u>637.34</u> (714.40)	<u>62.58</u> (72.15)		0
	df	1805	1802			

Note the numbers 3 and 1802 at the subscripts of F-critical$_{3,1802}$ are the *df* of the numerator and denominator F statistics in Equation 7.5.

I also consider two additional F tests to examine the difference between Honshu and Hokkaido recordings, considering only data from source region (i.e., only South event data in one set of tests, and only North event data in a second set of tests). In this case, the F-statistic is computed as:

$$F_l = \frac{(RSS_l - \sum_{k=0}^{1} RSS_{l,k})/(\sum_{k=0}^{1} m_{l,k} - m_l)}{\hat{\sigma}_l^2} \tag{7.7}$$

where l is either 0 or 1, and the denominator is,

$$\hat{\sigma}_l^2 = \frac{\sum_{k=0}^{1} RSS_{l,k}}{\sum_{k=0}^{1}(N_{l,k} - m_{l,k})} = \frac{\sum_{k=0}^{1} RSS_{l.k}}{\sum_{k=0}^{1} df_{l,k}} \tag{7.8}$$

The combined model for these tests groups Honshu and Hokkaido recordings for a given

event group l=0 or 1, and RSS_l represents the RSS for that combined model. The results of two F-tests for l=0 (South Event) and l=1 (North Event) are given in Table 7.4. In most cases, the testing confirms that the separation of regions for each event group is justified, although there are exceptions. These exceptions occur at periods where the regional terms in Figure 7.11 are nearly zero (e.g., T = 0.005s for North events of Zea GMM, where the p-value is 0.35; or T = 0.8s for North events of Aea GMM, where the p-value is 0.48).

To incorporate the between-island regional terms into residuals analyses, I adjust the within-event residuals from Equation 7.4 as follows:

$$\delta W_{ijlk}^{reg} = \delta W_{ij} - \eta_{lk}^{reg} \tag{7.9}$$

where δW_{ijlk}^{reg} is the region-adjusted within-event residual. Figure 7.12 shows the distance variation of δW_{ijlk}^{reg} (with binned means and ± one standard derivation bars) for all data (Figure 7.12(a)), North events only (Figure 7.12(b)) and South events only (Figure 7.12(c)). Figure 7.12 applies to the Zea model; the same plots are provided in Figure 7.13 for the Aea model. For each figure, results are shown separately for South (Honshu) stations in blue and North (Hokkaido) stations in red. For the present study, the most critical results are those for Hokkaido stations and both event types, particularly over the distance range applicable to the OCCD study region. The two vertical lines drawn in Figures 7.12(b)-(c) indicate the distance range of ODCD stations across all events in the respective groups (∼100-200 km for North events, ∼320-500 km for South events).

The results in Figure 7.12(a) can be compared to those in Figure 7.10 to see the effect of the regional terms on residuals trends – those trends are slightly reduced but not eliminated. While the residual trends for North events are generally flat (Figure 7.12(b)), the much better-recorded South events produce mixed results (Figure 7.12(c)). The Zea residuals are reasonably flat for Hokkaido stations in the distance range of interest. The Aea GMM (Figure 7.13(b)) produces an upward trend for some periods (0.08 sec) and a trends for other periods that is generally flat within the distance range, but trends upward at the upper limit of the range (approximate 500 km or greater). To address this, I apply a 450 km cutoff to the Aea model for the case of South events and Hokkaido recordings. No further adjustments to

Table 7.4: F-test for significance of region effects for both sources and sites. Underlined results apply to the Zea GMM, results in parenthesis apply to the Aea GMM, and results without special markings apply to both.

		South Event model $l = 0$	**Submodels** $l = 0$ $k = \{0, 1\}$	**F-statistics**	**F-critical**$_{1,1503}$ **significance level p = 0.05**	**p-value**
T = 0.005s	*RSS*	950.91 (846.95)	894.66 (765.70)	94.50 (159.48)	3.85	0
	df	1504	1503			
T = 0.08s	*RSS*	998.71 (1182.01)	909.06 (1094.03)	148.23 (120.86)		0
	df	1504	1503			
T = 0.80s	*RSS*	922.59 (674.12)	911.62 (653.85)	18.09 (46.59)		0
	df	1504	1503			
T = 5.00s	*RSS*	558.50 (671.92)	527.15 (612.48)	89.39 (145.86)		0
	df	1504	1503			
		North Event model $l = 1$	**Submodels** $l = 1$ $k = \{0, 1\}$	**F-statistics**	**F-critical**$_{1,299}$ **significance level p = 0.05**	**p-value**
T = 0.005s	*RSS*	172.41 (129.06)	171.90 (115.28)	0.88 (35.74)	3.87	0.35 (0)
	df	300	299			
T = 0.08s	*RSS*	177.46 (187.4)	174.41 (151.21)	5.22 (71.73)		0.02 (0)
	df	300	299			
T = 0.80s	*RSS*	199.03 (146.22)	181.23 (145.97)	29.36 (0.50)		0 (0.48)
	df	300	299			
T = 5.00s	*RSS*	139.12 (111.31)	110.19 (101.92)	78.51 (27.53)		0 (0)
	df	300	299			

the Zea and Aea path models are applied for the analysis of site terms.

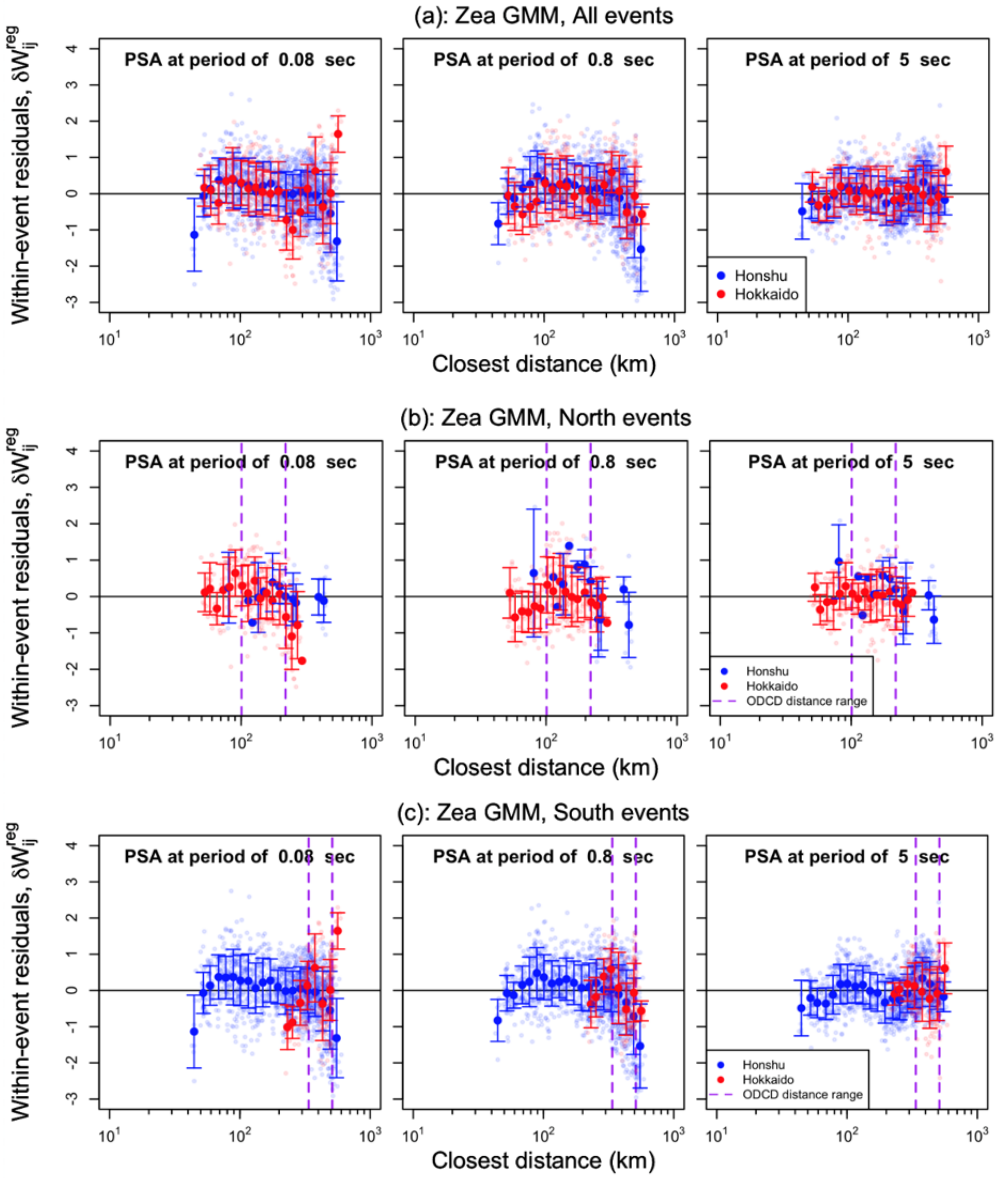

Figure 7.12: Trend of region-corrected within-event residuals with closest distance at periods of 0.08, 0.8, and 5 sec for (a) all data; (b) North events only; (c) South events only. Distance range of ODCD stations marked.

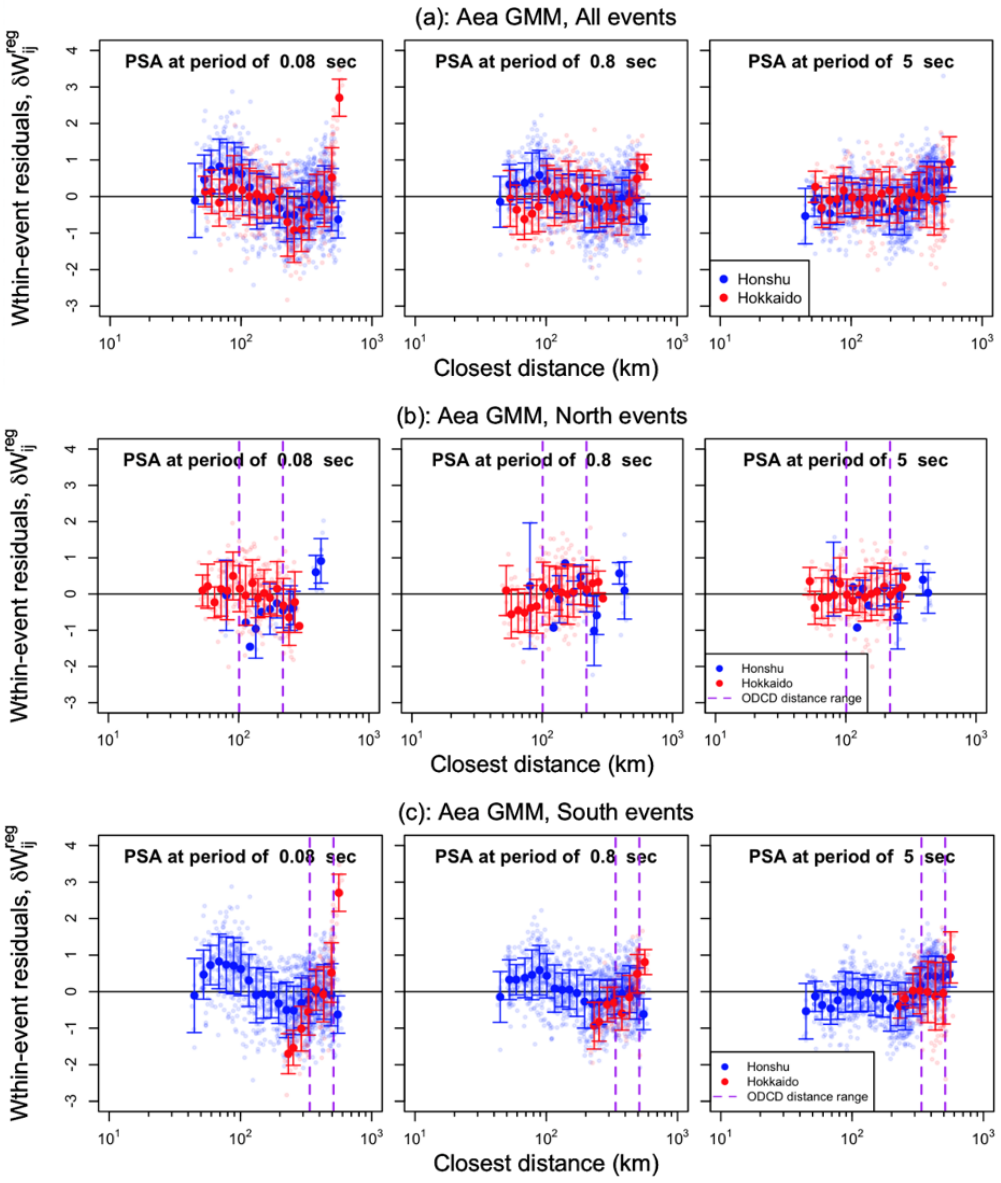

Figure 7.13: Trend of region-corrected within-event residuals with closest distance at periods of 0.08, 0.8, and 5 sec from Aea GMM for (a) all data; (b) North events only; (c) South events only. Distance range of ODCD stations marked.

7.3.4 Site terms

By adjusting residuals for event biases, $\eta_{E,i}$ and regional biases, η_{lk}^{reg}, the remaining region-adjusted within-event residual, δW_{ijlk}^{reg}, represents errors in the prediction of observed intensity measures from the GMM that can be attributed to the combination of systematic site

effects at each station and relatively random, event-to-event path errors. If the path errors are indeed random, they would average to zero when summed over many observations. With this in mind, I estimate the effect of site response, also called the site term, $\eta_{S,j}$, at site j as follows

$$\eta_{S,j} = \frac{1}{n_j} \sum_{i=1}^{n_j} \delta W_{ijlk}^{reg} \tag{7.10}$$

where n_j is the number of recordings for station j. As with the event term computation, this represents a frequentist interpretation of the problem statistics.

The site response model assumed to apply for a given intensity measure at a given site is taken as ([92]):

$$F_S = f_1 + f_2 \ln\left(\frac{x_{\mathrm{IM}ref} + f_3}{f_3}\right) \tag{7.11}$$

where F_S is site amplification in natural log units, $x_{\mathrm{IM}ref}$ represents the amplitude of shaking for a reference site condition (generally rock) for a particular earthquake at a particular site (expressed as an intensity measure), f_1 is the coefficient representing linear site response, f_2 represents the slope (generally negative) in amplification-ln($x_{\mathrm{IM}ref}$) space for $x_{\mathrm{IM}ref} >> f_3$, and f_3 represents a transitional value of the reference site intensity measure below which the site response is nearly linear, and above which the trend of amplification with $x_{\mathrm{IM}ref}$ is nearly linear in log-log space.

The site term in Equation 7.10 represents the misfit between the observed site response and the site response predicted by the ergodic model in the GMM. If the observations are primarily from weak ground motions that do not introduce a significant nonlinear response, the only site response coefficient from Equation 7.11 that can be evaluated empirically is f_1, which is taken as

$$(f_1)_j = \eta_{S,j} + F_{S,j} \tag{7.12}$$

where $F_{S,j}$ is the ergodic site response as evaluated from the selected model.

Figure 7.14 shows for each of the seven sites the region-adjusted within-event residuals δW_{ijlk}^{reg} and site terms (top) and the total site response (bottom) computed as in Equation 7.12, using the Zea GMM. Each of the sites exhibits a peak at a specific natural period. For example, at the Toitokki site (dark blue), the first peak site response occurs at a period

of about 0.5 sec, and the amplification at that period is approximately $e^{2.8} \approx 16.4$. This very high site amplification is likely associated with resonance and impedance effects from the soft upper peat layers relative to deeper, stiffer sediments. A somewhat surprising feature of this dataset is the similarity of the observed site responses across the seven sites. While some details change, for each site the amplification peaks between 0.5-0.9 sec, has a peak width of about one log cycle of period, a minimum amplification near 0.1 s, and a gradual increase in amplification towards PGA. As such, the Tokachi River setting provides a nearly ideal setting for the development of a regional site response model.

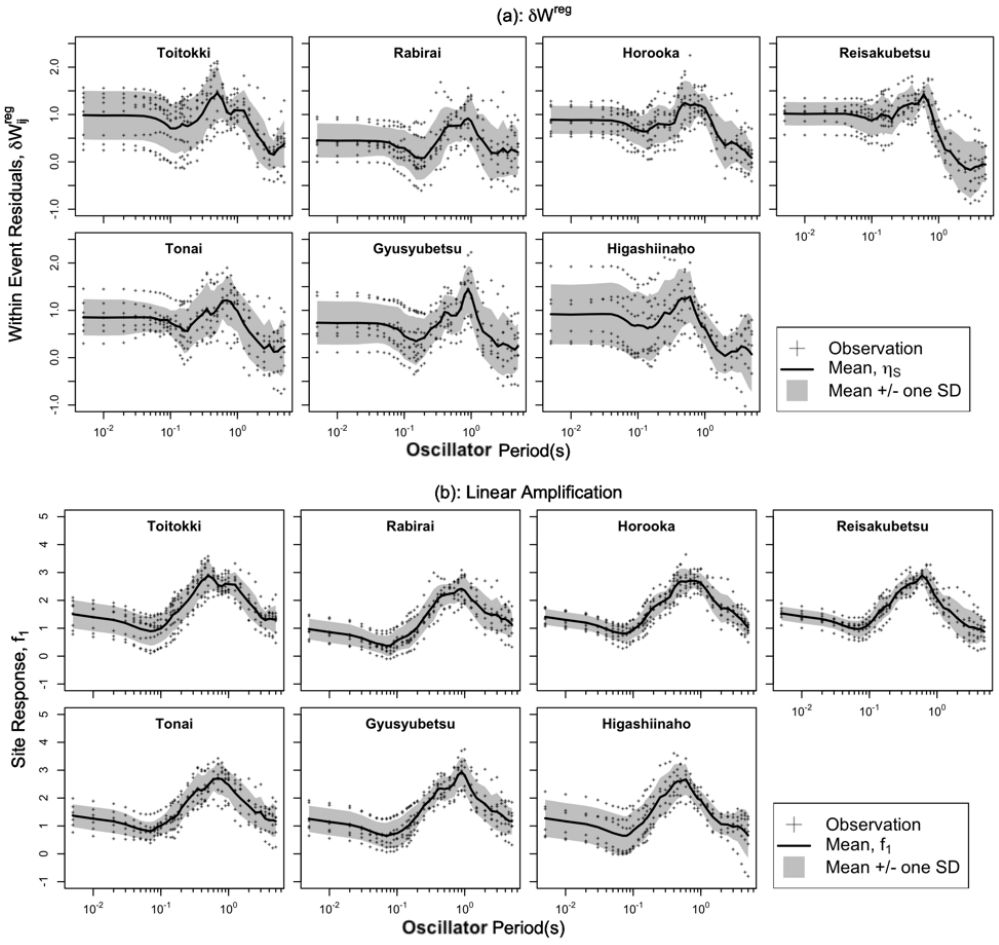

Figure 7.14: Region-adjusted within event residuals (a) and estimated site responses (b) for the seven Obihiro stations as derived from Zea GMM.

Figure 7.15 compares linear site response terms (f_1) for each site as derived from the

two reference GMMs. This comparison shows that despite the different source and path models in the reference GMMs, the derived site responses are quite similar. Because the site responses derived from the two models are consistent, either could be used for subsequent model development. I utilize results from the Zea GMM for this purpose.

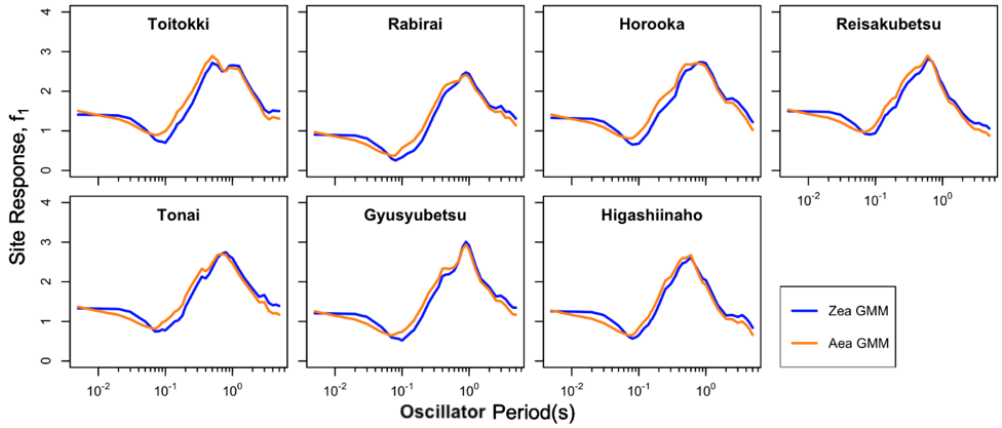

Figure 7.15: Comparison of site-specific linear site responses as derived using the Zea and Aea GMMs

7.4 Site amplification model development

In this section, I develop a site amplification function that takes site frequency as derived from microtremor-based HVSR (f_{peak}) as input to capture the observed site amplification in an average sense across the seven sites and which presumably would have general applicability across the study region shown in Figure 7.2. I also develop an alternative model in which the only site information is that it is located on peat in the general study region, but f_{peak} is unknown.

7.4.1 Site parameters

Because the peaty organic soil sites in the study region exhibit site amplification effects suggestive of a resonant ground response effect at a site frequency, I sought to use HVSR to estimate the frequency of the peak response (f_{peak}). The concept is to use f_{peak} as a site

parameter to be used in the regional ergodic model. It is desirable that the process used to estimate f_{peak} be independent of the ground motions, which can be best accomplished by measuring f_{peak} from microtremors. Before going forward, a point of clarification on notation – frequency f_p as used in the site amplification model (next subsection) is the fitted oscillator frequency of the peak site response, which is not an independent variable (it is derived from ground motions, hence it is not independent of those motions). There are two reasons why f_p and f_{peak} may not match: (1) one corresponds to oscillator frequency (f_p) and the other to frequency as used in Fourier analysis (f_{peak}) and (2) even when Fourier representations of site response are used, site response peaks may not match HVSR peaks. Regarding point (1), some prior models have taken the oscillator peak as 80% of the HVSR peak ([56]). Point (2) has been investigated in prior research, which has shown that f_{peak} is consistent with the frequencies of peak site response for many, but not all, soil sites ([14, 47, 25, 54, 65, 74, 75, 96]). In this study, f_p is allowed to deviate from f_{peak}; differences are set by the data, as described below.

7.4.2 Mean amplification

In order to capture the peaked shape of site amplification observed at the Obihiro sites, I selected a Mexican hat wavelet function[1]. This function is intended to capture site resonance effects that dominate amplification shapes at short to intermediate periods (T $<$ 2 sec). A linear decay function is used at longer periods (T $>$ 2 sec). The recommended site amplification function for linear conditions is as follows,

$$f_1(T, t_0) = \begin{cases} c_0 + \frac{2c_1}{\sqrt{3c_2}\pi^{1/4}}\left(1 - \left(\frac{\ln(Tf_p)}{c_2}\right)^2\right)e^{-\frac{1}{2}\left(\frac{\ln(Tf_p)}{c_2}\right)^2}, & T \leq T_{tr} \\ c_3 \ln\left(\frac{T}{T_{tr}}\right) + f_1(T_{tr}, f_p), & T > T_{tr} \end{cases} \tag{7.13}$$

where c_0 controls the overall level of site amplification, c_1 scales the amplitude of the hat function, c_2 describes the width of the PSA peak in natural log period space, $T_{tr} = 2$ sec is the transition period between the Mexican hat and linear functions, and c_3 describes the

[1] https://en.wikipedia.org/wiki/Mexican_hat_wavelet

linear decay of amplification with log period beyond T_{tr}. Frequency f_p is the frequency of the peak in the Mexican hat fitting function. A similar function was used by [55].

I performed a least squares fit of Equation 7.13 to the observed amplification for each of the seven sites, with the results in Figure 7.16 and Table 7.5. The p-values indicate that all coefficients are statistically significant except for c_3, which is not statistically distinct from zero. Nonetheless, I retain non-zero c_3 to improve fits at long periods.

Table 7.5: Coefficients for Mexican hat model parameters for each site

Station Name	Gyushubetsu	Higashiinaho	Horooka	Reisakubetsu	Rabirai	Toitokki	Tonai
c_0	1.519	1.016	1.435	1.534	1.403	1.289	1.268
Standard error	0.155	0.151	0.155	0.160	0.156	0.149	0.156
p-value	0	0	0	0	0	0	0
c_1	1.724	1.838	1.729	1.496	1.635	1.846	1.597
Standard error	0.345	0.343	0.347	0.337	0.344	0.337	0.329
p-value	0	0	0	0	0	0	0
c_2	1.362	1.398	1.387	1.202	1.355	1.358	1.162
Standard error	0.227	0.243	0.239	0.206	0.244	0.224	0.186
p-value	0	0	0	0	0	0	0
c_3	-0.647	-0.400	-0.756	-0.474	-0.613	-0.717	-0.210
Standard error	0.693	0.720	0.697	0.598	0.688	0.709	0.604
p-value	0.351	0.578	0.278	0.428	0.373	0.312	0.728
f_p (Hz)	1.550	1.319	1.480	2.062	1.530	1.343	2.008
Standard error	0.269	0.245	0.267	0.305	0.274	0.230	0.273
p-value	0	0	0	0	0	0	0

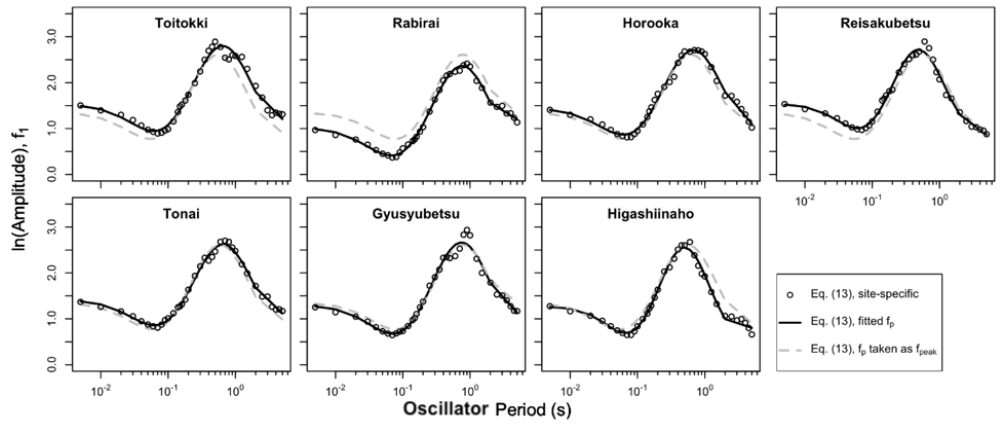

Figure 7.16: Fit of model to observed amplification when model coefficients are taken from site-specific optimization.

To develop the model for sites other than the seven stations in the study region, I examined the relationship between f_p and f_{peak} as shown in Figure 7.17. Confidence intervals on the best fit line (shown in the figure) encompass the 45 degree line and the intercept term is effectively null. I take $1.13 f_{\text{peak}}$ as the estimator of f_p for use in the Mexican hat function. All other coefficients are taken as constant across all sites. The other coefficients were obtained by minimizing the sum of square of errors after specifying f_p as above, with the resulting values in Table 7.6 in the row labelled "Model using f_p from f_{peak}". The resulting model predictions are compared to data and optimal fit of model to observed amplification for the seven Obihiro sites in Figure 7.17. The results are generally good, although some loss of fidelity occurs relative to the site specific (non-ergodic) fits and optimal fit of model shown in Figure 7.17.

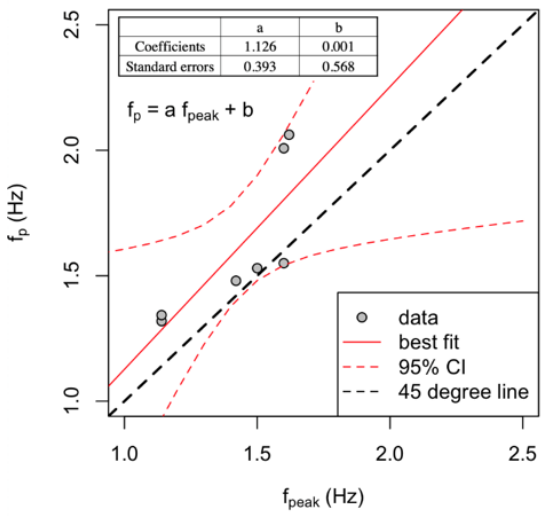

Figure 7.17: Relationship between HVSR peak frequency (f_{peak}) and peak in Mexican hat fitting function of site response (f_p). Note that f_p corresponds to a peak frequency for oscillator response.

Table 7.6: Coefficients for Mexican hat model parameterse

Model	c_0	c_1	c_2	c_3
Model using f_p from f_{peak}	1.34 ± 0.06	1.70 ± 0.13	1.34 ± 0.08	-0.55 ± 0.20
Model using $f_p = 1.60$ Hz ± 0.10 **(population mean)**	1.35 ± 0.06	1.67 ± 0.13	1.33 ± 0.09	-0.53 ± 0.26

I also develop a model for the case in which f_{peak} is unknown. In this case, I regress Equation 7.13 to the combined data set for all sites to obtain a new set of coefficients as shown in Table 7.6 in the row labelled "Model using $f_p = 1.60$ Hz ± 0.10 (population mean)"; this value of f_p was regressed as part of the model development, and represents a regional average site frequency. By combining all sites, the pulse width is slightly decreased and linear decay rate at long periods is slightly increased. The regional average curve is plotted relative to the observed amplification levels at all Obihiro sites in Figure 7.18.

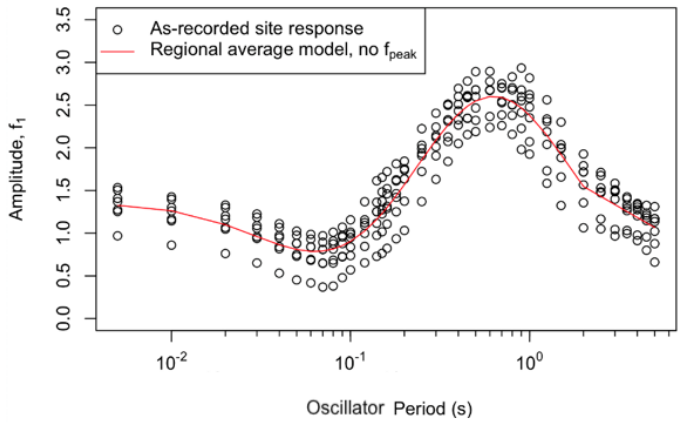

Figure 7.18: Fit of model to observed amplification when model coefficients are taken from regional average model.

7.4.3 Aleatory variability model and model bias

The standard deviation terms to use with the proposed site amplification model are τ for between-event variability and ϕ for within-event variability. The τ model is assumed to be unaffected by the site amplification model described here, and can be taken from GMMs. The ϕ model can be taken from the standard deviation of the within-event residuals obtained through the use of the Zea GMM or Aea GMM in combination with the proposed site amplification models. To develop this within-event standard deviation model, I compute residuals as in Equation 7.2, but now using the region-specific site amplification model in lieu of the Zea site term. After subtracting event terms (Equation 7.3) and regional terms (Equation 7.9), I then partition the within-event residuals as:

$$\delta W_{ij}^{reg} = c + \eta'_{S,j} + \epsilon_{ij} \tag{7.14}$$

where c is the model bias, $\eta'_{S,j}$ is the site term at site j obtained through the use of the modified GMM (the prime $\prime$ differentiates this site term from that in Equation 7.10) and ϵ_{ij} is the remaining residual. The model bias indicates the overall model misfit relative to the data (equivalent to the average of all δW_{ij}^{reg}). The standard deviation of $\eta'_{S,j}$ is denoted the site-to-site dispersion (ϕ_{S2S}) while the standard deviation of ϵ_{ij} is the single-station within-event dispersion (ϕ_{SS}).

These standard deviations are shown in Figure 7.19 for both the model employing regional average parameters and site-specific f_{peak} values. Figure 7.19(a) shows that ϕ_{S2S} is approximately 0.2 for both of the proposed models, which is significantly below average values for the entirety of Japan (from [8]). This is expected because of the relatively uniform geotechnical conditions in the study region. Figure 7.19(b) shows single-station standard deviations (ϕ_{SS}), which are similar to the Japan average values obtained previously from Kik-net data by [82]. The ϕ_{SS} values in Figure 7.19(b) are practically unaffected by using alternate regional site response models.

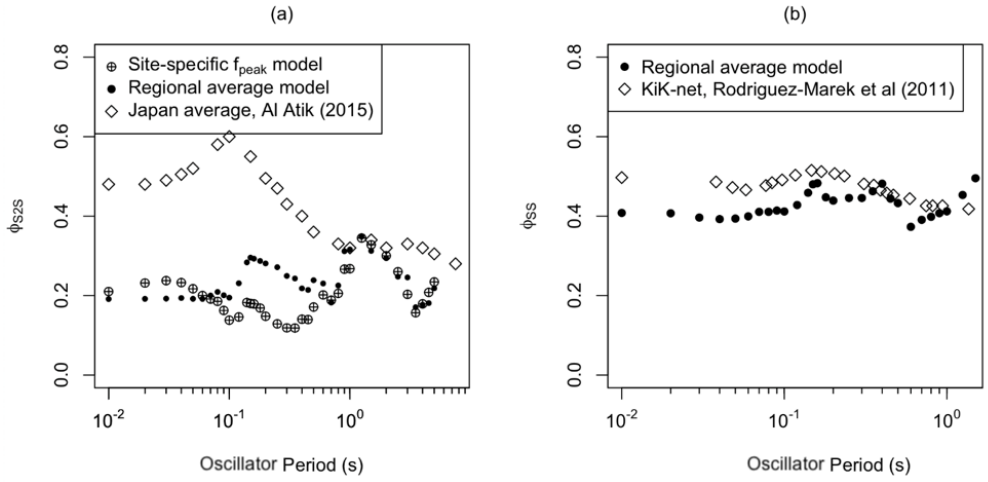

Figure 7.19: Comparison of within-event standard deviation terms from Obihiro stations (this study) and Japan averages: (a) site-to-site standard deviations as compared to Japan-average from [8]; (b) single-station standard deviation as compared to Japan-average from [82].

Figure 7.20 compares the model bias for the regional average and site specific models, both of which are effectively zero. Also shown for comparative purposes is the bias obtained using the site term in the Zea GMM, which is very large (indicating underprediction). The substantial bias of the GMM for the Obihiro sites demonstrates the need for site-specific site factors for these peaty organic soils.

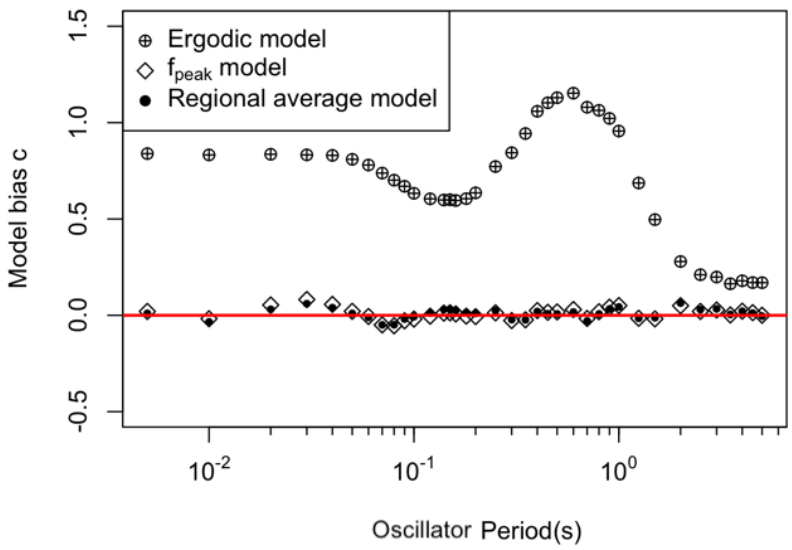

Figure 7.20: Comparison of model bias for the ergodic model of Zea GMM and the Zea GMM combined with the two proposed region-specific site amplification models.

7.4.4 Nonlinearity

The previously developed models for mean site response (Equation 7.13, Figure 7.16) are based on relatively weak ground motions from 8 events, and hence provide linear site amplification. To investigate nonlinear effects, I examine model misfits relative to the data from Event 10 (the 2003 Tokachi-Oki Earthquake), which produces significantly stronger ground motions than the other considered events at the ODCD stations (Figure 7.3).

The analysis of Event 10 follows the process used for other events. Equation 7.1 is used to compute total residuals, and Equation 7.2 is used to compute the event terms ($\eta_{E,10}$). Figure 7.21 compares the event terms for Event 10 to the other events considered. In the case of ODCD stations, the GMM used for residuals calculation is modified from the published version,

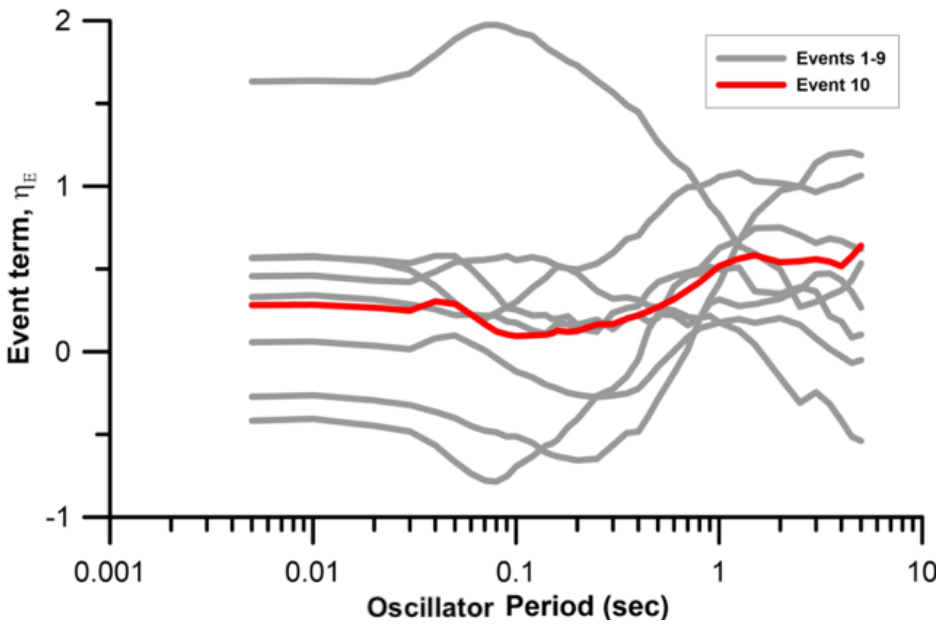

Figure 7.21: Event term for Event 10 compared to those for Events 1-9.

Region-adjusted within event residuals are computed using Equation 7.9. Figure 7.22 plots $\delta W_{reg,ij}$ for Event 10 along with those for the other events, using ODCD stations only. The residuals are plotted as a function of PGA_r, which is the median peak acceleration for the reference site condition from the Zea GMM for Site Class 2. If the site response from the various events recorded at the ODCD sites is effectively linear, then no trend in $\delta W_{reg,ij}$ would be expected with PGA_r. This is effectively the case for the Events 1-9 data for each of the intensity measures considered in Figure 7.22, with the possible exception of a small upward trend for 5.0 sec PSA. The Event 10 data, however, indicate PGA_r dependencies that are downward at short periods and upward at 5.0 sec

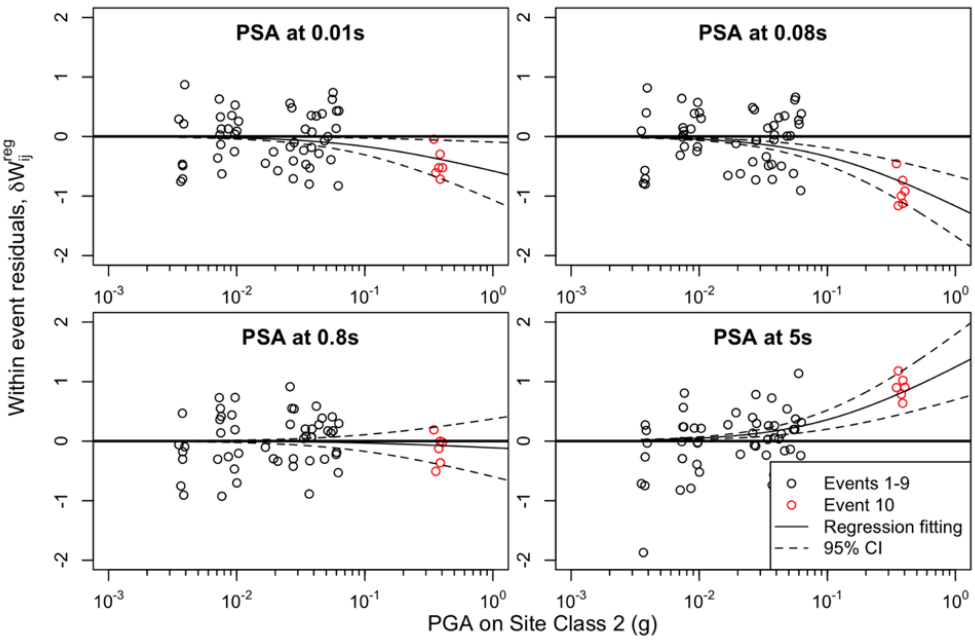

Figure 7.22: Region adjusted within event residuals for data recorded at ODCD stations versus reference site PGA_r (Site Class 2).

The trends of the results in Figure 7.22 are fit by regression using the relation in Equation 7.11 with $f_1 = 0$ (the setting of f_1 to zero is because of its inclusion in the model used for residuals analysis; Equation 7.16) and $f_3 = 0.1g$ (a typical value). As a result, only parameter f_2 is set by regression. Nonlinearity is evident from curvature in the fit line, and is quantified by $f_2 \neq 0$. The downward curvature at short periods is expected, and results from increased damping in sediments as strains increase. The upward trend at long periods is also fairly common. This typically occurs because nonlinearity softens the soil, increasing its fundamental period. Because the elastic (small strain) period is in the range of 1-2 sec, this softening will bring the soil deposits to resonance at longer periods, which would be reflected by increased long period PSA as indicated by the trend line. Furthermore, a prior study ([100]) on the 2004 Niigata Chuetsu-Oki earthquake also showed the reduced nonlinearity and they claimed that this is likely a property of the peat (more linear than inorganic soils). Figure 7.23 plots f_2 with period for application in Obihiro, along with recommended values for this parameter from [88] (a semi-empirical model for active tectonic regions, exercised

using the regional geometric mean V_{S30} of 150 m/s). The Obihiro data has generally the same pattern with period as the ergodic model, but with reduced nonlinearity, and positive values of f_2 at long periods.

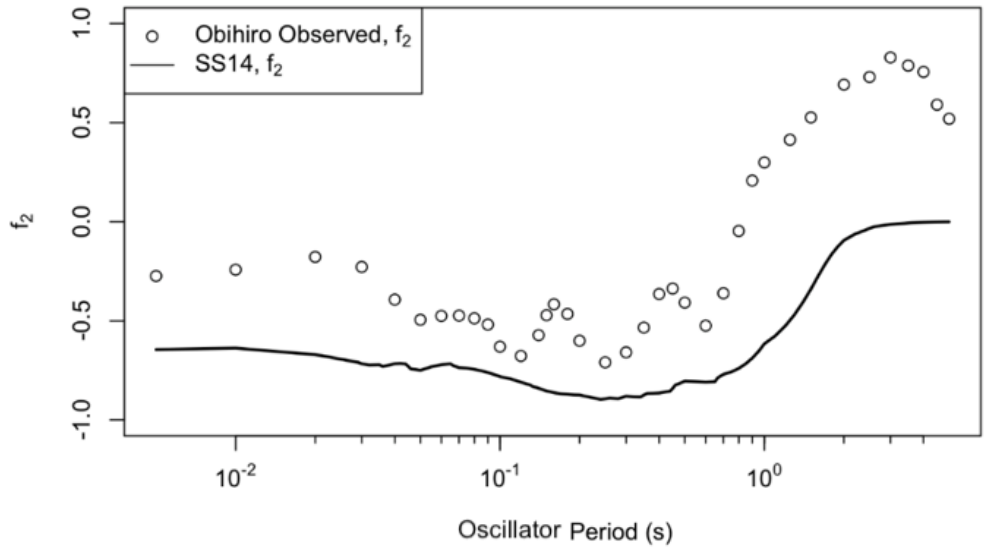

Figure 7.23: Nonlinear term f_2 as function of period as regresses from Obihiro data and from ergodic model for active regions (applied for $V_{S30} = 150m/s$)

7.5 Conclusions

Ground motion models generally include site terms intended for application over a range of $V_{S30} \approx 200$ to 1500 m/s. These model limits naturally lead to questions of how to capture site response effects for sites with conditions that fall outside of this range. I address this question for a very soft soil region (Ohibiro) in Hokkaido Japan underlain by peaty organic soils and other, non-organic, recent sediments. The range of V_{S30} in the study region is 100-210 m/s (geometric mean 150 m/s).

I evaluate non-ergodic site responses at seven Obihiro sites using data from nine earthquakes. This analysis required removing regional biases in path effects identified for conditions when ground motions propagate between islands (e.g., event is off the coast of Honshu and ground motions are recorded on Hokkaido). After correcting for these effects, and ap-

plying standard event term adjustment, site responses for the seven sites are found to have common characteristics, which include strong site resonances at periods of 0.5-0.9 sec that are associated with resonances of the soft and weak surficial soils in the region relative to stiffer underlying soils.

The recommended site response model consists of a modified Mexican Hat wavelet function (Equation 7.3), the most important parameter of which is a peak frequency f_p that is estimated from peaks of microtremor-based HVSR (f_{peak}) as $f_p = 1.13 f_{\text{peak}}$. The model can be applied without a site-specific measurement of f_{peak} by using a regional average of $f_p = 1.6$ Hz. Using data for an event that produces strong shaking, I derive an approximate nonlinear model, which has broadly similar characteristics to an ergodic model for active regions. Application of the regional model substantially reduces site-to-site aleatory variability from a general model from Japan (e.g., 0.48 to 0.20 for PGA).

The regional model for mean site response and within-event standard deviation are applicable to the Obihiro region along the Tokachi River, Japan, as shown in Figure 7.2. The model is based on data from seven sites, and could be in error for sites in the study region if they contain peat deposits of significantly different character or thickness. While the model is unlikely to be directly applicable to other regions, the modeling approach outlined herein can be applied to other regions with unusual geologic conditions that may substantially impact site response.

CHAPTER 8

Summary and Conclusions

8.1 Scope

In this research I study site response effects on earthquake ground motions. My approach is to analyze strong motion data to evaluate non-ergodic site response, and then evaluate the performance of predictive models (using data from California) or develop a predictive model (using data from Obihiro, Japan).

My work on data from California is presented in Chapters 2 - 6 of this dissertation, I augment the NGA-West2 ground motion database ([9]) with data from relatively recent events, and combine this data with profiles from the Shear Wave Velocity Profile Database ([5]) to compute observation-based site response at ground motion recording stations and then investigate the degree to which it can be estimated using alternate prediction approaches. To conduct the study, I began by converting the NGA-West2 data tables to a relational database format, and then supplemented that data with recordings from 25 earthquakes since late 2011 in California. Based on this expanded database, I identified 159 sites that have ample recordings (at least 10 events with $\mathbf{M} \geq 4$) and an on-site measured V_S profile (with at least 30 meters depth) for use in analysis. I developed protocols for assigning soil parameters when borehole data is limited (including unit weight, geotechnical damping, κ-informed damping, and $Q - V_S$ damping). I then conducted site-specific site response analyses and used a method that combines an ergodic V_{S30}-based site response with adjustments conditioned on parameters derived from horizontal-to-vertical spectral ratios (HVSR). I present and interpret results for individual sites and synthesize results for the full inventory of sites to investigate the predictability of site response with GRA, SRI, and HVSR mod-

els, and to investigate epistemic uncertainties associated with the application of all three site-specific site response methods.

The analysis of site response and model development for soft peaty organic soil sites in Obihiro Japan is presented in Chapter 7. I first established a dataset for the study region from national ground motion database for Japanese networks along with local data for peaty organic soils in Obihiro. I then analyzed non-ergodic site responses using data from 10 subduction zone earthquakes. Two subduction ground motion models were applied as reference models to investigate sensitivity of inferred site responses to the reference GMM. Inferred site responses were used to develop region-specific site amplification models with and without the availability of a site-specific site parameter, f_{peak}.

8.2 Summary of major findings

The first part of this research using the California data had the broad objective of investigating the effectiveness of ground response analysis, and other methods of site response analysis, through comparisons to observed site response as established from analysis of recordings. I describe and illustrate the application of a new approach using non-ergodic site responses derived from surface-only instruments as the basis for validation studies. Effectiveness of predictive models is judged, in this context, through bias and site-to-site uncertainty of predicted site response.

The technical contributions of the ground motion analysis work fall into two general categories. First, several procedural matters had to be developed to implement the work, and second, the results provide new and valuable insights into the effectiveness of site-specific site response analysis methods and their associated epistemic uncertainties.

Significant original procedural elements include the following:

1. I have developed procedures to implement ground response analyses and square-root impedance methods given limited available site information (i.e., no boring logs). As described in Chapter 4, I considered two types of available information to assign layer

boundaries (stratigraphy) and soil type information – the mapped surface geology and the V_S profile. Surface geology is used to estimate soil type near the ground surface. The V_S profile is used in combination with the surface unit assignment to estimate variations with depth.

2. I implemented a κ-informed damping model to leverage ground motion observations from sites as a means to constrain soil material damping. The procedure involves analysis of κ for each recording at a site, followed by subtraction of path κ derived on a record-specific basis given spatially variable path κ coefficients developed in this study. The result is a site κ, which provides a basis for adjustment of soil damping.

3. I developed new procedures for HVSR processing and developed a code implementing these procedures in R. New criteria for peak identification and Gaussian peak fitting were developed. Furthermore, I have proposed a new categorization method based on peaks in HVSR to classify sites.

4. I proposed new metrics to quantify goodness-of-fit for site response predictions relative to observations. I proposed and applied a normalized version of Fréchet distance to supplement mean correlation coefficient. I demonstrated that this metric is effective at identifying sites with and without "good" data to model fits.

5. I proposed "inverse transfer function method" (ITF) to deconvolve surface records to estimate input motions for a reference soil layer for use in GRA (Section 4.2.4). I demonstrated that GRA would over-estimate site amplification if the surface records had been used.

The insights into the effectiveness of site-specific site response analysis methods and their associated epistemic uncertainties can be summarized as:

1. Despite the depth of the profiles considered in this work being relatively small (30 to 255 m; site period ranging from 0.06 to 1.02 sec), ground response analyses (or square-root-impedance analyses) are able to improve site response predictions relative

to ergodic models (reduce normalized Fréchet distance within soil column period) for approximately 36% of sites.

2. The inability of site-specific ground response methods (GRA and SRI) to improve prediction accuracy for the 64% sites could stem from three potential sources: (1) simulations of one-dimension wave propagation do not accurately characterize the physics of site response; (2) the measured V_S profile from the site does not accurately represent site conditions, either because of strong site heterogeneity or inaccurate measurements; (3) portions of the site profile beneath the profile depth significantly impact the site response in the frequency range of the measured profile.

3. The three problems identified in (2) above are common to some extent in virtually all site response simulations, so understanding their collective impact is of practical importance. The unknown influence of these factors in forward applications that do not have the benefit of on-site recordings introduces epistemic uncertainties, which I quantify. Lacking any knowledge of whether a given site is well represented with one-dimensional simulations, this epistemic uncertainty is only slightly reduced from the site-to-site variability in ergodic models. However, for the subset of sites whether this modeling is effective, the epistemic uncertainty is substantially reduced by up to 0.10 in natural log unit (from 0.4 to 0.3 at 0.06 sec).

4. Given the significant differences in epistemic uncertainties for sites with unknown vs. known applicability of one-dimensional methods as an effective means of representing site response, the ability to identify this condition a priori is of substantial practical importance. I investigated five potential predictors of ground response analysis effectiveness, most of which represent impedance effects in different ways. Contrary to prior work using a much more limited dataset from vertical arrays, I find that ranges of these parameters indicating high impedance conditions provide for more effective site response predictability, with arguably the velocity of the base layer (V_{Sb}) having the strongest predictive power. These features were not observable with single-period residuals, but were visible with the Fréchet distance parameter.

5. Damping models informed by site-specific κ perform better than alternative models, as indicated by reduced bias relative to alternative damping models for all sites. However, there are over-estimation of damping from this method for some sites, as discussed in Section 6.6.

6. Ground response analysis is more effective at minimizing epistemic uncertainty than square-root impedance methods although there is some sensitivity to damping models.

7. When divided into groups with HVSR-based clear peaks, no peaks, and ambiguous peaks, observed site responses have different levels of site response complexity and site-to-site variability. The site response for no-peak sites is relatively "simple" (smooth variations of amplification with oscillator period) and can be well predicted by a simple, period-independent adjustment of an ergodic model. For the clear peak and ambiguous peak categories, the more complex site response features are only partially captured by an existing HVSR-based model that was developed for conditions in Japan.

8. As measured by dispersion reduction relative to an ergodic model, HVSR models are ineffective at short periods ($T <\sim 0.6$ sec) but are effective at longer periods ($T >\sim 1.0$ sec). The reason for the different model effectiveness for different period ranges is not well understood.

9. For sites with peaked HVSR signatures and peaked site response, the HVSR peaks occur at slightly lower frequencies than the oscillator frequency of the peak site response. Site response amplitudes are lower on average.

10. The performance of the HVSR model for clear peak and ambiguous peak sites was strongly influenced by false positives (peaks identified from HVSR that are not present in site response) and wrong detected peak locations. Moreover, for about 2/3 of the sites with peaks in both HVSR and site response, the peak frequencies are reasonably aligned (within a factor of 2), whereas for 1/3 the peaks are misaligned. These challenges reduce the effectiveness of HVSR-based modeling in this study.

In the second part of research, the major research findings can be summarized as,

1. A region-specific linear site amplification model with and without site parameter, f_{peak}, for peaty organic soil sites in Hokkaido was developed.

2. There are complexities in path effect when subduction events occur adjacent to one island (e.g., Honshu) and are recorded on a separate island (e.g., Hokkaido). These effects are not amenable to modeling with an anelastic coefficient, and are captured here with a constant shift.

3. As observed by other investigators, I find that Japan has strong regional variations in anelastic attenuation within both islands.

8.3 Future work

Because this study has demonstrated a new means by which to evaluate site response and use it for model validation purposes, the potential future implementations for other data sets are nearly limitless. Additional future work that would benefit calculations of the type performed here include:

1. The only available Subduction models at the time when Obihiro study was conducted were Aea and Zea models. As multiple NGA-Subduction models (e.g., [78]) have been developed, I will re-analyze the data using the new models.

2. Further validate and improve methods developed in this study to assign soil parameters where the sites do not have boring logs. The initial validation was conducted by using nine sites that are part of this study. Further investigation using more sites is needed.

3. Through more comprehensive data analyses, refine spatial estimates of path κ.

4. Investigate alternative goodness of fit parameters, borrowing from the Fréchet distance concept, but considering an average distance instead of a peak value and considering alternate normalization strategies.

5. Improve peak identification algorithms to reduce the rate of false positives and false negatives, which significantly impacts model performance for site response prediction.

6. Develop a California-specific HVSR site response model.

Studies of the type performed here for California would benefit from improved site characterization. There has been a trend in recent years for site characterization to focus on the upper 30 m, but for site response studies of the type performed here, deeper characterization to firm rock layers is especially useful. These investigations should ideally include the development of stratigraphic logs that include detailed soil type descriptions.

APPENDIX A

Appendix

The supplements materials are archived on my Github site at: `https://github.com/wltcwpf/CSMIP-Report-Supplements`. The materials on the site include 1) a Google drive link to the site where it saves all the plots of HVSR from strong motion and noise data along indicators from Analyst I and II regarding the presence of a peaks; 2) plots of comparison between HVSR and non-ergodic site responses (named as "HVSR_SiteResponse_Comparison.pdf"); 3) plots of site responses with Gaussian fitting function (named as "SiteResponse_plots.pdf"); 4) plots of GRA, SRI, and HVSR site response models for all sites (named as ''Linear_Amplications_GRA.pdf", ''Linear_Amplications_SRI.pdf", and ''Linear_Amplications_HVSR.pdf", respectively); and 5) station table of 159 sites (named as "Station_Table.csv").

References

[1] Abrahamson, N., Kuehn, N., Gulerce, Z., Gregor, N., Bozorgnia, Y., Parker, G., Stewart, J.P., Chiou, B., Idriss, I.M., Campbell, K., Youngs, R. (2018). Update of the BC Hydro Subduction Ground-Motion Model using the NGA-Subduction Dataset. *Pacific Earthquake Engineering Research Center*. June. Volume 02.

[2] Abrahamson, N. A., Silva, W. J., and Kamai, R. (2014). Summary of the ASK14 ground motion relation for active crustal regions. *Earthquake Spectra*. **30**, pp 1025-1055.

[3] Afshari, K., Stewart, J.P. (2019). Insights from California Vertical Arrays on the Effectiveness of Ground Response Analysis with Alternative Damping Models. *Bulletin of the Seismological Society of America*. **109**, pp 1250-1264.

[4] Afshari, K, Stewart, J.P., Steidl, J.H. (2019). California ground motion vertical array database. *Earthquake Spectra*. **35**, pp 2003-2015.

[5] Ahdi, S.K., Sadiq, S., Ilhan, O., Bozorgnia, Y., Hashash, Y.M.A., Kwak, D.Y., Park, D., Yong, Y., and Stewart, J.P. (2018). Development of a United States Community Shear Wave Velocity Profile Database. *in Seismic Hazard Analysis, Earthquake Ground Motions, and Regional-Scale Assessment, Geotechnical Special Publication No. 291 of the Geo-Institute of the American Society of Civil Engineers, Selected Papers from Sessions of the 5th Conference on Geotechnical Earthquake Engineering and Soil Dynamics (GEESD-V)*. eds. S.J. Brandenberg and M.T. Manzari, Austin, TX, USA, 10-13 June 2018, 330-339.

[6] Ahdi, S. K., Stewart, J. P., Ancheta, T. D., Kwak, D. Y., Mitra, D., 2017. Development of V_S profile database and proxy-based models for V_{S30} prediction in the Pacific Northwest region of North America. *Bulletin of the Seismological Society of America*. **107**, pp 1781-1801.

[7] Al Atik, L., Abrahamson, N.A., Bommer, J.J., Scherbaum, F., Cotton, F., Kuehn, N. (2010). The variability of ground motion prediction models and its components. *Seismological Research Letters*. **81**, pp 794-801.

[8] Al Atik, L., (2015). NGA-East: Ground-Motion Standard Deviation Models for Central and Eastern North America. *Pacific Earthquake Engineering Research Center*. June, Volume 07.

[9] Ancheta, T. D., Darragh, R. B., Stewart, J. P., Seyhan E., Silva, W. J., Chiou, BS-J., Wooddell, K. E., Graves, R. W., Kottke, A. R., Boore, D. M., Kishida, T., and Donahue, J. L. (2014). NGA-West2 database. *Earthquake Spectra*. **30(3)**, pp 989-1005.

[10] Anderson, J. G. (1991). A preliminary descriptive model for the distance dependence of the spectral decay parameter in southern California. *Bulletin of the Seismological Society of America*. **81**, pp 2186-2193.

[11] Anderson, J.G. and Hough, S.E. (1984). A model for the shape of the fourier amplitude spectrum of acceleration at high frequencies. *Bulletin of the Seismological Society of America*. **74(5)**, pp 1969-1993.

[12] Bates D., Maechler, M., Bolker, B., Walker, S. (2015). Fitting Linear Mixed-Effects Models Using lme4. *Journal of Statistical Software*. **67**, pp 1-48.

[13] Bayless, J., and Abrahamson, N. A., (2019). Summary of the BA18 Ground-Motion Model for Fourier Amplitude Spectra for Crustal Earthquakes in California. *Bulletin of the Seismological Society of America*. **109(5)**, pp 2088-2105.

[14] Bonilla, L.F., Steidl, J. H., Gariel, J.-C., and Archuleta, R.J. (2002). Borehole response studies at the Garner Valley downhole array, Southern California. *Bulletin of the Seismological Society of America*. **92**, pp 3165-3179.

[15] Bonilla, L. F., Steidl, J. H., Lindley, G. T., Tumarkin, A. G., and Archuleta, R. J. (1997). Site amplification in the San Fernando Valley, California: Variability of site-effect estimation using the S-wave, coda, and H/V methods. *Bulletin of the Seismological Society of America*. **87**, pp 710-730.

[16] Boore, D.M. (2003a). Simulation of ground motion using the stochastic method. *Pure and Applied Geophysics*. **160**, pp 635-675.

[17] Boore, D.M. (2003b). A Compendium of P- And S-Wave Velocities from Surface-To-Borehole Logging: Summary and Reanalysis of Previously Published Data and Analysis of Unpublished Data. *U.S. Geological Survey Open-File Report 03-191*. 14 p.

[18] Boore, D.M. (2010). Orientation-independent, nongeometric-mean measures of seismic intensity from two horizontal components of motion. *Bulletin of the Seismological Society of America*. **100**, pp 1830-1835.

[19] Boore, D.M. (2013). The uses and limitations of the square-root- impedance method for computing site amplification. *Bulletin of the Seismological Society of America*. **103(4)**, pp 2356-2368.

[20] Boore, D. M., Bommer, J. J. (2005). Processing of strong-motion accelerograms: needs, options and consequences. *Soil Dynamics and Earthquake Engineering*. **25**, pp 93-115.

[21] Boore, D.M., Joyner, W.B. (1997). Site amplifications for generic rock sites. *Bulletin of the Seismological Society of America*. **87(2)**, pp 327-341.

[22] Boore, D. M., Stewart, J. P., Seyhan, E., Atkinson, G. M. (2014). NGA-West2 equations for predicting PGA, PGV, and 5% damped PSA for shallow crustal earthquakes. *Earthquake Spectra*. **30(3)**, pp 1057-1085.

[23] Bora, S.S., Scherbaum, F., Kuehn, N., and Stafford, P.J. (2016). On the relationship between Fourier and response spectra: Implications for the adjustment of empirical ground-motion prediction equations (GMPEs). *Bulletin of the Seismological Society of America*. **106(3)**, pp 1235-1253.

[24] Cabas, A., Rodriguez-Marek, A. and Bonilla, L.F. (2017). Estimation of site-specific Kappa (κ_0)-consistent damping values at KiK-net sites to assess the discrepancy between laboratory-based damping models and observed attenuation (of seismic waves) in the field. *Bulletin of the Seismological Society of America*. **107**, pp 2258-2271.

[25] Cadet, H., Bard, P.-Y., Duval, A.-M., and Bertrand, E. (2012). Site effect assessment using KiK-net data: Part 2-Site amplification prediction equation based on f0 and Vsz. *Bulletin of Earthquake Engineering*. **10**, pp 451-489.

[26] Campbell, K.W., (2009). Estimates of shear-wave Q and κ_0 for unconsolidated and semiconsolidated sediments in Eastern North America. *Bulletin of the Seismological Society of America*. **99**, pp 2365-2392.

[27] Campbell, K. W., and Bozorgnia, Y. (2014). NGA-West2 ground motion model for the average horizontal components of PGA, PGV, and 5 *Earthquake Spectra*. **30**, pp 1087-1115.

[28] Campbell, K.W., (2009). Estimates of shear-wave Q and ?0 for unconsolidated and semiconsolidated sediments in Eastern North America. *Bulletin of the Seismological Society of America*. **99**, pp 2365-2392.

[29] Chang, S.W. (1996). Seismic response of deep stiff soil deposits. *Ph.D. Thesis*. University of California, Berkeley.

[30] Chapman, M. C., Talwani, P., and Cannon, R. C. (2003). Ground-motion attenuation in the Atlantic Coastal Plain near Charleston, South Carolina. *Bulletin of the Seismological Society of America*. **93**, pp 998-1011.

[31] Chiou, B. S.-J., and Youngs, R. R. (2014). Update of the Chiou and Youngs NGA model for the average horizontal component of peak ground motion and response spectra. *Earthquake Spectra*. **30**, pp 1117-11153.

[32] Choi, W. K. (2008). Dynamic properties of ash-flow tuffs. *Ph.D. thesis*. Department of Civil Engineering, University of Texas, Austin, Texas.

[33] Contreras, V., Stewart, J. P., Kishida, T., Darragh, R. B., Chiou, B.S.J., Mazzoni, S., Kuehn, N., Adhi, S. K., Wooddell, K., Youngs, R. R., Bozorgnia, Y., Boroschek, R., Rojas, F., Órdenes, J., (2020). Chapter 4: Source and Path Metadata, in *Data Resources for NGA-Subduction Project, PEER Report 2020/02*. Pacific Earthquake Engineering Research Center, University of California, Berkeley, CA.

[34] Cook, R. D., and Weiberg, S. (1999). *Applied regression including computing and graphics*. Wiley & Sons, New York.

[35] Cox, B.R. and Beekman, A.N. (2011). Intramethod variability in ReMi dispersion measurements and VS estimates at shallow bedrock sites. *Journal of Geotechnical and Geoenvironmental Engineering*. **137(4)**, pp 354-362.

[36] Darendeli, M.B., (2001). Development of a new family of normalized modulus reduction and material damping curves. *Ph.D. Thesis*. Department of Civil Engineering, University of Texas, Austin, TX.

[37] Di Alessandro, C., Bonilla, L. F., Boore, D. M., Rovelli, A., and Scotti, O. (2012). Predominant-period site classification for response spectra prediction equations in Italy. *Bulletin of the Seismological Society of America*. **102**, pp 680-695.

[38] Dickenson, S.E. (1994). The dynamic response of soft and deep cohesive soils during the Loma Prieta earthquake of October 17, 1989. *Ph.D. Thesis*. University of California, Berkeley.

[39] Eberhart-Phillips, D. (2016). Northern California seismic attenuation: 3D Q_P and Q_S models. *Bulletin of the Seismological Society of America*. **106**, pp 2558-2573.

[40] Field, E. H., and Jacob, K. H. (1993). The theoretical response of sedimentary layers to ambient seismic noise. *Geophysical Research Letters*. **20**, pp 2925-2928.

[41] Fumal, T.E. and Tinsley, J.C. (1985). Mapping shear wave velocities of near surface geologic materials. *U.S. Geological Survey*. Professional Paper 1360.

[42] Fumal, T.E., Gibbs, J.F., and Roth, E.F. (1982). In-situ measurements of seismic velocity at 22 locations in the Los Angeles, California region. *U.S. Geological Survey Open-File Report 82-833*. 138 pp. Data reprocessed by Boore, D.M. (2003b).

[43] Gibbs, J.F., Boore, D.M., Tinsley, J.C., and Mueller, C.S. (2001). Borehole P- and S-wave velocity at thirteen stations in southern California. *U.S. Geological Survey Open-File Report 01-506*. 117 pp. Data reprocessed by Boore, D.M. (2003b).

[44] Gibbs, J.F., Tinsley, J.C., Boore, D.M., and Joyner, W.B. (1999). Seismic velocities and geological conditions at twelve sites subjected to strong ground motion in the 1994 Northridge, California, earthquake: A revision of OFR 96-740. *U.S. Geological Survey Open-File Report 99-446*. 142 pp. Data reprocessed by Boore, D.M. (2003b).

[45] Gibbs, J.F., Tinsley, J.C., Boore, D.M., and Joyner, W.B. (2000). Borehole velocity measurements and geological conditions at thirteen sites in the Los

Angeles, California region. *U.S. Geological Survey Open-File Report 00-470*. 118 pp. Data reprocessed by Boore, D.M. (2003b).

[46] Ghofrani, H., Atkinson, G., (2011). Forearc versus backarc attenuation of earthquake ground motion. *Bulletin of the Seismological Society of America*. **101(6)**, pp 3032-3045.

[47] Ghofrani, H., Atkinson, G.M., and Goda, K. (2013). Implications of the 2011 M 9.0 Tohoku Japan earthquake for the treatment of site effects in large earthquakes. *Bulletin of Earthquake Engineering*. **11**, pp 171-203.

[48] Ghofrani, H., Atkinson, G. M., (2014). Site condition evaluation using horizontal-to-vertical response spectral ratios of earthquakes in the NGA-West 2 and Japanese databases. *Soil Dynamics and Earthquake Engineering*. **67**, pp 30-43.

[49] Goulet, C. A., Kottke, A., Boore, D. M., Bozorgnia, Y., Hollenback, J., Kishida, T., Der Kiureghian, A., Ktenidou, O. J., Kuehn, N. M., Rathje, E. M., et al. (2018). Effective amplitude spectrum (EAS) as a metric for ground motion modeling using Fourier amplitudes. 2018 Seismology of the Americas Meeting, Miami, Florida. 14-17 May 2018.

[50] Hashash, Y.M.A., Musgrove, M.I., Harmon, J.A., Groholski, D.R., Phillips, C.A., and Park, D. (2016). DEEPSOIL 6.1, User Manual. Urbana, IL, Board of Trustees of University of Illinois at Urbana-Champaign.

[51] Hassani, B., Atkinson, G. M. (2016). Applicability of the site fundamental frequency as a V_{S30} proxy for Central and Eastern North America. *Bulletin of the Seismological Society of America*. **106(2)**, pp 653-664.

[52] Hassani, B., Atkinson, G. M. (2018a). Site-effects model for Central and Eastern North America based on peak frequency and average shear-wave velocity. *Bulletin of the Seismological Society of America*. **108(1)**, pp 338-350.

[53] Hassani, B., Atkinson, G. M. (2018b). Application of a site-effects model based on peak frequency and average shear-wave velocity to California. *Bulletin of the Seismological Society of America*. **108(1)**, pp 351-357.

[54] Hassani, B., Yong, A., Atkinson, G. M., Feng, T., and Meng, L. (2019). Comparison of site dominant frequency from earthquake and microseismic data in California. *Bulletin of the Seismological Society of America*. **109(3)**, pp 1034-1040.

[55] Harmon, J, Hashash, Y.M.A., Stewart, J.P., Rathje, E.M., Campbell, K.W., Silva, W.J., Xu, B., Musgrove, M., Ilhan, O. (2019a). Site amplification functions for central and eastern North America - Part I: Simulation dataset development. *Earthquake Spectra*. **35**, pp 787-814.

[56] Harmon, J, Hashash, Y.M.A., Stewart, J.P., Rathj, E.M., Campbell, K.W., Silva, W.J., Ilhan, O. (2019b). Site amplification functions for central and eastern North America - Part II: Modular simulation-based models. *Earthquake Spectra*. **35**, pp 815-847.

[57] Hauksson, E., and Shearer, P. (2006). Attenuation models (Q_P and Q_S) in three dimensions of the southern California crust: Inferred fluidsaturation at seismogenic depths. *Journal of Geophysical Research*. **111**, pp B05302.

[58] Hough, S.E., and Anderson, J.G. (1988). High-frequency spectra observed at Anza, California: Implications of Q structure. *Bulletin of the Seismological Society of America*. **78**, pp 692-707.

[59] Idriss, I.M. (1993). Assessment of site response analysis procedures. Report to National Institute of Standards and Technology, Gaithersburg, Maryland, Department of Civil and Environmental Engineering, University of California, Davis.

[60] Idriss, I.M., (2011). Use of Vs30 to represent local site conditions. *The 4th LASPEI/IAEE International Symposium Effects of Surface Geology on Strong Ground Motions, Santa Barbara, CA*.

[61] Joyner, W.B., Warrick, R.E., Fumal, T.E. (1981). The effect of Quaternary alluvium on strong ground motion in the Coyote Lake, California, earthquake of 1979. *Bulletin of the Seismological Society of America*. **71(4)**, pp 1333-1349.

[62] Kaklamanos, J., Bradley, B.A., (2018). Challenges in predicting seismic site response with 1D analyses: Conclusions from 114 KiK?net vertical seismometer arrays. *Bulletin of the Seismological Society of America*. **108**, pp 2816-2838.

[63] Kaklamanos, J., Bradley, B.A., Thompson, E.M., Baise, L.G.. (2013). Critical parameters affecting bias and variability in site-response analyses using KiK-net downhole array data. *Bulletin of the Seismological Society of America*. **103**, pp 1733-1749.

[64] Kawase, H., Mori, Y., and Nagashima F. (2018). Difference of horizontal-to-vertical spectral ratios of observed earthquakes and microtremors and its application to S-wave velocity inversion based on the diffuse field concept. *Earth, Planets and Space*. **70**, 1.

[65] Kawase, H., Sánchez-Sesma, F. J., Matsushima, S., (2011). The Optimal Use of Horizontal-to-Vertical Spectral Ratios of Earthquake Motions for Velocity Inversions Based on Diffuse-Field Theory for Plane Waves. *Bulletin of the Seismological Society of America*. **101(5)**, pp 2001-2014.

[66] Kim, B., Hashash, Y.M.A., Stewart, J.P., Rathje, E.M., Harmon, J.A., Musgrove, M.I., Campbell, K.W., and Silva, W.J. (2016). Relative differences between nonlinear and equivalent-linear 1D site response analyses. *Earthquake Spectra*. **32**, pp 1845-1865.

[67] Kishida,T., Bozorogina, Y., Abrahamson, N. A., Ahdi, S. K., Ancheta, T. D., Boore, D. M., Campbell, K. W., Darragh, R. B., Magistrale, H., Stewart, J. P., (2017). Development of the NGA-Subduction Database. *Proc. 16th World Conference on Earthquake Engineering*. Santiago, Chile (Paper No. 3452).

[68] Kishida, K., Giacinto, D.-D., Iaccarino, G. (2017) Comparison of Manual and Automated Ground Motion Processing for Small- to-Moderate-Magnitude Earthquakes in Japan. *Earthquake Spectra*. **33(3)**, pp 875-894.

[69] Konno, K., and Ohmachi, T. (1998). Ground-motion characteristics estimated from spectral ratio between horizontal and vertical components of microtremor. *Bulletin of the Seismological Society of America*. **88(1)**, pp 228-241.

[70] Kramer, S.L. (1996). *Geotechnical Earthquake Engineering*. Prentice Hall.

[71] Ktenidou, O.-J., Cotton, F., Abrahamson, N. A., and Anderson, J. G. (2014). Taxonomy of κ: A review of definitions and estimation approaches targeted to applications. *Seismological Research Letters*. **85**, pp 135-146.

[72] Kwak, D.Y., Stewart, J.P., Mandokhai, S.?J., Park, D. (2017). Supplementing VS30 with H/V spectral ratios for predicting site effects. *Bulletin of the Seismological Society of America*. **107**, pp 2028-2042.

[73] Kwok, A.O.L., Stewart, J.P., Kwak, D.Y., Sun, P.-L. (2018). Taiwan-specific model for VS30 prediction considering between-proxy correlations. *Earthquake Spectra*. **34**, pp 1973-1993.

[74] Lachet, C., Hatzfeld, D., Bard, P.-Y., Theodulidis, N., Papaioannou, C., Savvaidis, A., (1996). Site effects and microzonation in the city of Thessaloniki (Greece) comparison of different approaches. *Bulletin of the Seismological Society of America*. (**86(6)**, pp 1692-1703.

[75] Lermo, J., Chávez-García, F. J., (1993). Site effect evaluation using spectral ratios with only one station. *Bulletin of the Seismological Society of America*. **83(5)**, pp 1574-1594.

[76] Menq, F., (2003). Dynamic properties of sandy and gravelly soils. *PhD Thesis*. Department of Civil Engineering, University of Texas, Austin, TX.

[77] Parker, G. A., Harmon, J. A., Stewart, J. P., Hashash, Y. M. A., Kottke, A. R., Rathje, E. M., Silva, W. J., Campbell, K. W. (2017). Proxy-Based V_{S30} Estimation in Central and Eastern North America. *Bulletin of the Seismological Society of America*. **107(1)**, pp 117-131.

[78] Parker, G. A., Stewart, J. P., Boore, D. M., Atkinson, G. M., Hassani, B. (2020). NGA-Subduction Global Ground-Motion Models with Regional Adjustment Factors. *PEER Report 2020/03*. Pacific Earthquake Engineering Research Center, Berkeley, CA.

[79] Pinheiro J., Bates D., DebRoy S., Sarkar D., R Core Team (2019). nlme: Linear and Nonlinear Mixed Effects Models. R package version 3.1-140.

[80] Rathje, E.M., Dawson, C., Padgett, J.E., Pinelli, J.-P., Stanzione, D., Adair, A., Arduino, P., Brandenberg, S.J., Cockeril, T., Esteva, M., Haan, F.L. Jr., Hanlon, M., Kareem, A., Lowes, L., Mock, S., and Mosqueda, G. (2017). DesignSafe: A new cyberinfrastructure for natural hazards engineering. *Natural Hazards Review*. **18(3)**.

[81] Robertson, P.K., (2012). James K. Mitchell Lecture: Interpretation of in-situ tests some insights. *Proc. 4th Int. Conf. on Site Charactrization, ISC4, Porto de Galinhas - Brazil, 3-24.*

[82] Rodriguez-Marek, A., Montalva, G. A., Cotton, F., Bonilla, F., (2011). Analysis of Single-Station standard deviation using the KiK-net Data. *Bulletin of the Seismological Society of America*. **101(3)**, pp 1242-1258.

[83] Rodriguez-Marek, A, Rathje, E.M., Bommer, J.J., Scherbaum, F., Stafford, P.J. (2014). Application of single-station sigma and site response characterization in a probabilistic seismic hazard analysis for a new nuclear site. *Bulletin of the Seismological Society of America*. **104**, pp 1601-1619.

[84] Rogers, A.M., Tinsley, J.C., and Borcherdt, R.D. (1985). Predicting relative ground response. *U.S. Geological Survery Professional*. Paper 1360, pp 221-248.

[85] Sadiq, S., Ilhan, O., Ahdi, S.K., Bozorgnia, Y., Hashash, Y.M.A., Park, D., Yong, A., and Stewart, J.P. (2018). A proposed seismic velocity profile database model. *11th National Conf. on Earthquake Engineering (11NCEE).* Earthquake Engineering Research Institute, Los Angeles, USA, 25?29 June 2018.

[86] Schnabel, P.B. (1973). Effects of local geology and distance from source on earthquake ground motions. *Ph.D. thesis*. University of California, Berkeley.

[87] SESAME, (2004). Guidelines for the Implementation of the H/V spectral ratio technique on ambient vibrations: Measurements, processing and interpretation: European Commission, Project No. EVG1-CT-2000-00026, accessed September 2012, at http://sesame.geopsy.org/Papers/HV_User_Guidelines.pdf

[88] Seyhan, E., Stewart, J. P. (2014). Semi-empirical nonlinear site amplification from NGA-West 2 data and simulations. *Earthquake Spectra*. **30(3)**, pp 1241-1256.

[89] Seyhan, E., Stewart, J.P., Ancheta, T.D., Darragh, R.B., and Graves, R.W. (2014). NGA-West 2 site database. *Earthquake Spectra*. **30**, pp 1007-1024.

[90] Silva, W., Darragh, R.B., Gregor, N., Martin, G., Abrahamson, N., and Kircher, C. (1998). Reassessment of site coefficients and near-fault factors for building code provisions, Technical Report Program Element II: 98-HQ-GR-1010, Pacific Engineering and Analysis., El Cerrito, California USA.

[91] Stafford, J.S., Rodriguez-Marek, A., Edwards, B., Kruiver, P.P., and Bommer, J.J., (2017). Scenario dependence of linear site-effect factors for short-period response spectral ordinates. *Bulletin of the Seismological Society of America*. **107**, pp 2859-2872.

[92] Stewart, J. P., Afshari, K., Goulet, C. A. (2017). Non-Ergodic site response in seismic hazard analysis. *Earthquake Spectra*. **30(3)**, pp 1241-1256.

[93] Stewart, J. P., Afshari, K., Hashash, Y.M.A. (2014). Guidelines for performing hazard-consistent one-dimensional ground response analysis for ground motion prediction. *PEER Report 2014/16*. Pacific Earthquake Engineering Research Center, Berkeley, CA.

[94] Stewart, J. P., Liu, A. H., Choi, Y., (2003). Amplification factors for spectral acceleration in tectonically active regions. *Bulletin of the Seismological Society of America*. **93(1)**, pp 332-352.

[95] Tao, Y., Rathje, E.M. (2019). Insights into modeling small-strain site response derived from downhole array data. *Journal of Geotechnical and Geoenvironmental Engineering*. **145**, pp 04019023.

[96] Theodulidis, N., Archuleta, R. J., Bard, P.-Y., and Bouchon, M. (1996). Horizontal to vertical spectral ratio and geological conditions: The case of Garner Valley downhole array in southern California. *Bulletin of the Seismological Society of America*. **86**, pp 306-319.

[97] Thompson, E.M., (2018). An Updated Vs30 Map for California with Geologic and Topographic Constraints: U.S. Geological Survey data release. *DOI: 10.5066/F7JQ108S*.

[98] Thompson, E.M., Baise, L.G., Tanaka, Y., Kayen, R.E. (2012). A taxonomy of site response complexity. *Soil Dynamics and Earthquake Engineering*. **41**, pp 32-43.

[99] Thompson E.M., Wald, D.J., Worden, C.B. (2014). A Vs30 Map for California with Geologic and Topographic Constraints. *Bulletin of the Seismological Society of America*. **104**, pp 2313-2321.

[100] Tokimatsu, K., and Sekiguchi, T. (2006). Effects of nonlinear properties of surface soils on strong ground motions recorded in Ojiya during 2004 mid Niigata prefecture earthquake. *Soils and Foundations*. **46(6)**, pp 765-775.

[101] Tsai, Y-T, Brandenberg, S. J. , Mikami, A., Sato, T., Stewart, J. P. (2017). Dataset for empirical assessment of seismic performance for levees founded on peaty organic soils. *Proc. Geo-Risk 2017 : Impact of Spatial Variability, Probabilistic Site Characterization, and Geohazards*. Geotechnical Special Publication No. 285, Denver, CO.

[102] Tuan, T. T., Scherbaum, F. and Malischewsky, P. G. (2011). On the relationship of peaks and troughs of the ellipticity (H/V) of Rayleigh waves and the transmission response of single layer over half-space models. *Geophysical Journal International*. **184**, pp 793-800.

[103] Tukey, J. W. (1967). An introduction to the calculations of numerical spectrum analysis. *Spectral Analysis of Time Series*. pp 25-46.

[104] Urzúa, A., Dobry, R., and Christian, J.T. (2017). Is Harmonic Averaging of Shear Wave Velocity or the Simplified Rayleigh Method Appropriate to Estimate the Period of a Soil Profile?. *Earthquake Spectra*. **33(3)**, pp 895-915.

[105] Van Houtte, C., Drouet, C., Cotton, F. (2011). Analysis of the origins of κ (kappa) to compute hard rock to rock adjustment factors for GMPEs. *Bulletin of the Seismological Society of America*. **101**, pp 2926-2941.

[106] Vantassel, J., (2020). jpvantassel/hvsrpy: latest (Concept). Zenodo. http://doi.org/10.5281/zenodo.3666956.

[107] Wakamatsu, K., and Mastuoka, M. (2013). Nationwide 7.5-Arc-Second Japan Engineering Geomophologic Classification Map and V_{S30} Zoning. *Journal Disaster Research*. **8(5)**, pp 904-911.

[108] Wald, D.J., and Allen, T.I. (2007). Topographic slope as a proxy for seismic site conditions and amplification. *Bulletin of the Seismological Society of America*. **97**, pp 1379-1395.

[109] Wang, P., Stewart, J. P., Bozorgnia, Y., Boore, D. M. (2017). R Package for Computation of Earthquake Ground Motion Response Spectra. *Report No. 2017/09*. Pacific Earthquake Engineering Research Center, UC Berkeley, CA.

[110] Wathelet, M., Chatelain, J.-L., Cornou, C., Di Giulio, G., Guillier, B., Ohrnberger, M. and Savvaidis, A. (2020). Geopsy: A User-Friendly Open-Source Tool Set for Ambient Vibration Processing. *Seismological Research Letters*. **91(3)**, pp 1878-1889.

[111] Wills, C.J., and Clahan, K.B. (2006). Developing a map of geologically defined site-condition categories for California. *Bulletin of the Seismological Society of America*. **96**, pp 1483-1501.

[112] Wills, C.J., Gutierrez, C.I., Perez, F.G., and Branum, D.M. (2015). A Next Generation VS30 Map for California Based on Geology and Topography. *Bulletin of the Seismological Society of America*. **105**, pp 3083-3091.

[113] Xu, B., Rathje, E.M., Hashash, Y.M.A., Stewart, J.P., Campbell, K.W., and Silva, W.J. (2020). κ_0 for soil sites: Observations from Kik-net sites and their use in constraining small-strain damping profiles for site response analysis. *Earthquake Spectra*. https://doi.org/10.1177/8755293019878188.

[114] Yong, A., (2016). Comparison of measured and proxy-based VS30 values in California. *Earthquake Spectra*. **32**, pp 171-192.

[115] Yong, A, Hough, S.E., Iwahashi, J., and Braverman, A. (2012). A terrain based site conditions map of California with implications for the contiguous United States. *Bulletin of the Seismological Society of America*. **102**, pp 114-128.

[116] Yong, A., Martin, A., Stokoe II, K.H., and Diehl, J. (2013). ARRA-funded VS30 measurements using multi-technique approach at strong-motion stations in California and central-eastern United States. *U.S. Geological Survey Open-File Report*. 2013-1102.

[117] Zalachoris, G., Rathje, E.M. (2015). Evaluation of one-dimensional site response techniques using borehole arrays. *Journal of Geotechnical and Geoenvironmental Engineering*. **141**, pp 04015053.

[118] Zhao, J. X. et al., (2016a). Ground-Motion Prediction Equations for Subduction Interface Earthquakes in Japan Using Site Class and Simple Geometric Attenuation Functions. *Bulletin of the Seismological Society of America*. **106(4)**, pp 1518-1534.

[119] Zhao, J. X. et al., (2016b). Ground-Motion Prediction Equations for Subduction Slab Earthquakes in Japan Using Site Class and Simple Geometric Attenuation Functions. *Bulletin of the Seismological Society of America*. **106(4)**, pp 1535-1551.